NANOENGINEERED THIN FILMS FOR SOLID OXIDE FUEL CELLS

A Dissertation

by

QING SU

Submitted to the Office of Graduate and Professional Studies of
Texas A&M University
in partial fulfillment of the requirements for the degree of

DOCTOR OF PHILOSOPHY

Chair of Committee,	Haiyan Wang
Committee Members,	Perla Balbuena
	Andreas Holzenburg
	Xinghang Zhang
Head of Department,	Ibrahim Karaman

December 2013

Major Subject: Materials Science and Engineering

ABSTRACT

Solid oxide fuel cells (SOFCs) are very attractive as energy generation devices because of their high energy efficiency, flexible fuel selections and clean energy conversion. To avoid cell cracking and formation of non-conducting compounds at electrolyte/electrode interfaces issues caused by high operating temperatures (~1000 ℃ for conventional SOFCs), intermediate temperature SOFCs (ITSOFCs) in the range of 500-700 ℃ have attracted extensive research interests. However, the polarization loss of cathode and ohmic loss of electrolyte significantly increases under reduced temperatures which lead to decreased cell performance and power output. To address the above issues, the efforts in this work are focused on engineering microstructure of cathode, electrolyte and their interface to achieve high performance.

First, a bi-layer method has been developed to prepare $La_{0.5}Sr_{0.5}CoO_3$ (LSCO) cathode by combining a pulsed laser deposition (PLD) technique and a screen printing method. It provides a cost-effective approach to fabricate thick and high quality cathode films and the method could also be applied to many other cathode systems. Second, detailed PLD interlayer thickness effect is investigated. The mechanical and electrochemical properties of those hybrid cathodes are examined and correlated with the microstructure of the cells with different interlayer thicknesses. Third, partial oxygen pressure AC impedance study has been carried on those bi-layer cathodes with different interlayer thicknesses. The guidelines for designing high-performance bi-layer cathodes with optimum performance and low cost are proposed. Fourth, the design of a

$La_{0.8}Sr_{0.2}MnO_{3-\delta}/Zr_{0.92}Y_{0.08}O_2$ thin interlayer with a vertically-aligned nanocomposite (VAN) structure between the electrolyte and oxygen electrode is demonstrated for solid oxide reversible fuel cells. The VAN structure significantly improves the overall cell performance and also acts as a transition layer that improves adhesion and relieves both thermal stress and lattice strain. Fifth, Two-phase $(Ce_{0.9}Gd_{0.1}O_{1.95})_{0.5}/(Zr_{0.92}Y_{0.08}O_{1.96})_{0.5}$ nanocomposite thin films with vertically aligned structure are grown as the electrolyte for thin film solid oxide fuel cells (TFSOFCs). More than 50% increase in overall power density is achieved compared with that of the cells without VAN electrolyte.

DEDICATION

I dedicate this dissertation to my family and to my teachers.

ACKNOWLEDGEMENTS

No words can describe all my appreciation to my advisor, Dr. Haiyan Wang. She provides me a precious opportunity to study at Texas A&M University where group atmosphere is like a family. She guides me into the world of scientific research and helped me to build a strong ethic of working. Without her continuous guide and ongoing motivation, my research can never come this far. I was so lucky that I could study for my Ph.D. under her supervision and these four years will be the most important period of my life.

I would like to send my special appreciation to all my committee members, Dr. Perla Balbuena, Dr. Andreas Holzenburg and Dr. Xinghang Zhang for their great help and continued attention on my research work. Also, I thank the professors including Dr. Fred Strieter, Dr. Andreas Holzenburg, Dr. Xinghang Zhang, Dr. Miladin Radovic, Dr. Xing Chen, etc., for their great classes to offer me research background.

I want to thank all my lab friends, Sungmee Cho, Zhenxing Bi, Chen-Fong Tsai, JoonHwan Lee, Michelle Myers, Li Chen, Fauzia Khatkhatay, Aiping Chen, ZhuYuanyuan, Jiao Liang, Wenrui Zhang, Jie Jian, Clement Jacob and Tommy Lynch, for making my time at Texas A&M University a great experience. Special appreciation goes to our collaborators including Dr. Quanxi Jia at Los Alamos National Lab, Dr. Serquis at Centro Atómico Bariloche, Argentina, Dr. Jacobson at University of Houston and Dr. Manthiram at University of Texas at Austin for their great help on my research. I

would like also thank my friends, Dawei, Yue, Youxing, and Da! I had a more meaningful life in College Station together with you all.

Lastly, thanks to my family, particularly, my wife Li Zhang and my parents, for their love, support and encouragement. Thanks to my son, David Su, for making me to grow and carry responsibilities with love and gratitude.

TABLE OF CONTENTS

Page

ABSTRACT ii

DEDICATION iv

ACKNOWLEDGEMENTS v

TABLE OF CONTENTS vii

LIST OF FIGURES x

LIST OF TABLES xvii

1. INTRODUCTION 1

1.1 Overview 2
1.2 Fuel Cells 2
1.3 Solid Oxide Fuel Cells 5
1.4 Thin Film SOFC 11
1.5 SOFC Components 12
1.6 Thin Film Preparation Method 20
1.7 Challenges 25
1.8 Current Research Review on SOFCs 25
1.9 Solid Oxide Reversible Fuel Cells (SORFCs) 53
1.10 Summary 54

2. RESREACH METHODOLOGY 56

2.1 Pulsed Laser Deposition 56
2.2 Thin Film Microstructure and Crystalline Characterizations 64
2.3 AC Impedance Spectroscopy 79
2.4 Single Cell Power Measurement 81

Page

3. ENHANVED ELECTROCHEMICAL PROPERTIES OF BI-LAYER $La_{0.5}Sr_{0.5}CoO_{3-\delta}$ CATHODE PREPARED BY A HYBRID METHOD 83

3.1 Overview 83
3.2 Introduction 84
3.3 Experimental 86
3.4 Results and Discussion 88
3.5 Conclusions 98

4. EFFECT OF INTERLAYER THICKNESS ON THE ELECTROCHEMICAL PROPERTIES OF BI-LAYER CATHODES FOR SOLID OXIDE FUEL CELLS 99

4.1 Overview 99
4.2 Introduction 100
4.3 Experimental 102
4.4 Results and Discussion 105
4.5 Conclusions 120

5. OXYGEN PARTIAL PRESSURE IMPEDANE STUDIES OF INTERLAYER EFFECT ON POROUS ELECTRODES OF $La_{0.5}Sr_{0.5}CoO_{3-\delta}$ 121

5.1 Overview 121
5.2 Introduction 122
5.3 Experimental 124
5.4 Results and Discussion 126
5.5 Conclusions 142

6. VERTICALLY ALIGNED NANOCOMPOSITE ELECTROLYTES WITH SUPERIOR OUT-OF-PLANE IONIC CONDUCTIVITY FOR SOLID OXIDE FUEL CELLS 144

6.1 Overview 144
6.2 Introduction 145
6.3 Experimental 149
6.4 Results and Discussion 151
6.5 Conclusions 172

Page

7. VERTICALLY ALIGNED NANOCOMPOSITE $La_{0.8}Sr_{0.2}MnO_{3-\delta}/Zr_{0.92}Y_{0.08}O_{1.96}$ THIN FILMS AS ELECTRODE/ELECTROLYTE INTERFACIAL LAYER FOR SOLID OXIDE REVERSIBLE FUEL CELLS 173

7.1 Overview 173
7.2 Introduction 174
7.3 Experimental 177
7.4 Results and Discussion 179
7.5 Conclusions 193

8. SUMMARY AND CONCLUSIONS 194

REFERENCES 198

LIST OF FIGURES

FIGURE		Page
1.1	Illustration of a fuel cell comprising of an electrolyte, an anode and a cathode	3
1.2	Summary of the five main types of fuel cells and their characteristics	4
1.3	Schematic diagram of a SOFC showing the roles of anode, cathode, and electrolyte	7
1.4	Actual and ideal cell potential in SOFCs	9
1.5	Three types of thin film SOFCs configurations	12
1.6	Schematic diagram of Ni/YSZ anode three-phase boundaries shows charge transportation and chemical reactions	15
1.7	(a) Schematic representation of the screen-printing process. (b) The typical screen printing mask and samples prepared by screen printing	22
1.8	The examples of different microstructure achieved by pulsed laser deposition (a) vertically aligned nanocomposite, (b) nanoporous film	24
1.9	The fluorite structure of solid oxide electrolyte	27
1.10	Comparison of ionic conductivity of various solid oxide electrolytes. Stabilized bismuth oxides (ESB-$Er_{0.4}Bi_{1.6}O_3$ and DWSB-$Dy_{0.08}W_{0.04}Bi_{0.88}O_{1.56}$) show superior ionic conductivity compared with that of doped ceria (GDC-$Gd_{0.1}Ce_{0.9}O_{1.95}$ and SNDC-$Sm_{0.075}Nd_{0.075}Ce_{0.85}O_{2-\delta}$) and stabilized zirconia (YSZ-$Y_{0.16}Zr_{0.92}O_{2.08}$).	31
1.11	TEM micrograph showing a cross sectional view of an eight-layer Gd_2O_3-doped CeO_2 and ZrO_2 film grown on Al_2O_3(0001)	33
1.12	Plot of the measured parallel conductivity enhancement as a function of misfit	35
1.13	Schematic representations of different cathode reaction mechanisms. The cathode is a (a) poor or (b) good ionic conductor	38

FIGURE Page

1.14 Unit cell representing the ABO_3 perovskite structure 41

1.15 (a) Polyhedral view of a K_2NiF_4 structure consisting of a succession of ABO_3 perovskite layers alternating with AO rock salt layers. (b) Schematic illustration of a double perovskite structure with composition $AA'Co_2O_{5+x}$ where B ions are coordinated in pyramids (BO5) and octahedra (BO6) with oxygen vacancies along (1 0 0) in the A plane 44

1.16 (a) Schematic illustration of a symmetric cell and a VAN interlayer where ‘‘L’’ and ‘‘C’’ stand for LSCO and CGO columns, respectively. (b) High-resolution TEM images of a typical LSCO/CGO VAN structure grown by PLD on STO substrate 52

2.1 Schematic illustration of a single target pulsed laser deposition system ... 57

2.2 Schematic illustration of the laser target interaction stages during the short pulsed laser period 60

2.3 Schematic illustration shows the four different phases presented during the laser-target interaction 62

2.4 (a) A two dimensional periodic array of atoms forming different planes in the crystal, (b) diffraction of a set of planes with inter-plane distance d followed by Bragg’s Law 65

2.5 The illustration of a typical TEM system with analytical capabilities 68

2.6 The intensity of the Airy rings from two neighboring pinholes. A resolution limit of $d_1/2$ is given by the intensity distributions from each of the pinholes separately and the maximum intensity from one pinhole coincides with the first minimum from the other 70

2.7 Two basic operation modes of TEM system: (a) the diffraction mode and (b) the imaging mode 71

2.8 Multiple steps in the calculation of a high-resolution TEM image by the multi-slice method 73

2.9 Schematic diagram of the scanning of convergent probe for STEM imaging. 75

FIGURE Page

2.10 Schematic illustration of typical SEM equipment 78

2.11 (a) AC impedance analysis through a sinusoidal current or voltage perturbation which is measured and analyzed in terms of gain and phase shift as a function of frequency (w). (b) A typical example of equivalent circuit for fitting the impedance curve. (c) Example of impedance plot of a dense $La_{0.5}Sr_{0.5}CoO_{3-\delta}$ film on single-crystal YSZ at 750 ℃..... 80

2.12 Schematically illustration of the SOFC power measurement 82

3.1 XRD θ-2θ plots for (A) LSCO powders for screen printing, (B) screen printing LSCO film on CGO pellet and (C) bi-layer LSCO film..... 88

3.2 Plan-view SEM images of screen printing LSCO layer (A) directly on CGO pellet, (B) on PLD LSCO layer deposited at RT, (C) on PLD LSCO layer deposited at 300 ℃ and (D) on PLD LSCO layer deposition at 500 ℃. (E) Cross-sectional TEM image of screen printing LSCO on PLD seed layer deposited at 500 ℃. All samples were annealed at 1150 ℃ for 2 hours 90

3.3 (A) The equivalent circuit model used to fit the impedance data and the impedance spectra of the SP LSCO/PLD LSCO/CGO/PLD LSCO/SP LSCO symmetrical cell collected at 873K and pO_2=0.2 atm. The PLD LSCO layers were deposited at (B) RT and (C) 500 ℃. The points are experimental data and the lines are fitted data..... 92

3.4 The ASR of the symmetric cells with and without PLD LSCO layer as a function of measurement temperature at pO_2=0.2 atm 95

3.5 Plan-view (A, C, E) and cross section SEM images (B, D, F) of screen printing LSCO layer on the PLD seed layer after impedance measurement. The PLD layers were deposited at (A) and (B) RT; (C) and (D) 300 ℃; (E) and (F) at 500 ℃..... 97

4.1 The X-ray diffraction (XRD) patterns of the LSCO cathode film with and without the PLD interlayer. The inset shows a magnification of XRD peaks around 47.5 degree. The symbol * refers to LSCO peak and the symbol # refers to CGO peak. 105

FIGURE Page

4.2 Cross-section SEM images of screen printing LSCO layer (a) directly on CGO pellet, on PLD LSCO interlayer with different thickness (b) 53 nm, (c) 106 nm, (d) 530 nm. All samples were annealed at 1150 ℃ for 2 hours 107

4.3 The plan-view SEM images of screen printed cathode (a) without and (b) with PLD interlayer and (c) the cross-section TEM image of bi layer cathode 108

4.4 (a) The specific impedance data of symmetric cells with cathode prepared by the screen printing only method and the hybrid method with 500 nm PLD interlayer at 600 ℃ and (b) the ASR of the symmetric cells with different PLD LSCO interlayer thickness and without PLD LSCO layer as a function of measurement temperature in air. The inset in (b) shows a magnified ASR plot of the symmetric cells with PLD LSCO interlayer thickness range from 106 nm to 530 nm at 600 ℃ 111

4.5 The hardness and ASR at 600 ℃ of the symmetric cells as the function of PLD LSCO interlayer thickness 113

4.6 The proposed scheme of different microstructure (a) and the different microstructure of single cells: (b) without PLD LSCO interlayer, (c) with ~100 nm PLD LSCO interlayer 115

4.7 The power density of single cells with and without PLD LSCO interlayer from 650 ℃ to 800 ℃ 117

4.8 The cross-section SEM images of single cells (a) without and (b) with the PLD interlayer after power density measurement 119

5.1 The cross-sectional SEM images the cathode films (a) without and (b) with the LSCO PLD interlayer. The magnified image exhibits the vertical LSCO nanocolumns with nanopores in between 127

5.2 A typical AC impedance spectrum of the LSCO/CGO/LSCO symmetrical cell 129

5.3 The temperature dependence of the area specific resistances for the symmetrical cells at different oxygen partial pressures 131

5.4 Impedance curves by the curve fitting using the equivalent circuit model 132

FIGURE Page

5.5 The temperature dependence of the surface exchange resistances for the symmetrical cells at different oxygen partial pressures 134

5.6 Dependence of the surface exchange on oxygen partial pressure. The numbers are the exponents in a $(pO_2)^{-n}$ fit..... 136

5.7 ln(j)-η_{act} plots for LSCO cathode with different interlayer thicknesses at 700 ℃..... 138

5.8 The temperature dependence of the oxygen mass transfer resistances for the symmetrical cells at different oxygen partial pressures 141

6.1 (a) Illustration of a conventional thin-film multilayers strategy with lateral interfaces to enhance the in-plane ionic conductivity where "Y" and "G" stands for YSZ and GDC electrolyte, respectively. (b) Schematic diagram of a self-assembled vertically aligned nanocomposite (VAN) film with vertically aligned interfaces to increase the out-of-plane ionic transportation..... 148

6.2 X-ray diffraction (XRD) pattern of (a) the YSZ and GDC composite target showing no inter-reaction between YSZ and GDC and (b) a typical YSZ/GDC nanocomposite film deposited at 10 Hz showing an epitaxial growth of YSZ/GDC nanocomposite film. (c) Illustration of YSZ and GDC 45 degree in-plane rotation matching on STO substrate ... 153

6.3 Cross-sectional TEM images for the YSZ/GDC nanocomposite films on STO(001) deposited at a) 1 Hz and b)10 Hz, which clearly demonstrate different column size by different deposition frequencies. The selected area electron diffraction (SAED) patterns of YSZ/GDC nanocomposite films on STO(001) deposited at c) 1 Hz and d)10 Hz indicating a 45 degree rotation matching on STO substrate. The cross-sectional STEM images e) and f) plan-view TEM images of YSZ and GDC nanocomposite thin film show the phase separation and arrangement 156

6.4 An Arrhenius plot of ionic conductivity as a function of temperature showing enhanced ionic conductivity for YSZ/GDC VAN electrolyte compared to pure GDC and YSZ thin film. The inset is a specific impedance plot of GDC film and YSZ and GDC VAN film at 600 ℃..... 158

6.5 (a) Cross-sectional HRTEM image of YSZ/GDC VAN thin film and (b) its corresponding FFT image suggest the strain coupling along the vertical YSZ/GDC interfaces 161

FIGURE Page

6.6 Cross-sectional backscattered SEM images of single cells with VAN electrolyte a) in the middle of YSZ and GDC electrolyte and b) on the top of YSZ and GDC electrolyte 163

6.7 (a) Schematic illustration of YSZ/GDC composite electrolyte coated on polycrystalline substrate, (b) cross-sectional TEM image of YSZ/GDC composite electrolyte coated on polycrystalline substrate showing alternating YSZ and GDC columns either vertical aligned or slightly tilted, (c) high resolution TEM image and (d) STEM image of YSZ/GDC composite electrolyte demonstrating dual-phase electrolyte without formation of solid solution 165

6.8 The power densities of single cells a) without VAN, (b) with VAN in middle of the electrolyte and (c) on the top of the electrolyte, demonstrating the enhanced cell performance by applying VAN electrolyte. (d) The V-I curve of the single cells with and without VAN electrolyte at 800 ℃ 169

6.9 The post measurement backscattered SEM images of single cell with YSZ/GDC VAN electrolyte (a) in the middle and (b) on the top, showing excellent cell integrity after high temperature cell measurement 171

7.1 Schematic diagram of an anode supported single cell with VAN interlayer where “L” and “Y” refer, respectively, to LSM and YSZ columns 177

7.2 XRD pattern of LSM/YSZ composite film deposited at 700 ℃ 181

7.3 (a) The cross-sectional TEM images for the LSM/YSZ nanocomposite films on STO (001) deposited at 10 Hz. (b) The cross-sectional STEM images of LSM and YSZ nanocomposite thin film 182

7.4 Plan-view SEM images of the screen printing LSM/YSZ cathode (a) with and (b) without VAN interlayer 184

7.5 (a) The equivalent circuit model used to fit the impedance data and (b) the typical impedance plot the LSM/YSZ cathode with and without VAN interlayer at 700 ℃ showing the enhanced electrochemical performance for cathode with VAN. The inset table lists fitting results for the LSM/YSZ cathode with and without VAN interlayer 186

FIGURE Page

7.6 An Arrhenius plot of ASR of LSM/YSZ cathode with and without VAN interlayers as a function of temperature 188

7.7 I–V curve of the anode-supported single cells (a) without and (b) with the LSM/YSZ interlayer at different temperatures of 650 ~ 800 ℃ 190

7.8 The after-measurement cross-sectional SEM images of LSM/YSZ cathode with VAN interlayer 192

LIST OF TABLES

TABLE		Page
1.1	A summary of typical materials for SOFC components	13
1.2	Summary of oxygen self-diffusion and oxygen surface exchange data and overall conductivity for different SOFC cathode materials.....	39

1. INTRODUCTION

This chapter presents the motivation and objectives of the research in this dissertation. It is now well known that carbon dioxide (CO_2) gas emission from fossil fuel combustion leads to not only global warming but also the environmental concerns including air pollution, acid precipitation, ozone depletion.[1] New clean energy forms that are more environmental benign, are greatly needed. Fuel cell, typically solid oxide fuel cells (SOFCs), is a device that directly converts chemical energy in fuel to electrical energy with high energy conversion efficiency. It meets the requirement to reduce the fossil fuel consumption and increase the environmental friendly energy supply so as to become one of the most promising candidates for future power generation systems. This chapter reviews the background and current status of SOFCs, and summarizes the recent work to enhance the performance of SOFCs and the prospective of microstructure engineering of SOFCs.

The introduction section starts with a brief introduction on fuel cells and SOFCs as well as their working principles. Thin film SOFCs and three major SOFC components are introduced in Section 1.4 and 1.5. Various thin film preparation methods are introduced in Section 1.6. Challenges and current research areas are reviewed for electrolyte and cathode based on materials exploration and materials microstructural engineering approaches.

1.1 Overview

Over the past several decades, SOFCs have been widely studied as a promising candidate for clean power generation. The main barrier for SOFCs is decreased cell performance at intermediated operating temperatures. To overcome such barrier, microstructure engineering presents novel approaches to achieve enhanced cell performance in intermediated temperature range. This work focuses on minimizing the polarization loss of cathode and ohmic loss of the electrolyte by nano-engineering cathode, electrolyte and their interface.

1.2 Fuel Cells

Fuel cells are energy conversion devices that are used to directly convert the chemical energy of a fuel gas to electrical energy or heat. Without the need for direct combustion as an intermediate step, they give much higher conversion efficiency than conventional methods. The basic structure of fuel cells are consists of a porous anode, a porous cathode and a dense electrolyte layer in between seen as Fig 1.1. Typically, fuel cells generate electricity inside a cell through electrochemical reactions when a constant fuel is supplied to the anode side and an oxidant is fed to the cathode. [2] It could continuously operate as long as both reactant and oxidant are provided.

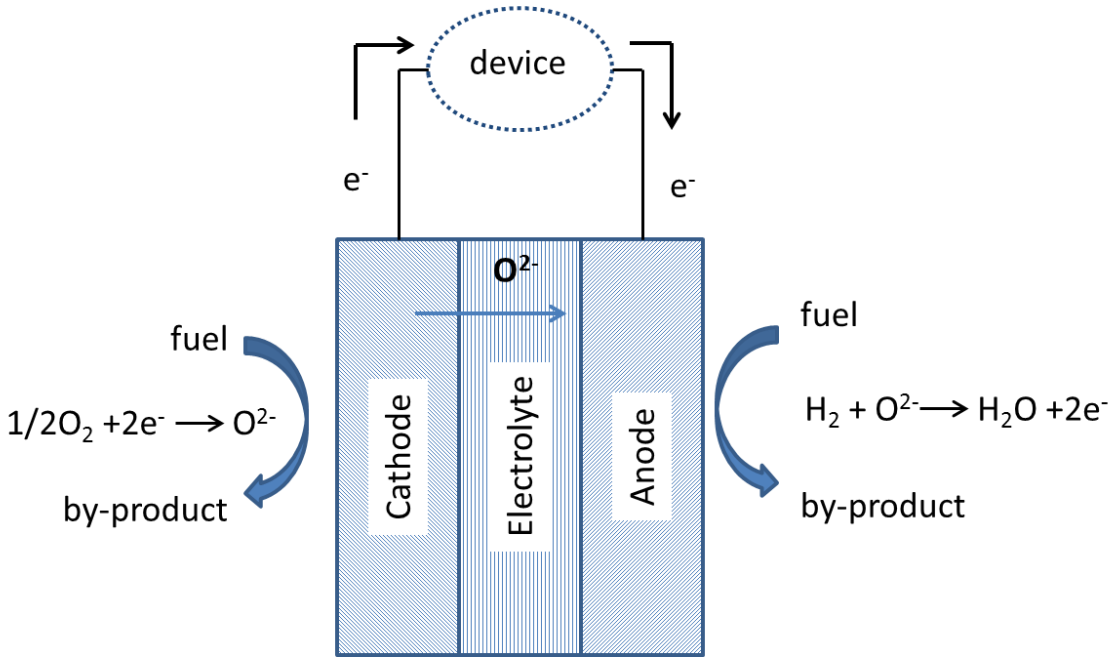

Fig.1.1. Illustration of a fuel cell comprising of an electrolyte, an anode and a cathode.

Based on the working mechanism and selection of the electrolyte, fuel cells can be classified into five major types, i.e., polymer electrolyte fuel cell (PEFC), alkaline fuel cell (AFC), phosphoric acid fuel cell (PAFC), molten carbonate fuel cell (MCFC), and SOFC as shown in Fig.1.2.[3] For example, PEFC and PAFC are with proton-conducting electrolyte while MCFC, SOFC and AFC conducts CO_3^{2-} ions, O^{2-} ion, OH^- ions, respectively. Furthermore, these fuel cells can also be classified by the operating temperature, which plays a determining role in the fuel processing and electrolyte materials selections. AFC, PEMFC, and PAFC usually work at lower temperature and essentially require relatively pure hydrogen to be supplied to the anode ensuring the

good overall power output. Compared with other types of fuel cells, MCFC and SOFC which operate at higher temperatures are capable of oxidizing not only hydrogen, but both CO and H_2. It offers advantages in fuel diversity.

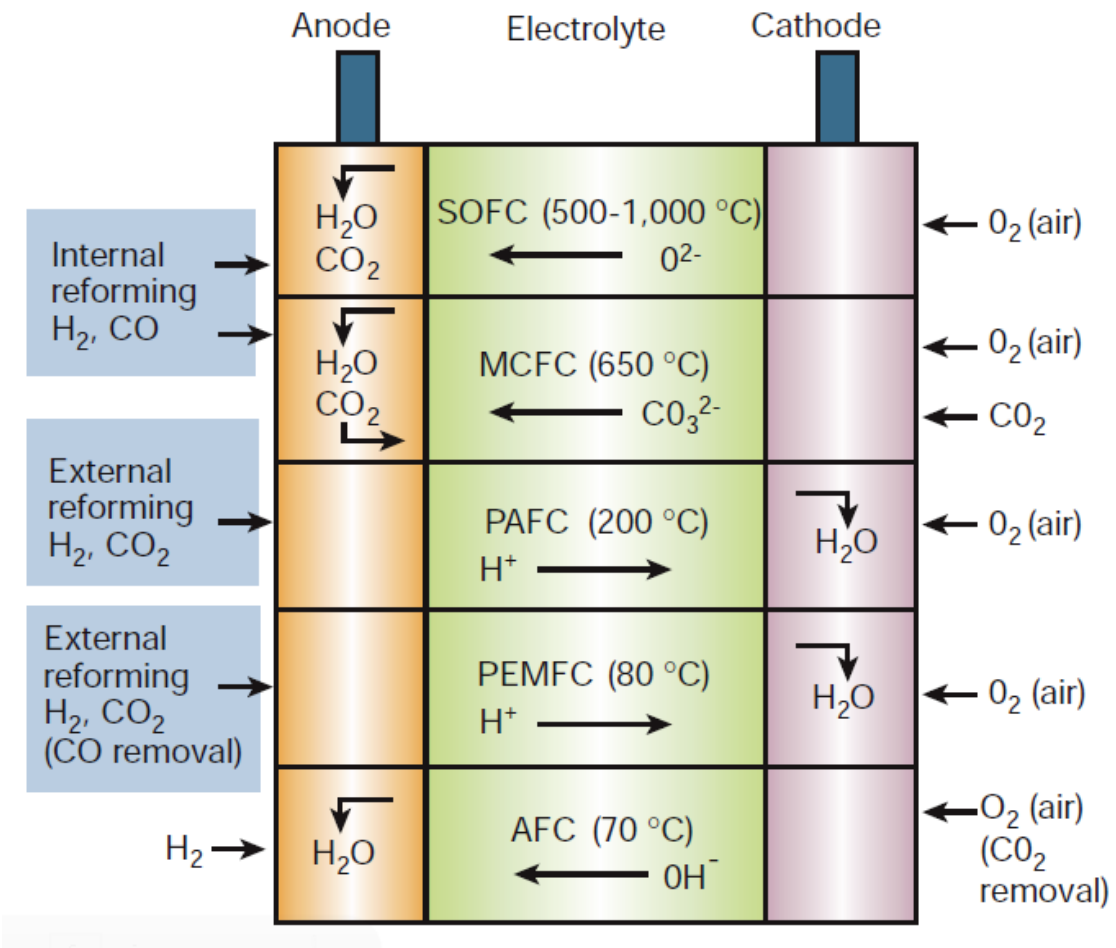

Fig.1.2. Summary of the five main types of fuel cells and their characteristics. Reproduced with permission from ref 3. Copyright 2001 Nature Publishing Group.

1.3 Solid Oxide Fuel Cells

Solid oxide fuel cells, as one type of fuel cells, have received wide research attention because they are one of the most efficient, environmentally clean and effective energy sources which convert chemical energy of a fuel gas directly into electrical energy. [4-6] All cell components are made of complex oxides and oxygen ion in SOFCs acts as charge carrier. Usually, high operating temperatures (800-1000 ℃) is adopted to ensure an adequate ionic and electronic conductivity.

The high operating temperature enables fast electrochemical kinetics of the electrode materials providing possibility to replace platinum catalyst. In addition, waste heat can be recycled and utilized for maintaining the system temperature resulting in even higher fuel utilizing efficiency. Because the high operating temperature enables the internal in situ reforming hydrocarbons, variable fuels including hydrogen, hydrocarbons, and H_2/CO mixture gas can be used as a fuel in the cell.[7, 8]

SOFC could be combined and stacked together to provide desirable voltage and power output for various applications including mobile, military, vehicle, auxiliary power unit, and large-scale stationary systems. One of the most promising applications for SOFCs is large stationary power generation plant (>100 MW) with coal as the primary fuel. In addition, SOFC portable charging systems for mobile devices such as smart phones, mobile handsets, digital cameras, MP3 music/video players, etc. came into market recently. It is expected to provide solutions to the challenges in finding clean energy technology for the world.

1.3.1 Principles of SOFC

SOFC, as an all solid state power system, generates electricity by conducting the electrochemical reactions at the electrodes. The fuel and the oxidant are supplied to porous catalytic anode and cathode respectively, and the existing electrochemical potential enables the chemicals to react. The dense electrolyte provides ion (negative) transport channels and avoid fuel and oxidant mixing and as shown in Fig 1.3. For example, oxygen will be reduced at the cathode via the half-cell reaction:

$$2e^- + \tfrac{1}{2} O_2 \rightarrow O^{2-}$$

Thus O^{2-} ions will transport through the electrolyte and react with the fuel (for this case, hydrogen) at the anode to form a circuit. The electron flow will deliver portion of the reversible work of the reaction to the external circuit. The internal losses in the cell including the ohmic resistance of the electrolyte, as well as the overpotential losses at the anode and cathode, determine the percentage of reversible work converted to electrical work. [9]

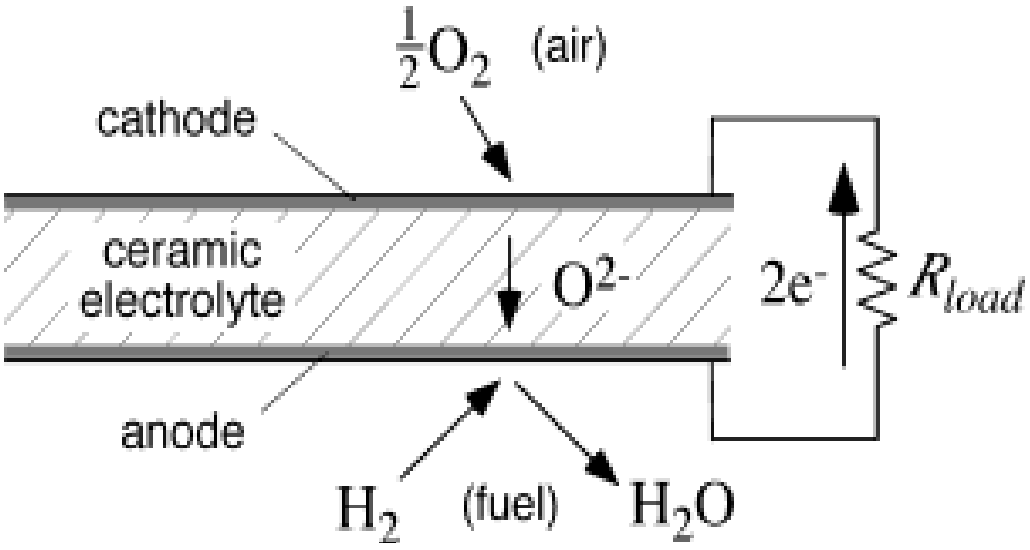

Fig.1.3. Schematic diagram of a SOFC showing the roles of anode, cathode, and electrolyte.

1.3.2 Nernst Equation and Irreversible Polarization Loss for SOFCs

The reversible potential of fuel cells can be expressed by Nernst equation 1.1 as [10]

$$E = E^0 + \frac{RT}{nF} \ln\left(\frac{P_{H_2} * P_{O_2}^{1/2}}{P_{H2O}}\right) \quad (1.1)$$

It provides a relationship between the ideal equilibrium potential (E) and the ideal potential (E°) when the cell reaction takes place at a different partial pressure of reactants and products. From the Nernst equation, it is expected that the cell potential increases in the overall cell reaction when there is an increase in the partial pressure of the reactants and a decrease in the partial pressure of the products. For instance, by

increasing the oxygen and hydrogen pressures, the ideal equilibrium potential at a given temperature can be increased.

Under the standard condition for SOFCs, the ideal potential of a fuel cell (E°) is 1.229 volts which is proportional to the change in the standard Gibbs free energy in the fuel cell system. The actual cell potential is always lower than its equilibrium potential due to irreversible losses of polarization, and overpotential. They are divided into three main polarizations: activation polarization (η_{act}), ohmic polarization (η_{ohm}) and, concentration polarization (η_{conc}) seen as in Fig 1.4.[11] In the low current density regime, the activation polarization is dominated by the rate of the electrochemical reaction in the electrodes which is mainly due to the oxygen reduction into oxygen ion process. The ohmic polarization which results from the resistance of oxygen ions transportation through the electrolyte becomes the main loss in intermediated current density regime. Finally, the concentration polarization corresponds to mass transfer between the flow channel and the active reaction zone. It becomes prominent in high current density regime where it is difficult to supply sufficient reactant flow to the cell reaction sites.

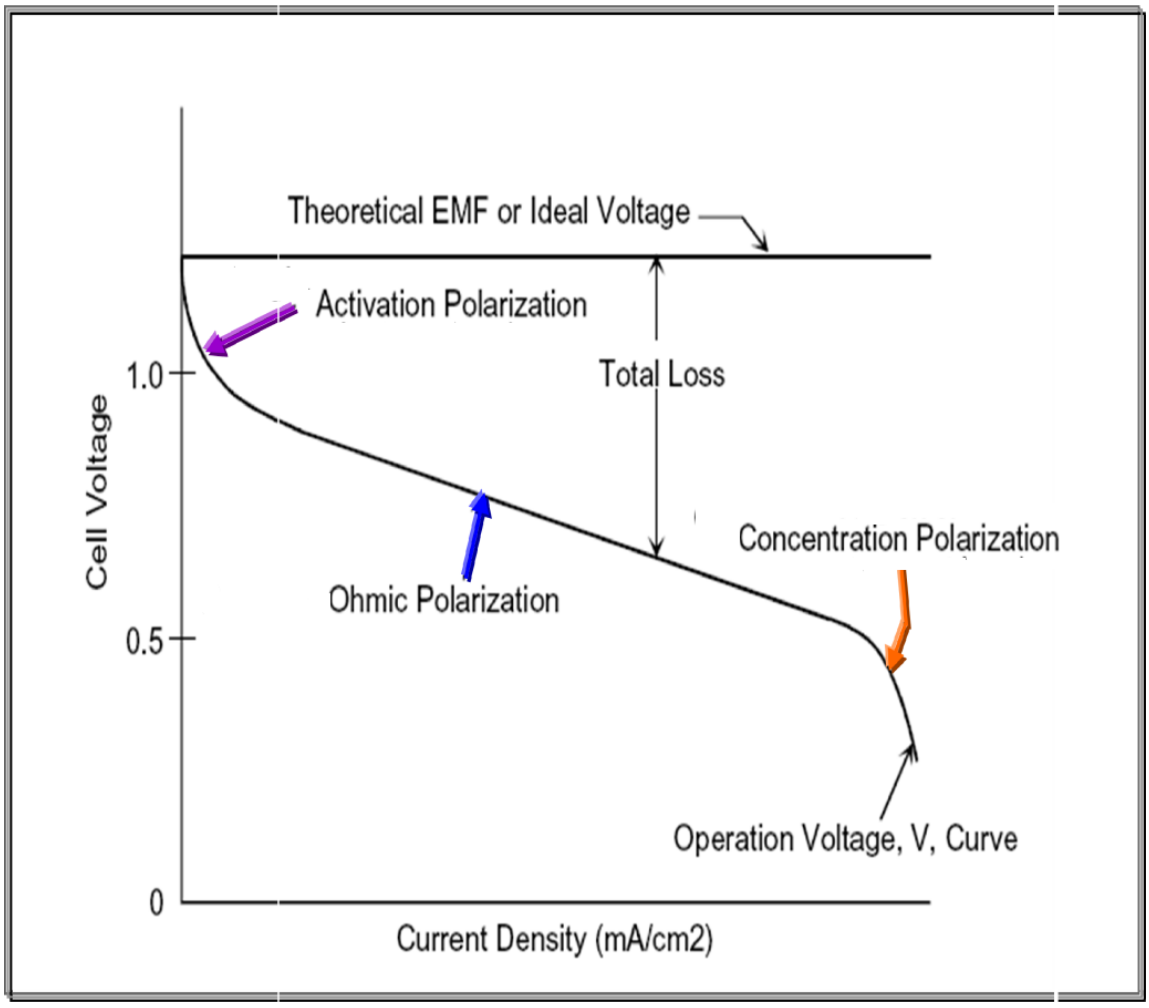

Fig.1.4. Actual and ideal cell potential in SOFCs.

1.3.3 Advantages and Disadvantages of SOFC

The advantages and disadvantages of the SOFC are based on its material selection, fabrication techniques, and different system requirements. [12]

First, compared with fuel cells based on liquid electrolytes, SOFCs have the advantages of vibration free, higher system efficiency, higher power density, and simpler designs than other types of fuel cell. Several main aspects of SOFCs benefits are listed as follows:

(1) The high efficiency of SOFC could reach up to 70% in pressurized hybrid system compared with 30-40% efficient for engines and modern thermal power plants.

(2) Additional power can be produced by taking advantages of its waste heat.

(3) Because the byproduct is steam rather than liquid water, water management is not required.

(4) SOFCs can be used to utilize various fuels including propane, butane, CO_2, CH_4, N_2, and CO.

On the other hand, due to a high operating temperature (800-1000 ℃) in SOFCs, it decreases the cell lifetime and limit the materials selections, leading to increase the overall cost of the fuel cell substantially. The disadvantages of SOFC also include:

(1) Material costs especially for interconnect and construction materials are high.

(2) The degradation of the performance of stack components takes place due to the use of volatile chromium containing ceramics and alloys.

(3) The high operating temperature leads to corrosion and breakdown of cell components.

(4) It suffers from low start-up rate.

1.4 Thin Film SOFC

Because of issues caused by high operating temperatures (800-1000 ℃), intermediate temperature (600–800 ℃) SOFCs are proposed to lower materials and manufacture cost, enhance structural integrity of the cells, extend selection of materials, and increase lifetime of the cells.[1, 3, 13, 14] However, the oxygen electrode polarization resistance significantly increases at low operating temperatures and ionic conductivity of electrolyte greatly reduces. Both become the major limiting factors in the overall performance of the intermediate temperature SOFCs. Thin film SOFC comes as one of the main research focuses for intermediate temperature SOFCs. For example, to overcome the ionic conductivity reduction at low temperature, one way is to reduce the electrolyte layer thickness by thin film approach. To replace the conventional thick YSZ electrolyte, several thin film deposition techniques including Chemical vapor deposition (CVD), PLD, sol-gel deposition and sputtering have been adopted to fabricate thinner electrolyte. [15-19] In the past few decades, there is a progressive trend towards fabricating thinner SOFC components, especially for electrolyte. It is a determining factor for enhancing SOFC performance, e.g., the thickness of the electrolyte must be reduced from ~200μm to a few microns to minimize the ohmic polarization loss and avoid the compromising power output at low operating temperatures. Thin film SOFC also has other advantages including easiness of processing, miniaturization and stacking. The schematic diagram illustrates three typical types of thin film SOFC configurations as shown in Fig 1.5. At least one component of the SOFC should be thicker than 30μm to ensure the structural integrity of the fuel cell. Compared with cathode-supported and

electrolyte-supported SOFC, anode-supported SOFC has superior performance because of thinner cathode and electrolyte, and low polarization resistance from thick anode disk. [20]

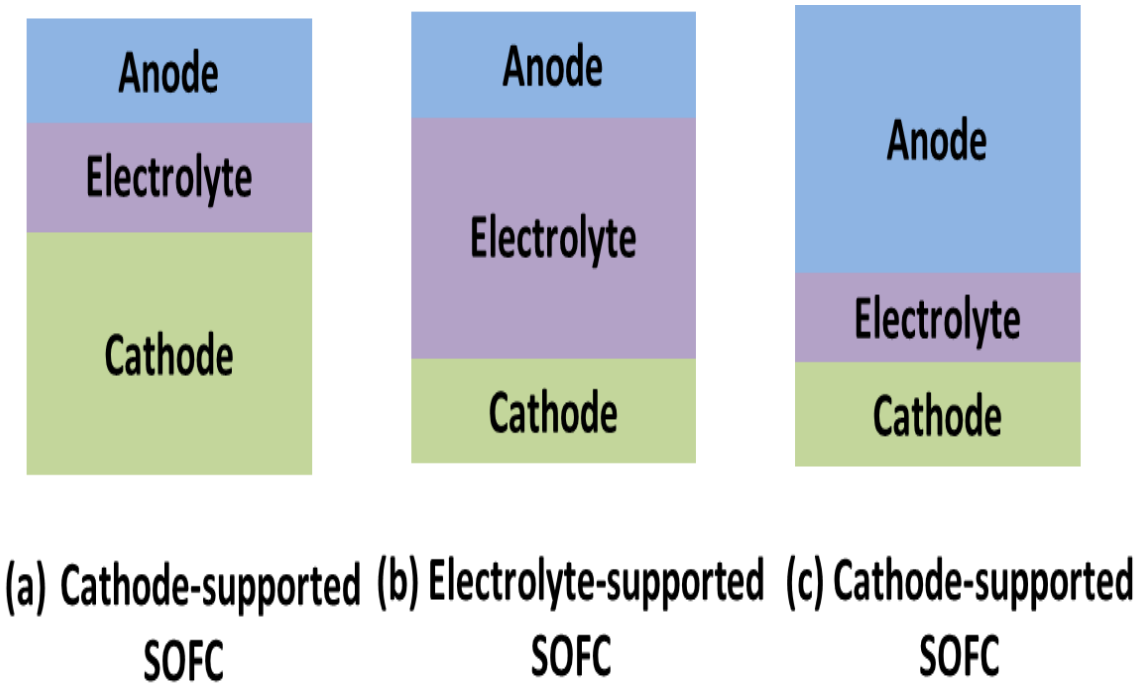

Fig 1.5. Three types of thin film SOFCs configurations.

1.5 SOFC Components

Generally, SOFCs are composed of three main components: cathode, electrolyte and anode. The general requirements for electrode are high catalytic activity, high electric conductivity and high porosity to allow gas transport to the reaction sites. For electrolyte, it needs to be fully dense to separate the oxidant and fuel gas with good

mechanical stability and high ionic conductivity. In addition, all components should have the chemical/mechanical stability (e.g., chemical phase, morphology), chemical compatibility and comparable thermal expansion coefficient with other components. A summary of typical materials for SOFC components is listed as Table 1. 1. [21]

Table 1.1. A summary of typical materials for SOFC components.

Components	**Materials**	**TEC ($*10^{-6}K^{-1}$)**
Electrolyte	**$Ce_{0.8}Sm_{0.2}O_{1.9}$**	**11.4**
	$Ce_{0.8}La_{0.2}O_{1.9}$	**11.8**
	CeO_2	**11.8**
	8 mol% YSZ	**10.3**
Cathode	**$LaMnO_3$**	**11.2**
	$La_{0.8}Sr_{0.2}MnO_3$	**12.4**
	$La_{0.6}Sr_{0.4}Co_{0.2}Fe_{0.8}O_{3-x}$	**12.5**
	$La_{0.5}Sr_{0.5}CoO_{3-x}$	**20.0**
Anode	**Ni-YSZ**	**11-12**
Interconnect	**Fe-Cr-Ni alloy**	**15-20**
	$La_{0.8}Sr_{0.2}CrO_3$	**11.1**
	$La_{0.9}Cr_{0.1}Mg_{0.1}O_3$	**9.5**

1.5.1 Anode

The anode materials have to meet a number of requirements including a stable porous microstructure where it allows the fuels easily transport to the electrolyte, desirable electronic and ionic conductivity, and good catalytic activity. In addition, they must be stable to avoid reactions with sulfur containing molecules and carbon dioxide when operated on hydrocarbon fuels. [22-24] In general, the selection of anode material depends on the properties of a specific electrolyte. The electrochemical reactions are thought to take place at the triple phase boundaries (TPBs) which are the boundaries of electrode, electrolyte and gas phase. In addition, it contains several physical and chemical processes including oxygen ion conducting, electron conducting, and the fuel gas phase diffusion and chemical reaction.[25] Schematic diagram of Ni/YSZ anode three-phase boundaries in Fig. 1.6 shows electronic and ionic charge transfer and chemical reactions at the boundaries.

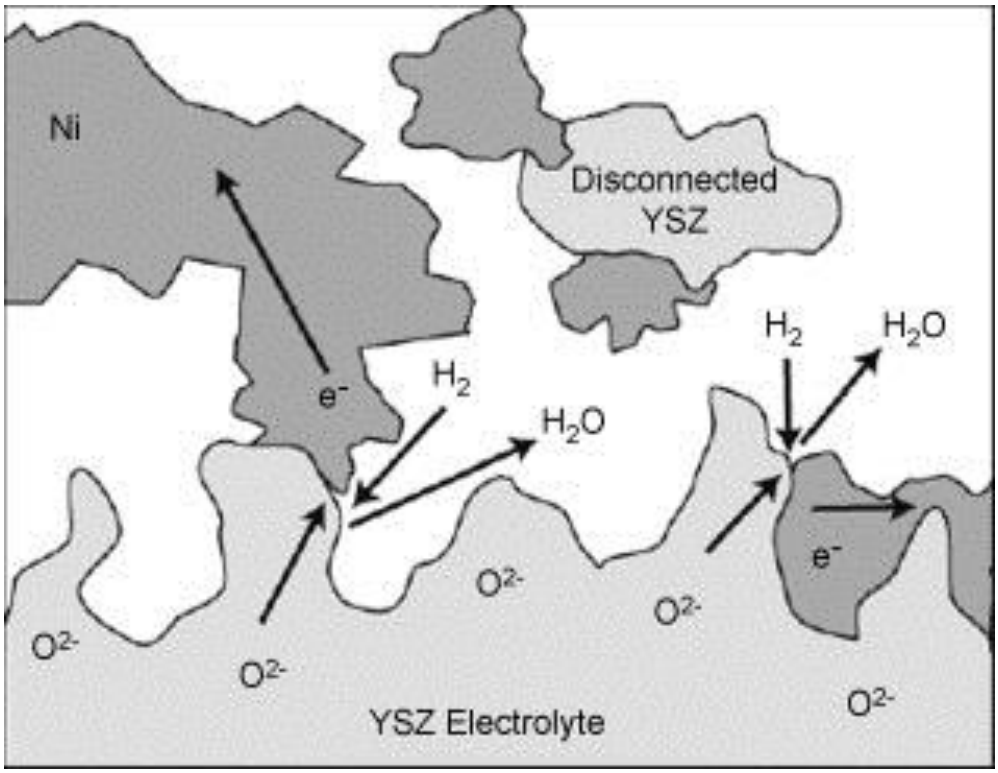

Fig. 1.6. Schematic diagram of Ni/YSZ anode three-phase boundaries shows charge transportation and chemical reactions. Reprinted with permission from ref 25. Copyright 2007 Elsevier

The majority of anode research has focused on a ceramic metal mixture of nickel/yttria zirconia (Ni/YSZ) cermet because of its good chemical stability, catalytic activity, and cost-effectiveness operated at a high temperature of 1000 ℃. Besides, the cermet mixture with YSZ helps to match thermal expansion coefficient (TEC) with other cell components stabilizing the microstructure. In addition, there is no solid state reaction between NiO and YSZ except at very high temperatures, [26] therefore, cermets

could be easily prepared by co-sintering NiO and YSZ followed by hydrogen reduction. Nickel is an excellent and cost-effective catalyst for both hydrogen utilization and steam reforming, but carbon deposition and subsequent dissolution in nickel particles takes place when it is exposed to sulfur atmosphere. [27] An alternate approach has been used to replace the Ni component with cobalt, copper and other noble metals or replace YSZ with ceria-based oxide, other perovskite oxide.[28-32] Although impressive development has been achieved for alternative anode materials, further study is still ongoing to address the problems including the low electronic conductivity and the low catalytic activity compared with nickel.

A summary of the important requirements for the anode is given as follows[33]:

(1) Retaining porous microstructure with good electronic/ionic conductive phases.

(2) Comparable TEC with the electrolyte to avoid electrode cracking or delaminating.

(3) Low polarization resistance for electrochemical reaction.

(4) Long term chemical and mechanical stability in reducing conditions at high temperatures.

(5) High catalytic activity of the fuel so as to support electrochemical reaction with oxygen ions.

1.5.2 Electrolyte

The SOFC electrolyte is a dense ceramic oxide layer with high oxygen ion conductivity which allows the kinetics of the oxygen ion transport to be sufficient for the cell performance. Mainly three electrolyte systems as yttria stabilized zirconia (YSZ), gadolinium- or samarium-doped ceria (CGO or CSO) and strontium, magnesium-doped lanthanum gallate (LSGM) have been widely investigated for SOFCs. A combination of the ionic conductivity and accessible minimal electrolyte layer thickness determines the minimal operating temperature of these systems. Assuming an electrolyte thickness of 10 μm and an ionic conductivity of $1*10^{-2}$ $S{\cdot}cm^{-1}$, the minimal operating temperatures are ~700 ℃ for YSZ, ~550 ℃ for LSGM, and ~550 ℃ for CGO. [34]

Yttria-stabilized zirconia (YSZ), as most common and well-studied electrolyte, has a high oxygen ion conductivity of 0.1 S/cm at 1000 ℃.[35] Due to its low ionic conductivity, pure ZrO_2 does not serve as a good electrolyte. The substitution of Y^{3+} on Zr^{4+} cation generates oxygen vacancies as well as stabilizes cubic fluorite structure. YSZ has good high temperature mechanical and electrical properties. However, it tends to react with perovskite oxide electrodes containing lanthanum at high temperatures which leads to formation of $La_2Zr_2O_7$ resistive layers. In addition, the high operating temperature requirement limits material selections for SOFC components and reduces the life time of the cells.

Particularly, LSGM exhibits high oxygen ion conductivity (0.12 S/cm at 800 ℃) and is more compatible with perovskite cathode materials, e. g., lanthanum cobaltite.[36-38] However, the LSGM electrolyte suffers from the reaction with nickel electrodes

which causes incompatibility with anode materials. This drawback could be overcomed by adding a CeO_2 buffer layer between anode and LSGM electrolyte.

Ceria doped with rare earth metals oxide including 0.1-0.2 Gd_2O_3 and Sm_2O_3 has received wide research interests as an alternative electrolyte because of its high conductivity at lower temperatures than doped bismuth. [39, 40] Doped ceria oxides are more stable than bismuth oxides. However, the reduction of ceria from Ce^{4+} to Ce^{3+} takes place in reducing conditions, leading to increased electronic conductivity and decreased theoretical voltage. As the operating temperature decreases, the width of the electrolytic domain will increase and the electronic conductivity is no longer a problem at 500 ℃.[22]

Finally, the requirements of electrolyte for SOFC applications are summarized as below:

(1) Chemical, morphological stabilities under the oxidation and reduction conditions.

(2) Adequate ionic conductivity and low ohmic loss in the dual atmospheres.

(3) Chemical compatibility with other components.

(4) Full density to prevent gas cross-over and leakage.

1.5.3 Cathode

Cathode is a critical component in SOFCs because the oxidation reaction in cathode determines the overall efficiency of the fuel cell. [9, 41, 42] Typically, the cathodes must be porous to allow easy transportation of oxygen molecules to the

electrode/electrolyte interface. There are several material requirements for cathode. First, it must have high electro-catalytic activity and electronic conductivity to minimize the ohmic and polarization resistance. Electrons which are produced or consumed by the oxygen reduction reactions at the electrode surfaces must be transported to or from the external circuit. In addition, the electrodes should be chemically and mechanically stable at the operating temperature with respect to the electrolyte and the current collector. The thermal expansion coefficient of the cathode must match to that of the current collector and the electrolyte to give stable interfaces because SOFC is cycled between room temperature and the operating temperature. Moreover, the cathode must have stable microstructures such as constant porosity and surface area under operating conditions.

Operation of SOFCs at intermediate temperatures (500-700 ℃) requires improved catalytic property and electric conductivity for cathodes. For example, at high temperatures (1000 ℃), the manganese oxide cathode material $La_{0.9}Sr_{0.1}MnO_3$ (LSM) is chemically stable under oxidizing conditions, has a good thermal expansion match with YSZ and has adequate electronic conductivity.[43, 44] However, the cathodic polarization with LSM electrodes is substantially increased because of the poor ionic conductivity at lower operating temperatures. With reducing the temperature from 1000 to 500 ℃, the polarization resistance of LSM gives an increase from <1 to 2000 ohm cm^2 which is way outside of the practical range. New cathode materials with much lower polarization resistances and compatible thermal expansion coefficients are needed for SOFCs operating at intermediate temperature range. The cathode materials containing cobalt is restricted by their large thermal expansion coefficients ($>20*10^{-6}$ K^{-1}) compared

with that of the common electrolytes. The general requirements for the cathode are summarized below: [45]

(1) High electronic conductivity under oxidizing atmosphere (preferably more than 100 S cm^{-1}).

(2) Chemical compatibility and similar thermal expansion coefficient (TEC) with the electrolyte and interconnect materials.

(3) Porous microstructure allowing gaseous oxygen to readily diffuse through the cathode to the cathode/electrolyte interface.

(4) Chemical and mechanical stability under an oxidizing atmosphere during fabrication and operation.

(5) High catalytic activity for the oxygen reduction reaction (ORR).

(6) Cost-effectiveness and easy processing.

1.6 Thin Film Preparation Method

The components of SOFC are prepared by chemical, physical methods and ceramic powder processes. Among them, screen printing method and pulsed laser deposition method are most widely adopted method to fabricate the cells. Considering different fabrication methods will result in different component microstructures and performances, the principles of screen printing method and pulsed laser deposition are reviewed followed by discussion about their advantages and disadvantages.

1.6.1 Screen Printing

Screen printing, as one of the most conventional and widely used thin film fabrication methods for thin film cathode layer, allows for full 2-dimensional patterning of the printed layer. The main difference between screen printing and other printing and coating techniques is a large wet film thickness and a requirement for a relatively high viscosity and a low volatility of the coating solution. The process which is illustrated in Fig. 1.7 involves a screen of woven material (i.e. synthetic fiber or steel mesh) glued to a frame under tension.[46] The pattern is obtained by squeegeeing a highly viscous paste consisting of a mixture of ceramic powder, organic binder and plasticizer through the open meshes of a screen mask. Parameters including viscosity of the paste, screen printing angle, grain size, surface properties, screen tension and packing density of the powders have to be optimized. In order to ensure the adhesion between the screen printed films and the substrates, a high temperature thermal treatment is generally adopted. The sintering temperature, time and atmosphere are also important for high quality films.[47]

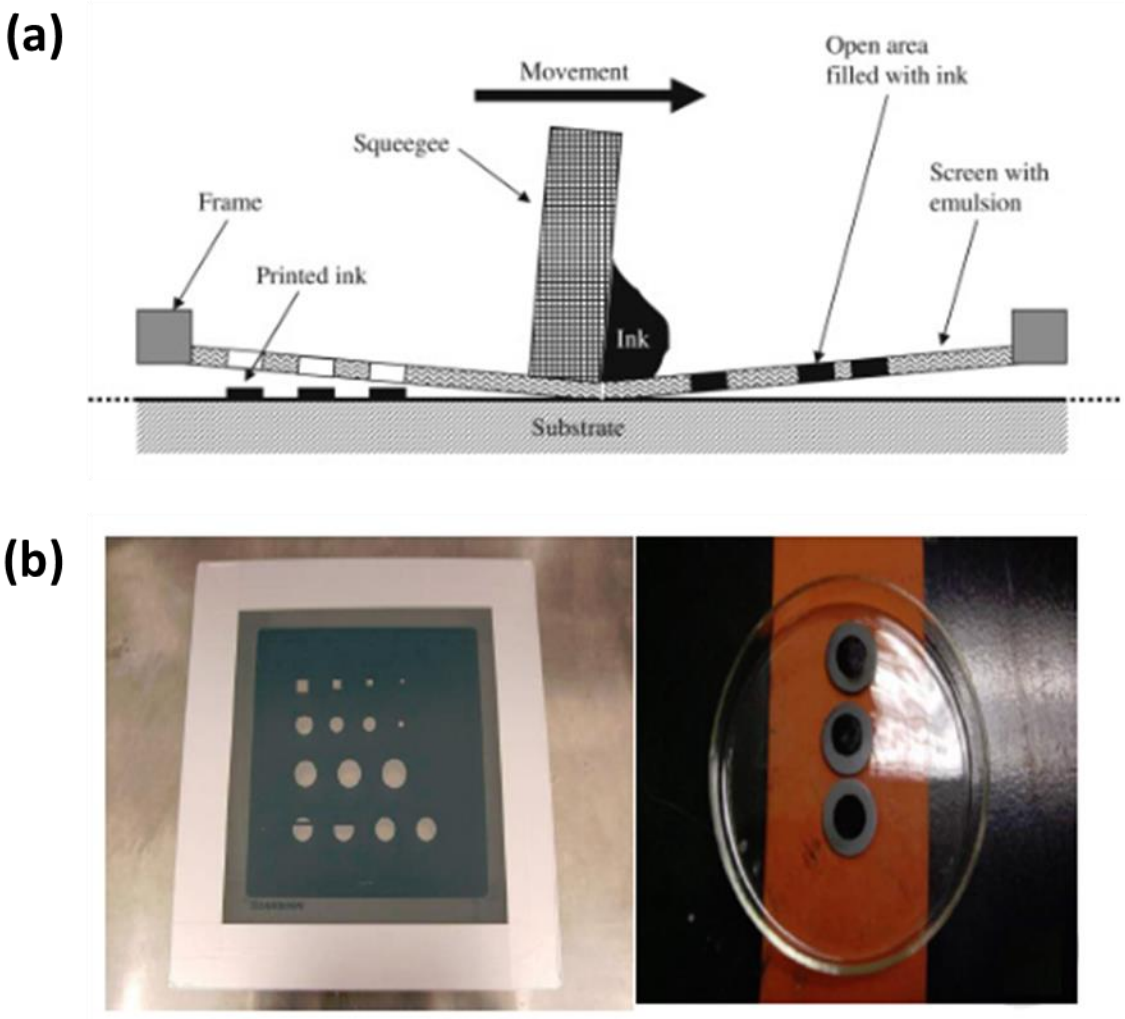

Fig. 1.7. (a) Schematic representation of the screen-printing process. Reprinted with permission from ref 46. Copyright 2009 Elsevier. (b) The typical screen printing mask and samples prepared by screen printing.

The screen printing method offers an easy and cost effectiveness to prepare thick films; however, the heat treatment could lead to possible delamination and crack issue because of huge difference in thermal expansion coefficient between cathode and

electrolyte in SOFCs. [48] In addition, screen printing method is widely applied to prepare cathode films which require both porous microstructure and good adhesion with electrolyte. There is always a compromise between improved surface areas (lower firing temperature) vs. improved interfacial contact (higher firing temperature) for the cathode films prepared by screen printing method. Careful optimization is needed to achieve desired cathode performance.

1.6.2 Pulsed Laser Deposition

Pulsed laser deposition (PLD) is a physical vapor deposition technique where a focused pulsed laser beam with high density strikes a target of the material. This material is vaporized from the target to form a plasma plume because of laser induced heat and the plume containing atoms, molecules, electrons, ions, clusters, particulates etc. will diffuse and deposit on a substrate as a thin film. This process can take place both in ultra-high vacuum and in the presence of a background gas. For example, oxygen atmosphere is commonly used for oxides deposition.

Due to the high laser energy, it enables evaporation of all target materials with promising kinetic energy which results in good stoichiometry between the target and thin film as well as high quality film. In addition, there is little contamination in the system because of high vacuum process and the result is repeatable. Recently, PLD has been applied to fabricate thin film electrolyte or prepare the cathode with different microstructures including nanoporous, fully dense and vertically align nanocomposite by varying of deposition parameters, seen as Fig. 1.8.[17, 49-51] The electrode exhibits

superior performance with novel microstructure. However, PLD is limited by the low growth rate and high processing cost for processing cathode layer exceeding micron range.

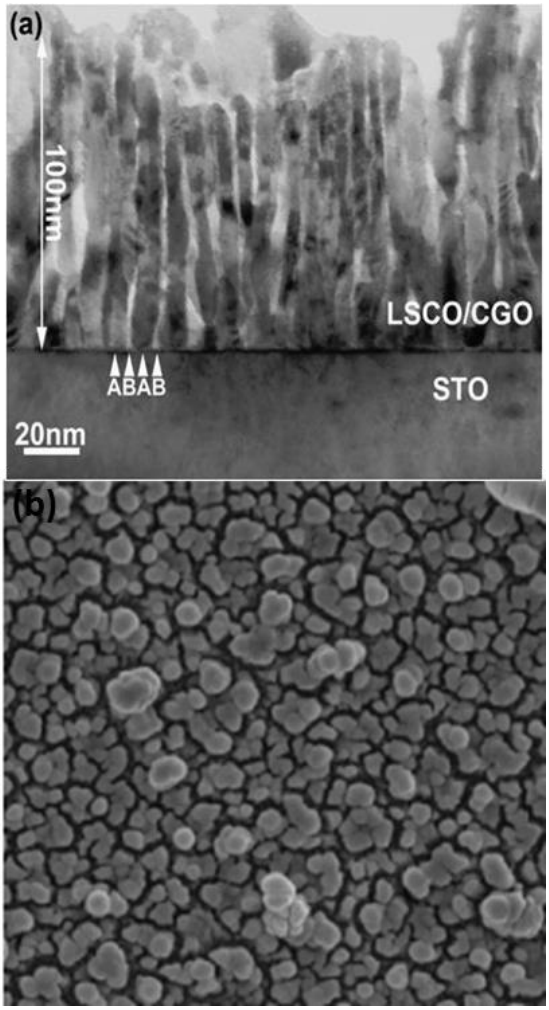

Fig. 1.8. The examples of different microstructure achieved by pulsed laser deposition (a) vertically aligned nanocomposite, (b) nanoporous film. Reprinted with permission from ref 50. Copyright 2007 Elsevier.

1.7 Challenges

The previous sections introduce the background of SOFCs. Start from this section, the challenges of SOFCs will be presented followed by review of current research efforts on addressing those problems. The main challenge in SOFC is to balance the performance, cost and reliability. Conventional SOFCs operate at high temperatures between 800- 1000 ℃ to allow internal reforming and promote rapid electro catalysis without the need for precious metals such as platinum.[3] But high operating temperature limits the selection of materials and facilitates the degradation which comprises the cost and the reliability. [52, 53] Over the past couple of decades, research has been focused on lower of operating temperature to intermediate temperature range (600-800 ℃) or even lower, which will benefit the cost and reliability, however decrease the performance. The main research interests right now focus on addressing the increasing polarization losses of cathode and ohmic loss of electrolyte at intermediate temperatures or even lower temperatures by exploring new materials and engineering the materials microstructure.

1.8 Current Research Review on SOFCs

1.8.1 Electrolyte Material Exploration

For SOFCs, the selection of the electrolyte predicates the other components including cathode and anode in consideration of chemical and thermo-mechanical stability with the electrolyte. [52] Therefore, electrolyte material exploration is reviewed first in this section.

Because of its attractive ionic conductivity, stability in both oxidizing and reducing environments, and compatibility with the electrode materials superior stability, [53, 54] the typical electrolyte used in SOFCs system is yttria-stabilized zirconia (YSZ). The decent oxygen ion conductivity of YSZ at high temperature is due to partial occupancy of energetically equivalent anion sites of the fluorite structure as seen Fig. 1.9. For YSZ, the host cations Zr^{4+} are partially replaced by lower-valent cations Y^{3+} and the missing charges are balanced by the formation of oxygen vacancies in the oxygen ion crystal, resulting in desirable ionic conductivity. [55]

The most commonly used composition for YSZ is 8 mol % Y_2O_3 stabilized ZrO_2. The ionic conductivity could reach ~0.1 S cm^{-1} at 1000 ℃ but this high operating temperature leads to significant problems with other components. However, the ionic conductivity of YSZ significantly decreases at lower operating temperatures due to the high activation energy of YSZ electrolyte. It hinders the further applications of low temperature SOFCs.

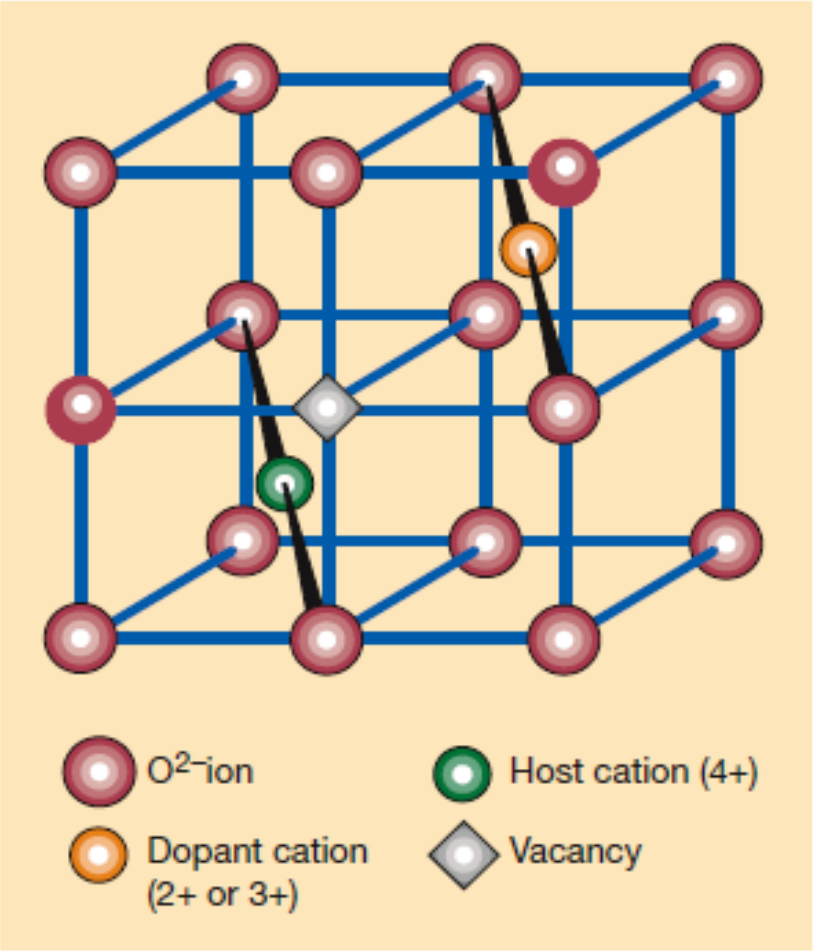

Fig. 1.9. The fluorite structure of solid oxide electrolyte. Reproduced with permission from ref 55. Copyright 2000 Nature Publishing Group.

Because of its higher conductivity, Scandia-stabilized zirconia (ScSZ) is an alternative electrolyte to YSZ operated at intermediate temperature. [56, 57] Among all the zirconium oxides, 8-12 mol % Scandia doped ScSZ has the highest oxygen ion conductivities.[58] Arrhenius plots of the ZrO_2-Ln_2O_3 systems showed curvatures characteristic of defect-dopant association and the ionic conductivity decreases with

increasing Ln^{3+} radius. The high ionic conductivity of ScSZ results from the low association enthalpy of defects because of the similar radii of Sc^{3+} and Zr^{4+}. ScSZ (10-15 mol %), with a rhombohedral structure, transforms to a cubic structure above 600 ℃ which can be stabilized at room temperature by adding small amounts of other dopants such as Y_2O_3.[59]

The oxygen deficient ABO_3 perovskite oxides offer another category of alternative candidates for SOFC electrolyte. A lanthanum gallate-based electrolyte is a typical example which has a similar thermal-expansion coefficient with yttria-stabilized zirconia (YSZ). [60] It was reported by Goodenough that oxygen ionic conductivity of $\sigma > 1*10^{-2}$ S cm at 600 ℃ for $La_{0.9}Sr_{0.1}Ga_{0.8}Mg_{0.2}O_{2.85}$. The apparent activation energy below 600 ℃ is 1.07 eV which is slightly larger than the 0.98 eV of YSZ and the conductivity behavior deviates from Arrhenius plot above 600 C. Subsequently, the ionic conductivity was optimized as a function of composition in more detail. [36, 61] The optimized composition was found as $La_{0.8}Sr_{0.2}Ga_{0.83}Mg_{0.17}O_{2.815}$ with highest values of σ=0.17 and 0.08 S/cm at 800 and 700 °C, respectively. However, due to the low mechanical stability of LSGM and the high costs of gallium, problems raise by using of LSGM-electrolyte-substrates. In addition, Ga-evaporation in a reducing atmosphere as well as reaction between LSGM with NiO leads to severe problems at high operating temperatures.

To address limitations of electrolyte operated at low temperature, ceria-based electrolytes such as gadolinia-doped ceria (GDC) which also has fluorite structure have been developed. Because of their high ionic conductivity and compatibility with high-

performance electrode materials such as cobalt containing perovskite oxide cathodes, they have been attracted extensive research interests. An important disadvantage of doped ceria electrolytes is Ce^{4+} is partially reduced to Ce^{3+} under reducing conditions and become n-type electronic conductors leading to reduced output voltage. [62, 63]

Different dopants and dopant concentrations were investigated to improve processing and stability of ceria-based electrolytes at low pO_2, for example, $Ce_{0.85}Gd_{0.1}Mg_{0.05}O_{1.9}$, $Ce_{1-a}Gd_{a-y}Sm_yO_{2-0.5a}$, $Ce_{1-x-y}Gd_xPrO_{2-z}$, and $Ce_{0.8}Sm_{0.2-x}Y_xO_{1.9}$ showed positive results for electrolyte stability.[64-67] The enhanced stability of electrolyte was achieved at the cost of an ionic conductivity reduction. Nevertheless, the results promoted addition studies to optimize the dopants and to understand how they affect the properties. Also, several transition metal oxides including MnO_2, Fe_2O_3, and Co_3O_4 etc. were examined as effective sintering aids for the sintering of ceria electrolyte at lower temperature.[68-70] Although doped ceria was demonstrated as a promising electrolyte material compatible with high-performance cathode for fuel cells operating between 500-650 ℃, more work is needed on addressing the low output voltage for ceria-based SOFCs.

Bismuth-based electrolyte with a layered structure resulting in two-dimensional oxygen ion conduction has also been investigated. [71, 72]. Those oxides have superior oxygen ion conductivity compared with zirconia-based and ceria-based electrolyte seen as Fig. 1.10. For example, δ-Bi_2O_3, with a random distribution of oxygen ions in a fluorite-related structure, has desired ionic conductivity (>1 S/cm at 800 ℃). However, it was stable only between 730 ℃ and its melting point (804 ℃). It was demonstrated by

Takahashi *et al.* that the δ-phase can be stabilized to lower temperatures by partial substitution for Bi with Y_2O_3 and Er_2O_3 dopants. [73, 74]. Unfortunately, the rare earth oxide stabilized δ-Bi_2O_3 phases transformed to the vacancy-ordered rhombohedral phase leading to significantly decreased conductivity when the operating temperature reached above 600 ℃. [75] The instability of bismuth oxide resulted from reduction to bismuth metal under reducing conditions becomes the biggest problem for practical application. Insert a more stable electrolyte layer (for example CGO or CSO) on the anode side to form bilayer electrolyte structures has been examined as an approach to solve this problem. [76] Recently, a new system as $Dy_{0.08}W_{0.04}Bi_{0.88}O_{1.56}$ (DWSB) was demonstrated as a promising electrolyte material operated at lower temperature (<600 ℃).[52] But it is still needed to apply bilayer electrolyte structure to examine power output. In sum, the ionic conductivity of electrolyte usually comes as expense of stability. More work is required to be done to optimize and performance and balance performance with stability.

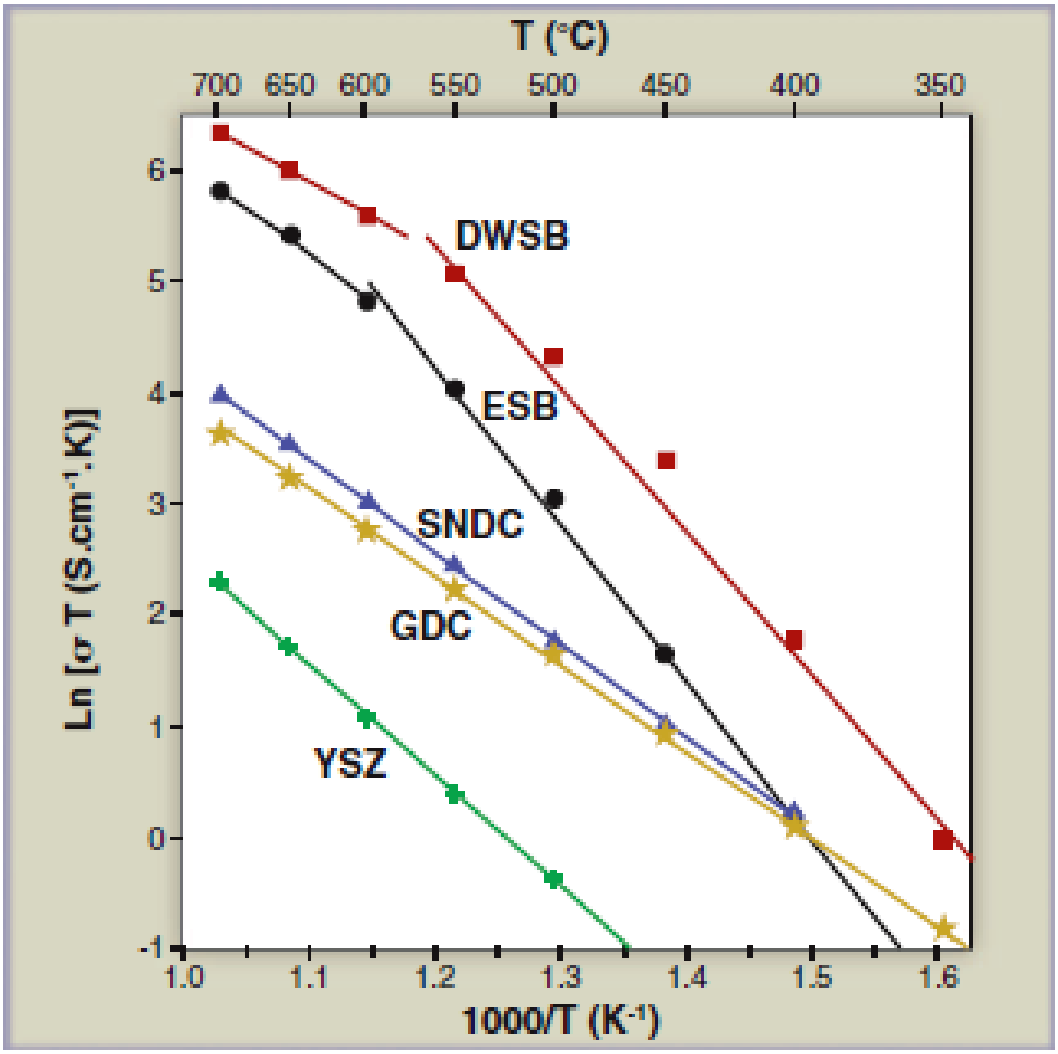

Fig. 1.10. Comparison of ionic conductivity of various solid oxide electrolytes. Stabilized bismuth oxides (ESB-$Er_{0.4}Bi_{1.6}O_3$ and DWSB-$Dy_{0.08}W_{0.04}Bi_{0.88}O_{1.56}$) show superior ionic conductivity compared with that of doped ceria (GDC-$Gd_{0.1}Ce_{0.9}O_{1.95}$ and SNDC-$Sm_{0.075}Nd_{0.075}Ce_{0.85}O_{2-\delta}$) and stabilized zirconia (YSZ-$Y_{0.16}Zr_{0.92}O_{2.08}$). Reprinted with permission from ref 52. Copyright 2007 AAAS.

1.8.2. Microstructure Engineering of Electrolyte

The oxygen ion conductivity of materials is also greatly influenced by their microstructures, i.e. grain size distribution and the properties of grain boundary. For example, grain boundaries are the crystallographic mismatch zones where mismatch of the lattices, impurities (or second phase segregation), space charge, or a combination of all of these determine the materials properties. [53] In many materials systems, grain boundaries provide a region of relatively rapid mass transport compared to the bulk properties of the crystallites. [77, 78] However, in zirconia and ceria-base electrolyte systems, the grain boundary ionic conductivity is expected to be lower than the bulk value due to the formation of electric space charge layers at grain boundaries. [79, 80] An unblocking grain boundary effect of ionic conductivity was observed recently. The ionic conductivity of YSZ thin film was found to increase with decreasing the film thickness to tens or hundreds of nanometer range. [81] In addition, the grain size dependence of conductivity has been investigated and higher ionic conductivity has been observed in nanocrystalline electrolytes.[82, 83] These results suggested that, when the grain size decreased to nanometer range, the ionic conductivity of the electrolyte could be dominated by interface transportation rather than intragrain transportation.

Based on the above findings, a multilayer strategy has been applied to create heterogeneous interfaces and was widely used to study the interfacial effect of two ionic conducting systems.[84] For example, oxygen plasma-assisted molecular beam evaporation (MBE) is used to grow Gd-doped CeO_2 and Gd-doped ZrO_2 multilayers on Al_2O_3(0001), as shown in Fig. 1.11. [85]

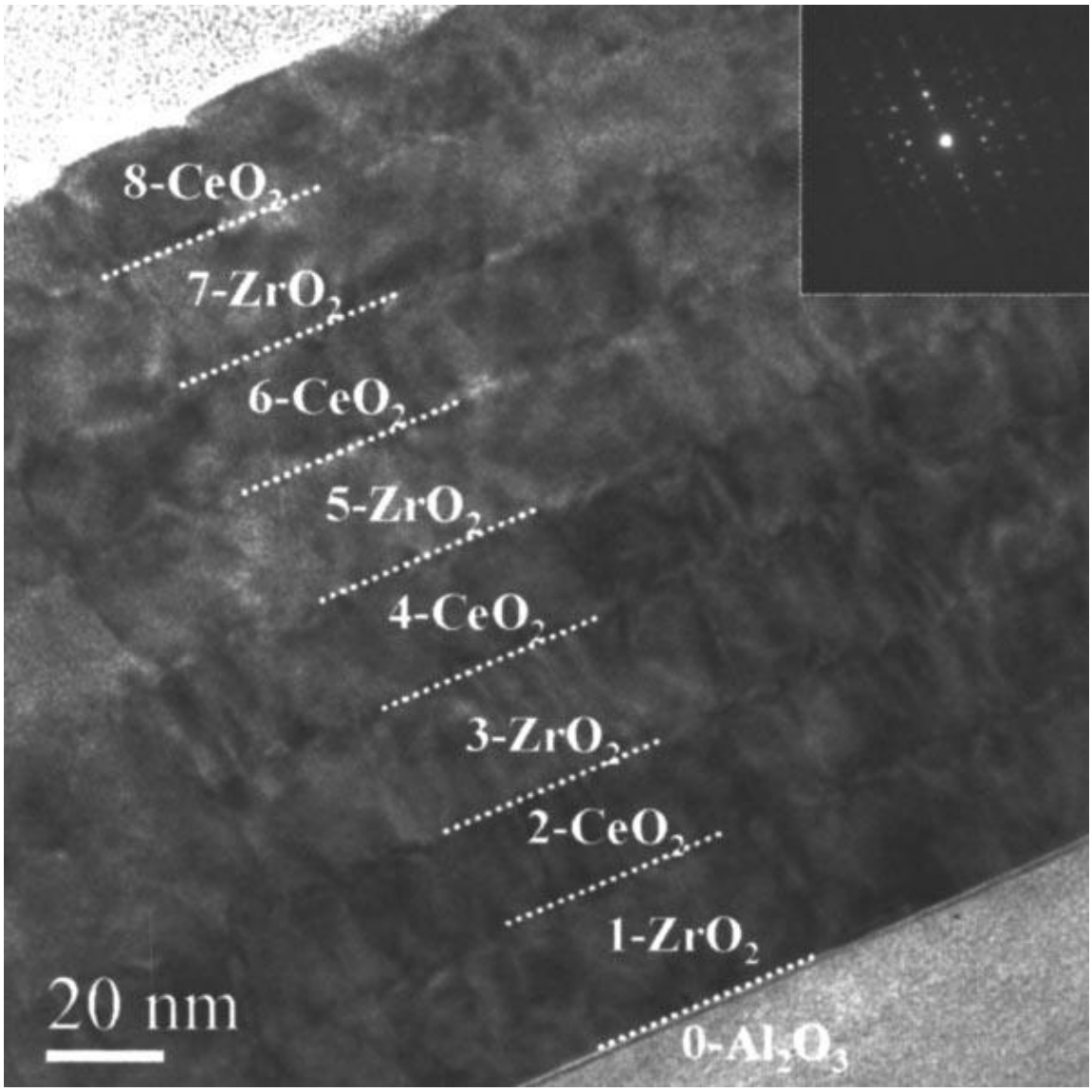

Fig. 1.11. TEM micrograph showing a cross sectional view of an eight-layer Gd_2O_3-doped CeO_2 and ZrO_2 film grown on Al_2O_3(0001). Reprinted with permission from ref 85. Copyright 2005 AIP Publishing LLC.

In this system, microstructural defects, indicated by structural characterization, such as dislocations exist in the layers as well as at interfaces. Those defects result from the lattice mismatch between two materials. It was found that the overall oxygen ionic conductivities increased continuously with decreasing individual thickness while the total film thickness kept constant. There was maximal around one order of magnitude ionic conductivity increase compared to bulk conductivity of single-phase Gd doped CeO_2. The effects of microstructural defects, which may increase the solubility of Gd in CeO_2 layers or the mobility of the oxygen vacancies is proposed to be attributed to the conductivity increase.

The hetero-epitaxial interfaces between ZrO_2-based oxide and other insulating oxides including Y_2O_3, Lu_2O_3 and Sc_2O_3 were systematically investigated by Korte *et al.* in Janek's group.[86, 87] By detailed comprehensive analysis of YSZ/Y_2O_3, YSZ/Lu_2O_3, and YSZ/Sc_2O_3 multilayers (YSZ denotes Y-doped ZrO_2), they concluded that systems with moderate lattice mismatch were dominated by elastic strain: YSZ/Lu_2O_3 with a slight tensile strain, YSZ/Y_2O_3 with a significant tensile and Sc_2O_3 films with a significant compressive strain. For the oxygen ion conductor such as YSZ, there is an exponential dependence of the ionic conductivity $\sigma_{O^{2-}_{int}}$ in the ionic conductor close to the interface on the migration volume ΔV_v^M of vacancies and on the lattice misfit f_{12}:

$$\ln(\sigma_{O^{2-}_{int}}/ \sigma_{O^{2-}_{vol}}) \sim \Delta V_v^M f_{12} \quad (2)$$

where $\sigma_{O^{2-}_{int}}/ \sigma_{O^{2-}_{vol}}$ is the ratio of ionic conductivity of the interface regime and the bulk.[88] Considering YSZ has a vacancy-type diffusion mechanism, the migration volume is usually positive.[87] Thus, a tensile strain favors the oxygen ion conductance

and a compressive strain hampers it. [89, 90] This strain dependent oxygen ion conductance features was found to be nicely fulfilled as Fig. 1.12.

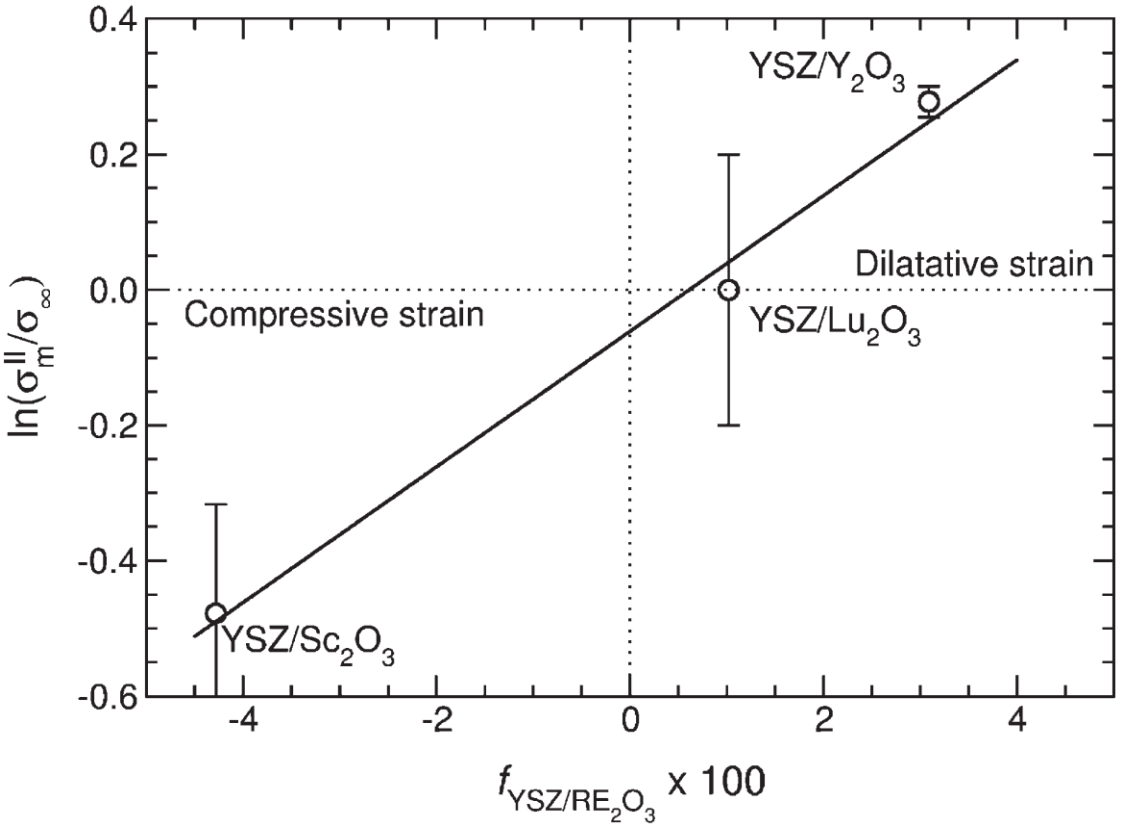

Fig. 1.12. Plot of the measured parallel conductivity enhancement as a function of misfit. [87]

Recently, Garcia-Barriocanal *et al.* investigated lateral conductivities of epitaxial grown yttria-stabilized zirconia (YSZ) and $SrTiO_3$ (STO) triple layers. [91] By

maintaining STO thickness as a constant value of 10 nm, the thickness of YSZ layer changed from 62nm to 1 nm. It was reported that the conductivity increases by two to eight orders of magnitude compared to bulk conductivity of YSZ and the activation energy decreased as YSZ thickness decreased. The authors proposed the enhancement due to direct or indirect effects of strain. Several following work has been carried on to study the strain and interface structure of YSZ/STO heterostructures. [92, 93] Those results suggest that tailor the interface structure by strain could open a new field to achieve high ionic conductivity.

1.8.3 Cathode Material Exploration

Cathode where oxygen reduction reaction takes place is believed to play a vital role in determining the overall SOFC performance. To illustrate the various coupled reactions and transport processes occurring at the different types of interfaces, two schematic models for the cathode reactions are shown in Fig. 1.13. For an electrode with low oxygen ion conductivity such as $La_{0.9}Sr_{0.1}MnO_3$ (LSM), its behavior is described in Fig 1.13a. The steps of oxygen reduction reaction of cathode include diffusion of oxygen gas molecular onto pore spaces, oxygen dissociation, oxygen ion diffusion to the TPBs and ion transfer into the electrolyte. It is generally believed that the electrochemical reactions can only occur at the very confined area close to TPBs where the oxygen ion conductor, electronic conductor, and the gas phase come in contact.[94, 95] The oxygen reduction reaction cannot take place if there is a breakdown in connectivity in any one of the three phases. [9]

Compared with the reactions in poor ionic conducting cathode, a schematic illustration of reaction in a mixed conducting cathode is shown in Fig. 1.13b. In this case, oxygen molecules which diffuse into the porous structure are reduced to oxygen ions not only at the triple phase boundaries between the cathode material, electrolyte, and gas phase but at the surface of a mixed conducting cathode material. The reduced oxygen ions diffuse either along the surface to the electrolyte or through the cathode material. The transfer of those ions to the electrolyte is either across the solid-solid interface between the cathode and the electrolyte or in the vicinity of the triple phase boundary. It is expected that the mixed conductor would show lower polarization resistance because of the larger area available for reaction and ion transfer across the interface. Gas phase diffusion into the porous structure becomes important at high current density and it must be also considered.

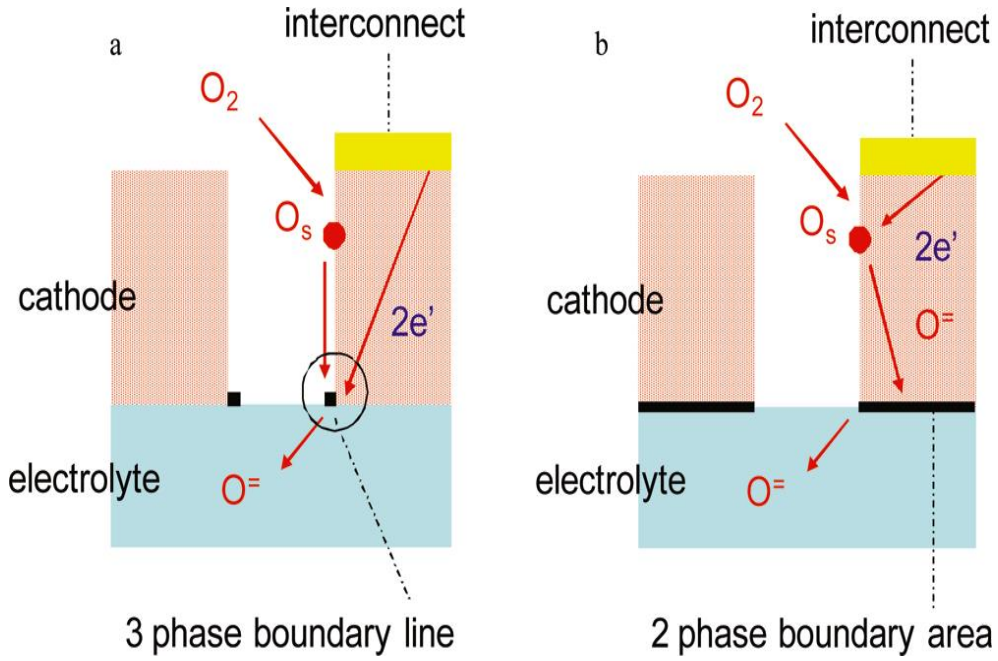

Fig. 1.13. Schematic representations of different cathode reaction mechanisms. The cathode is a (a) poor or (b) good ionic conductor.[22] Reprinted with permission from ref 22. Copyright 2010 American Chemical Society.

Exploring new cathode materials with lower polarization loss is based on intrinsic properties. For example, the cathode polarization resistance is described by the ALS model in terms of the electrode microstructure (tortuosity, porosity, and surface area), the oxygen ion diffusion coefficient (D), and the surface exchange velocity (k) at the appropriate oxygen pressure.[96] Several cathode material systems have been explored to enhance oxygen self-diffusion coefficient and oxygen surface exchange rate and typical examples are summarized as Table 1.2.[97] Those cathode oxide materials

are mainly with three types of structure including perovskite, K_2NiF_4, and ordered double perovskites.

Table 1.2 Summary of oxygen self-diffusion and oxygen surface exchange data and overall conductivity for different SOFC cathode materials

	D^*/cm^2s^{-1} T=500 ℃	E_a^D/eV	$k^*/cm\ s^{-1}$ T=500 ℃	E_a^k/eV	$\sigma/(S*cm^{-1})$ T=500 ℃	Ref
$La_{0.8}Sr_{0.2}MnO_{3-\delta}$	$4.5*10^{-20}$	2.80	$3.1*10^{-11}$	1.30	120-130	[97, 98]
$La_{0.8}Sr_{0.2}CoO_{3-\delta}$	$9.0*10^{-14}$	2.22	$2.8*10^{-9}$	1.32	1500-1600	[97-99]
$La_{0.5}Sr_{0.5}MnO_{3-\delta}$	$1.5*10^{-10}$	1.41	$3.9*10^{-7}$	0.81	1300-1800	[97-99]
$La_{0.6}Sr_{0.4}Co_{0.2}Fe_{0.8}O_{3-\delta}$ /$Ce_{0.8}Gd_{0.2}O_{2-\delta}$	$1.2*10^{-10}$	1.39	$3.3*10^{-9}$	1.60	250-300	[99, 100]
$Ba_{0.5}Sr_{0.5}Co_{0.8}Fe_{0.2}O_{3-\delta}$	$1.2*10^{-7}$	0.50	$1.1*10^{-6}$	1.76	10-55	[101]
$La_2NiO_{4+\delta}$	$3.3*10^{-9}$	0.56	$7.0*10^{-9}$	0.60	55-65	[102]
$La_2CoO_{4+\delta}$	$2.5*10^{-8}$	0.12	$3.2*10^{-6}$	0.03	1-5	[103]
$GdBaCo_2O_{5+\delta}$	$2.8*10^{-10}$	0.60	$7.5*10^{-8}$	0.81	550-925	[104]
$PrBaCo_2O_{5+\delta}$	$3.6*10^{-7}$	0.48	$6.9*10^{-5}$	0.67	400-700	[105]

1.8.3.1. ABO_3 Perovskite Oxides

A significant number of oxide cathode materials with perovskite structure have been investigated for intermediate temperature SOFCs integrated with YSZ, CGO, and LSGM electrolytes. The general formula of perovskite-type oxide is ABO_3, in which A and B is cation with a total charge of +6. The higher valence B cations (such as, Ti, Ni, Fe, Cr, Co, and Zr, etc.) are coordinated to six oxygen anions and occupy the much smaller space while A cations (such as, La, Ca, Sr, and Pb, etc.) are larger and coordinated to twelve oxygen anions. It is possible for full or partial substitution of A or B cations with cations of different valence to adjust its properties. The vacancies at the oxygen lattice sites can be introduced when the overall valence of the A-site and B-site cations (n + m) adds up to less than six and the missing charge is made up. [106, 107] Fig. 1.14 shows the typical structure of the cubic perovskite ABO_3.

Because of its high electrical conductivity, high electrochemical activity for the O_2 reduction reaction, high thermal stability, and compatibility with YSZ, GDC, and LSGM at operating conditions in the 800-1000 ℃ range, the perovskite lanthanum strontium manganite (LSM) is still one of the most important cathode materials for SOFCs. In addition, LSM shows excellent long-term performance stability and microstructural stability among cathode materials. However, oxygen reduction reaction only takes place at the confined area closed to TPBs and its performance at lower operating temperatures needs to be improved. The current status of LSM is reviewed by Jiang in details.[108]

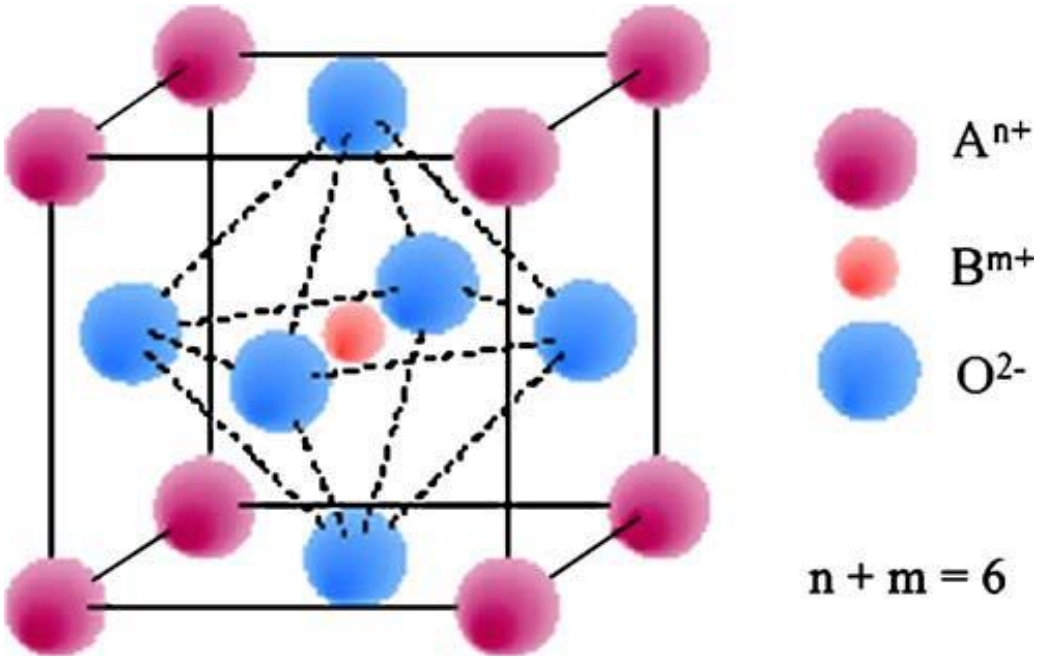

Fig. 1.14. Unit cell representing the ABO_3 perovskite structure.

To expand the oxygen reduction reaction area and enhance the catalytic property, other perovskite cathodes with mixed electronic and ionic conductivities were developed. For example, A-site doped lanthanum ferrite perovskites (LSF) with adjustable thermal-expansion coefficients are promising cathode materials operated at lower temperatures with YSZ. [109, 110] With a barrier layer of CSO, there was no formation of insulating phases such as La- and Sr-zirconates up to 1400 ℃ between Sr-doped lanthanum ferrite and YSZ.[111] Both A site doping of other alkaline earth metals (aluminum) and B site doping (nickel) have been studied for LSF and were tested in single cell and half-cells.[112, 113] Aluminum doping did not change the intrinsic activity of the base LSF

materials, but it segregated to the surface, reducing or blocking the number of active catalytic sites. On the other hand nickel doping decreased catalytic activity.

Cobalt containing perovskites (c.a. $La_{1-x}Sr_xCoO_{3-\delta}$) exhibiting high mixed electronic and ionic conductivities and exceptional electrochemical activity for oxygen reduction become interesting candidates for intermediate temperature SOFCs. Unfortunately, they react with conventional YSZ electrolyte at low temperatures (700 ℃) to form insulating phases and degrade the fuel cell performance. In addition, there is huge thermal expansion coefficient difference between cobalt containing perovskites and electrolytes (YSZ, LSGM, etc.) resulting in a delamination at the cathode/electrolyte interface or cracking of the electrolyte. [114] The area specific resistance (ASR) and TEC are expected to decrease by substituting the La cation with an alternative cation such as Gd, Pr or doping Cu, Mn into the Co sites. [45] Cobalt containing perovskites have chemical stability with doped ceria electrolyte. Because of its high catalytic activity at temperatures in the 500-700 ℃ range, the main application of cobaltites is as cathode in SOFCs at this temperature range where the kinetics of the oxygen reduction reaction limit the overall cell performance. The Fe-doped cobalt containing cathodes with an optimized composition $La_{0.6}Sr_{0.4}Co_{0.2}Fe_{0.8}O_{3-x}$ have been developed for application with CGO operating at 550 ℃. [115, 116] In this system, the cobalt provides the desirable catalytic while large iron content reduces the thermal expansion.

$Sm_xSr_{1-x}CoO_3$ (SSC) and $Ba_{0.5}Sr_{0.5}Co_{0.8}Fe_{0.2}O_{3-x}$ (BSCF) are two other cobalt containing perovskite exhibiting exceptional performance with ceria or LSGM in SOFCs. Both single phase SSC and SSC composite cathodes including SSC-

$La_{0.8}Sr_{0.2}Ga_{0.8}Mg_{0.2}O_3$ (LSGM) and SSC-$Gd_{0.1}Ce_{0.9}O_{1.95}$ (CGO) exhibited good catalytic activity. [117, 118] In order to reduce the thermal expansion coefficient of SSC and optimized its performance, iron-doped SSC cathodes have also been studied by crystal structure, thermal expansion coefficient, electrical conductivity, and cathode polarization. [119]

BSCF, as an excellent oxygen permeation membrane material in the last decade, was first applied by Haile and Shao as a cathode material in a solid oxide fuel cell.[120] The area specific resistances of BSCFO cathode on a $Sm_{0.2}Ce_{0.8}O_{1.9}$ electrolyte-based fuel cell reaches as low as 0.055-0.071 ohms cm^2 at 600 ℃, and 0.51-0.60 ohms cm^2 at 500 ℃. It raised much research interest as a promising cathode and has been studied by several groups. Zhou *et al.* reviewed the current status of BSCF system.[121, 122] Further studies showed that addition of silver improved the performance of BSCF electrodes because silver with high oxygen mobile helped oxygen ion migrate to the electrolyte-electrode interface resulting in excellent cathode performances reported.[122] However, the high TEC of BSCF (20×10^{-6} K^{-1} between 50 ℃ and 1,000 ℃) indicates that thermal cycling could be problematic for cells using this cathode material.[45] Make composite cathode BSCF by introducing certain amount of electrolyte is possible to solve the issue of thermal expansion, but it reduces the BSCF performance.

1.8.3.2. K_2NiF_4 Structures

Because of the high diffusivity of the interstitial oxygen ions, oxides with the perovskite related K_2NiF_4 structure such as Ln_2NiO_{4+x}, (Ln=La, Pr, Nd) are of interest for SOFC cathodes. [123] The structure of K_2NiF_4, seen as Fig. 1.15a, can be described as a succession of ABO_3 perovskite layers alternating with AO rock salt layers.

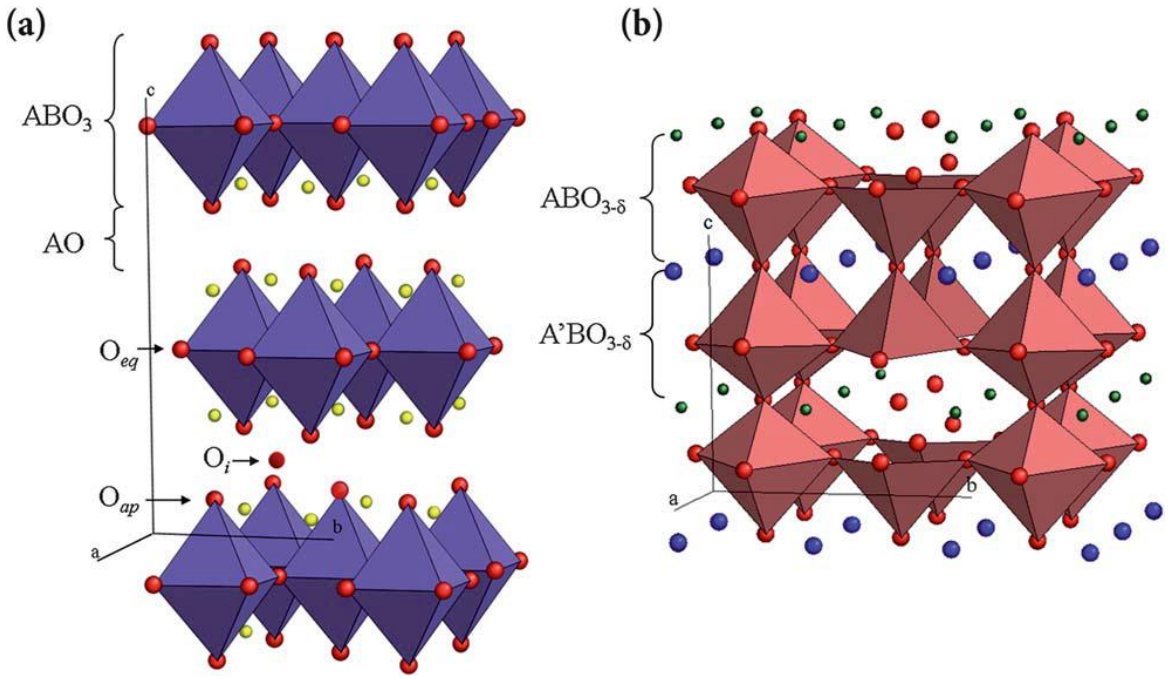

Fig. 1.15. (a) Polyhedral view of a K_2NiF_4 structure consisting of a succession of ABO_3 perovskite layers alternating with AO rock salt layers. (b) Schematic illustration of a double perovskite structure with composition $AA'Co_2O_{5+x}$ where B ions are coordinated in pyramids (BO5) and octahedra (BO6) with oxygen vacancies along (1 0 0) in the A plane. Reprinted with permission from ref 97. Copyright 2010 Royal Society of Chemistry.

The incorporation of interstitial oxygen anions into the rock salt layers where they are tetrahedrally coordinated by La^{3+} cations results in the oxygen excess in La_2NiO_{4+x} cathode. For example, x can reach as high as 0.18 in La_2NiO_{4+x} and the maximum value of x is 0.22 in Pr_2NiO_{4+x} at ambient temperature. Besides its high oxygen mobility and a relatively low lattice expansion induced by variations in temperature and oxygen partial pressure, [124] there is reasonably matched thermal expansion coefficient between La_2NiO_{4+x} compounds ($11\text{-}13*10^{-6}K^{-1}$) and the widely-used electrolytes including YSZ, CGO, LGSM etc. For K_2NiF_4 structure oxides, substitutions on both the La and Ni sites of the La_2NiO_{4+x} compounds can enable a wide range of different transport properties. Effect of doping at the La position with alkaline earths have been investigated by several systems.[125] The surface exchange and self-diffusion coefficient of $La_{1-y}Sr_yNiO_{4+x}$, y=0.0, 0.1 were measured by isotope exchange and depth profiling in the temperature range 640-842 ℃.[126] It was found that the oxygen diffusivity of $La_{1-y}Sr_yNiO_{4+x}$ was higher than that of LSCF and 1 order of magnitude lower than mixed conductor $La_{0.3}Sr_{0.7}CoO_{3-\delta}$ (LSCO). Also, electrical properties of La_2NiO_{4+x} was reported to show metallic behavior by strontium doping and its conductivity increased with increasing strontium doping content which reaches 273 S cm^{-1} at x=0.75. [127] For $(Pr,La)_2NiO_{4+x}$ solid solutions, impedance measurement results indicated that they were more compatible with CGO than YSZ because of interfacial reaction between the electrode and YSZ electrolyte leading to an order of magnitude higher polarization resistance. In addition, substitution of Ni with other transition metal including Cu and Co has been studied and showed promising intrinsic properties.[128,

129] However, the performance of SOFCs prepared with La_2NiO_{4+x} cathodes falls below the expectation although they show decent intrinsic properties. Therefore, further research is required to examine the causes.

1.8.3.3. Ordered Double Perovskites

The ordered double perovskite oxides represented by the general formula $AA'Co_2O_{5+x}$ (A = rare earths, Y and A' = Ba, Sr) attract extensive research attentions because of rapid oxygen ion transport and fast surface exchange. [130] As seen in Fig. 1.15b, these compounds with the "112" type structure are consisted of double layers of square pyramidally coordinated cobalt cations and the Ba^{2+} cations stand in the Co double layers which are separated by layers of lanthanide cations. $PrBaCo_2O_{5+x}$ and $NdBaCo_2O_{5+x}$ (x= 0.92, 0.18) are representative examples of this class of compounds with ordered double perovskite structures. [131, 132]

Although there is a considerable literature on the structural chemistry and low-temperature properties of the ordered double perovskite, it starts to be considered as suitable cathode until the high-temperature properties of $GdBaB_2O_{5+x}$ (B=Mn, Co) was reported by Taskin *et al.* which exhibits high rates of oxygen transport and fast surface exchange kinetic.[133] Independently, both thin films and bulk properties of $PrBaCo_2O_{5+x}$ were measured and showed high oxygen diffusivity and rapid surface exchange kinetics which could result in very low area specific resistance of electrodes. [134, 135] At 600 ℃, the measured area specific resistance of the composite cathode could reach as low as 0.15 ohm cm^2.[136]

One of the potential limiting factors for application of barium-containing systems is their susceptibility to carbonate formation in the presence of CO_2. The AC impedance spectroscopy was used to investigate the electrode performance of $LnBaCo_2O_{5+d}$ below 700 ℃ and the results showed a reaction with CO_2. [137] It was studied by Tarancon *et al.* $GdBaCo_2O_{5+x}$ cathodes are found to stabilize in atmospheres of CO_2 (500 ppm to 100%) at that temperatures up to 700 ℃ and it exhibited excellent performance with both CGO and LSGM electrolytes.[138] Recently, the composite cathodes performance of $REBaCo_2O_{5+x}$ (RE=La, Pr, Nd, Sm, and Eu) were investigated by CGO electrolyte-supported symmetrical cell and the results indicated that the polarization resistance of those electrodes decreased as the ionic radius decreased from La to Eu. [22]

Although those electrode microstructures were not optimized, the polarization resistances are still low. For example, the ASR values of $EuBaCo_2O_{5+x}$+CGO electrode are 0.095 ohm cm^2 at 700 ℃ and 0.49 ohm cm^2 at 600 ℃. [139] It was investigated by Manthiram *et al.* that the properties of $REBaCo_2O_{5+x}$ oxides with RE= Nd, Gd, Sm, and Y as cathodes in single-cell SOFCs were observed to decrease with decreasing size of the rare earth ions.[140] In addition, ASR value of $SmBa_{0.5}Sr_{0.5}Co2O_{5+x}$ electrodes in a symmetric cell using CGO was obtained as 0.092 ohm cm^2 at 700 ℃. By Sm and Sr doping, the thermal expansion coefficient decreased from>$20*10^{-6}K^{-1}$ to $13.6*10^{-6}K^{-1}$ at 700 ℃ in the composite and improved the chemical stability of cathodes in contact with both CGO and LSGM electrolytes.[141] The reduce thermal expansion coefficient could be also achieved by substitution cobalt by Ni in $NdBaCo_{2-x}Ni_xO_{5+x}$ system where TEC showed $16.7*10^{-6}K^{-1}$ while the cathode performance maintained in a single SOFC.[142]

Although the double perovskites show promising properties for application as SOFC cathode, only limited data and a small number of compositions are available at this stage. Considering the structure of ordered double perovskite materials is anisotropic, they typically exhibit different ionic and electronic transport properties along different crystallographic directions. Therefore, the use of ordered double perovskite cathodes with well oriented thin films could enhance the observed decay of their excellent anisotropic properties; on the other side, the cathode performance averages in all directions for polycrystalline structure of randomly oriented grains. More optimization work needs to be done for the real applications.

In the last several two decades, significant advances have been achieved for exploration of new cathode materials for intermediate temperature SOFC; however, there are still several limitations for cathode materials selection. First, due to the inherent complexity of oxygen reduction reaction and convoluted nature of electrochemical and chemical processes, it is very difficult to provide a step-by-step description. From the state-of-the-art model, oxygen reduction reaction is expected to be simultaneously limited by at least four physical processes including ad(b)sorption of oxygen, ambipolar transport to the solid-solid interface, interfacial electrochemical kinetics, and ionic transport in the ionic sub-phase.[9] The quantification of the contribution for each process is unable to process hindering future design of new cathode materials. Second, there is a generally much bigger thermal expansion coefficient for those new cathode materials exhibiting better catalytic properties and faster surface exchange rate. It brings the problem about integrity of the new cathode materials with conventional electrolyte

such as YSZ, CGO and LSGM. How to balance the performance with stability is another issue needed to be addressed. In addition, another neglected issue is that all cathode materials suffer from nonstationary behavior like degradation. However, there is limited data for the degradation behavior and the reported performances of SOFC cathodes vary significantly from lab to lab making it difficult to compare. If these experiment variables were better identified and standardized, it would not only aid cathode development but benefit fundamental research.

1.8.4 Microstructure Engineering of Cathode

Besides developing new cathode materials with enhanced intrinsic properties, engineering its microstructure provides another approach for enhancing cathode performance. For the conventional cathode like LSM, the oxygen reduction reaction only takes place at the confined area of TPB. Therefore, the strategy for those materials is to expand the TPB length so as to increase of the number of active reaction sites and improve electrode performances. Different methods including reduce the grain size, optimize the sintering process, and adopt new approaches to fabricate nanoporous LSM cathode etc. are used to increase the LSM cathode performance.[143-145] For the mixed conducting cathode, the oxygen reduction reaction expands to certain thickness (microns range) of the cathode, nanostructured electrode with significantly higher surface areas exhibits superior electrochemical properties. The wet impregnation method which has been developed in recent years has showed promise in preparing nano grain size cathode with enhanced surface area.[146] For example, it was found by Vohs *et al.* that

preparation an LSM-YSZ cathode by the infiltration method exhibited outstanding electrochemical performance.[147] Also, infiltrated $Sm_{0.5}Sr_{0.5}CoO_{3-x} - Ce_{0.9}Gd_{0.1}O_{1.95}$ composite cathode showed low polarization resistance of 0.1 ohm cm^2 at 600 ℃.[148] The impregnation of nanoscale particles which form connected networks in solid oxide fuel cell electrodes significantly increased the reaction sites so as to decrease the resistance of the oxygen reduction reaction within cathodes. However, the durability of cathodes prepared by infiltration method raise a big concern over long periods at high temperatures because the nanosized particles tend to aggregate at a high temperature. In addition, different microstructures and properties of cathode will be achieved with different synthesize methods. For example, compared with materials prepared by a conventional solid-phase reaction, a sol–gel or glycine–nitrate combustion method prepares the materials with much smaller grain size and higher surface area resulting in better cell performances.[149, 150] Before considering incorporation into practical applications, the feasibility of scale-up and cost of these processes must be taken into account.

To minimize the TECs mismatch and increase the cathodic performances, cathodes graded in compositions were designed and fabricated for SOFCs where the composition and electrode properties changed smoothly from one phase (LSM) to another phase (LSC).[151, 152] It was reported that the gradually changed composition with graded interface resulted in better cell integrity and enhanced cell performance. The functional graded cathodes were deposited on YSZ electrolytes by screen-printing, slurry spray, and slurry coating with improved electrochemical performances.[153-155] The

cathode/electrolyte interfacial polarization resistances decreased and power density increased by applying graded cathode, however, the long-term stability of those electrodes need further examination.

On the other hand, interface modification by implementing a thin interlayer to lower the reaction barrier and increase the catalytic reaction probability provides another promising approach for enhancing cell performance and durability.[51, 156] A $La_{0.5}Sr_{0.5}CoO_{3-\delta}$ /$Gd_{0.1}Ce_{0.9}O_{1.95}$ vertically aligned nanocomposite (VAN) interlayer has been applied between the cathode and the electrolyte, seen as in Fig. 1.16. It effectively increased the cathode/electrolyte interface as well as the TPBs length resulting in enhanced power density of the cells. [51] Those results suggest that the microstructural variations in the electrolyte and the electrode could affect the reaction kinetics of the cell, lower the polarization resistance at the electrode/electrolyte interface and enhance the power output in SOFCs. [41, 49, 95, 157]

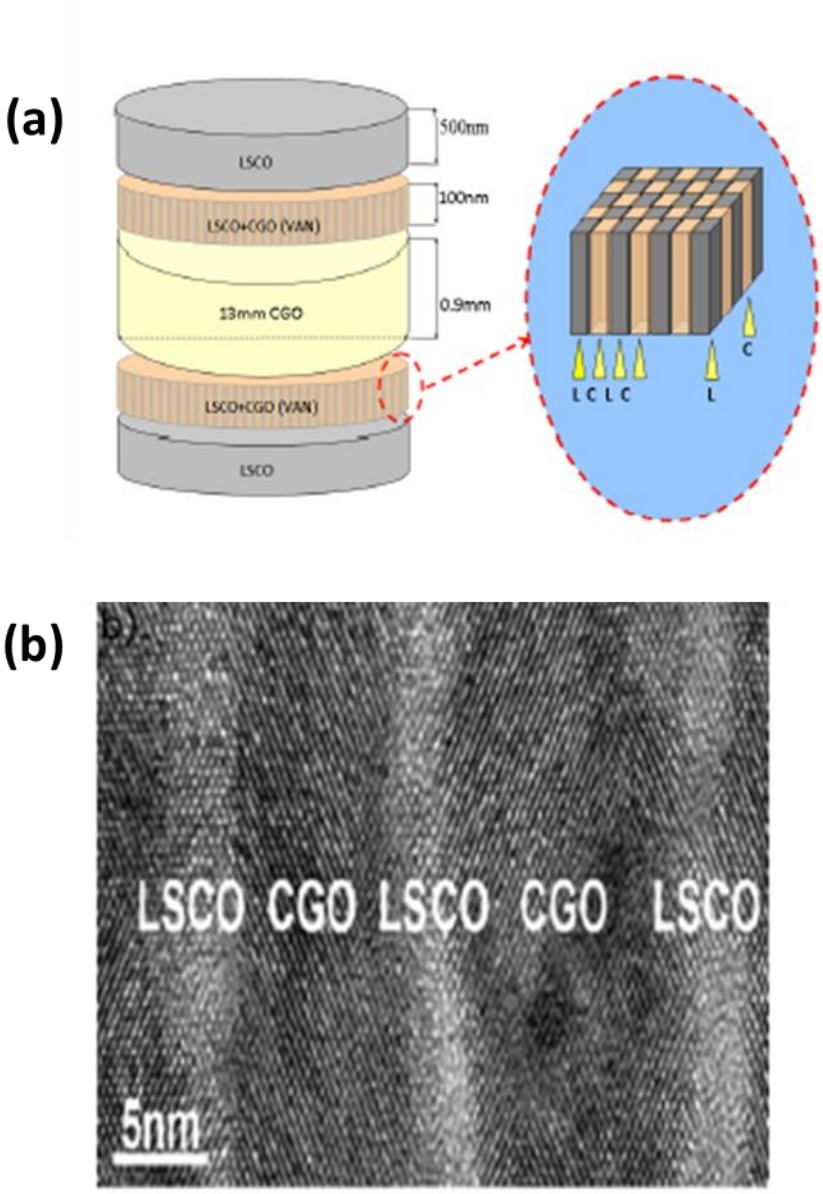

Fig. 1.16. (a) Schematic illustration of a symmetric cell and a VAN interlayer where ‘‘L’’ and ‘‘C’’ stand for LSCO and CGO columns, respectively. (b) High-resolution TEM images of a typical LSCO/CGO VAN structure grown by PLD on STO substrate. Reprinted with permission from ref 51. Copyright 2009 John Wiley and Sons.

1.9 Solid Oxide Reversible Fuel Cells (SORFCs)

Besides SOFC, Solid Oxide Reversible Fuel Cells (SORFCs), as one of promising energy conversion and storage device, have attracted extensive research interests.[158] SORFCs can utilize the heat and electrical power to produce fuel and store energy in other fuel form.[159] Furthermore, other renewable energy sources including solar energy, wind energy and nuclear energy could combine with SORFC systems to store energy in the form of hydrogen.[160] All of those benefits enable SORFCs have a wide range of applications on clean energy.

Similar to SOFCs, SORFCs have cell structure composed of hydrogen electrode, electrolyte and oxygen electrode and the criteria of materials selection are very alike. One major challenge for SORFCs is that the oxygen electrode polarization resistance significantly increases at low operating temperature. However, the high operating temperature leads to fast degradation rate and limitation of materials selection. Another main issue for SORFCs is the interfacial electrical and mechanical degradation of oxygen electrode. It was investigated by Liu *et al.* that the interface degradation of LSM/YSZ electrode has been identified as the loss of TPBs length and formation of secondary phase.[161] In addition, Knibbe *et al.* examined the degradation behavior of oxygen electrode and delamination or hole/pore formation along the grain boundaries of YSZ electrolyte close to the LSM/YSZ oxygen electrode was observed under high current densities.[162] The degradation mechanism proposed by Virkar and Chen was due to insufficient interfacial ionic conductivity between electrolyte and oxygen electrode causes high internal oxygen pressure. It leads to tensile strain close to the

oxygen electrode/electrolyte interface and formation of hole/pores or delamination.[163, 164] Therefore, more work about interfacial engineering the electrode/electrolyte interface and the durability test of SORFCs need to be done to test and improve their performance.

1.10 Summary

Because of its high efficiency and low emission, the SOFC technology is very attractive as the demand of energy generation systems. To bring the SOFCs operating temperature to intermediate range is needed for foreseeable industrial applications. As the SOFC operating temperatures decrease, the significant increased cathode polarization loss and electrolyte ohmic loss becomes one of limiting factors for the SOFC efficiency. Great efforts have been focused on exploring new materials and engineering microstructure of cathode, electrolyte and cathode/electrolyte interface to achieve enhanced SOFC performance at low operating temperatures. In addition, prepare reliable electrolyte with thickness in micron ranges is developed using thin film techniques to increase its ionic conductivity and improve the power output of the cells.

Furthermore, the fundamental mechanism for the limitation factors of the oxygen reduction reaction in cathode with different microstructure and thickness is needed to be understood for new materials design and future development. In this aspect, the thesis focuses on the following research directions:

In the first part of the main content (Chapter III), a pulsed laser deposition (PLD) technique and a screen printing method are combined to prepare a bi-layer

$La_{0.5}Sr_{0.5}CoO_3$ (LSCO) cathode. Those bi-layer cathodes have been demonstrated with excellent adhesion, porous microstructure and much lower polarization loss than that of the single layer cathode.

In order to understand the effects of those bi-layer cathodes, in the second part of the thesis (Chapter IV and V), detailed PLD interlayer thickness and partial oxygen pressure AC impedance study are carried on. The guidelines for designing high-performance bi-layer cathodes with optimum performance and low cost are proposed.

Besides the polarization loss of cathode, ohmic loss of electrolyte is another main loss. To increase the ionic conductivity of electrolyte without comprising its stability, two-phase $(Ce_{0.9}Gd_{0.1}O_{1.95})_{0.5}/(Zr_{0.92}Y_{0.08}O_{1.96})_{0.5}$ nanocomposite electrolyte with vertically aligned structure are demonstrated for thin film solid oxide fuel cells in the third part of the main content (Chapter VI). More than 50% increase in overall power density is achieved compared with that of the cells without VAN electrolyte.

In the fourth part of the thesis (Chapter VII), a vertically-aligned nanocomposite (VAN) interlayer approach is adopted for solid oxide reversible fuel cells to broaden the scope of application of microstructure engineering. The design of a $La_{0.8}Sr_{0.2}MnO_{3-\delta}/Zr_{0.92}Y_{0.08}O_2$ thin interlayer between the electrolyte and oxygen electrode is demonstrated which significantly improves the overall cell performance and also acts as a transition layer facilitating adhesion and relieving both thermal stress and lattice strain. The goal of the efforts in this thesis is to lower the SOFC processing cost, enhance the cell performance, and improve the cell durability.

2. RESEARCH METHODOLOGY

2.1 Pulsed Laser Deposition

Laser is an acronym for "Light Amplification by Stimulated Emission of Radiation". Basically, to generate a very collimated, monochromatic and coherent beam of laser, three key elements, resonance structure, gain medium and pumping source are needed to be combined in a system. In the pulsed laser mode, the output of a laser varies with respect to time in the form of alternated 'on' and 'off' periods. The laser has widely applications in many areas including military, medical, metallurgy and semiconductor manufacturing. Especially, pulsed laser deposition (PLD) has been successfully developed in the past 30 years and becoming one of broadly applicable techniques for ceramic thin film deposition.[165, 166]

Physical vapor deposition (PVD), condensation of vaporized materials from the target onto various surfaces in a vacuum chamber, is a variety of thin film deposition methods. PLD, as one of the standard PVD techniques, is with very simple system setup. As seen in Fig. 2.1, a typical PLD system basically consists a substrate holder and a target holder in a vacuum chamber which maintained by a first level mechanical pump and a second level turbomolecular pump.[167] The bulk ceramic targets are placed with an incident angle of 45 ^{o} to the laser beam and right confront to the substrate holder. A high power pulsed laser, used as external energy, will shot onto the target surface vaporizing the materials which transport onto the substrate surface. The distance between deposited substrate and the target is usually maintained at ~ 5 cm. The

temperature of substrate holder can be maintained from room temperature to ~1000 ℃ by precisely temperature control which can be achieved with embedded computer controlled thermal couples. High quality and epitaxial thin films can be achieved with proper film grown parameters including the substrate temperature, laser energy density, pulse repetition rate and proper working gas.

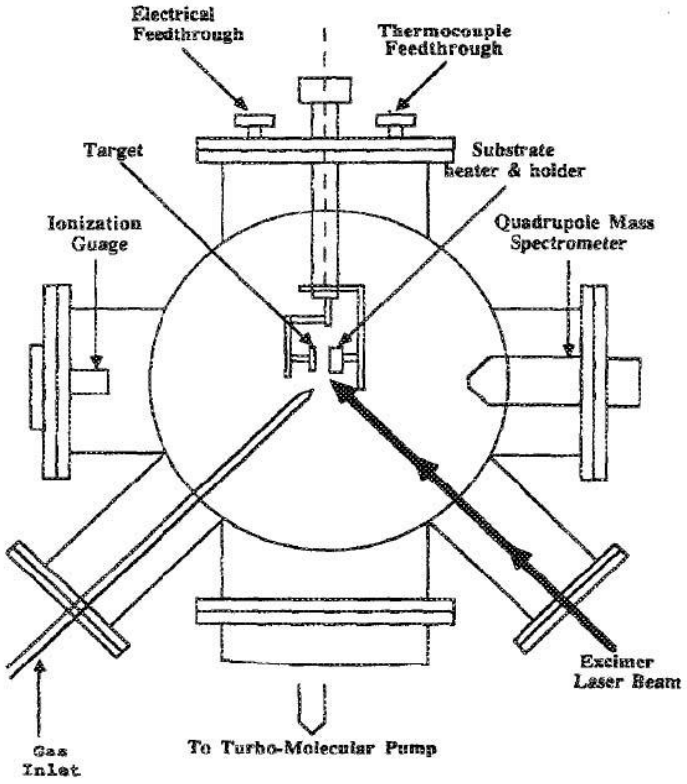

Fig. 2.1. Schematic illustration of a single target pulsed laser deposition system. Reprinted with permission from ref 167. Copyright 1990 AIP Publishing LLC.

General speaking, the useful range of laser wavelengths in PLD is between 200nm and 400nm for thin film growth. Excimer laser and Nd^{3+}:YAG lasers are most widely deposition source for PLD. Yttrium aluminum garnet (YAG) lasers, as solid-state systems, generate high output laser energies by using two YAG rods in an oscillation modes, while the excimer is a gas laser system where the excimer molecules are formed by mixture their component gases. KrF which is one of the highest gain systems for electrically discharged excimer lasers with 248 nm wavelength has been used in this work. In order to steer and focus the beam, a set of optical components including lenses, apertures and mirrors are placed in between the output of laser and the deposition chamber. The beam splitters can be used to split the laser beam into two or more separate beams which can help build multiple deposition systems with multiple chambers but sharing with only one laser source.

PLD, as an extremely versatile technique, can be used to prepare a wide range of thin film materials. Compared to its simple experimental setup, the PLD technique has a complex physical phenomenon. It involves several complicate chemical and physical processes including the laser-target interaction, the interaction of laser beam with evaporated materials and adiabatic plasma expansion combining both equilibrium and nonequilibrium processes. The electromagnetic energy of the incident laser will first converted into electronic excitation and then into thermal, chemical and mechanical energy once a laser beam was hit on a target surface. These energy transactions will result in material evaporation, ablation, excitation, plasma formation and exfoliation. A plume which consists of a mixture of energetic species including small particles, molted

globules, clusters, molecules, atoms, ions, and even electrons will formed by the material evaporation.

In 1990, the basic PLD physical principles is descripted by R. K. Singh and J. Narayan systematically in the following subsections.[168] The physical stages in PLD, separated as three separate regimes, are the laser-target interactions during and after the laser radiation. Those three regimes include: 1) the interaction of the laser beam and the target material resulting the evaporation of the surface layers, 2) the interaction of the evaporated material with the incident laser beam resulting an isothermal plasma formation and expansion, and 3) the anisotropic adiabatic expansion of the plasma leading to the characteristic nature of the laser deposition process. The first two regimes take place at the beginning of laser radiation and through the laser pulse duration (~25 ns duration). Right after the laser pulse terminates, the last adiabatic expansion happens. Fig. 2.2 illustrates the first laser-target interaction regime during the short pulsed laser period.

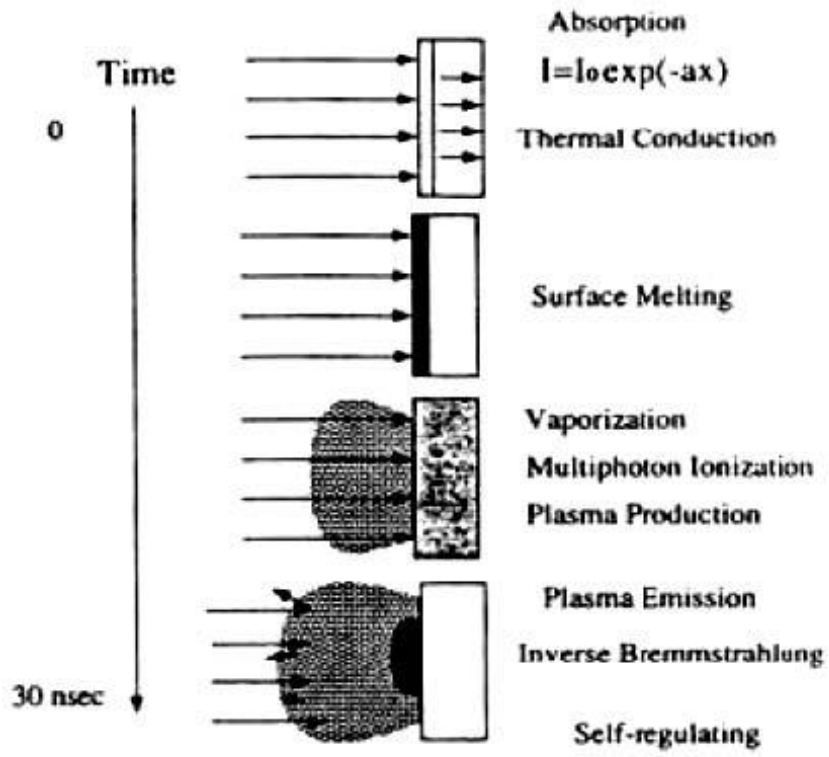

Fig. 2.2. Schematic illustration of the laser target interaction stages during the short pulsed laser period.[168] Reprinted with permission from ref 168. Copyright 1990 The American Physical Society.

The interaction between laser pulses and target material causes the melting and evaporation of the surface layers. The interaction will be affected by both the pulsed laser and target material properties. A one-dimensional heat flow equation can be applied to simulate the case of three-dimensional heat flow and to address the heating and melting process with appropriate boundary conditions. The heat flow equation is given by:

$$\frac{\rho_i(T)C_p(T)\alpha T_i(x,t)}{\alpha_t} = \frac{\alpha(\frac{K_i(T)\alpha T_i(x,t)}{\alpha_x})}{\alpha_t} + I_0(t)\{1-R(T)\}e^{-\alpha(T)x} \quad (2.1)$$

where t is the time, i refers to the solid and liquid interfaces, x is the direction perpendicular to the sample, $\rho_i(T)$ is the temperature dependent density, $C_p(T)$ is the thermal heat capacity, $a(T)$ is the absorption coefficient, $R(T)$ is the temperature dependent reflectivity, $I_0(t)$ is the time dependent incident laser intensity and K_i is the thermal conductivities of solid and liquid phases at the interface. The accurate numerical solutions of this equation can be provided by the finite difference method to characterize the properties of pulsed laser irradiated material.

The high-power pulsed laser beam irradiation on target surface resulting in a high temperature (>2000K) will further lead to an emission of the positive ions and electrons out of the surface. From the Richardson's equation, the emission of electrons can be described in exponential increasing as a function of the temperature. And the Langmuir-Saha equation can be used to calculate the thermal emission of ions from shown as below:

$$\frac{i_+}{i_0} = \frac{g_+}{g_0} e^{(\phi - I)KT} \quad (2.2)$$

where i_+ and i_0 are the positive and neutral ion fluxes respectively, ϕ is the electron work function, g_+ and g_0 are the statistical weight of the positive ionic and neutral states, respectively, and I is the ionization potential of the evaporated material.

Higher density ions will be produced near the surface of the target while the plasma regime is being constantly augmented at the inner edge by the evaporated materials.

Because the outer edge of the plasma regime is transparent to the laser beam, the target surface will continually absorb energy from laser radiation. A schematic illstration in Fig. 2.3 shows that there are totally four different regions could be distinguished as during the incidence of the laser: 1) the unaffected bulk target, 2) the evaporating target surface, 3) the area near the surface absorbing laser beam energy and 4) the rapidly expanding outer edge which is transparent to the laser beam.[168]

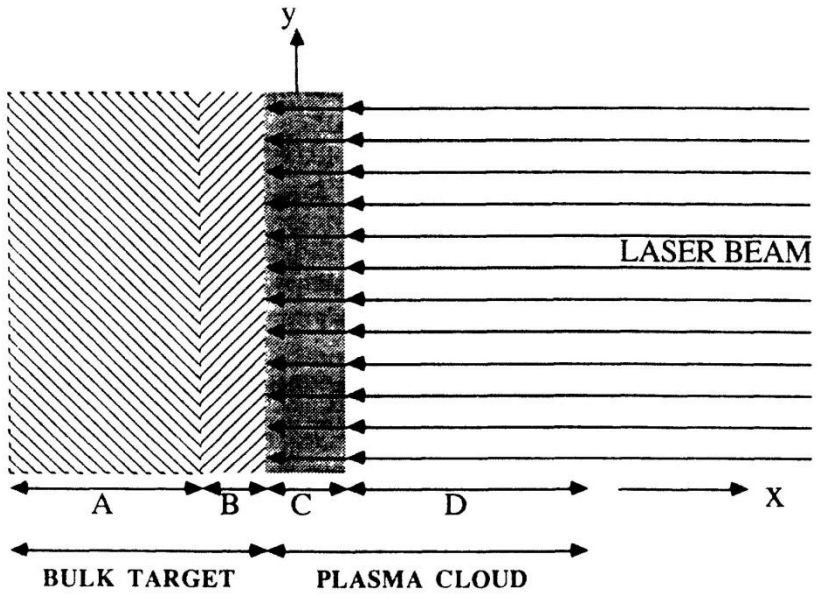

Fig. 2.3. Schematic illustration shows the four different phases presented during the laser-target interaction. Reprinted with permission from ref 167. Copyright 1990 AIP Publishing LLC.

The adiabatic expansion of the plasma in vacuum working chamber will give rise to the laser-deposition process after the plasma formation and its initial isothermal expansion. In this regime, the heat is converted to kinetic energy of the plasma and the velocity of the plasma will decrease as the thermal energy of the plasma will increase. Mainly there are two points which can help address the slow temperature drop. First of all, the energy regain from ions recombination processes balances the cooling process. Secondly, the plasma expands only in one direction considering the initial dimensions are much larger than the transverse directions in an order of 10s. The final stage of PLD includes the deposition of ablated materials onto the substrate and its nucleation and growth as thin film on the substrate surface. The quality of the deposited thin film is determined by this stage. The high energy ejected species by laser-target interaction may induce various damages on the substrate. The energetic species will lead to sputtering of the substrate surface atoms and formation of a collision region between the incident flux flow and the sputtered atoms. Thin film starts to grow on the substrate when the condensation rate is higher than that of the flux and a thermal equilibrium condition can be reached.[169]

Equipped with other techniques will bring the future development of the PLD technique. For example, the precise growth rate control on an atomic level can be achieved with the introduction of high-pressure reflection high-energy electron diffraction (RHEED) in PLD and a in situ growth study can become possible.[170] And the development of ultrafast laser ($<10^{-11}$/s pulses) can result in a fully atomized continuous flow of the ablated material, preparing films with super quality. Also, PLD

would be able to coat large size substrates (>200mm) given the recent results obtained with coated-conductor systems. And PLD equipment and new products for both R&D and production are being commercialized at a steady pace.[166]

2.2 Thin Film Microstructure and Crystalline Characterizations

The characterization methods for deposited thin films in this thesis include non-destructive and destructive techniques allowing the determination of microstructure, crystalline quality, defect and impurities presence, etc.

2.2.1 X-ray Diffraction (XRD)

X-ray diffraction (XRD), as a very convenient, versatile and non-destructive technique, reveals detailed chemical composition and crystallographic structure information of natural and manufactured materials. Once a monochromatic X-ray beam strikes on a material, it will diffract into different specific directions. A three-dimensional plotting of the crystal can be simulated from the angles and the intensities of the diffracted beams. It offers not only an effective approach to determine the orientation of a single crystal or grain but also help identify the crystal structure of an unknown material or even measure the size, shape and internal stress of small crystalline regions.[171]

Bragg's Law, as the most fundamental formula, refers to the simple equation as below:

$$n\lambda = 2d\sin\theta \tag{2.3}$$

Where the variable d is the distance between atomic layers in a crystal, and the variable lambda (λ) is the wavelength of the incident X-ray beam; n is an integer shown in Figure 2.4. It explains why X-ray beams at certain angles of incidence are reflected by the cleavage faces of crystals. [172]

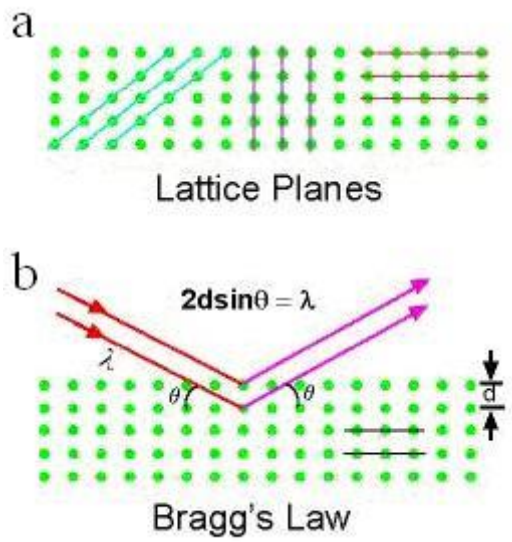

Fig. 2.4. (a) A two dimensional periodic array of atoms forming different planes in the crystal, (b) diffraction of a set of planes with inter-plane distance d followed by Bragg's Law.

The Bragg's Law conditions are satisfied by different d-spacings in materials by varying the angle theta. The XRD patterns which are characteristic of the sample are produced by plotting the angular positions and intensities of the resultant diffracted

peaks of radiation. When a mixture of different phases is present, the resultant diffract patterns are formed by addition of the individual patterns. Although Bragg's Law was developed to explain the interference pattern of X-rays scattered by crystals, other beams including ions, electrons, neutrons, and protons with a wavelength similar to the distance between the atomic or molecular structures of interest could be examined by diffraction to study structure of all states of matter.

Thin film x-ray diffraction refers to an x-ray diffraction techniques collection which is used to characterize thin film samples. The thin film epitaxial quality are critical for performance in microelectronic and optoelectronic devices. Before using x-ray diffraction to characterize thin film samples, several special points needed to be taken into account. First, x-ray measurements use reflection geometry but the substrates are generally too thick for transmission. Second, it is required high angular resolution because of sharp peaks from semiconductor materials due to very low defect densities in the material. Therefore, multiple bounce crystal monochromators are adopted for these measurements to provide a highly collimated x-ray beam. Besides the traditional precisely lattice constants measurement, several other measurements including x-ray reflectivity, glancing angle x-ray diffraction, high resolution x-ray diffraction, residual stresses analysis, texture analysis and rocking curve measurements are also very important and can be done on thin film samples by x-ray diffraction.[173]

2.2.2 Transmission Electron Microscopy (TEM)

Transmission electron microscopy (TEM), as one of the most efficient and versatile tools, is widely used for materials characterization. Because of the limited image resolution in traditional optical microscopes which imposed by the wavelength of visible light, TEMs were developed to increase the image resolution by using electrons. In this dissertation, the morphology, interfaces, crystallography as well as chemical information of nanocomposite thin films was characterized by TEM works. TEM facilities including the JEOL 2010 analytical microscope (200KV, LaB_6 filament with 0.23nm point resolution) and FEI Tecnai F20 analytical microscope (200KV, ZrO_2/W Schottky firld emitter with 0.27 point resolution, Z-contrast dark-field STEM imaging using the HAADF detector) were used in this work. Both the regular single-tilt and double-tilt holders have also been used for material characterizations.

A typical TEM system, as shown in Fig. 2.5, consists of four parts: the electron source, electromagnetic lens system, sample stage and imaging systems which all combined in a vacuum column. [174] The electron source is made of a cathode and an anode. When the cathode is being heated, it will emit electrons and a negative cap confines those electrons into a loosely focused beam. The positive anode accelerates the beam towards the specimen. The electrons in the center will pass through the small hole of the anode while electrons at the rim of the beam will fall onto the anode. After leaving the electron source, electromagnetic lens and metal apertures are used to the tightly focus electron beam. Because only electrons within a small energy range can pass through the system, the electrons in the electron beam will have a well-defined energy.

Another electromagnetic lens system and a screen are consisted of the imaging system. The electromagnetic lens system contains two lens systems, one is to refocus the electrons after they pass through the specimen, and the other is to enlarge the image and projecting it onto the screen. The screen having a phosphorescent plate glows when being hit by electrons. [175-177]

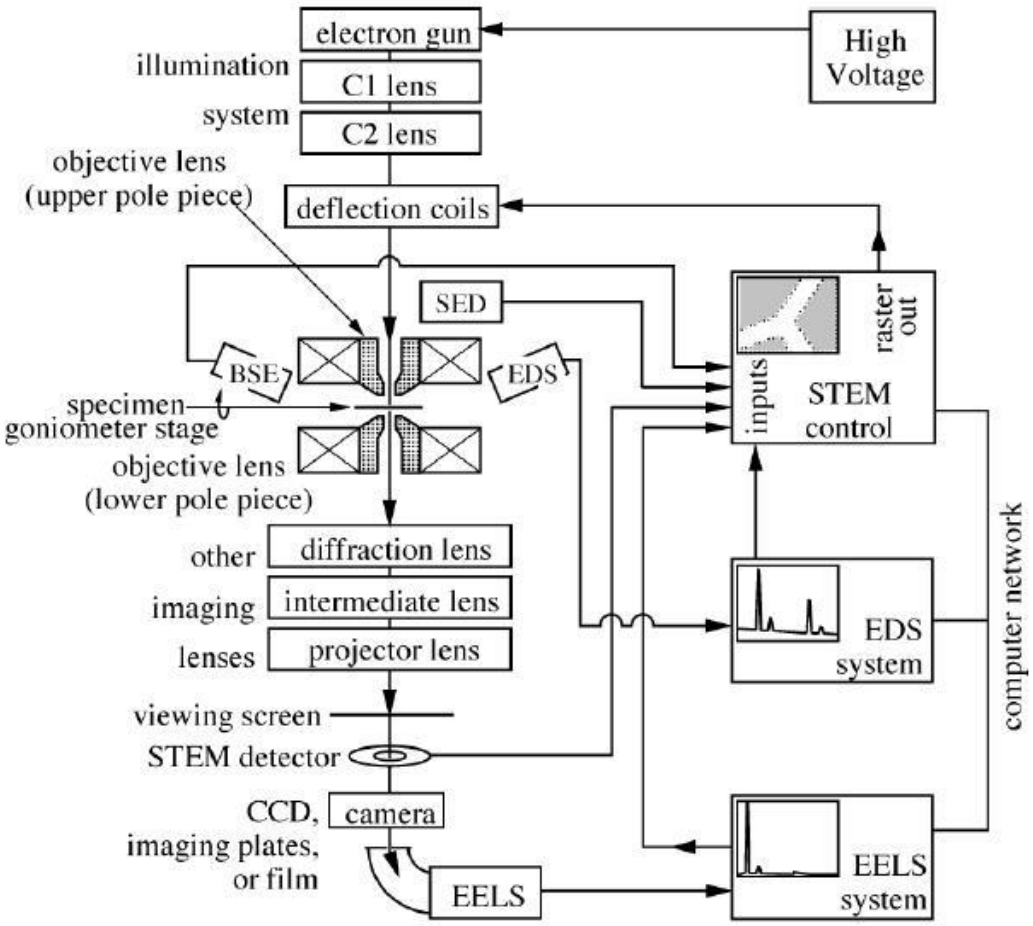

Fig. 2.5. The illustration of a typical TEM system with analytical capabilities. Reprinted with permission from ref 177. Copyright 2009 Springer eBook.

The resolution of TEM can be defined as to distinguish the closest spacing as separate entities of two points which can clearly be seen through the microscope. Because the light from a very small point in the object suffers diffraction and even an infinitesimally small point becomes a small Airy disc in the image, it limits the resolution of a microscope. Therefore, the aperture must be as large as is feasible to make this disc as small as possible. The criterion proposed by Rayleigh works well in most cases and has been used extensively ever since; the two points can be distinguished when the maximum intensity of an Airy disc coincides with the first minimum of the second. It is illustrates by Fig. 2.6 that the resolution limit is $d_1/2$. Microscopes apertures are normally characterized in terms of the semi-angle (α) which subtends the specimen. Then, the resolution could be derived from diffraction theory by an expression:

$$r = \frac{0.61\lambda}{n\sin\alpha} \tag{2.4}$$

Where *n* is the refractive index of the medium between the object and the lenses, λ is the wavelength of the radiation, and α is the semi-angle of collection of the magnifying lens. The $n\sin\alpha$ is usually called as the numerical aperture (NA).

TEM with short wavelength of electrons can achieve not only the high resolution images but also the further magnification of the images. The degree of enlargement of the diameter of a final image compared to the original determines magnification. In practice, a distance measured between two points on an image divided by the distance measured between these same two points on the original object equals to magnification. At least three magnifying lenses are in a TEM including the objective, intermediate, and

projector lenses. The final magnification is determined by the product of the individual magnifying powers of all of the lenses in the system.[175]

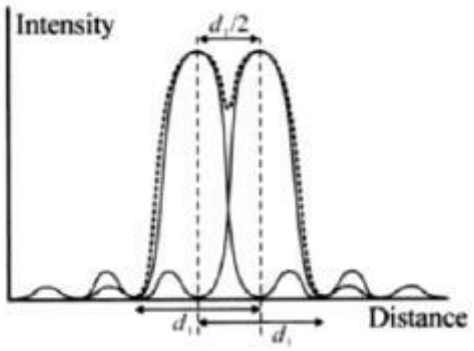

Fig. 2.6. The intensity of the Airy rings from two neighboring pinholes. A resolution limit of $d_1/2$ is given by the intensity distributions from each of the pinholes separately and the maximum intensity from one pinhole coincides with the first minimum from the other.

As shown in Fig. 2.7, there are two basic operation modes of the TEM system: the diffraction mode and imaging mode. Diffraction mode and imaging mode can be easily switched in the TEM by changing the focal length of the intermediate lens. In the image mode, the image plane coincides with the image plane of the objective lens; while in the diffraction mode, the image plane coincides with the back focal plane of the objective lens. Considering the specimen always shows little contrast in the simple imaging mode,

objective apertures are inserted at the back focal plane of the objective lens in the conventional imaging mode to increase the contrast, which is called diffraction contrast. A bright-field (BF) image will be formed when the aperture is positioned allowing only the transmitted (undiffracted) electrons to pass, When only some diffracted electrons are allowed to pass, a dark-field (DF) image will be formed. [176]

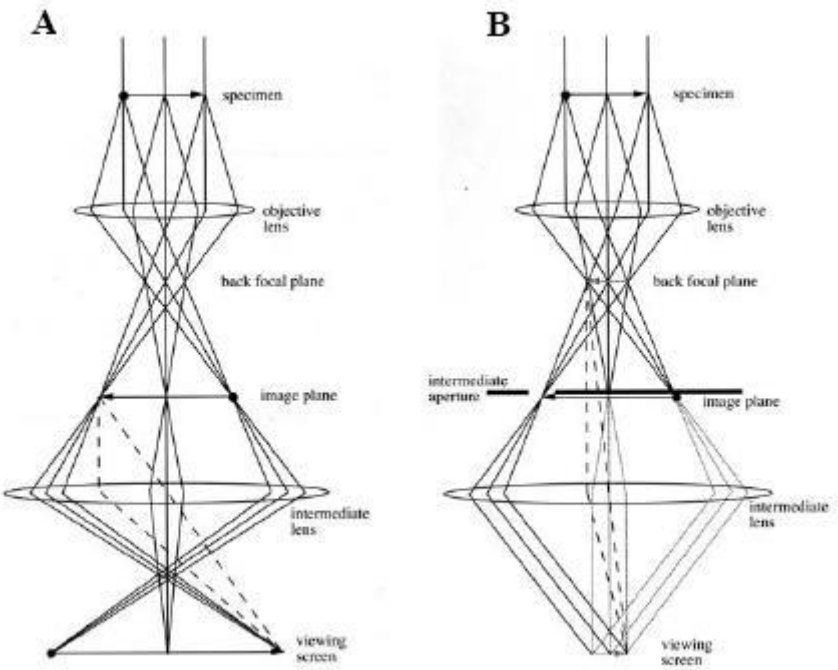

Fig. 2.7. Two basic operation modes of TEM system: (a) the diffraction mode and (b) the imaging mode. Reprinted with permission from ref 177. Copyright 2009 Springer eBook.

High resolution TEM, as an imaging mode of the TEM, allows the imaging of the crystallographic structure of a sample at an atomic scale. Because of the high resolution, it is a powerful tool to study microstructure and nanoscale properties of crystalline material such as polymer, metals and ceramics. There are several aspects and related simulation work need to be satisfied to achieve HRTEM. The proper specimen holders must be used and the objective lens need be adjusted to obtain the shortest possible focal length. Carefully adjustments need to be done, such as the use of higher accelerating voltages, to achieve higher resolution. Field emission guns are adapted to further lessened chromatic aberration since the energy spread of electrons generated from such guns is considerably narrower. For most specimens, larger objective lens apertures are used to minimize diffraction effects but it leads to lower contrast, smaller apertures may be used to increase contrast but resolution will be diminished. In addition, they must be free of dirt because it has a more pronounced effect on astigmatism. Small condenser lens apertures will diminish spherical aberration at the expense of overall illumination. Specimen preparation techniques offer another way to enhance the resolution capability. For example, extremely thin sections will reduce chromatic aberration.

In HRTEM images, the parameters of the microscope and the specimen determine the image contrast. The image contrast interpreted in terms of columns of atoms is possible only for a narrow range of experimental conditions. Multi-slice method, a dynamical calculation of diffracted amplitudes of electron beams, can help to simulate the beam-specimen interaction as shown in Fig. 2.8. The incident wave function is calculated by the effect of the first slice on the phase and the resulting wave function is

then propagated through free space to the next slice. Only until the desired specimen thickness is achieved, this process stops. Assuming Δz is sufficiently small, the method is highly accurate. [176]

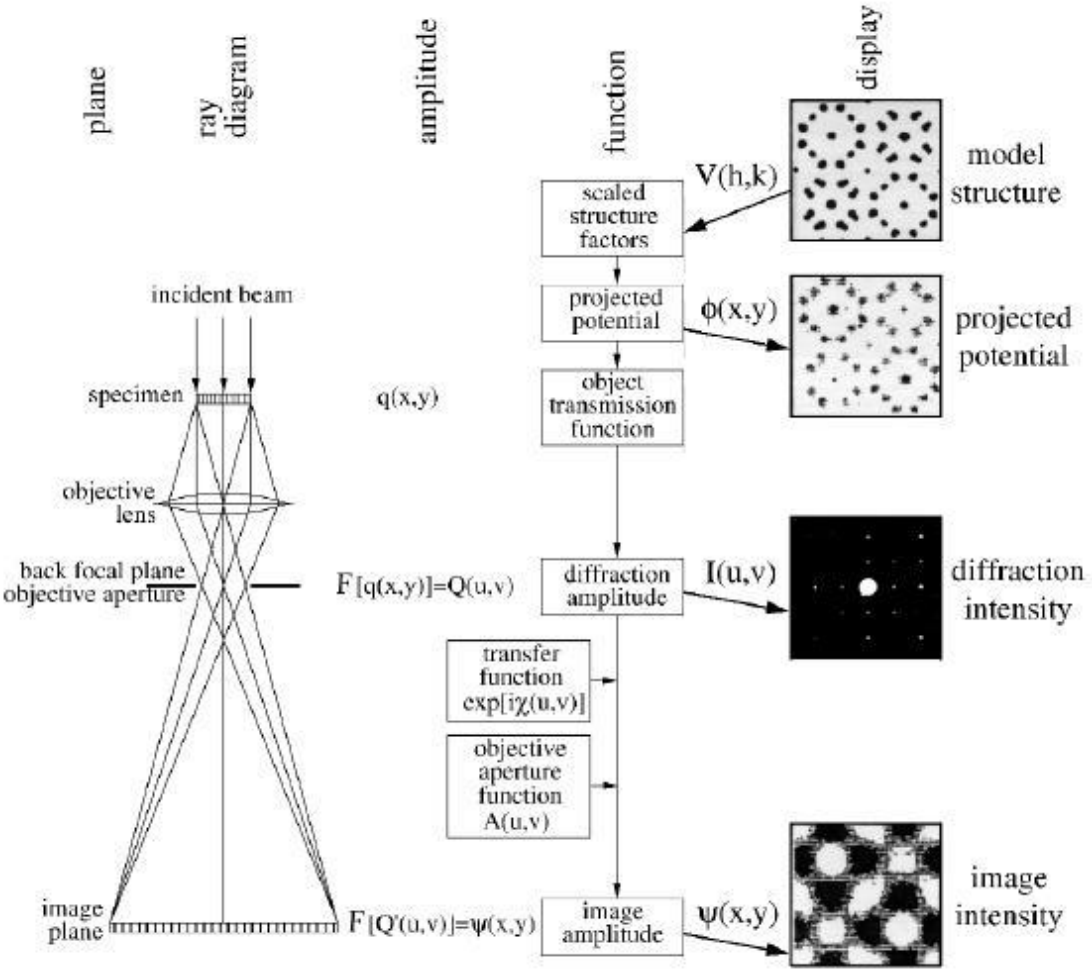

Fig. 2.8. Multiple steps in the calculation of a high-resolution TEM image by the multi-slice method. Reprinted with permission from ref 177. Copyright 2009 Springer eBook.

The scanning transmission electron microscope (STEM) where the beam scan parallel to the optic axis at all times so that it mimics the parallel beam in parallel to its scanning is another working mode of TEM. The schematics of scanning the convergent probe for STEM images are shown in Fig. 2.9. When the probe scan across the specimen surface, the double-defection process ensures it remains parallel to the optics axis. The rastering of the beam across the sample enables these microscopes for analysis techniques including mapping by electron energy loss spectroscopy (EELS), energy dispersive X-ray (EDX) spectroscopy and annular dark-field imaging (ADF). These signals can be obtained and simultaneously be allowed for direct correlation of image and quantitative data. It is possible to form atomic resolution images by using a STEM and a high-angle detector because the contrast is directly related to square of the atomic number (Z^2-contrast image). Compared with the conventional high resolution electron microscopy technique which uses phase-contrast, STEM directly uses interpretable z-contrast images. [177]

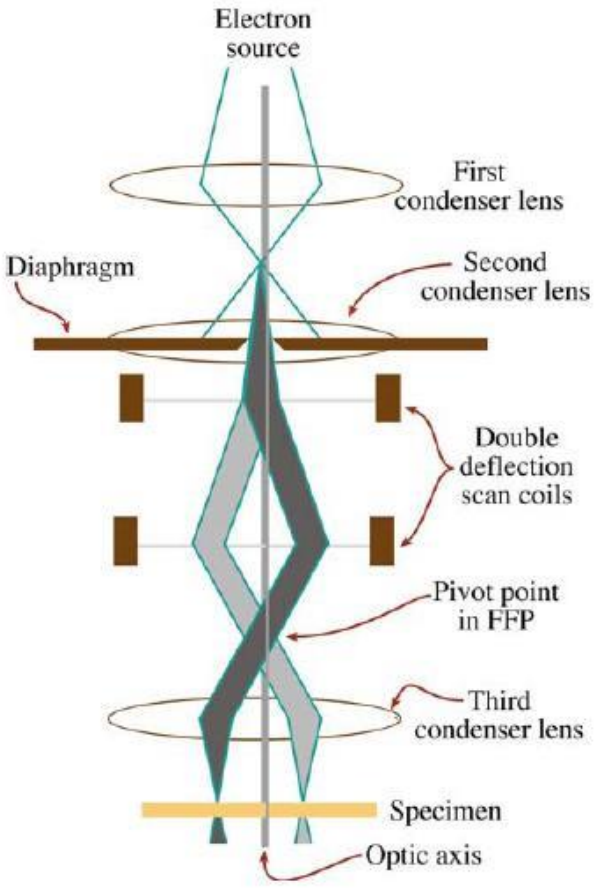

Fig. 2.9. Schematic diagram of the scanning of convergent probe for STEM imaging. Reprinted with permission from ref 177. Copyright 2009 Springer eBook.

The main challenge of TEM specimen preparation is to finally achieve a thin region less than 100nm in the sample to get electron transmit. To select specimen preparation methods, it depends on the material information you are looking for and the material features. In this dissertation, microstructure and interfaces of complex oxide thin films are studied. Therefore, cross-section TEM specimen plan-view TEM specimen are

prepared to see the film-substrate interface and the nanocomposite films growth morphologies. Manually, the thin films specimen preparation follows the following steps: (1) thin slice cutting from bulk sample; (2) slices glue and pre-thinning; (3) grounding and polishing the slice and (4) final thinning. The pre-thinning can be achieved by tripod polisher with the help of diamond lapping films and diamond polishing paste. Either electro-polishing or ion-milling can be used for the final thinning process. Ion-milling is a powerful tool to finally reduce the sample thickness down to 100nm scale. Various factors including ion energy, angle of incidence, vacuum, initial surface topology, ion orientation and beam energy can be adjusted. FIB assisted method is another TEM specimen preparation method that has been rapidly adopted by the semiconductor industry. In a FIB-SEM dual system, the ion gun produces well-controlled Ga ions beam to cut on either side to leave a thin wall. The wall can be further ion-polished to get really thin for TEM and finally it will be attached to a probe for lift out and place it on a supporting film.

2.2.3 Scanning Electron Microscope (SEM)

Scanning electron microscope (SEM) is a characterization tool to collect various signals at the surface of solid specimens by using a focused beam of high energy electrons. The signals derived from interactions between electron and sample reveal information about the sample including texture, chemical composition, and crystalline structure. The fundamental principal of SEM is that accelerated electrons with significant amounts of kinetic energy, interact with sample and generate signals such as

secondary electrons for producing SEM images, backscattered electrons (BSE), and diffracted backscattered electrons (EBSD) for determining crystal structures and orientations of minerals, photons, visible light (cathodoluminescence) and heat. Among them, secondary electrons and backscattered electrons are widely used to image samples. The surface morphology and topography on samples can be shown by secondary electrons while backscattered electrons are used for illustrating contrasts in composition in multiphase samples i.e. for rapid phase discrimination. Since inelastic collisions of the incident electrons with electrons in discrete orbital (shells) of atoms in the sample generate X-ray and the yield X-rays are of a fixed wavelength related to the difference in energy levels of electrons in different shells for a given element. Therefore, it could be used to identify and even quantify the elements. Because x-rays generated by electron interactions do not lead to volume loss of the sample, SEM analysis is considered to be non-destructive and could be used to analyze the same materials repeatedly. Fig 2.10 shows schematic illustration of SEM equipment. In most cases, the information of a selected area of the surface of the sample is collected to generate a 2-dimensional image that displays spatial variations in these properties. In a scanning mode by traditional SEM techniques, areas ranging from approximately 1 cm to 5 microns in width can be imaged (magnification ranging from ~20X to ~30,000X, spatial resolution of 50 to 100 nm). In addition, qualitatively or semi-quantitatively information including chemical compositions, crystalline structure, and crystal orientations could be obtained by conducting the SEM analyses of selected point locations on the sample.

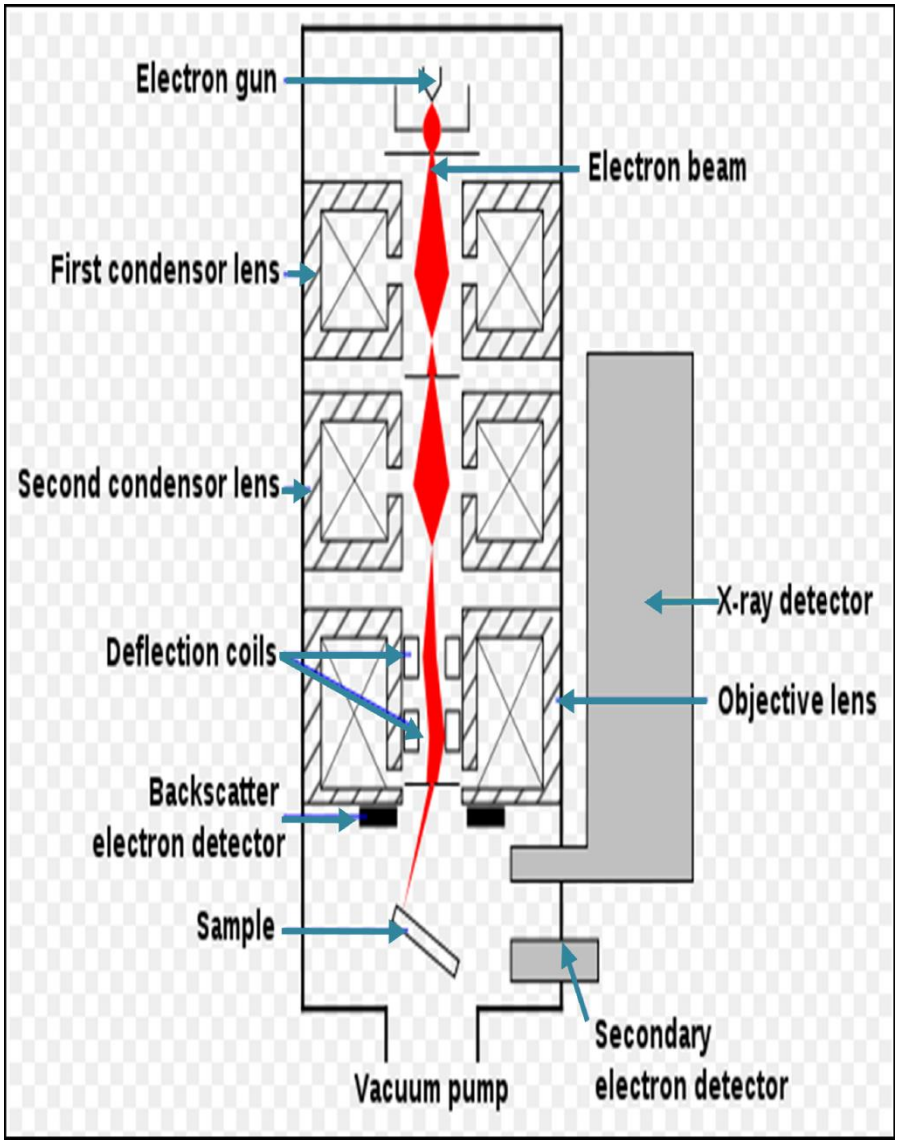

Fig 2.10. Illustration of typical SEM equipment.

2.3 AC Impedance Spectroscopy

The AC impedance method, as a powerful technique for fuel cell diagnosis, can give information on individual losses including oxygen reduction reaction kinetic, mass-transfer, and electrolyte membrane resistance losses.[9, 40, 178] Compared with other electrochemical methods, AC impedance spectroscopy is a non-destructive method to evaluate a wide range of materials, including coatings, anodized films, batteries and fuel cells. As seen in Fig. 2.11a, when a small sinusoidal ac signal (typically a few millivolts) is applied, the excitation of ac response from the cell over a range of frequencies can be observed.[179] The amplitude and the phase shift relationship between the excitation and response signals in term of the frequency determine the characteristic impedance: $Z(j\omega) = Z' + jZ''$. The resultant data can be plotted in form of Nyquist plot or as magnitude and phase as function of frequency (Bode plot) which can be fitted by the equivalent circuit (a typical example shown in Fig. 2.11b). Considering the complexity of SOFC, several processes including electrical, electrochemical and chemical and mass transport contribute to the observed impedance plot. The equivalent circuit tries to separate and identify those processes and reaction steps via time scale. A typical example of a dense $La_{0.5}Sr_{0.5}CoO_{3-\delta}$ film on single-crystal YSZ at 750 ℃ in oxygen is shown in Fig. 2.11c. The total impedance in this case interpret as separate cause: the electrolyte impedance (high frequency), an interfacial impedance at medium frequency (MF), and a low-frequency (LF) impedance associated with O_2 oxidation/reduction at the surface of the film. [178, 180]

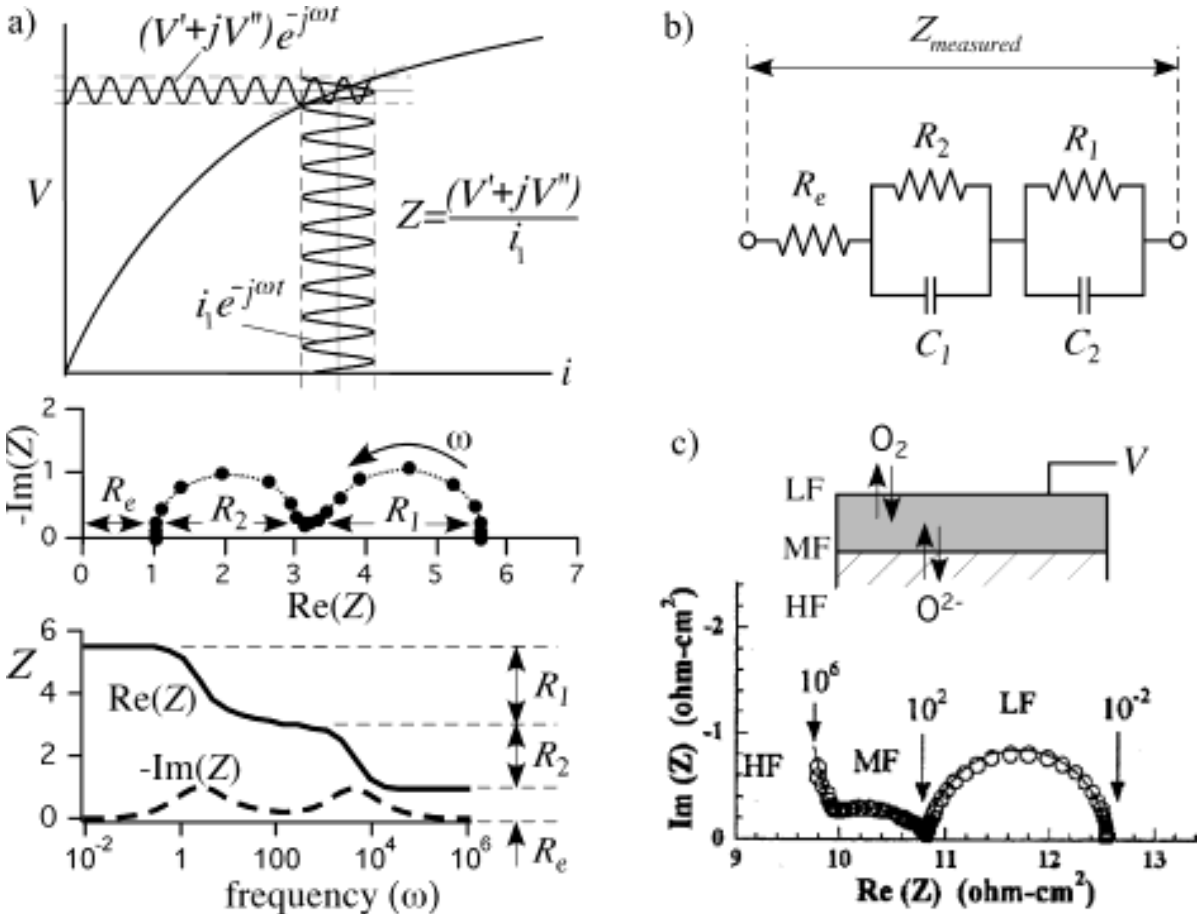

Fig 2.11. (a) AC impedance analysis through a sinusoidal current or voltage perturbation which is measured and analyzed in terms of gain and phase shift as a function of frequency (w). (b) A typical example of equivalent circuit for fitting the impedance curve. (c) Example of impedance plot of a dense $La_{0.5}Sr_{0.5}CoO_{3-\delta}$ film on single-crystal YSZ at 750 ℃. Reprinted with permission from ref 180. Copyright 2001 AIP Publishing LLC.

For investigating the electrochemical properties of the electrolyte and cathode, AC impedance is the main tool discussed in this dissertation. The electrochemical cells were prepared with either the in-plane configuration (electrolyte) or symmetric cell (electrode). Platinum strips (Heraeus CL11-5100, Pt ink) were prepared by screen printing method used as current collectors. The typical AC impedance measurement was conducted in the frequency range of 10^{-1} – 30MHz from 300 to 700 ℃ in air.

2.4 Single Cell Power Measurement

Single Cell Power Measurement is used to measure the power output of anode-supported single cells. Those cells were sealed by glass and assembled as shown in Fig. 2.12. When the temperature in the furnace stabilized, the air was applied in the cathode side and the hydrogen was input to the anode sides. At such circumstance, the cell voltage and output current was acquired at the same time.

In this thesis, the bilayer electrolyte YSZ/GDC and interlayer were deposited on the anode disks of NiO/YSZ using PLD technique. The cathode powders which were ball milled for 48hrs in ethanol using zirconia milling media mixed with an organic binder (Heraeus V006) to make slurry. It subsequently applied on the thin film electrolyte by screen printing method and the effective electrode area of the cell was ~1cm^2. During the single-cell performance test, Humidified H_2 (~3% H_2O at 30 ℃) with a constant flow rate of 80 mL min^{-1} and air with at a constant flow rate of 120 mL min^{-1} were supplied as the fuel and the oxidant, respectively. Platinum grids and wires used as current collectors were attached onto porous electrodes. Current-voltage (IV)

measurements were performed by an Arbin BT2000/fuel cell test station with two electrode configuration. More experimental detailed including the firing temperature of various cathodes, anode disks will be presented in the following chapters.

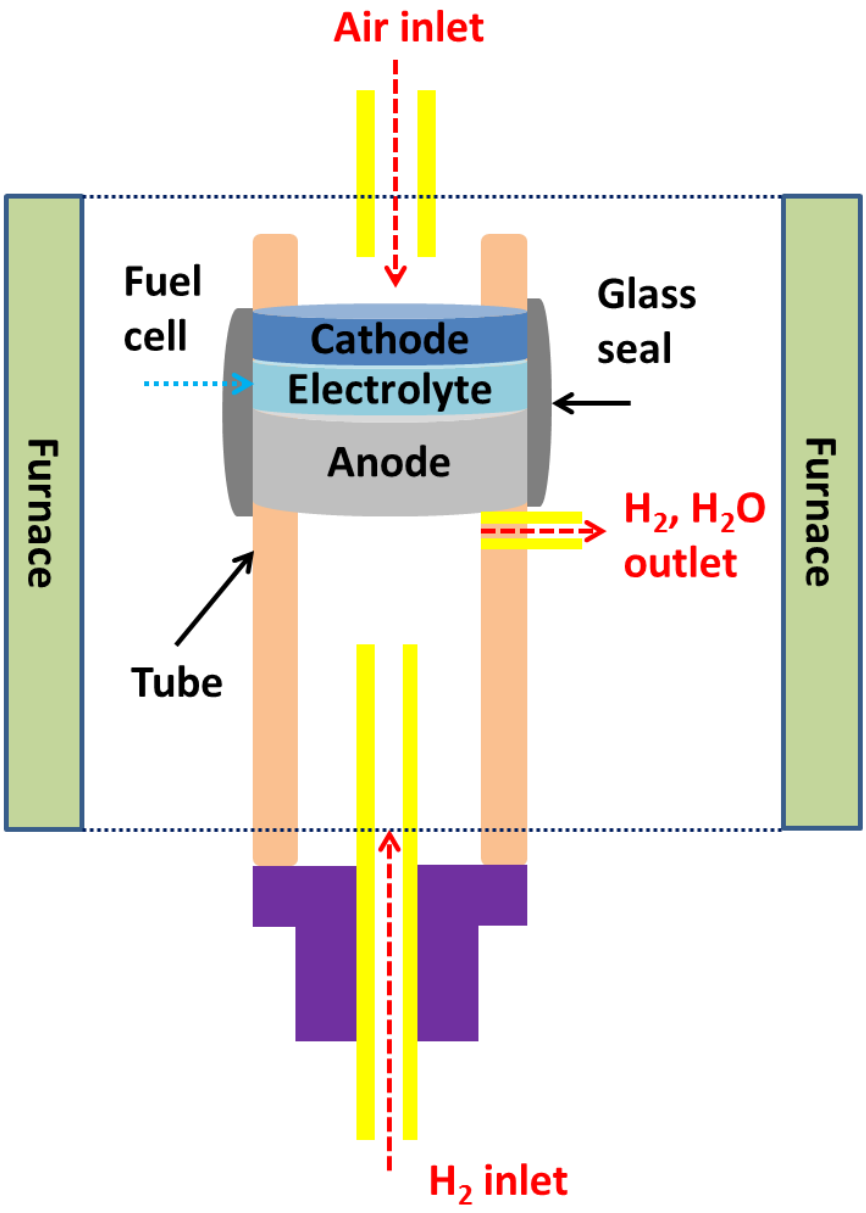

Fig 2.12. Schematically illustration of the SOFC power measurement.

3. ENHANVED ELECTROCHEMICAL PROPERTIES OF BI-LAYER $La_{0.5}Sr_{0.5}CoO_{3-\delta}$ CATHODE PREPARED BY A HYBRID METHOD*

3.1 Overview

Bi-layer $La_{0.5}Sr_{0.5}CoO_{3-\delta}$ (LSCO) cathodes are processed by a hybrid method that combines a seed layer prepared by a pulsed laser deposition (PLD) technique and a conventional cathode layer (~7 μm in thickness) by a screen printing method. By inserting the PLD seed layer with the thickness of ~500 nm or less, robust cathode films with desired microstructure and excellent adhesion properties with the underlying electrolyte layer, are successfully fabricated. The area specific resistance (ASR) of the hybrid cathode layers decreases about 5 times compared with that of the single layer cathode films prepared by the conventional screen printing method. The hybrid approach provides a cost-effective way to fabricate thick cathode films with significantly enhanced electrochemical properties for solid oxide fuel cells (SOFCs).

---

* Reprinted with permission from "Enhanced electrochemical properties of Bi-layer $La_{0.5}Sr_{0.5}CoO_{3-\delta}$ cathode prepared by a hybrid method" by Q. Su, S. Cho, Z. Bi, A. Chen, and H. Wang, Electrochimica Acta, 56 (2011), 3969 – 3974. Copyright (2013).

3.2 Introduction

Solid oxide fuel cells (SOFCs) have attracted extensive research interests because of their high energy efficiency and clean energy conversion.[1, 4] Because of higher cost-effectiveness, wider fuel options and higher fuel efficiency compared with other fuel-cell type, thin film SOFCs (TFSOFCs) are considered as one type of the most promising alternative energy sources. Recent research of TFSOFCs mainly focuses on two aspects: (1) to decrease the operation temperature to 500-700 ℃ or lower, (2) to increase the power output density by optimizing the electrolyte and cathode microstructures in the cells.[181] Cathode, as one of the major components, where oxygen reduction and transportation takes place, is believed to play a key role in determining the overall SOFC performance and therefore attracts a wide range of research efforts.[108, 182, 183]

Screen printing is one of the most conventional and widely used thin film fabrication methods for thin film cathode layer.[184] It is an easy method and is cost-effective to process thick films over 10 μm. However, a high temperature thermal treatment (over 1100 ℃) is required after the screen printing process. The thermal treatment often leads to a significant shrinkage in film thickness, crack formation and a possible delamination of the film.[48, 185] This has raised concerns in the reproducibility and reliability of the cathode layer processed by screen printing. Pulsed laser deposition (PLD) is another thin film deposition technique which is used to processing cathode thin films with well-controlled microstructure by adjusting deposition parameters.[186-188] In our previous work, cathode layers with desired

nanopores [50, 189] and vertically aligned nanocomposite structures [51] were successfully fabricated by PLD and show excellent electrochemical properties. The well-controlled microstructure helps reduce the polarization resistance and enhance the overall SOFC performance. However, the low growth rate and high processing cost are the two limiting factors for processing the cathode layer exceeding micron range by PLD. For example, to grow a 5~6 μm thick cathode, it may take 1~2 hours of PLD deposition depending on materials and laser energy (The estimation is based on the growth rate of 2 Å/pulse and the pulse rate of 5-10Hz).

In this paper, a hybrid method combining both the screen printing and PLD techniques is applied in the growth of the thick cathode layer. A thin cathode film was first deposited as a seed layer by PLD, and then followed by a thick cathode layer processed by the screen printing method. The hybrid method reduces the cost significantly compared with the PLD only method since processing a 500 nm thick PLD seed layer will only take about 10 minutes or less depending on the pulse rate. This approach could significantly reduce the cost of PLD deposition while still taking the advantage of PLD approach, e.g., well controlled microstructure, columnnar grains with vertically aligned nanopores, and excellent film adhesion properties between the film and the substrate. Therefore it combines the advantages of both growth techniques, e.g., cost effectiveness of screen printing technique and well-controlled microstructure of PLD.

In this study, $La_{0.5}Sr_{0.5}CoO_{3-\delta}$ (LSCO) is chosen as the cathode material for a demonstration of this hybrid method for the following reasons. First, LSCO is one of the

well-studied cathode materials in the literatures.[48, 184, 190, 191] Second, there are issues for LSCO film such as crack formation and film shrinkage during thermal treatment due to large thermal expansion. Those issues also exist in many other cathode systems. If this hybrid method works, it could be applied to many other cathode systems.

3.3 Experimental

3.3.1. LSCO Powder Processing and BET Measurement

The LSCO powders were synthesized by the conventional solid state reaction method through mixing stoichiometric amounts of commercial La_2O_3 (99.99%), $SrCO_3$ (99.9%), Co_3O_4 (99.9%). The raw powders were first ball milled in a stainless steel container for 2 hours, then pressed into ceramic pellets and annealed at 1050 ℃ for 10 hours. After that, the pellets were grounded into powders, pressed into ceramic pellets again and sintered at 1200 ℃ for 10 hours to form the perovskite phase. These dense pellets were used as PLD targets. The right composition LSCO pellets were crushed and ball-milled for 30 hours to refine the LSCO powders to the surface area of 3.19 g/m^2 measured by BET surface adsorption method.

3.3.2 Symmetric Cells Fabrication by PLD and Screen Printing

The LSCO seed layers (~500 nm in thickness) were deposited on pressed $Ce_{0.9}Gd_{0.1}O_{1.95-\delta}$ (CGO) disks and $SrTiO_3$ (STO) (001) single crystal substrates in a PLD system with a KrF excimer laser (Lambda Physik Compex Pro 205, λ=248 nm, 2 Hz). The laser beam with a 45 ° incidence angle was focused to obtain an approximate energy density of 5 $J \cdot cm^{-2}$. The base pressure was around 10^{-6} Torr and the deposition pressure

was 200 mTorr under oxygen atmosphere. The substrate temperature was varied from room temperature (RT) to 500 ℃ to achieve the optimum film crystallinity and microstructure in the PLD seed layer and the following screen printing layer. The slurry for screen printing was prepared using the LSCO powders processed by the same solid state reaction method as above mentioned. The LSCO slurry was then screen printed on CGO substrates with and without the PLD seed layers to fabricate the symmetric cells for impedance measurement. Then the cells were annealed at 1150 ℃ for 2 hours. The PLD seed layer thickness was controlled at around 500 nm. A symmetric cell with PLD single layer only was also fabricated as comparison.

3.3.3 Microstructure Characterizations and ASR Measurements of Symmetric Cells

The microstructure of these films was characterized by a high resolution field emission scanning electron microscope (FE-SEM, JEM-7500F Cold Emission SEM) and a transmission electron microscope (TEM, JEOL 2010 analytical microscope with a point-to-point resolution of 0.23 nm). Platinum grids were gently pressed onto porous electrodes and were used as current collectors. Using a potentiostat/impedance analyzer (Reference 600^{TM}, Potentionstat/ Galvanstat/ ZRA, GAMY INSTRUMENTS), AC impedance spectroscopy measurements were conducted in a frequency range of 10^{-2}–3×10^{5} Hz at the temperature varied from 300 to 700 ℃. The AC impedance data were measured after a waiting period of one hour for reaching stabilized temperatures.

3.4 Results and Discussion

The X-ray diffraction (XRD) θ-2θ patterns of the LSCO powder, the screen printing LSCO film on CGO pellet and the bi-layer LSCO film prepared by the hybrid method are shown in Fig. 3.1A, 3.1B and 3.1C, respectively. XRD data for all three samples match well with the standard PDF card (#048-0122) indicating the pure perovskite LSCO phase with polycrystalline structure. There is no obvious variation in the crystal structure between the LSCO powders and the films on CGO pellets.[191]

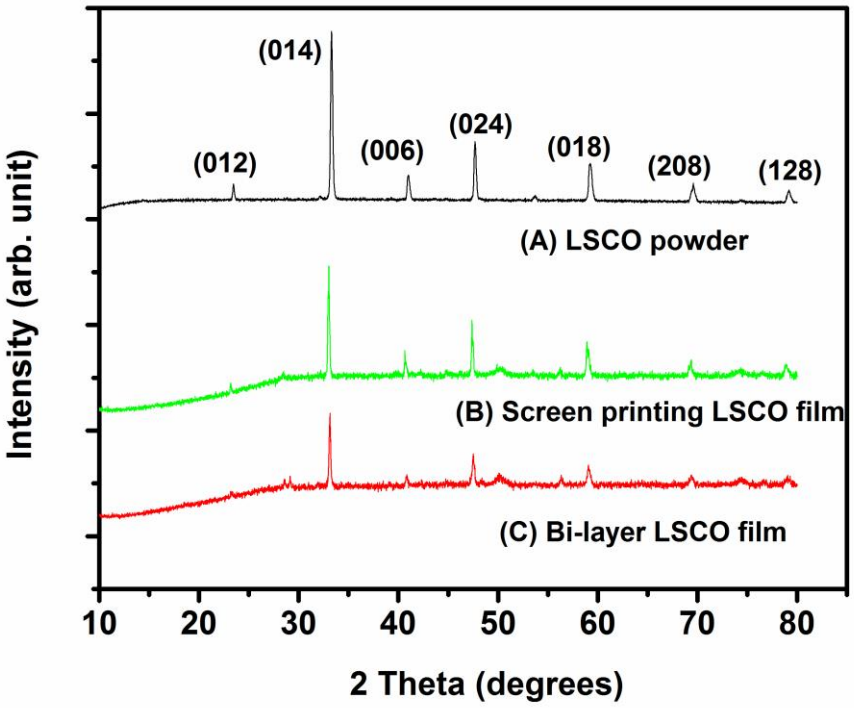

Fig. 3.1. XRD θ-2θ plots for (A) LSCO powders for screen printing, (B) screen printing LSCO film on CGO pellet and (C) bi-layer LSCO film.

The surface morphology of LSCO cathode films with and without the PLD seed layer characterized by SEM, are shown in Fig. 3.2A, B, C and D. The surface of the screen printing only film shows random microcracks with a low film density as seen in Fig. 3.2A. Compared with the screen printing only films, the LSCO films prepared by the hybrid method as seen in Fig. 3.2B (PLD at RT), C (PLD at 300 ℃) and D (PLD at 500 ℃) show significantly enhanced surface coverage and film density with uniform nanopores. The nanopore size decreases as the deposition temperature of the PLD layer increases from RT to 500 ℃. All the hybrid films show a better mechanical strength than the screen printing only ones. Significantly decreased porosity by inserting the PLD seed layer indicates that the seed layer may have provided more nucleation sites for the LSCO screen printing layer under the same thermal treatment so that the LSCO powders tend to nucleate with the PLD seed layer rather than agglomerate into big clusters. To examine the adhesion property between the PLD seed layer and the screen printing layer, cross-section TEM (XTEM) was conducted as shown in Fig. 3.2E. It is clearly shown that there is good grain connectivity between the PLD seed layer and the porous screen printing LSCO layer. For example, there are several locations in Fig. 3.2E where the grains in the screen printing layer nucleate directly from the PLD layer underneath.

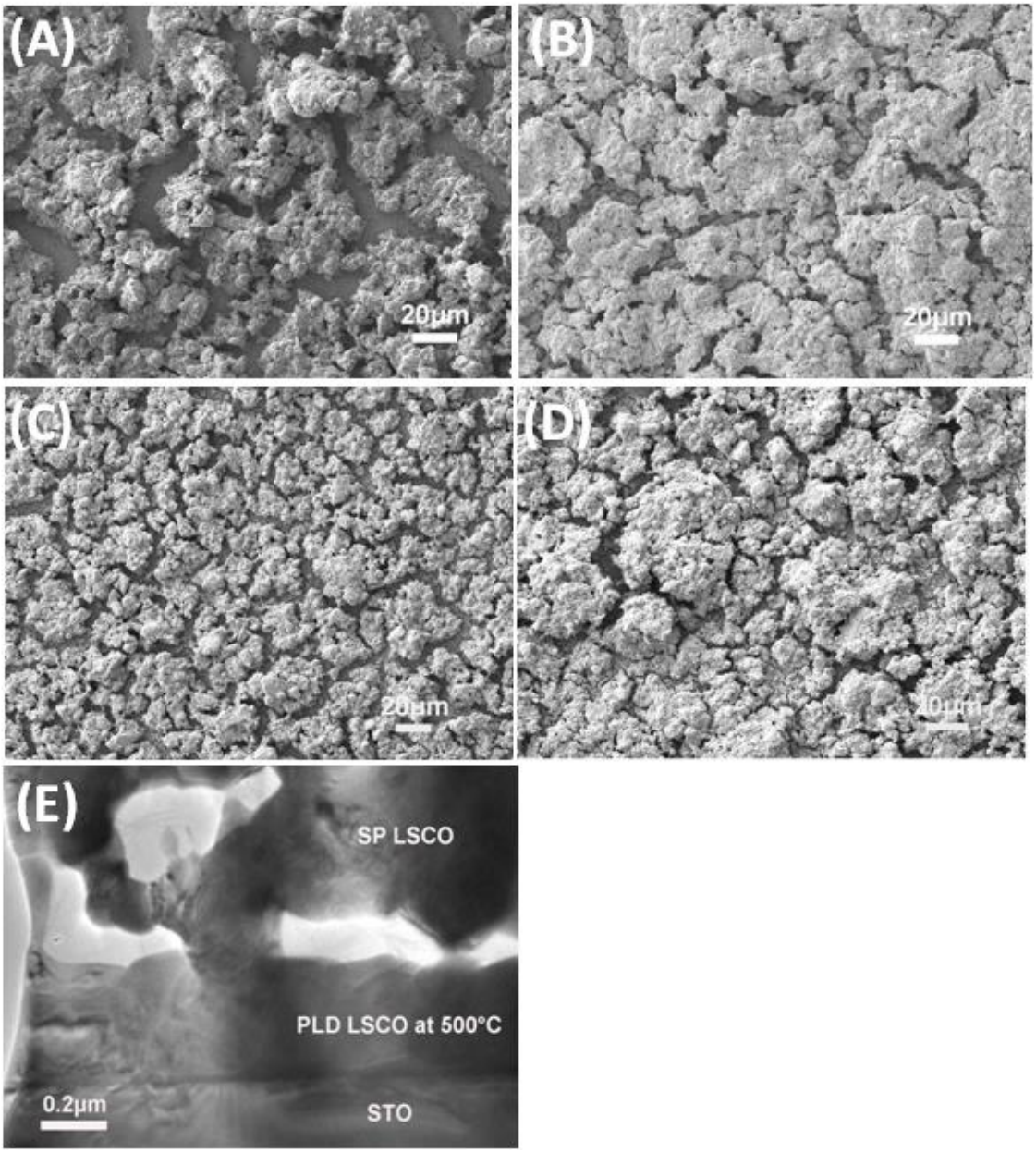

Fig. 3.2. Plan-view SEM images of screen printing LSCO layer (A) directly on CGO pellet, (B) on PLD LSCO layer deposited at RT, (C) on PLD LSCO layer deposited at 300 ℃ and (D) on PLD LSCO layer deposition at 500 ℃. (E) Cross-sectional TEM image of screen printing LSCO on PLD seed layer deposited at 500 ℃. All samples were annealed at 1150 ℃ for 2 hours.

To measure the electrochemical performance of the LSCO cathode prepared by the hybrid method, symmetric cells were processed with the LSCO seed layer deposited by PLD on both sides of a pressed CGO disk followed by the screen printing LSCO layer. The same deposition and annealing conditions were used to ensure a fair comparison. The AC electrochemical impedance spectroscopy (EIS) data (solid lines) and fitted results (dash lines) of the symmetric cells are shown in Fig. 3.3B and 3.3C, respectively at the measurement temperature of 600 ℃. Those symmetric cells were prepared by the hybrid method with the PLD seed layer deposited at RT and 500 ℃. There are three distinct regimes for the impedance spectra: high frequency (HF), intermediate frequency (IF) and low frequency (LF) regimes. The following equivalent circuit model as seen in Fig. 3A was used to fit and analyze the impedance spectra:

$$R_1\text{-}L_1\text{-}(R_2CPE_2)\text{-}(R_3CPE_3)$$

where R_1 represents the resistance of bulk electrolyte (CGO) in high frequency, L_1 accounts for the inductance of the wiring used for impedance measurement, R_2 is assigned to a coupled response of interfacial resistance and grain boundaries of the CGO substrates in IF.[178, 180, 192] In both HF and IF regimes, oxygen partial pressure plays little or no effect on the magnitude of impedance spectra.[51] R_3 relates to electrode reaction resistance which is mainly dominated by the surface exchange process and decreases significantly with the increase of the oxygen partial pressure. CPE_x accounts for the depressed semicircles.

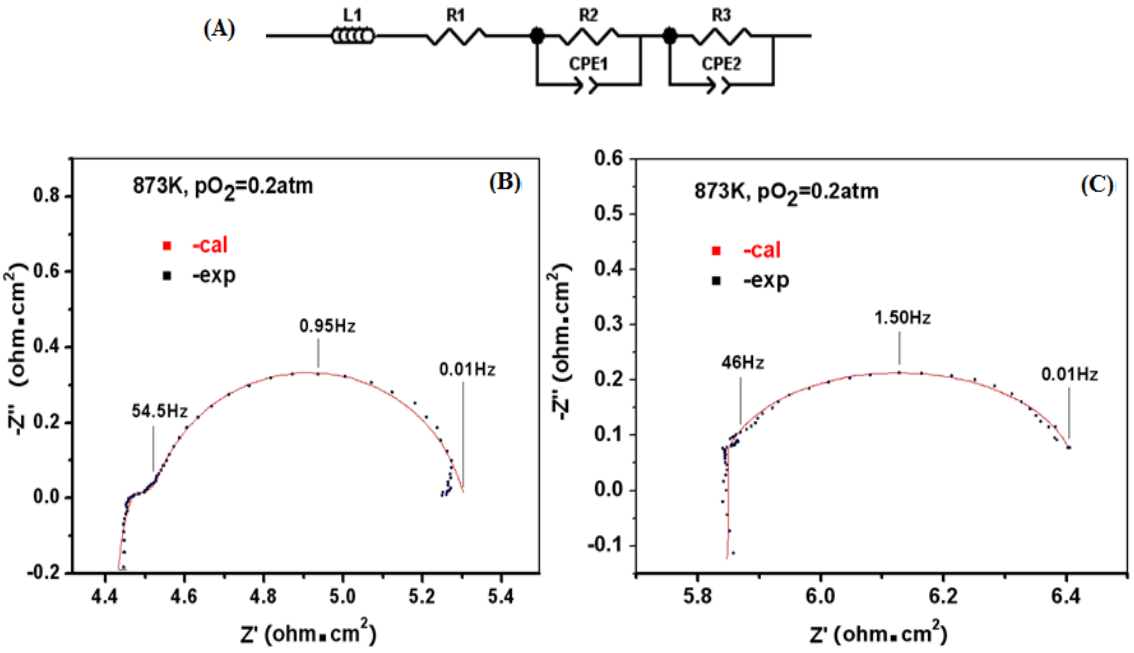

Fig. 3.3. (A) The equivalent circuit model used to fit the impedance data and the impedance spectra of the SP LSCO/PLD LSCO/CGO/PLD LSCO/SP LSCO symmetrical cell collected at 873K and pO_2=0.2 atm. The PLD LSCO layers were deposited at (B) RT and (C) 500 ℃. The points are experimental data and the lines are fitted data.

The area specific resistance (ASR) of the symmetric cells is calculated from the following equation 3.1:

$$ASR = R_p * A / 2 \quad (3.1)$$

where Rp is the electrode polarization resistance and A is geometric electrode area. The electrode polarization resistance is obtained from the difference between two intercepts of the LF semicircle with the Z' axis. The Arrhenius plot of ASR as a function of

measurement temperature for the PLD only cathode layer, cathode layers with and without the PLD seed layer is plotted in Fig. 3.4 and compared with previous reports on LSCO cathodes prepared by conventional screen printing method.[51, 190, 193] The ASR of LSCO cathode prepared by the screen printing only method is ~2 Ω cm^2 at 600 ℃. By inserting the PLD seed layer deposited at different temperatures, the ASR of all bi-layer cathode films has a significant decrease. For example, the ASR value drops to 0.38 Ω cm^2 at 600 ℃ for the sample with the PLD seed layer deposited at 500 ℃. These results suggest that a desired cathode/electrolyte interface plays a key role in the cathode performance. The ASR of the symmetric cell with the PLD seed layer only was measured for comparison. The ASR value is 0.1 Ω cm^2 at 600 ℃ which is similar to our previous report.[50, 51] The low ASR value of the PLD seed layer was attributed to the vertically aligned nanopores in the structure. Comparing all the bi-layer cathode cases, ASR decreases more significantly by inserting the PLD seed layers deposited at higher temperatures (300-500 ℃) than those deposited at RT, which may be contributed to the nanopore structure, excellent crystallinity and strong adhesion between the seed layer and the screen printing layer. The lowest ASR achieved using the bi-layer structure is ~0.35 Ω cm^2 at 600 ℃ which is 5 times lower than that of the screen printing only cathode film. It was reported that the ASR could decrease by inserting a dense cathode layer which increases the effective contact area at the cathode/electrolyte interface or oxygen ion may transport faster via grain boundaries.[194, 195] Compared with the dense cathode interlayer, the PLD seed layer with vertically aligned nanopores could better enhance the oxygen transportation to triple phase boundaries (TPBs). Moreover, it

could offer more nucleation sites for the nucleation of the screen printing cathode layer which will lead to better crystallinity of the screen printing layer and thus better cell performance. It is interesting to note that all the LSCO cathode films prepared, either by screen printing method or by hybrid method, have a similar slope in the ASR plots. The activation energies for LSCO films prepared by different methods are calculated to be ~1.14 eV indicating that the surface charge exchange process dominants the cathode reaction. [178, 196]

Several main reasons account for the advantages of the insertion of the PLD seed layers that enhance the electrochemical and mechanical properties of the LSCO cathode. First, a better adhesion of the screen printing layer is achieved by inserting the PLD seed layer compared with the screen printing only layer.

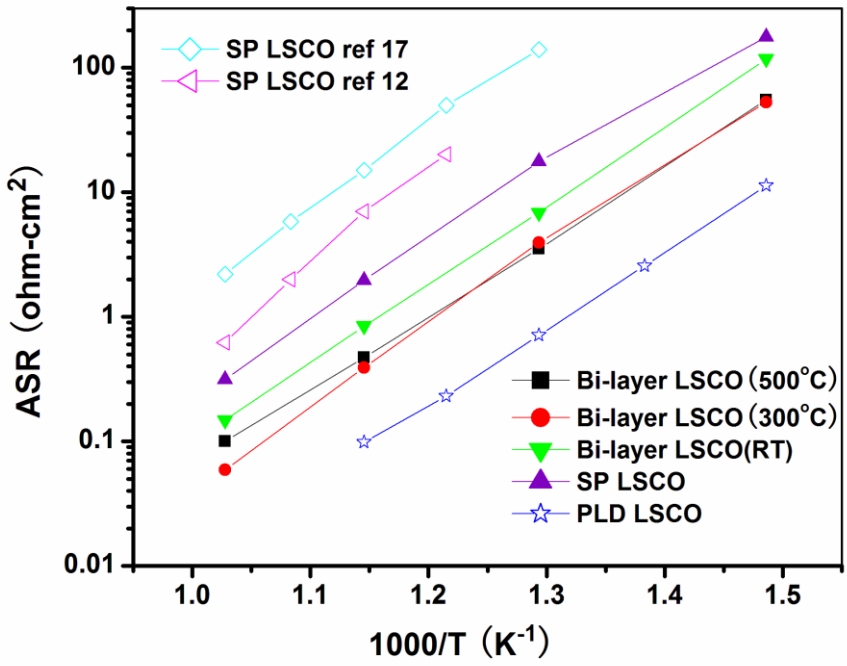

Fig. 3.4. The ASR of the symmetric cells with and without PLD LSCO layer as a function of measurement temperature at pO_2=0.2 atm.

Fig. 3.5 (A-F) compares the plan-view and cross-section SEM of the screen printing layers with the PLD layer after the impedance measurement. Fig. 3.5A and B, C and D, and E and F show the surface and cross-section views for the samples with the PLD seed layer deposited at RT, 300 ℃ and 500 ℃, respectively. Clearly the surface looks identical to that of the samples before the measurements and there is no crack formation in the view area. The cross-section images for all the samples show very clear

interfaces between the screen printing layer, the PLD seed layer and the underlying CGO disk. No obvious crack formation or delamination was found in the samples. The better adhesion may be resulted from the more nucleation sites for the screen printing layer provided by the PLD seed layer. Second, there may be a lower energy barrier of homogeneous nucleation for the hybrid method than that of the heterogeneous nucleation in the case of the screen printing only layer. It is clearly seen that there is excellent grain connectivity between the PLD seed layer and the screen printing layer for all cases even after high temperature measurements. Third, the PLD seed layer with nanopore structure could enhance the catalytic reaction probability at the gas–cathode–electrolyte TPBs at the cathode-electrolyte interface by increasing effective contact areas. It helps decrease the ASR of the cathode and improve the overall SOFC performance. Last, there is no significant structural degradation such as secondary phase formation or interfacial diffusion for the cathode prepared by the hybrid method at different temperatures after the high-temperature thermal measurements. Overall, the PLD seed layer offers better adhesion, more nucleation sites, higher density TPBs and better structural integrity to the screen printing layer, and thus leads to a high performance and reliable cathode layer.

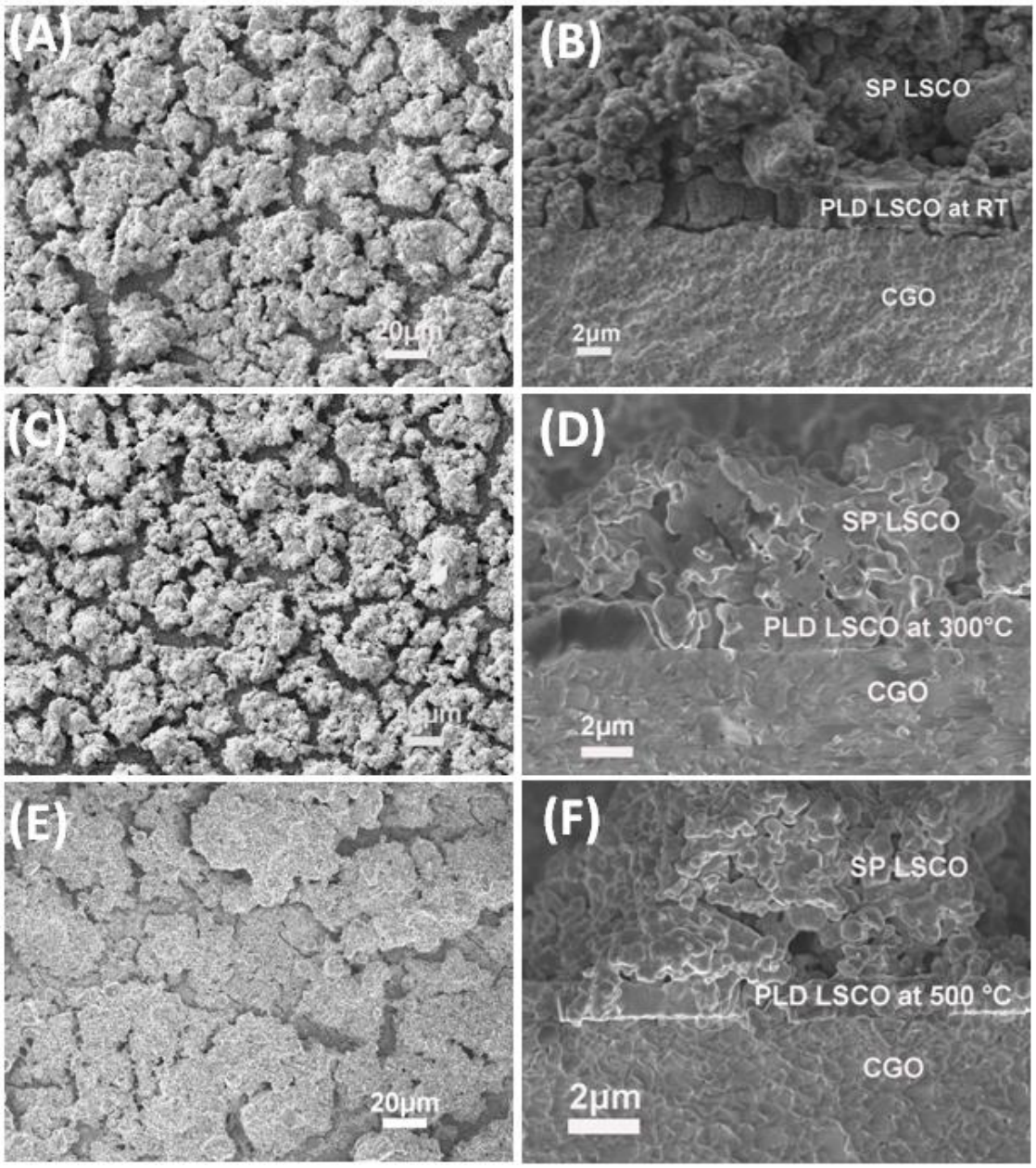

Fig. 3.5. Plan-view (A, C, E) and cross section SEM images (B, D, F) of screen printing LSCO layer on the PLD seed layer after impedance measurement. The PLD layers were deposited at (A) and (B) RT; (C) and (D) 300 ℃; (E) and (F) at 500 ℃.

3.5 Conclusions

In summary, the bi-layer cathodes have been successfully fabricated by combining the PLD and screen printing methods. The XRD data show that the bi-layer LSCO films have pure polycrystalline perovskite phase. Compared with the screen printing LSCO layer directly on CGO electrolyte, the LSCO layer with PLD seed layer has higher film density with uniform nanopore structures, better mechanical properties and higher thermal stability. Based on the cross-section SEM and TEM analysis, there is good grain connectivity between the PLD seed layer and the screen printing LSCO cathode layer after thermal cycles. The ASR of these bi-layer cathodes is ~5 times lower than that of the single layer cathode because of the desired microstructure of the PLD seed layer. The PLD seed layer could also enhance the catalytic reaction probability at the gas-cathode-electrolyte TPBs by increasing the effective areas. It could provide better adhesion between the electrolyte and the screen printing cathode layer. After thermal cycle during high temperature impedance measurements, there is no delamination or crack formation in the bi-layer films. The hybrid method combines the advantages of both PLD and screen printing techniques and offers a cost-effective approach in fabricating thick and high quality cathode films.

4. EFFECT OF INTERLAYER THICKNESS ON THE ELECTROCHEMICAL PROPERTIES OF BI-LAYER CATHODES FOR SOLID OXIDE FUEL CELLS*

4.1 Overview

A hybrid method that combines an interlayer prepared by a pulsed laser deposition (PLD) technique and a conventional cathode prepared by a screen printing method is employed to fabricate bi-layer $La_{0.5}Sr_{0.5}CoO_{3-\delta}$ (LSCO) cathodes. Robust bi-layer cathode films are successfully fabricated with a porous microstructure and excellent integrity with the underlying electrolyte layer. By adjusting the thickness of the PLD interlayers from ~ 50 to ~ 500 nm, a systematic variation of the electrochemical and mechanical properties of the bi-layer cathodes is observed. Compared with single cells without an interlayer, the anode-supported single cells with an LSCO interlayer thickness of ~ 100 nm exhibit significant enhancement in the overall power performance.

---

* Reprinted with permission from "Effects of interlayer thickness on the electrochemical and mechanical properties of bi-layer cathodes for solid oxide fuel cells", Q. Su, D. Yoon, Y. Kim, W. Gong, A. Chen, S. Cho, A. Manthiram, A. Jacobson, and H. Wang, Journal of Power Sources, 218 (2012) 261–267. Copyright (2013).

4.2 Introduction

Because of their efficient and clean energy production, solid oxide fuel cells (SOFCs) have attracted extensive research interest.[1, 4, 95, 181] Compared with bulk SOFCs, thin film SOFCs (TFSOFCs) are more cost-effective, have wider range of fuel options and higher fuel efficiency, and are considered to be one of the possible energy harvesting alternatives.[49, 197] Recent research efforts mainly focus on lowering the TFSOFCs operating temperature (500-700 ℃ or lower) by exploring new materials and optimizing the component microstructures. Research has also focused on enhancing the long-term stability of THSOFCs.[48, 108, 183] The cathode and cathode/electrolyte interface, where oxygen reduction and transport take place, are believed to play a significant role on the overall SOFC performance and have, therefore, attracted ongoing research efforts.[13, 157]

Screen printing, a low cost simple process, is one of the most conventional and widely used fabrication methods to prepare cathode layers with thickness ≥ 10 μm.[198] The high-temperature thermal treatment (over 1100 ℃), which is required after the screen printing process to ensure the adhesion between the cathode and the electrolyte can, however, cause serious shrinkage in the film thickness, leading to cracks and possible delamination.[48, 108] This has raised concerns about the reproducibility and reliability of cathode layers prepared by screen printing. In contrast to screen printing, pulsed laser deposition (PLD) can be used to prepare thinner films with thicknesses from tens to hundreds of nanometers. PLD can be used to fabricate cathode thin films with well-controlled microstructure by adjusting the deposition parameters[51, 189], but the

cost is higher due to the low growth rate and high processing cost. For example, to grow a 5~6 μm thick cathode, it may take 2~4 hours of PLD deposition depending on materials and laser energy (the estimation is based on the growth rate of 0.5-1 Å/pulse and the pulse rate of 5-10Hz). The hybrid method reduces the cost significantly compared with the PLD only method. In our previous work, PLD was used to grow the interlayer with nanopororous microstructure followed by a thick cathode layer (~ 7 μm) prepared by the screen printing method [11]. The hybrid method was shown to combine the advantages of both techniques, namely the cost effectiveness of screen printing and the well-controlled microstructure provided by PLD for the preparation of thick cathode films with well controlled pore structures. A 500 nm thick PLD interlayer was used for the preliminary demonstration.

The interlayer approach has been applied in SOFCs to enhance performance and stability. For example, a composite LSCO-$Ce_{0.9}Gd_{0.1}O_{1.95}$ (CGO) interlayer between electrolyte and cathode has been used as a catalytic layer or transition layer to mitigate thermal stress and lattice strain at the interface.[51] Also, inserting an yttria-doped ceria (YDC) interlayer between the bulk electrolyte and the cathode has been demonstrated to enhance the performance of low-temperature solid oxide fuel cells. The interlayer helps to lower the reaction barrier and to enhance the catalytic reaction probability.[156] In the hybrid approach, the interlayer prepared by the PLD method with a nanoporous structure could provide channels for oxygen gas transport and increase the effective contact area at the gas–cathode–electrolyte triple phase boundaries (TPBs). Also, it provides more nucleation sites for the screen printing layer, consequently producing excellent adhesion

between the electrode and the electrolyte as well as a formation of uniform pores in cathode film. Because the interlayer is made of porous LSCO, which is a mixed conducting cathode material[190], it is expected that the interlayer thickness is closely related to the number of reaction sites, the reaction and diffusion rate of oxygen, and the microstructure of the electrodes. However, up-to-date, no detailed study of the effect of thickness variation of the interlayer on the cathode performance and reliability has been made. In this paper, PLD interlayers with different thicknesses are applied between the screen printed cathode and the electrolyte layer to prepare a set of TFSOFCs. The mechanical and electrochemical properties of those hybrid cathodes are examined and correlated with the microstructure to probe the effect of interlayer thickness. Some guidelines for designing high-performance bi-layer cathodes with optimum performance and low cost are proposed.

4.3. Experimental

4.3.1. LSCO Powder and PLD Target Processing

The PLD targets including LSCO, 8 mol % yttria stabilized zirconia (YSZ) (500 nm, Tosoh Co.), $Ce_{0.9}Gd_{0.1}O_{1.95}$ (CGO), 60 wt. % NiO + 40 wt. % $Ce_{0.8}Gd_{0.2}O_{1.95}$ (NiO-CGO, 500 nm, Praxair Inc.), and CGO electrolyte disks were all fabricated by solid-state reaction through mixing stoichiometric amounts of the raw powders: La_2O_3 (99.99%), $SrCO_3$, Co_3O_4 (99.9%), CeO_2 (99.9%), and Gd_2O_3 (99.9%). The sintering details can be found elsewhere [14]. The phase purity of LSCO, CGO, and YSZ were confirmed by X-ray diffraction (XRD). The LSCO powders for the preparation of screen printing slurry

were obtained from the LSCO target with a pseudo-cubic structure. The LSCO target was crushed into powders and then the powders were ball milled for 30 h to refine the particle size. The surface area of those powders was 3.2 g m^{-2} measured by Brunauer-Emmett-Teller (BET) surface adsorption method.

4.3.2. Symmetric Cells and Single Cells Fabrication

The LSCO interlayers with different thicknesses were deposited on pressed sintered $Ce_{0.9}Gd_{0.1}O_{1.95}$ (CGO) disks in a PLD system with a KrF excimer laser (Lambda Physik Compex Pro 205, λ=248 nm). The laser beam with approximately 5 $J \cdot cm^{-2}$ in energy density was focused on the targets at a 45 ° incident angle. The thicknesses of the PLD interlayer were controlled from ~ 50 to ~ 500 nm by deposition time to optimize the microstructure of the PLD interlayer and the subsequent screen printed layer. In order to fabricate the symmetric cells for impedance measurement, the LSCO slurry was screen printed onto CGO substrates coated with PLD interlayer of different thicknesses. The cells were then annealed at 1150 ℃ for 2 h with a ramping rate of 2 ℃ min^{-1}. To prepare the single cells, commercial NiO-CGO cermet powder was compacted into anode disks under uniaxial pressure using an 1 inch (2.54 cm) diameter die set. The disks were then sintered at 1300 ℃ for 3 h. Subsequently, a bi-layer electrolyte (1.5 μm YSZ deposited prior to a 6 μm CGO layer), a PLD LSCO thin-film cathode layer, and a screen printed LSCO cathode layer were deposited onto a NiO-CGO anode disk substrate under the conditions described in our previous work.[51, 199]

4.3.3. Microstructure and Mechanical Characterizations of Symmetric Cells

The microstructure of these films was first characterized by a high resolution field emission scanning electron microscope (FE-SEM, JEM-7500F Cold Emission SEM). The hardness of the cathode films was measured by a commercial Fischerscope HM2000XYp micro-indentation with Vickers indenter. The film was indented down to 500 nm and a minimum of twenty indents were performed on each specimen to obtain the average hardness value.

4.3.4 ASR of Symmetric Cells and Power Density Measurements of Single Cells

Platinum grids were gently pressed onto porous electrodes and were used as current collectors. Using a potentiostat/impedance analyzer (Reference 600^{TM}, Potentionstat/ Galvanstat/ ZRA, GAMRY INSTRUMENTS), AC impedance spectroscopy measurements were conducted in the frequency range of 10^{-2}–3×10^{5} Hz in the temperature range from 400 to 700 ℃. The AC impedance data were measured after a waiting period of an hour for temperature stabilization. The anode-supported single cells prepared with and without interlayer were used to evaluate the interlayer effect on the cathode performance. Humidified H_2 with a constant flow rate of 80 mL·min^{-1} and air with at a constant flow rate of 120 mL·min^{-1} were supplied as the fuel and the oxidant, respectively, during the single-cell performance test. Measurement details can be found elsewhere.[51, 199]

4.4. Results and Discussion

The X-ray diffraction (XRD) patterns of the LSCO cathode film with and without the PLD interlayer on CGO pellet are shown in Fig. 4.1. The symbol * refers to LSCO peak and the symbol # refers to CGO peak. The diffraction peaks of LSCO match well with the standard PDF card (#048-0122), which indicates a pure polycrystalline LSCO phase with a pseudo-cubic structure.[191] There is no obvious variation in the crystal structure between the LSCO cathodes with and without the PLD LSCO interlayer.

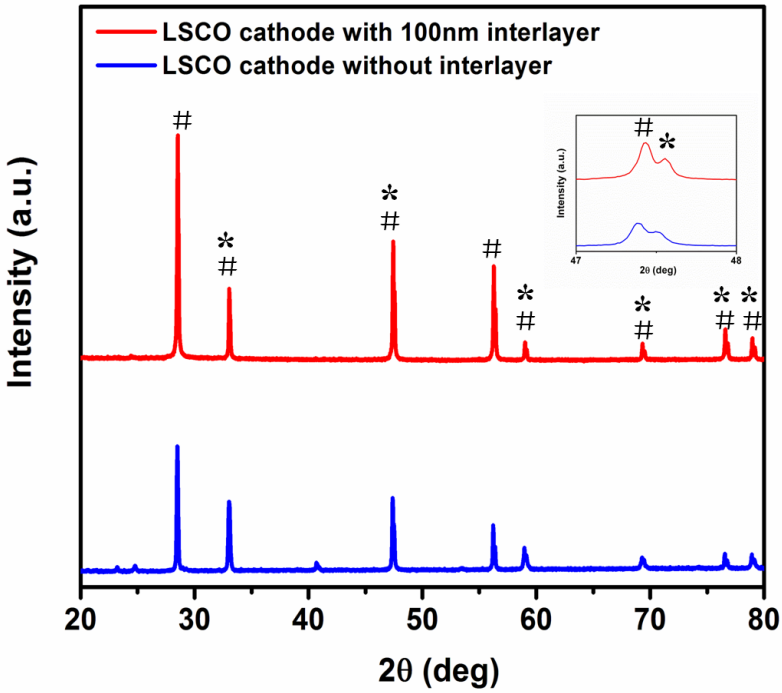

Fig. 4.1. The X-ray diffraction (XRD) patterns of the LSCO cathode film with and without the PLD interlayer. The inset shows a magnification of XRD peaks around 47.5 degree. The symbol * refers to LSCO peak and the symbol # refers to CGO peak.

To examine the interlayer effect on the microstructure of the LSCO cathode films, the cathode films with and without the PLD interlayer were characterized by cross-section SEM, as shown in Fig. 4.2a, b, c and d. Fig.4.2a and 2b show that LSCO particles agglomerated into big and dense grains when there is no PLD interlayer (Fig.4.2a) or when the PLD interlayer is very thin (< 50 nm, Fig 4.2b). Compared with the screen-printed only films and the bi-layer cathode films with a very thin PLD interlayer, the LSCO films prepared with thick PLD interlayer as seen in Fig. 4.2c (106 nm), and d (530 nm) show much smaller grains with uniform pores and good grain connectivity between the electrolyte and cathode films. The PLD interlayer thickness apparently plays an important role in the nucleation process of the screen printed layer.

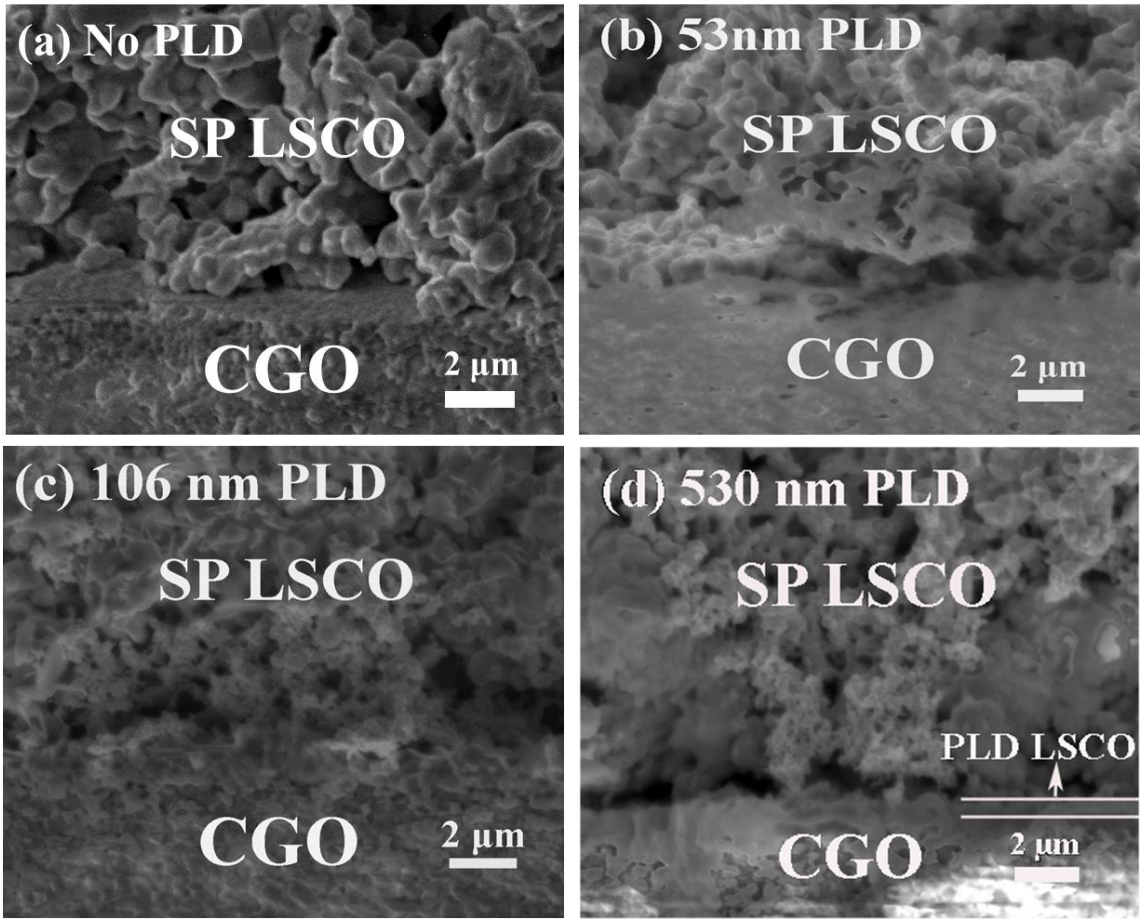

Fig. 4.2. Cross-section SEM images of screen printing LSCO layer (a) directly on CGO pellet, on PLD LSCO interlayer with different thickness (b) 53 nm, (c) 106 nm, (d) 530 nm. All samples were annealed at 1150 ℃ for 2 hours.

To further confirm the interlayer effect on the screen printed layer, the screen printed cathodes without and with a PLD interlayer were characterized by plan-view SEM and shown in Fig. 4.3a and b, respectively. It is clear that the sample with PLD interlayer shows the enhanced surface coverage and smaller grains indicating that the nano-porous PLD interlayer could greatly increase the nucleation sites for the following

screen-printed layer leading to uniform grain size and porous structure after sintering process. This is further supported by the cross-section TEM (XTEM) study in Fig. 4.3c, where a good grain connectivity between the PLD interlayer and the porous screen printed LSCO layer is clearly observed.

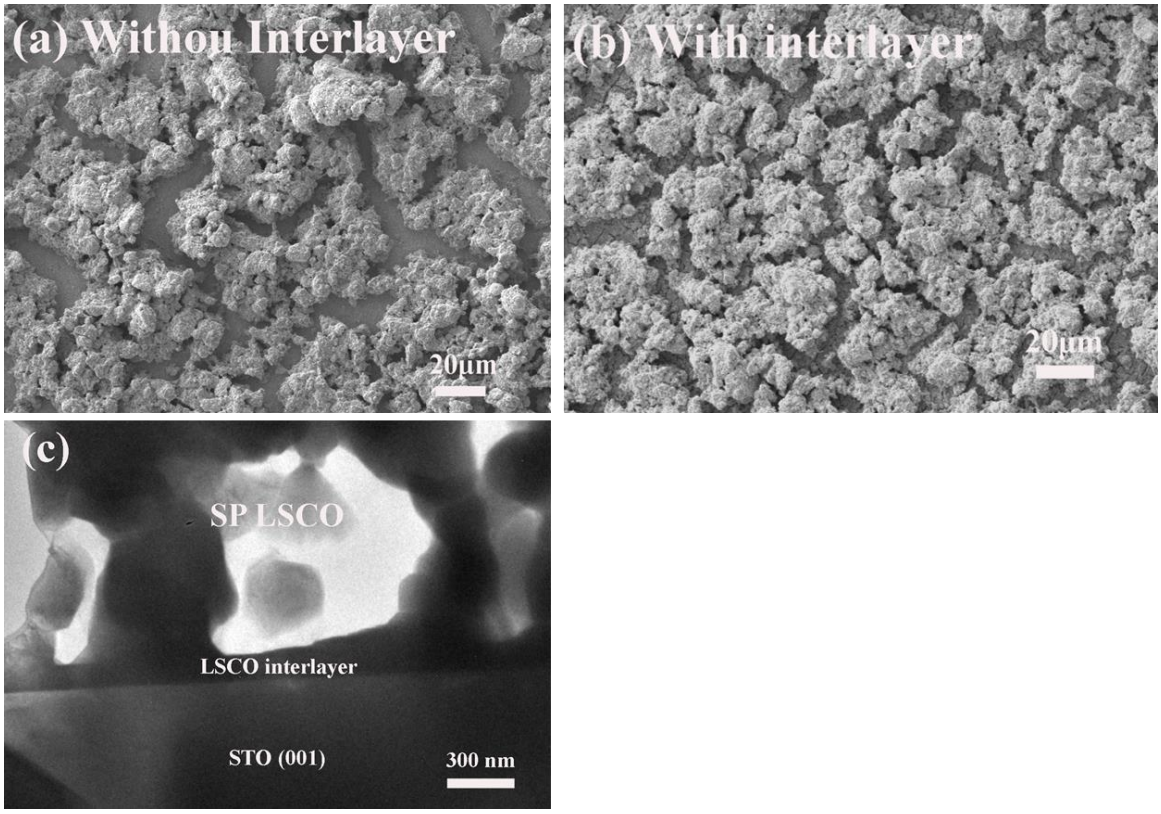

Fig. 4.3. The plan-view SEM images of screen printed cathode (a) without and (b) with PLD interlayer and (c) the cross-section TEM image of bi layer cathode.

To measure the electrochemical performance of the LSCO cathode with different PLD interlayer thicknesses and the samples without PLD interlayer, symmetric cells

with different PLD LSCO interlayer thicknesses were prepared. The PLD LSCO interlayer thickness was controlled through the deposition time. A relatively high temperature (1150 ℃) is used for all the samples because it is the optimized temperature for sintering the screen printed cathode film. To ensure a fair comparison between the single layer and bi-layer cathodes, the same sintering temperature for all samples was used. However it was found that the sintering temperature of the bi-layer cathode could be as low as 800 ℃ and there is still good grain connectivity between the screen-printed layer and the PLD interlayer and comparable electrochemical performance as those sintered at 1150 ℃. This is another advantage for incorporating a thin PLD interlayer. The specific impedance data of symmetric cells with cathode prepared by screen printing only method and hybrid method with ~500 nm PLD interlayer at 600 ℃ are plotted in Fig. 4.4a. The low frequency semicircle in Nyquist plot represents the polarization resistance.[189] There is a significant enhancement for the cathode prepared by the hybrid method compared to that prepared by the screen printing only method. The following equation was used to calculate the area specific resistance (ASR): ASR = R_p*A/2, where R_p is the electrode polarization resistance, which equals to the diameter of the low frequency semicircle and A is the geometric electrode area. An Arrhenius plot of ASR as a function of temperature for the cathode layers with different PLD interlayer thicknesses is plotted in Fig. 4.4b. The ASR of single layer LSCO cathode films prepared by conventional screen printing method and pulsed laser deposition are also plotted for comparison.[13, 50] Previously the ASR of screen printed LSCO cathode was reported to be 2 - 4 Ω cm^2 at 600 ℃, while the ASR of the PLD LSCO cathode was as

low as 0.09 Ω cm^2 at 600 ℃.[13] By comparison with ASR of the screen printed LSCO cathode, the ASR significantly decreases on inserting the PLD interlayer (Fig. 4.4b). The ASR of bi-layer cathode films decreases with increasing PLD interlayer thickness from ~ 50 to ~ 500 nm. A slight ASR decrease is observed with a PLD interlayer with the thickness of 53 nm. When the PLD interlayer thickness is ~ 100 nm, the ASR of bi-layer LSCO cathode drops to one fifth of those of the films prepared by the screen printing only method. The ASR seen as the inset in Fig. 4.4b, however, decreases only slightly for thicker PLD interlayers up to 530 nm. Since LSCO is a mixed electric-ionic conducting cathode material and the PLD interlayer plays the role of a catalytic layer, the decrease of ASR can be explained by the expanded oxygen reduction reaction zone. It is expected that the interlayer thickness effect could be more significant for the cathode materials with higher ionic conductivity such as $Ba_{0.5}Sr_{0.5}Co_{0.8}Fe_{0.2}O_{3-\delta}$ (BSCF), $PrBaCo_2O_{5+\delta}$, $La_2NiO_{4+\delta}$, etc.[22, 101, 105]

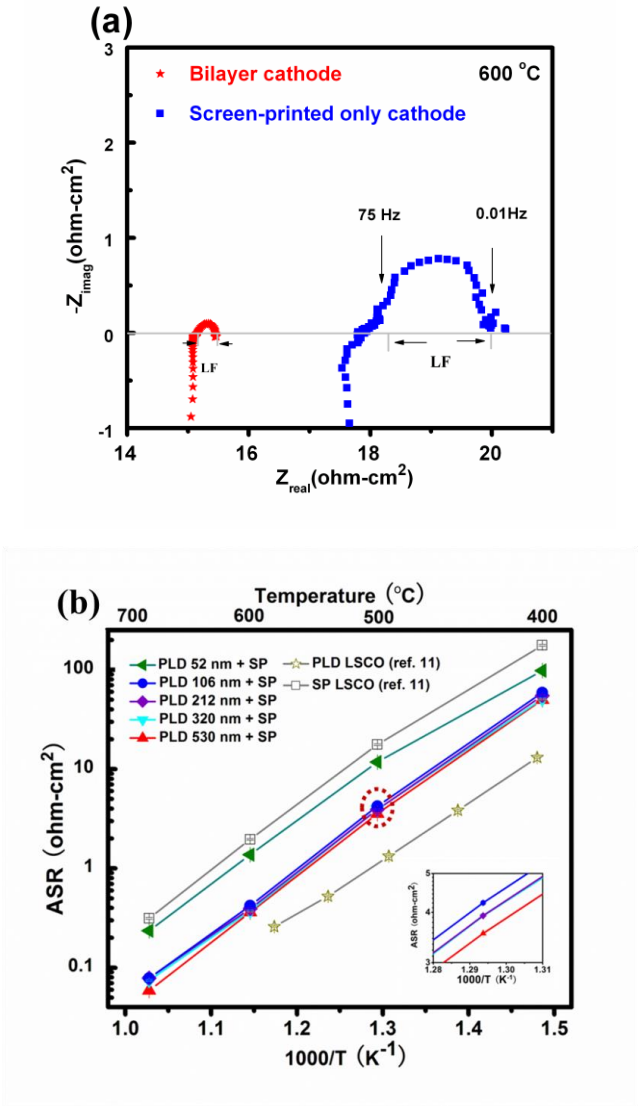

Fig. 4.4. (a) The specific impedance data of symmetric cells with cathode prepared by the screen printing only method and the hybrid method with 500 nm PLD interlayer at 600 ℃ and (b) the ASR of the symmetric cells with different PLD LSCO interlayer thickness and without PLD LSCO layer as a function of measurement temperature in air. The inset in (b) shows a magnified ASR plot of the symmetric cells with PLD LSCO interlayer thickness range from 106 nm to 530 nm at 600 ℃.

To further confirm the microstructure variation of those bi-layer cathode films with different PLD interlayer thicknesses, micro-indentation was conducted to test the hardness of those films. Because material hardness is inversely proportional to film porosity, hardness could be an indirect indicator of film porosity.[200] The error bar was estimated by taking into account both error from the hardness measurement and the data fitting. From Fig. 4.5, it is evident that the hardness has a sharp decrease as the PLD interlayer increases from 0 to 100 nm, which suggests the cathode films have a significant change in microstructure in this range. The sample without the PLD interlayer has mostly large grains (Fig. 4.2a) and shows a high hardness of ~ 2 GPa and high ASR of 2 Ω cm^2 at 600 ℃. However the sample with the 100 nm PLD interlayer has much finer grains (Fig. 4.2c) and high porosity in the sample and, therefore, has a lower hardness of 0.5 GPa and lower ASR value. This again demonstrates that the PLD interlayer with a nanoporous microstructure provides more nucleation sites for the screen printed cathode layer. The hardness remains relatively constant when the PLD interlayer thickness is increased to ~ 500 nm, which suggests that the screen printed layers have similar porosity when the PLD layer is $\geq$ 100 nm thick. Considering that the electrolyte surface is not perfectly flat, the microstructure of the thin films in the first tens of nanometer thickness range could still be isolated islands, which do not cover the entire surface of the electrolyte substrate based on the thin film growth model.[201, 202] Although it indeed provides more nucleation sites, the uncovered areas still have the screen printing particles agglomerated into large grains similar to the case of the screen printed only film. When the PLD interlayer thickness reaches 100 nm, it is expected that

most of the electrolyte surface is covered by the PLD interlayer and, therefore, the microstructure of the screen printed layer shows much smaller grains with pores. The microstructure and hardness of the cathode layers remains the same for the samples with thicker PLD layers.

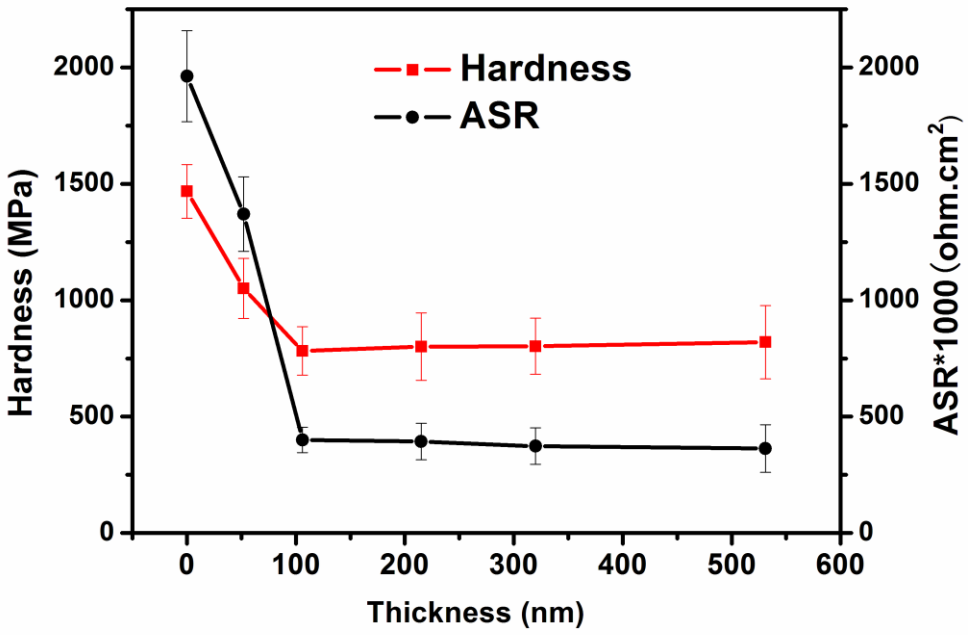

Fig. 4.5. The hardness and ASR at 600 ℃ of the symmetric cells as the function of PLD LSCO interlayer thickness

Based on the above results, schematics of the microstructures for LSCO cathode films with and without PLD LSCO interlayer are presented in Fig. 4.6a. The cathode film without PLD interlayer is consisted of scattered large grains on the uneven electrolyte surface and thus is low in film porosity. After inserting nanoporous PLD interlayers, the films show significantly enhanced surface coverage with uniform pores after high temperature sintering.

To demonstrate the PLD interlayer effect on the overall cell performance, the anode-supported single cells with and without PLD interlayers were prepared. The single cell with interlayer thickness of 100 nm was selected to ensure the enhancement with the minimal interlayer thickness. As seen from the cross-section SEM images of single cells with and without PLD interlayer, a dense and crack-free bi-layer electrolyte of YSZ (~ 1.5 μm) and CGO (~ 6.0 μm) was successfully prepared on the porous NiO-YSZ anode (Fig. 4.6b). A YSZ thin layer is applied to prevent the reduction of Ce^{4+} into Ce^{3+}, which occurs in hydrogen atmosphere and leads to a decrease in open circuit voltage (OCV).[203] Compared with the dense and large grains shown in Fig. 6b, the cathode with much higher porosity, smaller grains, and better adhesion with the electrolyte was observed (Fig. 4.6c) for the cell with the 100 nm PLD interlayer.

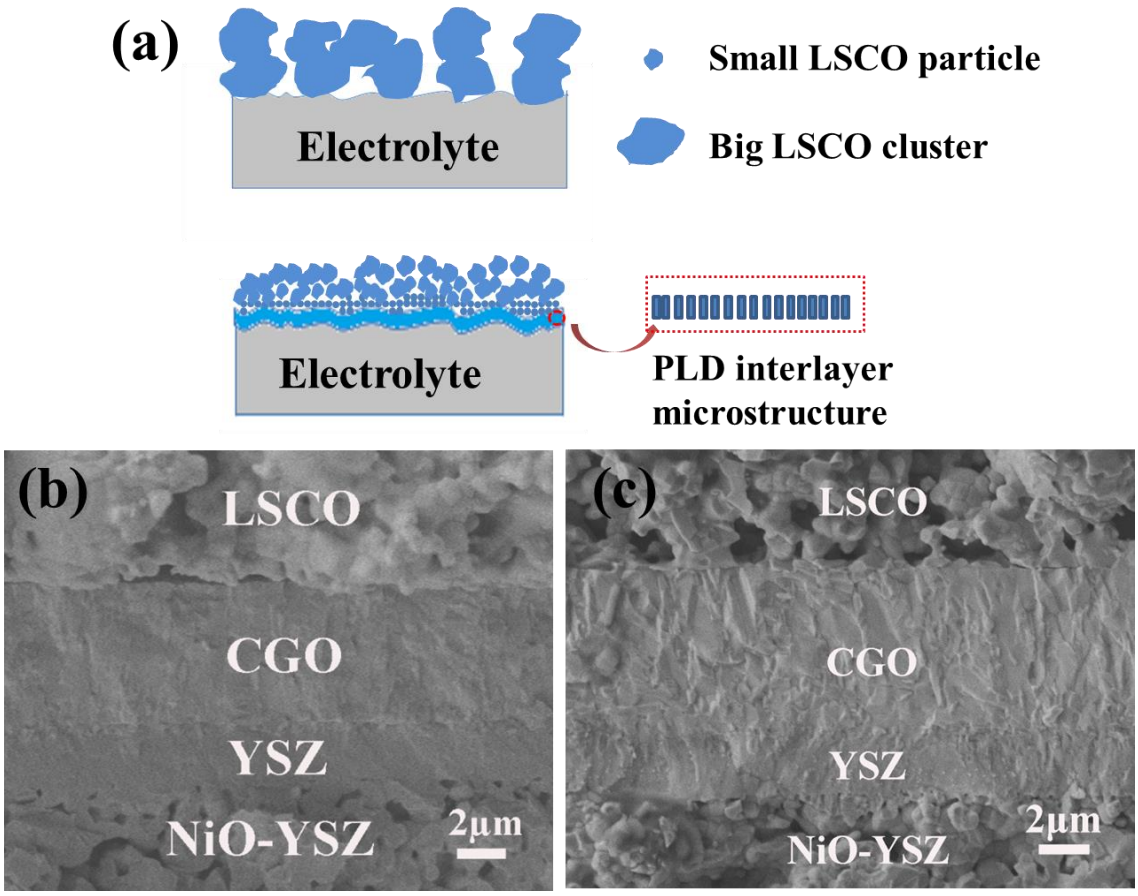

Fig. 4.6. The proposed scheme of different microstructure (a) and the different microstructure of single cells: (b) without PLD LSCO interlayer, (c) with ~100 nm PLD LSCO interlayer.

The current–voltage (I–V) characteristics of the anode-supported single cells were measured by a two-electrode set-up. Pt wires were used as electrical contacts held by Pt paste. The performance was measured at the temperatures ranging from 650 to 800

^{o}C. The cell voltage and power density as a function of current density for the sample without the PLD interlayer is shown in Fig. 4.7. The open circuit voltage (OCV) is 1.04 V at 650 ^{o}C, and the maximum power densities of the cell are 0.164 (highlighted with a red arrow), 0.264, 0.394, and 0.488 $W \cdot cm^{-2}$ at 650, 700, 750, and 800 ℃, respectively. The overall trend is that the power density decreases as the measurement temperature decreases, and the cell potential also decreases as a result of the increasing polarization losses across the cell with increasing current density. The cell with the PLD interlayer (Fig. 4.7) provides an OCV of 1.05 V at 650 ℃ and the maximum power densities of 0.276 (highlighted with red arrow), 0.412, 0.466, and 0.626 $W \cdot cm^{-2}$at 650, 700, 750, and 800 ℃, respectively. Compared with the cell without an interlayer, the cells with the interlayer have more than 50 % increase in the overall maximum power density at both 650 and 700 ℃ and ~ 30 % increase in the power density at 800 ℃.

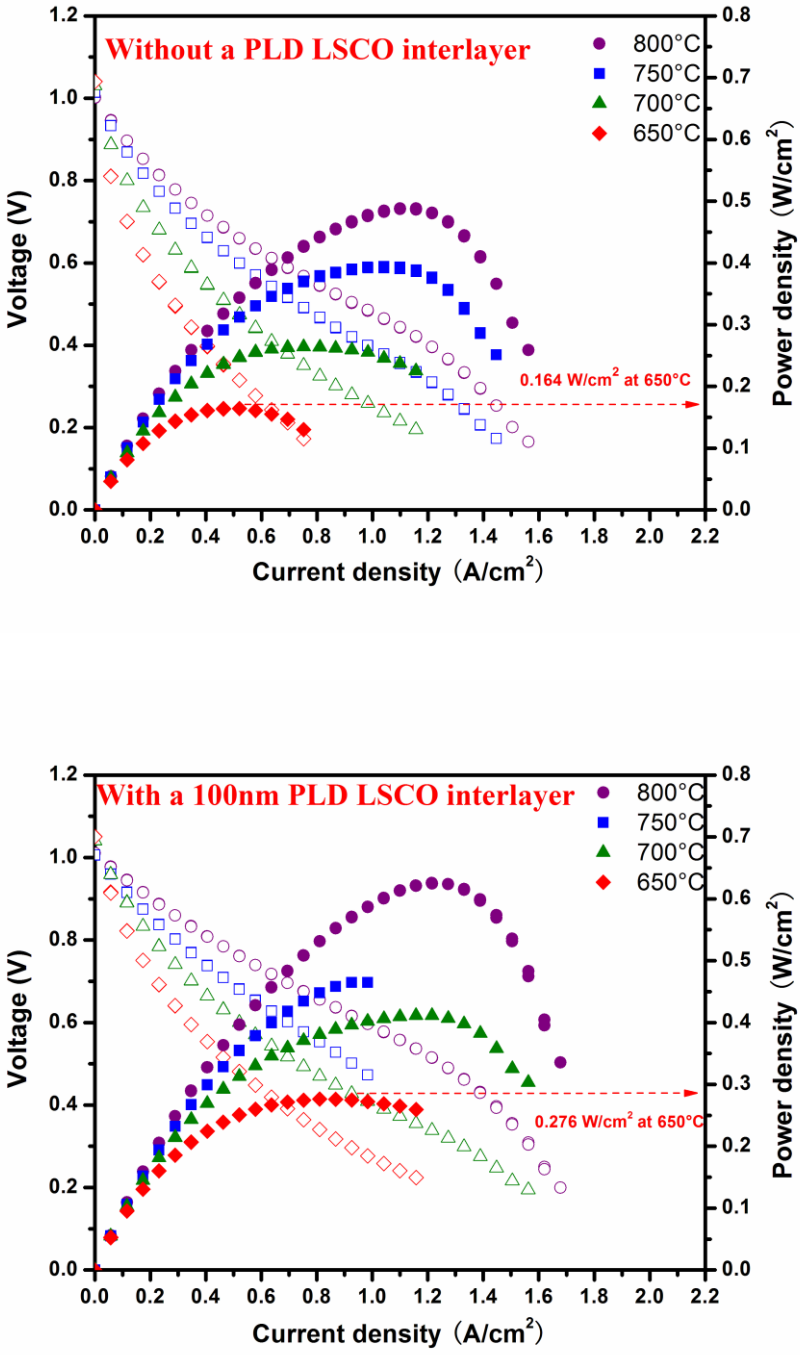

Fig. 4.7. The power density of single cells with and without PLD LSCO interlayer from 650 ℃ to 800 ℃.

The cross-section SEM images of the single cells with and without PLD interlayer are shown in Fig. 4.8a and b. It is clear that, after ~2-3 day power measurements, the single cells with PLD interlayer remains a sharp interface between the electrolyte and the cathode. However, for the sample without PLD interlayer, there is a small gap in several regions along the electrolyte/ cathode interface. In addition, it has been previously reported that nanoporous interlayer could present much larger thermodynamic factor than some of the powder samples.[189] The larger thermodynamic factor will result in a smaller change in the composition at different temperatures for cathode films[189], i.e., a longer lifetime and better cyclability for the cells with bi-layer cathode. The study suggests that the interlayer approach could improve the surface adhesion between the electrolyte and the cathode layer, and thus lead to the long term durability of the cells.

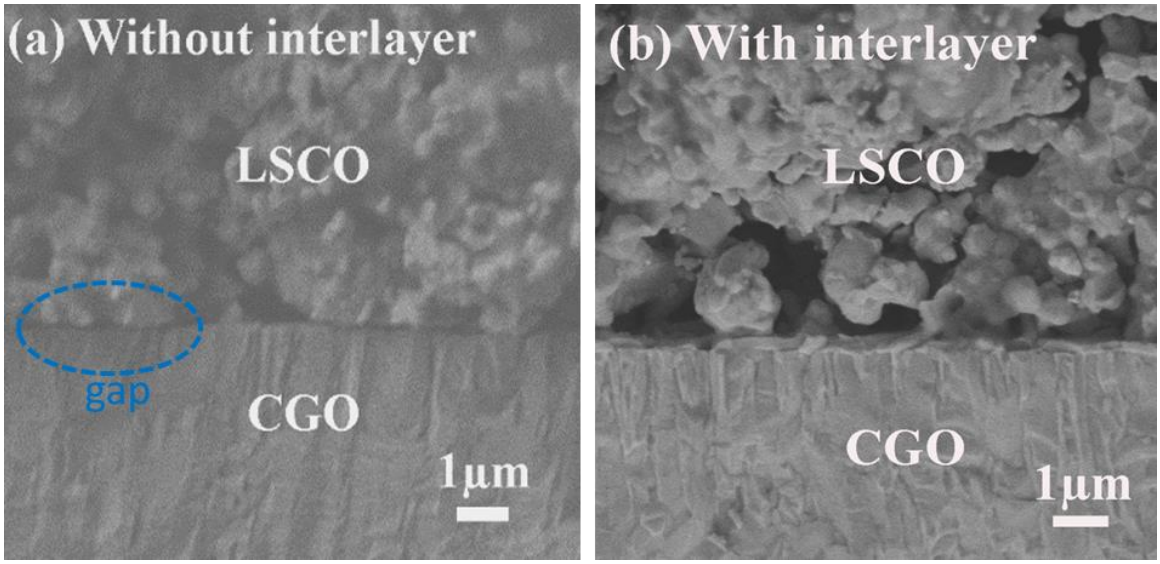

Fig. 4.8. The cross-section SEM images of single cells (a) without and (b) with the PLD interlayer after power density measurement.

4.5 Conclusions

Bi-layer cathodes with different PLD interlayer thicknesses have been successfully fabricated by combining PLD with the screen printing method. Compared with layers of screen printed LSCO directly onto a CGO electrolyte, the LSCO layers with a thin PLD interlayer (< 50 nm) shows moderate grain size and enhanced film porosity, while the LSCO layers with a thick PLD interlayer (thickness ≥1 00 nm) have much higher film porosity with small grains and uniform pore structures. The mechanical and electrochemical measurement results of those cathodes agree well with the microstructure analysis. There is a slight decrease in ASR and hardness if the applied interlayer thickness is thin (50 nm); while the ASR is about 5 times lower than that of the single layer cathode when the thickness is ≥ 100 nm and the film porosity and grain size reach their optimum level based on the hardness measurement. The anode-supported single cells with PLD interlayers demonstrated enhanced power performance at all temperatures compared with the cells without the interlayer. The maximum power densities of the single cells are 0.276, 0.412, 0.466, and 0.626 $W \cdot cm^{-2}$ at 650, 700, 750, and 800 ℃, respectively, with an OCV of 1.05 V at 650 ℃. There is a 50 % enhancement in power density in the temperature range from 650 to 700 ℃ and ~ 30% increase at 800 ℃. Overall, the results strongly support that the thin PLD interlayer improves the electrochemical performance of the cathode layer as well as the overall cell performance and cell integrity.

5. OXYGEN PARTIAL PRESSURE IMPEDANE STUDIES OF INTERLAYER EFFECT ON POROUS ELECTRODES OF $La_{0.5}Sr_{0.5}CoO_{3-\delta}$

5.1 Overview

Thick $La_{0.5}Sr_{0.5}CoO_{3-\delta}$ (LSCO) cathodes (~30 μm) have been successfully fabricated with and without nanoporous LSCO interlayer on both sides of a dense polycrystalline gadolinia doped ceria substrate by combining screen printing and pulsed laser deposition (PLD) methods. The electrochemical properties of these LSCO cathodes for oxygen reduction reaction have been determined by electrochemical impedance spectroscopy (EIS) at different interlayer thickness, temperature and oxygen partial pressure. The oxygen reduction of the LSCO electrode with and without interlayer is found to be co-limited by the oxygen mass transfer and surface exchange process. As the thickness of PLD interlayer increases, the surface exchange resistance of the cathode decreases which benefits from significantly enhanced reaction sites by inserting nanoporous LSCO interlayer. In addition, this nanoporous LSCO interlayer populates the nucleation sites for screen printing cathode resulting in reduced grain size and thus more uniform microstructure, which all contribute to the decreased mass transportation resistance for the LSCO cathode with nanoporous LSCO interlayer.

5.2. Introduction

Thin film solid oxide fuel cells (THSOFCs), as a clean energy-producing technology, have attracted extensive research interest with high efficiency (>60%) [1, 4, 9, 204, 205]. To lower cost and enhance stability, recent research efforts mainly focus on lowering the TFSOFCs operation temperature (500-700 ℃ or lower) by exploring new materials and engineering microstructure. [126, 206, 207] Considering the primary factor limiting power output is the slow rate of oxygen reduction at the cathode and cathode/electrolyte interface leading to significant cathodic polarization, the cathode and the cathode/electrolyte interface have attracted ongoing research efforts [105, 133]

Because of low cost and simple process, screen printing is one of the most widely used fabrication techniques to prepare thick cathode films with thickness ≥10 μm.[198] . However, a high temperature thermal treatment (usually over 1100 ℃) after the screen printing process can cause serious shrinkage in the film thickness, leading to cracks and possible delamination [48, 108]. Compared with screen printing method, pulsed laser deposition (PLD) is used to prepare much thinner films with the thickness from tens to hundreds of nanometers. The film microstructure could be tuned by adjusting the deposition parameters but the cost is higher due to the low growth rate. [208] In our previous work, thick and porous bi-layer cathodes have been achieved by combining PLD and screen printing methods, i.e., PLD was used to grow the nanopororous interlayer followed by a thick cathode layer (~30 μm) prepared by the screen printing method[41, 209]. This hybrid method was demonstrated to combine the advantages of both techniques, namely the cost effectiveness from screen printing and the well-

controlled microstructure achieved by PLD. Considering the cathode is made of LSCO, a mixed ionic and electronic conducting cathode material[210], it is expected that the interlayer thickness is closely related to the number of reaction sites, the reaction and diffusion rate of oxygen, and the microstructure of the electrodes. However, up-to-date, no detailed study of the effect of thickness variation of the interlayer on the bilayer cathode performance and reaction mechanism has been made.

AC impedance with various oxygen partial pressures, as a widely-used method to evaluate the cathode performance, has been used in previous studies of dense films or porous cathode films, [211-214] including LSCO cathode films.[189, 210, 211, 215] The $La_{0.5}Sr_{0.5}CoO_{3-x}$ dense films with thickness of 0.25 and 0.5 μm on YSZ single crystal substrates was investigated by Yang *et al.* in various oxygen pressures from 0.05 atm to 1 atm with temperatures between 500 and 750 ℃. It reported that the electrode reaction was limited by the surface exchange reaction.[211] Using a similar method, Kawada studied a 1.5 μm dense and thick $La_{0.6}Sr_{0.4}CoO_{3-x}$ polycrystalline film on a CGO substrate where the surface exchange process was concluded to be the rate-determining step.[215] The porous electrodes of $La_{1-x}Sr_xCoO_3$ (x=0.2, 0.3, and 0.4) with surface areas ~2 μm^{-1} was studied by Adler between 550 and 800 ℃ under different oxygen pressures. [210] The surface exchange coefficient and the oxygen vacancy diffusion coefficient were derived by using the Adler-Lane-Steele (ALS) model. Wang *et al.* used ALS model to analyze the ~0.5 μm nanocrystalline LSCO films prepared by pulsed laser deposition.[216] It was concluded that the fundamental material parameters (surface exchange and diffusion coefficients) did not significantly change for nanocrystalline

cathode and the very low area specific resistance (0.09 ohm cm^2 at 600 ℃) was due to the high surface area (80 μm^{-1}). In short, oxygen partial pressure impedance study is a powerful tool in probing the electrode electrochemical reaction process under different temperatures. Such tool could be very helpful in exploring the fundamental mechanisms on the interlayer enhanced electrode performance.

In this work, we have conducted a thorough AC impedance study under various oxygen partial pressures for the bi-layer cathode films with different nanoporous LSCO interlayer thicknesses. These cathodes were prepared on a dense polycrystalline CGO substrate by combining pulsed laser deposition and screen printing methods. The goal of this work is to examine the bilayer LSCO cathode performance under different temperatures, oxygen partial pressures and different interlayer thicknesses so as to provide some insights to design the optimum microstructure of mixed ionic-electronic conducting cathodes.

5.3. Experimental

5.3.1. LSCO Powder and PLD Target Processing

Both the hot-pressed LSCO target and $Ce_{0.9}Gd_{0.1}O_{1.95}$ (CGO) electrolyte disks were fabricated by solid state reaction through mixing stoichiometric amounts of the raw powders: La_2O_3 (99.99%), $SrCO_3$, Co_3O_4 (99.9%), CeO_2 (99.9%), and Gd_2O_3 (99.9%) followed by high temperature sintering. The LSCO with pseudo-cubic structure and CGO with fluorite structure were confirmed by X-ray diffraction (XRD). The LSCO powders for the preparation of screen printing slurry were obtained by crushing the

LSCO target. Then the powders were ball milled for 40 hours to refine the powder size. The measured surface area of those powders was 3.2 g/m^2 by Brunauer-Emmett-Teller (BET) surface adsorption method.

5.3.2. Symmetric Cell Fabrication

Deposition of the LSCO cathode layers was performed on pressed sintered $Ce_{0.9}Gd_{0.1}O_{1.95}$(CGO) disks in a PLD system with a KrF excimer laser (Lambda Physik Compex Pro 205, λ=248 nm). The laser beam was focused on the targets at a 45° incidence angle to obtain an energy density of approximately 5 $J \cdot cm^{-2}$. The thickness of the PLD interlayer (~100 nm and ~500 nm) was controlled by deposition time to optimize the microstructure of the PLD interlayer and the subsequent screen printed layer. In order to fabricate the symmetric cells for impedance measurement, the LSCO slurry was screen printed on CGO substrates with and without PLD interlayer followed by a high temperature annealing at 1150 ℃ for 2 h with a ramping rate of 2 ℃/min.

5.3.3. Microstructure Characterizations and Alternating Current (AC) Impedance Measurements of Symmetric Cells

The surface morphology of the symmetric cells was characterized by a high resolution field emission scanning electron microscope (FE-SEM, JEM-7500F Cold Emission SEM) and a transmission electron microscope (TEM, JEOL 2010 analytical microscope). Gold mesh current collectors were attached to the symmetrical cells prepared as described above. Gold mesh current collectors were attached to the

symmetrical cells prepared as described above. The cells were mounted in a furnace and their impedance spectra measured in a two probe configuration. The measurements were made by applying a small-amplitude AC voltage (10 mV) to the cell and monitoring the response current as a function of the AC frequency (from 1 mHz to 100 KHz). Impedance measurements were made in the temperature range of 500-750 ℃ in 50 ℃ increments and at pO_2 = 0.01, 0.1 and 1 atm for all the samples using a Solatron Electrochemical Interface (model 1287) and Solartron Impedance analyzer (model 1260).

5.4. Results and Discussion

To examine the interlayer effect on the microstructure of the LSCO cathode films, the cathode films with and without the PLD interlayer were characterized by cross-sectional SEM, as shown in Fig. 5.1a and b. Fig.1a shows that LSCO particles agglomerated into big and dense grains when there is no PLD interlayer. Compared with the screen-printed only films and the bi-layer cathode films with a very thin PLD interlayer, the LSCO films prepared with thick PLD interlayer as seen in Fig. 5.1b (530 nm) show much smaller grains with uniform pores and good grain connectivity between the electrolyte and cathode films. The magnified image is the low cross-sectional TEM image covering both the LSCO film and the CGO substrate. The interface between the film and the substrate is very clean with no indication of interface reaction or intermixing. It shows the film with a vertically aligned column-like microstructure with nanopores. The light contrast areas between the dark columns indicate porosity though some small-size nanoparticles of ~50 nm.

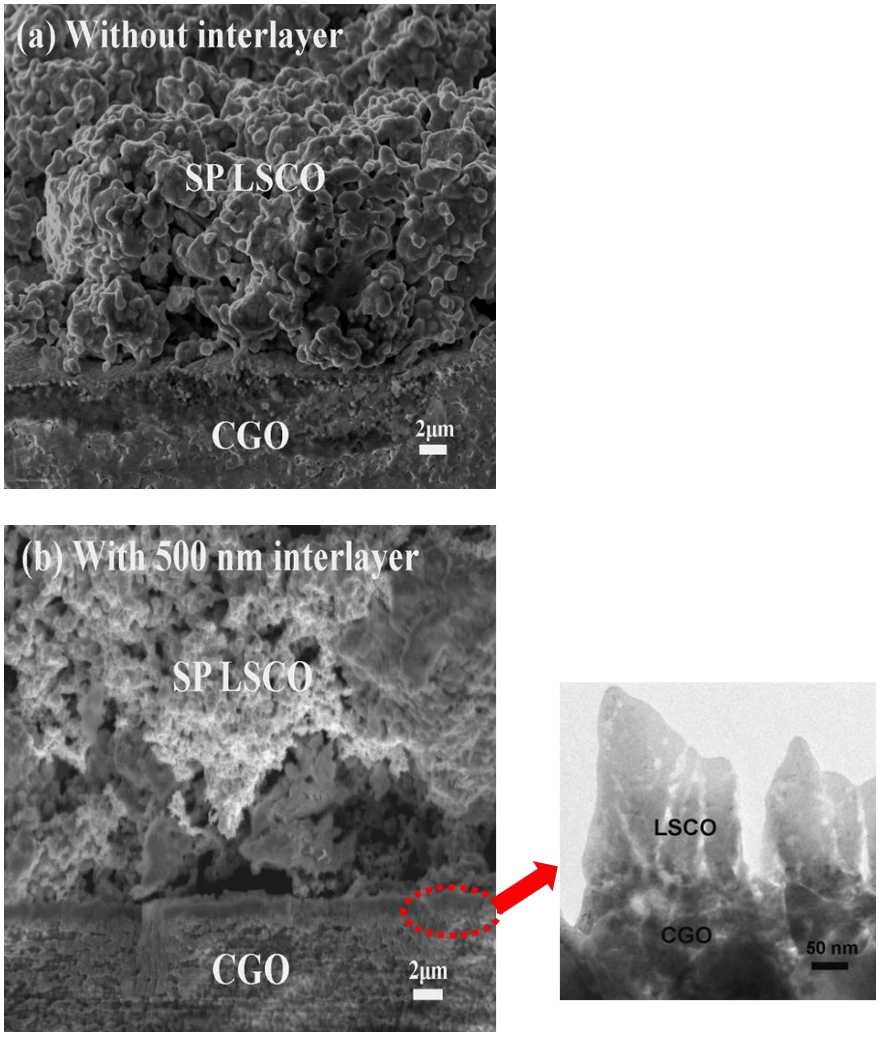

Fig. 5.1. The cross-sectional SEM images the cathode films (a) without and (b) with the LSCO PLD interlayer. The magnified image exhibits the vertical LSCO nanocolumns with nanopores in between.

Fig. 5.2 shows a typical AC impedance spectrum of the LSCO/CGO/LSCO symmetrical cell. It has two distinct regimes: high frequency (HF) and low frequency (LF) regimes. In all the spectra collected, oxygen partial pressures have little effect on the magnitude in HF regions. The resistance of the LF regime decreases rapidly with increase of the oxygen partial pressure. Wang *et al.* have determined that the critical length $L_d = D_{chem}/k_{chem} \geq 40$ μm at 619 ℃ for LSCO.[178] When the thickness of the mixed conducting oxide electrode is close to or lower than L_d, oxygen mass diffusion becomes one of the rate-limiting steps. In this study, the maximum film thickness used in the present experiments was ~ 30 μm, close to the critical length; therefore, the oxygen diffusion in the film is also expected to play a significant role for oxygen reduction reaction. For the LF regime, it is observed a ~45 ° line on Nyquist plot with a depressed semicircle. The depressed semicircle corresponds to the surface exchange process. [9] Considering the electrode thickness is close to L_d together with the observed ~45 ° line, the electrode reaction is expected to be co-limited by oxygen mass transfer and surface exchange process.

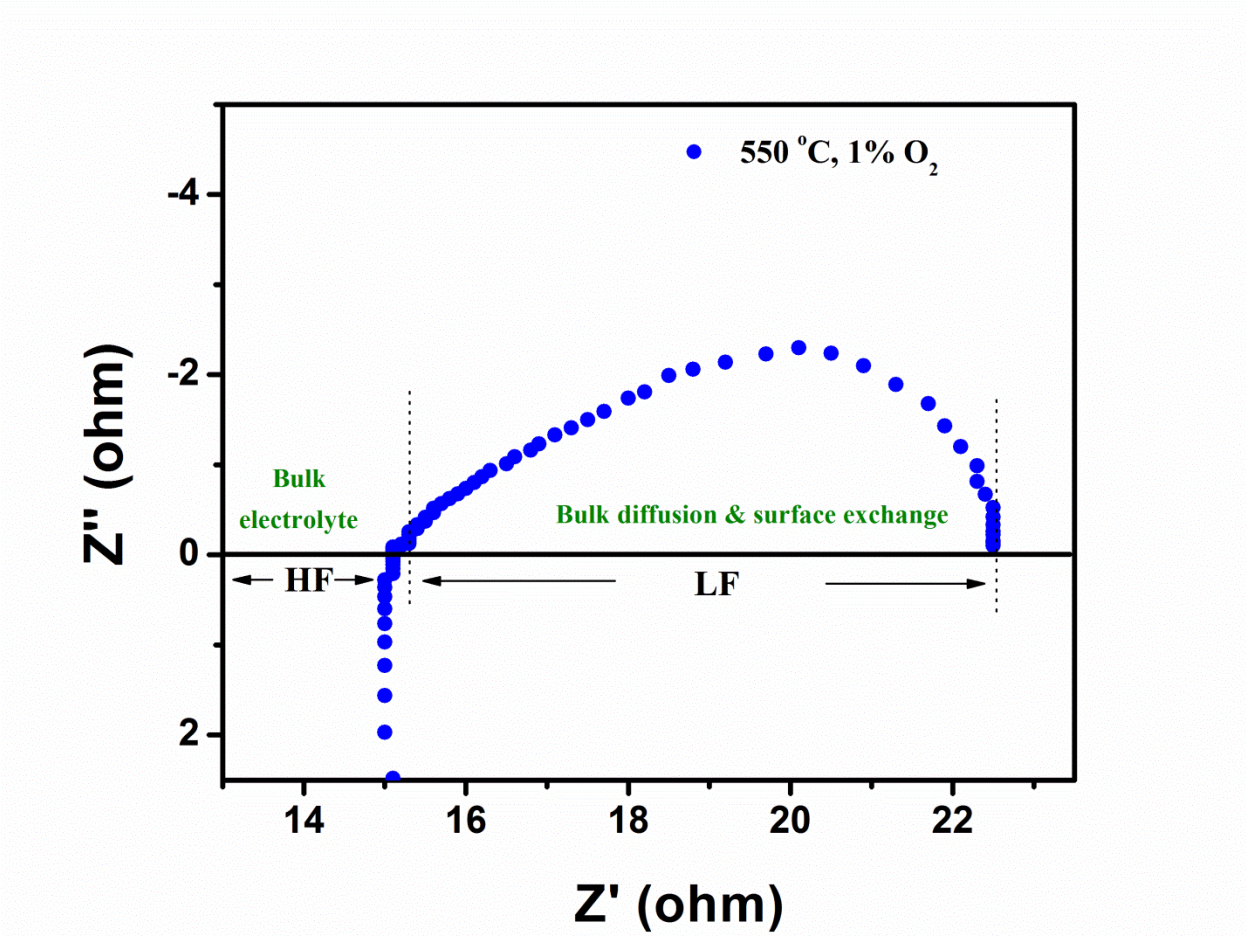

Fig. 5.2. A typical AC impedance spectrum of the LSCO/CGO/LSCO symmetrical cell.

The area specific resistance (ASR) of the cells with and without interlayer is calculated from R(LF) * electrode area/2 and is plotted in Fig. 5.3. R(LF) is extracted by subtracting the high-frequency intercept from the low-frequency intercept on the impedance plot. The area specific resistance of the cells decreases as the temperature increases due to the faster oxygen reduction kinetics, and also decreases with increasing oxygen partial pressure, i.e.,a higher pO_2 in the atmosphere facilitates oxygen reduction

in the electrode. The PLD interlayer in the electrodes clearly boosts the electrode performance and the area specific resistance of bi-layer cathodes decreases with increasing the PLD interlayer thickness. The 100 nm PLD interlayer at 750 ℃ and pO_2 = 1.0 atm decreases the ASR by 50% compared to the reference sample without any interlayer. Increasing the PLD interlayer thickness to 500 nm further improves the performance by an additional 40% under the same conditions. At pO_2 = 1.0 and 0.1 atm. the ASR depends linearly on the reciprocal temperature as expected for an activated process. At pO_2 = 0.01 atm a significant departure from linearity is observed suggesting that two processes are involved, one of which has a strong dependence on pO_2.

In order to interpret the impedance spectroscopy results, the impedance response of the cells is fitted by an equivalent circuit. The components of the equivalent circuit represent the physical processes involved in the oxygen reduction reaction at the electrode. The experimental data can be successfully modeled by the equivalent electrical circuit shown in Fig. 5.4.

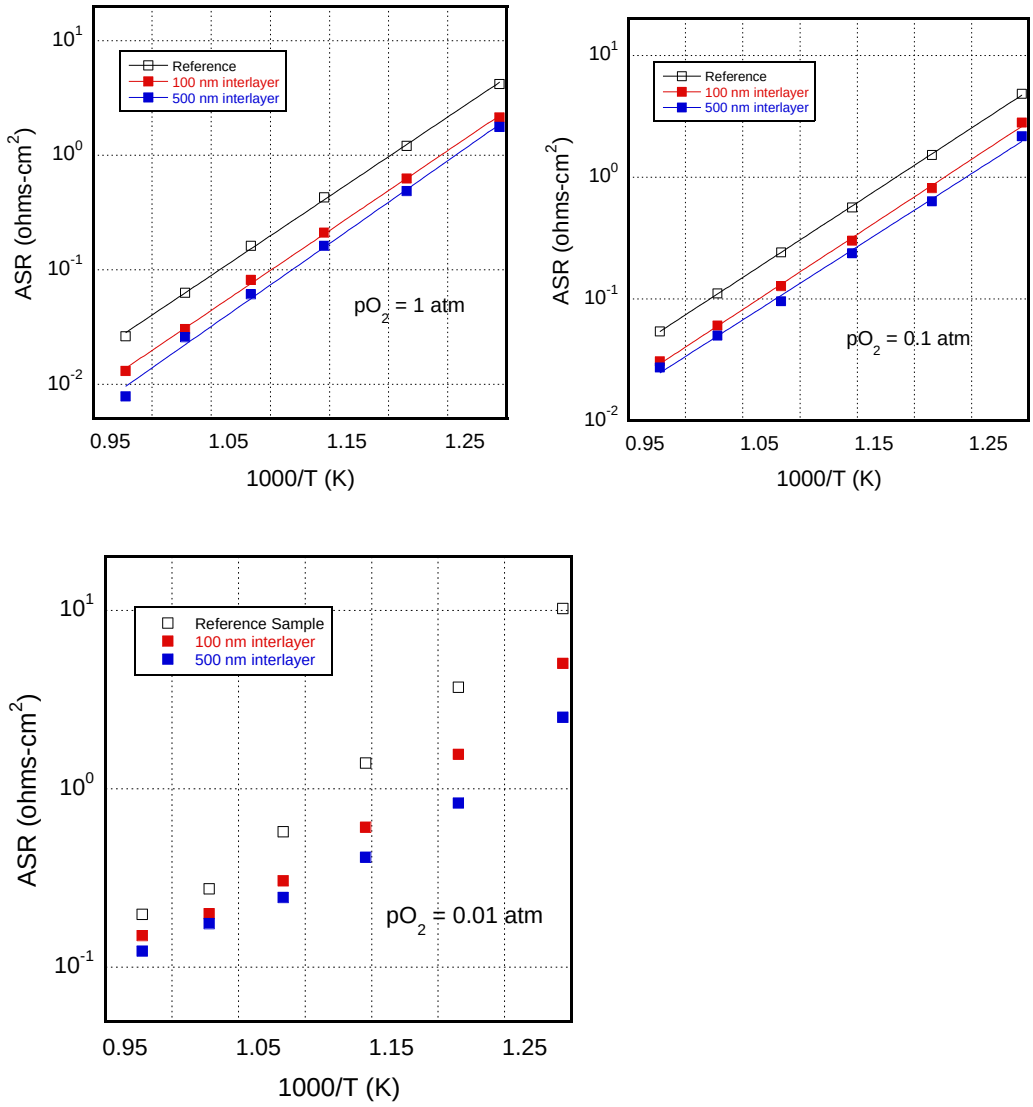

Fig. 5.3. The temperature dependence of the area specific resistances for the symmetrical cells at different oxygen partial pressures.

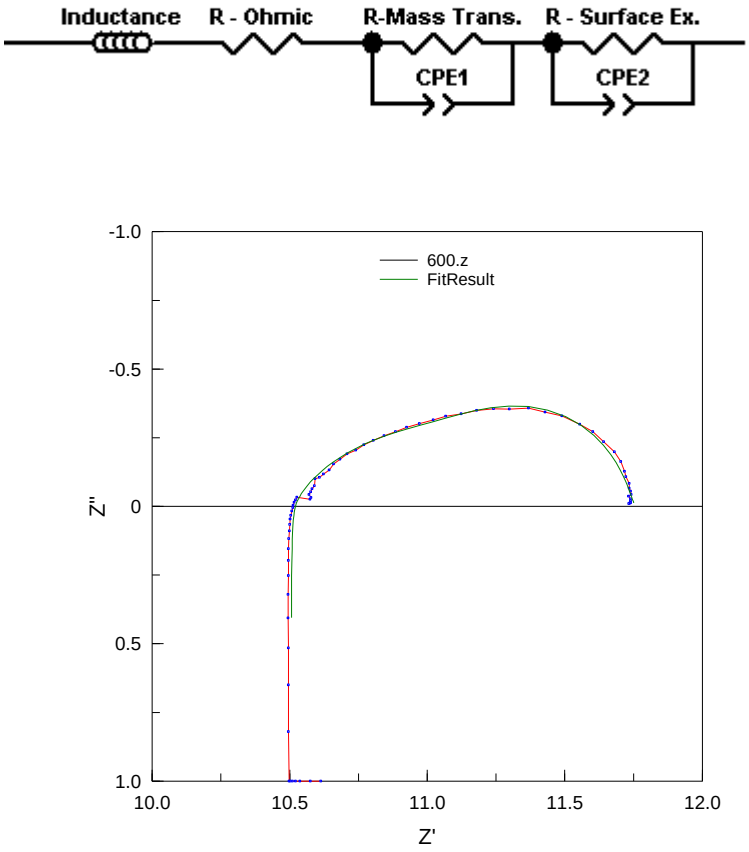

Fig. 5.4. Impedance curves by the curve fitting using the equivalent circuit model.

The inductance is due to the electrical connections between the cell and the instruments. The effects of inductances were often observed at higher frequencies. The overall ohmic resistance includes the ohmic resistance of the electrolyte, electrode, and current collectors, as well as the lead wire resistances. Two steps, mass transfer of oxygen and surface exchange at the active sites are, assumed at both electrodes. By fitting the impedance data of the cathode with and without interlayer, it is observed that

there is no significant difference in the interfacial resistance indicating the grain size does not play any important role for the interfacial properties. Constant phase elements are used to represent the depressed arcs in the impedance spectra. In general, for the reference sample the two processes are partially resolved in the impedance spectra. For the samples with interlayers the spectra are not well resolved except at the lowest pO_2 (0.01 atm) and the highest temperatures (650 and 700 ℃).

The impedance of each component of the symmetrical cells was determined by curve fitting using the above equivalent circuit model. As shown in Fig. 5.4, the obtained fitting curve agrees very well with the measured impedance at all frequencies. The lower frequency arcs in the impedance spectra are assumed to correspond to the surface exchange process, while the higher frequency arcs in the impedance spectra correspond to the diffusion through the electrode. The surface exchange process depends on pO_2 while the transfer reaction does not.

The temperature dependence of the surface exchange resistances for the symmetrical cells at different oxygen partial pressures is shown in Fig. 5.5. The surface exchange resistance decreases with the increase in temperature, oxygen partial pressure and the PLD layer thickness. Inserting the 100 nm PLD interlayer at 750 ℃ and pO_2 = 0.01 atm, the surface exchange resistance decreases by ~ 50% compared to that of the reference sample without any interlayer. Further increasing the PLD interlayer thickness to 500 nm improves the performance by an additional ~20% under the same conditions. Due to the high surface area provided by PLD nanoporous interlayer, increasing the PLD layer

thickness could increase the reaction sites of the cathode so as to decrease the surface exchange resistance.

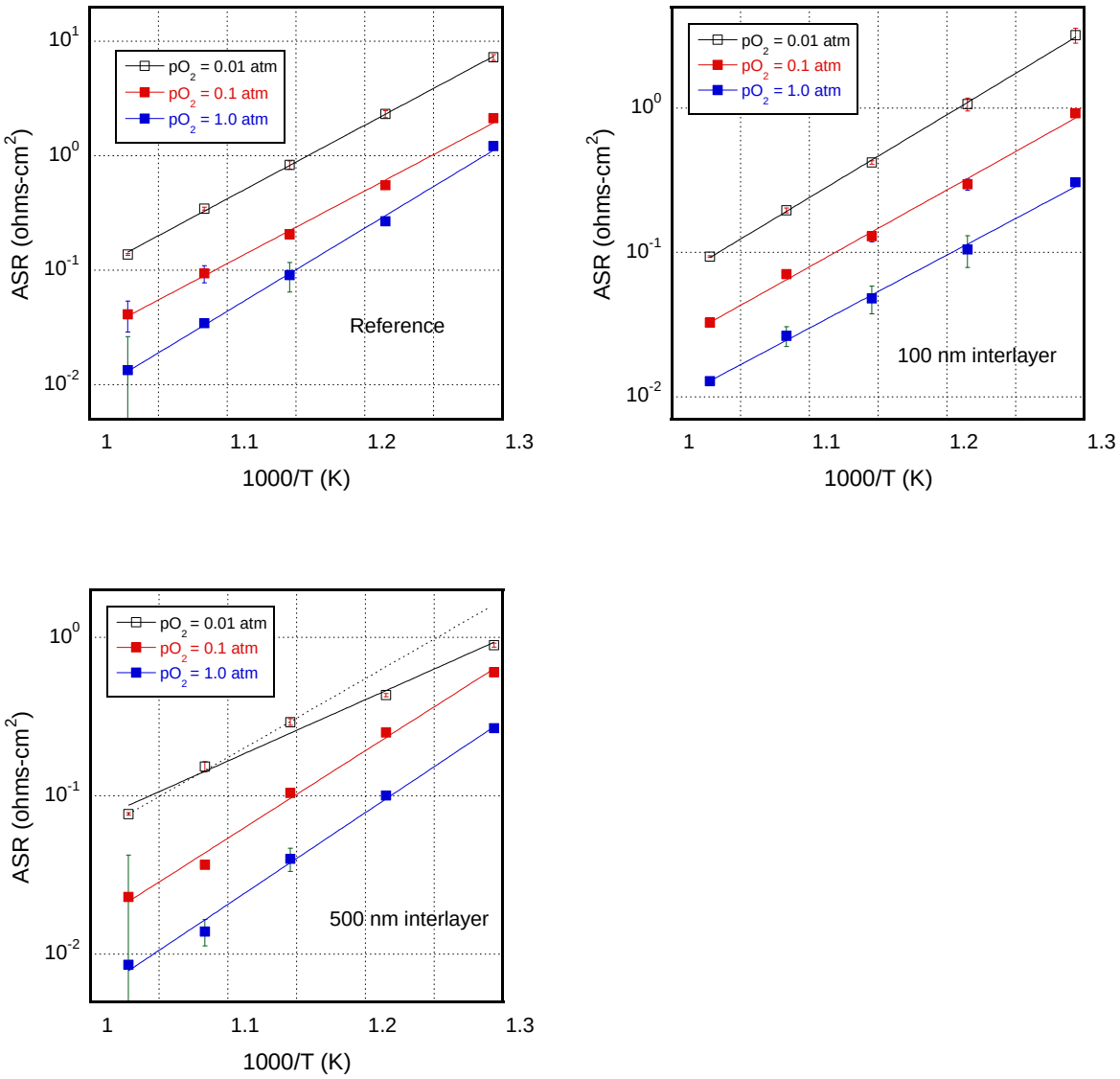

Fig. 5.5. The temperature dependence of the surface exchange resistances for the symmetrical cells at different oxygen partial pressures.

Fig. 5.6 displays the pO_2 dependence of the surface chemical exchange resistance of the cathode with and without interlayer at various temperatures. If considering surface oxygen reaction: $1/2O_2 + VO^{\cdot\cdot} \leftrightarrow O_o^x + 2h^{\cdot}$ and the pressure dependence of the oxygen vacancy concentration is very small, the surface exchange resistance could be expected to have a $pO_2^{-1/2}$ dependence.[217] As seen the fitting of the data in Fig. 6, a reasonable agreement with this relation is observed where exponents are close to 0.5. An exception exhibits for the cathode with the 500 nm-thick interlayer sample at 500-550 ℃ where the value is somewhat smaller (~0.3) and low oxygen partial pressure (0.01 atm). The deviation may be due to the slow start-up effect, oxygen vacancy concentration variation or the cathode kinetics, at this case, dominates by Knudsen diffusion in the pores of the electrode.[210]

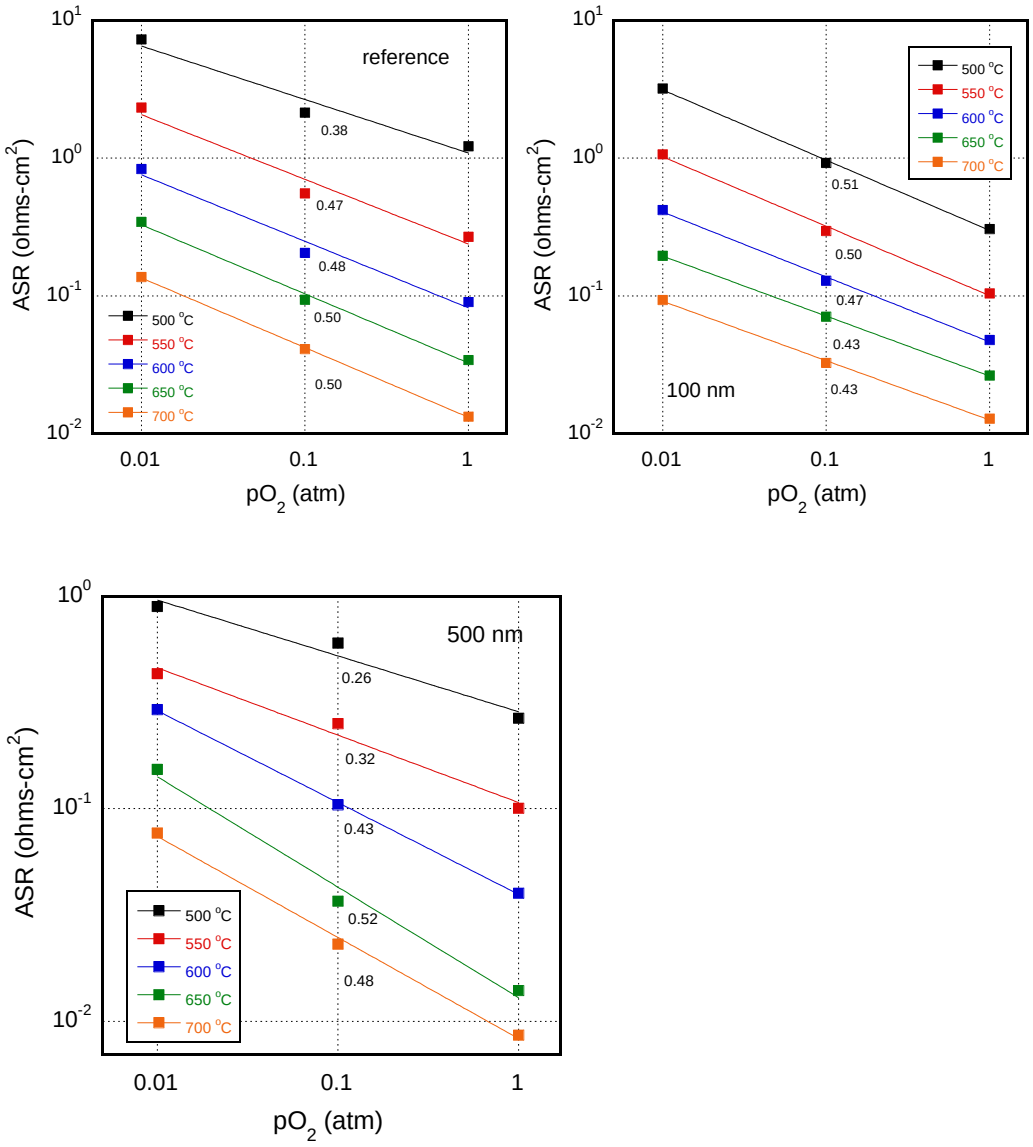

Fig. 5.6. Dependence of the surface exchange on oxygen partial pressure. The numbers are the exponents in a $(pO_2)^{-n}$ fit.

Considering the fundamental parameters of the nanocrystalline LSCO cathode such as surface exchange coefficient and diffusion coefficient are the same as the bulk screen printing layer,[216] the differences of the cathode with and without interlayer are

primarily the surface area density and cathode microstructure. To further examine the interlayer thickness effect, the power densities of the cells with and without interlayer were measured and fitted. It was reported that the cells with the 100 nm interlayer have more than 50% increase in the overall maximum power density at both 650 and 700 ℃ compared with the cell without an interlayer. [41] A later study shows a further ~ 40% power density increase for the single cell with 500nm LSCO interlayer. [41] Considering the cathode activation loss dominates and neglecting concentration losses at low current density regime, the activation overpotential of a fuel cell can be expressed as η_{act}= OCV - V_{meas} - j* ASR_e.[156] Here, OCV is the theoretical voltage of a fuel cell at thermodynamic equilibrium, V_{meas} is the measured voltage, j is the current density, and ASR_e is the area specific resistance of the electrolyte. Fig. 5.7 shows the η_{act} as function of ln(j) plots of LSCO cathode with and without interlayers at 700 ℃. Two parameters (j_0 and α) are obtained by fitting the power density with the Butler-Volmer equation (5.1):

$$\eta_{act} = -RT/\alpha nF \ln(j_0) + RT/\alpha nF \ln(j) \quad (5.1)$$

where R is the gas constant, F is the Faraday constant, j_0 is the exchange current density, α is the charge transfer coefficient, and n is set as 2 to reflect the two-electron process. For a typical curve, the interception of the fitted red line with y-axis yields the value of $\ln(j_0)$ while the slope of the fitted straight line can be calculated to obtain α. It is found that α value for the cathode with and without interlayer is within a comparable range indicating similar oxide ion incorporation kinetics for those cathodes. For cathode without interlayer, the value for j_0 was 0.050 A/cm^2 at 700 ℃. For the cathode with 100

nm interlayer, the corresponding value for j_0 was 0.098 A/cm^2. When the interlayer thickness increases to ~500 nm, the j_0 was 0.121 A/cm^2 at 700 ℃. Because j_0 is proportional to the activated reaction sites, the results demonstrate that the activated reaction sites of cathodes with the LSCO interlayer (>100 nm thickness) is ~2 times of the cathode without interlayer resulting in the enhancement of the cathode performance.

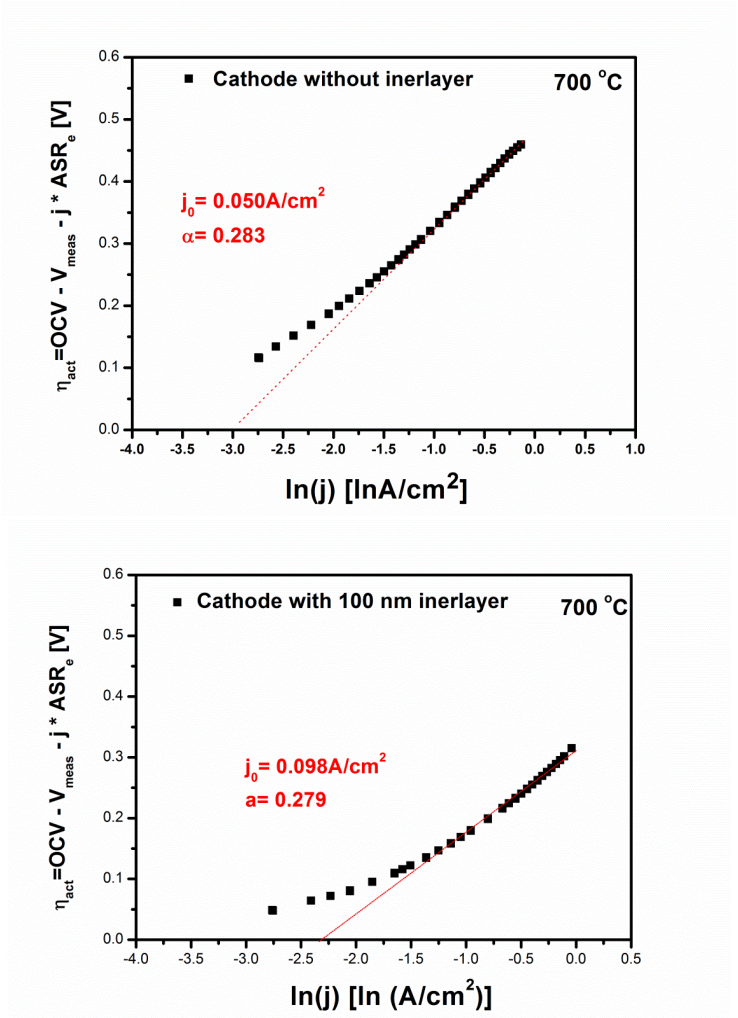

Fig. 5.7. ln(j)-η_{act} plots for LSCO cathode with different interlayer thicknesses at 700 ℃.

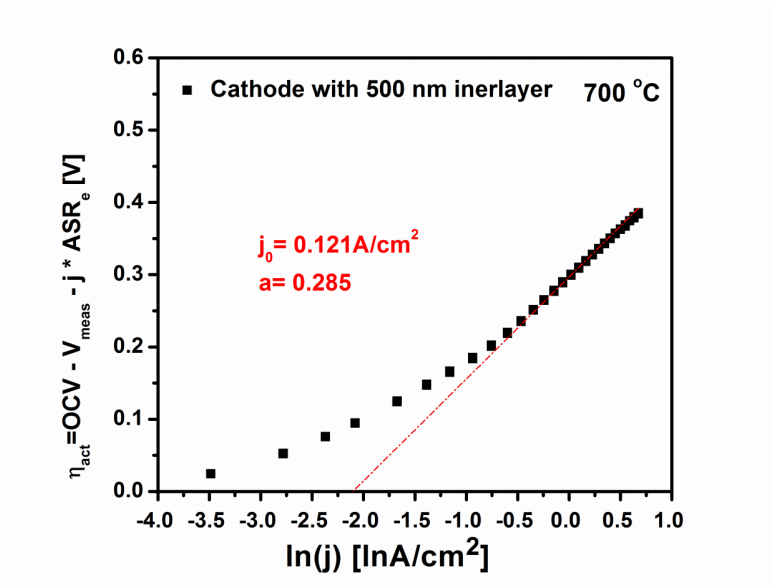

Fig. 5.7. Continued.

Thicker LSCO interlayer results in more reaction sites and therefore the enhanced cathode performance. For mixed ionic and electronic conducting cathode with expanded reaction area beyond triple phase boundaries, create more active surface areas so as to achieve more reaction sites is a widely adopted approach to enhance the cathode performance. Similarly, other reports also found that nanoscale mixed conducting cathodes prepared by infiltration,[218] metal organic deposition,[219] sol-gel[220] where all exhibited enhanced catalytic performance due to increased reaction sites. It is expected to achieve even higher enhancement for those newly developed cathode materials including $Ba_{0.5}Sr_{0.5}Co_{0.8}Fe_{0.2}O_{3-\delta}$, [101] $PrBaCo_2O_{5+\delta}$ and [105] $GdBaCo_2O_{5+\delta}$, [104] because of their extended reaction areas.

Temperature, oxygen partial pressure and the PLD layer thickness also have an effect on oxygen diffusion resistances in the electrodes as shown in Fig. 5.8. The

diffusion resistances decrease with the increase temperature because of the increase of the diffusion coefficient with temperature. The ASR values of diffusion resistance for the three electrodes are almost independent of pO_2 for the three electrodes except that at the lowest pO_2 and highest temperatures, the resistance remains constant suggesting that the oxygen supply rate becomes limited. Compared with diffusion resistance of LSCO cathode without PLD interlayer, there is a ~30% decrease of diffusion resistance for the cathode with 100 nm PLD interlayer. Further increase the PLD interlayer thickness, only a slight decrease of diffusion resistance is observed. It was reported in our previous work that the LSCO cathode with PLD interlayer (thickness $\geqslant$ 100 nm) have much higher film porosity with small grains and uniform pore structures compared with screen printed only LSCO cathode and the microstructure of cathode is almost the same if the PLD interlayer thickness keep increasing up to ~500 nm. [41] Considering the similar trend of diffusion resistance and microstructure as function of interlayer thickness, the decrease of diffusion resistance by implementing PLD interlayer may be correlated with smaller grain size and more porous microstructure for the cathodes with PLD interlayer. In addition, it is expected that the solid state oxygen transport includes the gas diffusion, oxide-ion bulk diffusion, grain boundary and dislocation core pathway together with surface diffusion. [116] The more porous microstructure of cathode results in lower oxygen mass transfer resistance indicating that uniform pores facilitate the oxygen gas diffusion and the pore surface benefits the oxygen effective surface diffusion of the cathode, similar to previous reports [116, 210, 221].

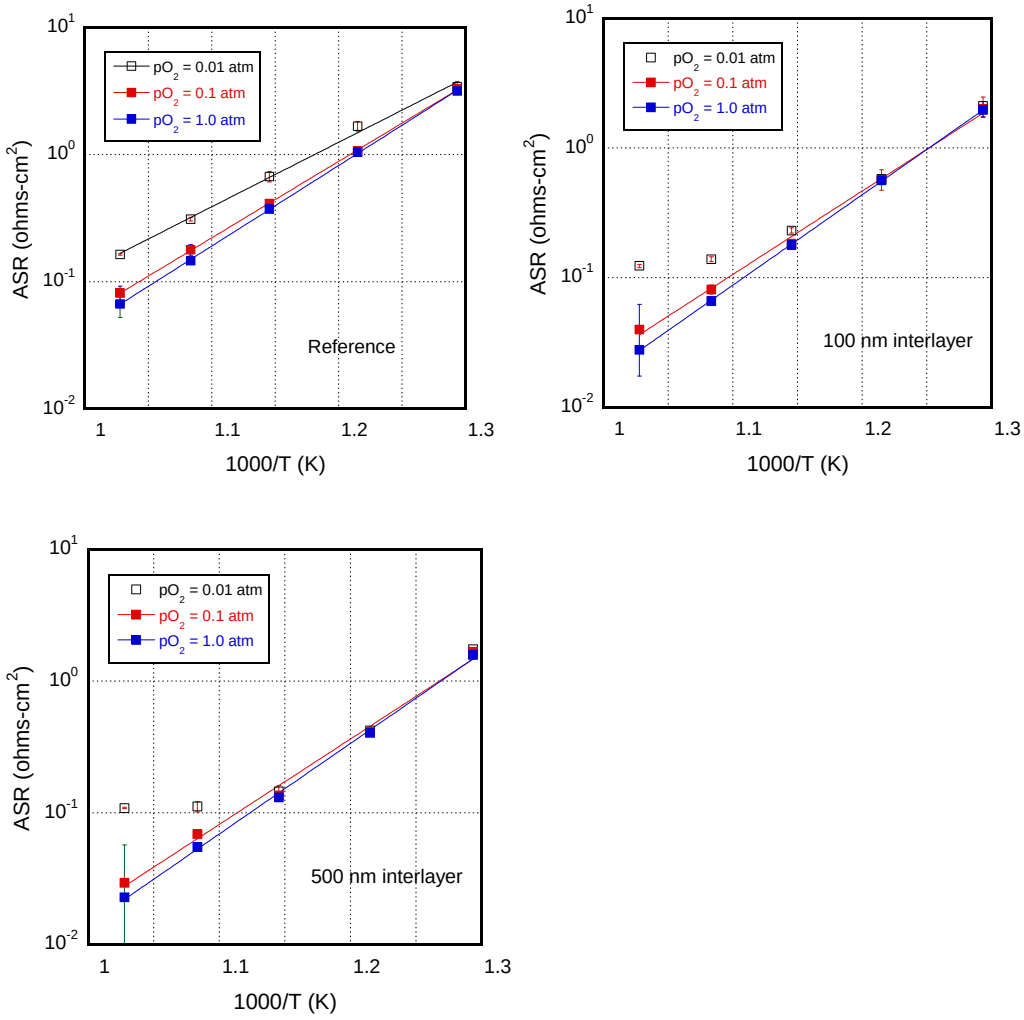

Fig. 5.8. The temperature dependence of the oxygen mass transfer resistances for the symmetrical cells at different oxygen partial pressures.

It is interesting to note, for the LSCO cathodes with and without interlayer, that the mass diffusion resistance is higher than cathode surface exchange resistance except for cathodes at low oxygen partial pressure (0.01 atm). Therefore, oxygen mass transfer process of LSCO cathodes with thickness higher than 30 μm plays an important role in determining overall ASR resistance of the cathode. Preparing the bilayer LSCO cathodes with thicker interlayer, the difference between surface exchange resistance and oxygen mass transfer resistance becomes smaller. The oxygen reduction reaction is equally co-limited by those two processes.

5.5 Conclusions

The electrochemical properties of LSCO cathode with and without nanoporous LSCO interlayer were studied with ac impedance spectroscopy under controlled temperature and pO_2 conditions. Two reaction steps, i.e., the gas phase oxygen exchange at the electrode surface and oxygen mass transfer, are co-limited the electrode kinetic performance. A corresponding equivalent circuit model is proposed to interpret the observed impedance spectra. The oxygen chemical surface exchange resistance decreases as a function of temperature and interlayer thickness. The surface exchange resistance decreases as interlayer thickness increases which is due to the increased activated reaction sites. The activated reaction sites of cathodes with the LSCO interlayer (>100 nm thickness) is ~2 times of the cathode without interlayer resulting in the enhancement of the cathode performance. Thicker LSCO interlayer results in more

reaction sites in the cathode. The oxygen mass transfer resistance also decreases because of more porous microstructure of the cathode with PLD interlayer.

6. VERTICALLY ALIGNED NANOCOMPOSITE ELECTROLYTES WITH SUPERIOR OUT-OF-PLANE IONIC CONDUCTIVITY FOR SOLID OXIDE FUEL CELLS*

6.1 Overview

Two-phase $(Ce_{0.9}Gd_{0.1}O_{1.95})_{0.5}/(Zr_{0.92}Y_{0.08}O_{1.96})_{0.5}$ (GDC/YSZ) nanocomposite thin films with vertically aligned structure are grown as the electrolyte for thin film solid oxide fuel cells (TFSOFCs). X-ray diffraction (XRD) and transmission electron microscopy (TEM) results confirm that GDC and YSZ grow as separated, high crystallinity nanocolumns with tunable column width on both single crystal and polycrystalline anode substrates. Impedance measurements demonstrate ~ 50% enhancement in ionic conductivity compared to pure single-crystal-like GDC thin film. The enhanced properties in the GDC/YSZ vertically aligned nanocomposite (VAN) system may be attributed to two-phase strain coupling and the fast ionic transport rate along the vertical interfaces. The VAN is applied in thin film SOFC as a part of the electrolyte in the single cells. The overall power density increases more than 50% compared with that of the cells without VAN electrolyte.

---

* Reprinted with permission from "Vertically aligned nanocomposite electrolytes with superior out-of-plane ionic conductivity for solid oxide fuel cells", Q. Su, D. Yoon, A. Chen, F. Khatkhatay, A. Manthiram, and H. Wang, Journal of Power Sources, 242 (2013) 455–463. Copyright (2013).

This work demonstrates the first VAN nanostructured electrolyte with the essential vertical ion-transport channels. The new VAN electrolyte provides superior out-of-plane ionic conductivity compared to those single phase electrolytes as well as the nanolayered electrolytes.

6.2. Introduction

Because of their high efficiency and wider range of fuel options, thin film solid oxide fuel cells (TFSOFCs) have attracted extensive research interests.[1, 4, 52, 222] The main issue for SOFCs is to achieve desired cell performance at intermediate temperatures (600-800 ℃) or lower.[4] However, the ionic conductivity of the electrolyte decreases significantly at low temperatures, leading to low power density. The most promising way to decrease the ohmic loss of the electrolyte at low temperatures is to reduce the electrolyte thickness, which, however, may raise concerns about the durability and mechanical stability of the electrolyte. Therefore, exploring higher conductivity electrolytes is critical for developing low-temperature (LT) SOFCs.[52]

Following the widely used Yttria stabilized zirconia (YSZ),[223, 224] much work has been done to investigate various alternateve electrolytes, among which aliovalent-doped ceria (doped CeO_2) and isovalent-cation–stabilized bismuthoxides have attracted much attention because of their superior ionic conductivity at low temperatures.[39, 225] Unfortunately, the higher conductivity comes at the expense of thermodynamic instability, which raises the concern about the electrolyte reliability. Besides material exploration, material nanostructure engineering provides another

possibility to enhance the ionic conductivity. In zirconia and ceria based electrolyte systems, the grain size dependence of conductivity has been investigated and higher ionic conductivity has been observed in nanocrystalline electrolytes.[82, 83] On the other hand, the ionic conductivity of YSZ thin film was found to increase when the film thickness decreases to below 30 nm, which demonstrates an unblocking grain boundary effect.[81] These results suggest that, when the grain size decreases to nanometer range, the ionic conductivity properties of the electrolyte could dominate by interface rather than intragrain.

Based on the above findings, a multilayer strategy (as shown in Fig.6.1a.) has been applied to create heterogeneous interfaces and is widely used to study the interfacial effect of two ionic conducting systems.[84] A typical example is the two-phase multilayered calcium and barium fluoride (CaF_2 and BaF_2). The fluoride ion conductance was drastically enhanced with increasing interface density,[84] which was attributed to the influence of space charge regions at the interfaces where the carrier density was significantly increased. Besides the two-phase multilayered fluoride systems, the ionic conductivity in multilayered oxide systems including YSZ/$SrTiO_3$ (STO), YSZ/Y_2O_3, YSZ/GDC etc. have also been reported to be enhanced.[85, 86, 91] The enhancement in multilayered oxide systems was correlated to the interfacial strain or fast transportation along interface rather than the space charge regions at the interfaces.[85, 91] This provides possibility to create fast transportation channels (interfaces) or tune the interfacial strain to enhance the ionic conductivity. Generally, the transportation parallel to the grain or phase boundaries is strongly enhanced, while the transportation

across the grain or phase boundaries is blocked for oxide systems.[226] Overall, the multilayer strategy helps to facilitate the diffusion along the parallel interfaces, but has limited impact on the transport property in the out-of-plane direction that is required for the oxygen ion transport in SOFCs.

To achieve enhanced vertical transport properties in electrolyte, self-assembled vertically aligned nanocomposite (VAN) structure with vertical interfaces is proposed and illustrated in Fig. 6.1b. Various VAN systems have been demonstrated in functional oxides for multiferroics,[227, 228] low field magnetoresistance materials,[229, 230] and others.[231, 232] Because the interface area within the composite is much larger than the contact area of each nanocolumn with the substrate, the VAN systems are free from substrate clamping constraints and are mainly controlled by vertical strain. This provides enormous potential to control strain vertically in much thicker films with correspondingly large volume.[227]

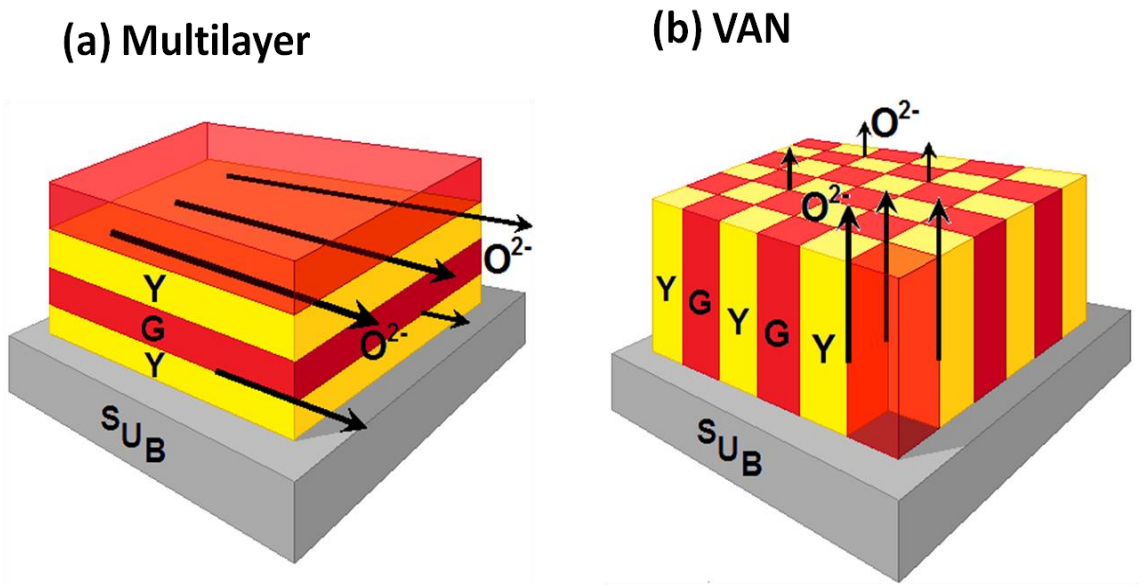

Fig. 6.1. (a) Illustration of a conventional thin-film multilayers strategy with lateral interfaces to enhance the in-plane ionic conductivity where "Y" and "G" stands for YSZ and GDC electrolyte, respectively. (b) Schematic diagram of a self-assembled vertically aligned nanocomposite (VAN) film with vertically aligned interfaces to increase the out-of-plane ionic transportation.

In this paper, Pulsed laser deposition (PLD) is used to fabricate a unique YSZ/GDC VAN structure in one-step on both single crystalline STO (001) and polycrystalline NiO-YSZ substrates based on the spontaneous phase ordering. The ionic conductivity of the VAN electrolyte is measured and compared with pure YSZ, GDC electrolyte and multilayer YSZ/GDC electrolyte. The possible mechanism for the enhanced ionic transport properties of VAN electrolyte is also proposed. The VAN

structure consisting of YSZ/GDC composite as electrolyte is introduced as part of electrolyte to achieve an overall enhancement in power output for SOFCs.

6.3. Experimental

6.3.1Targets and Anode Disks Processing

The PLD targets including $La_{0.5}Sr_{0.5}CoO_{3-\delta}$ (LSCO), 8 mol% yttria stabilized zirconia (YSZ) (500 nm, Tosoh Co.), $Ce_{0.9}Gd_{0.1}O_{1.95}$ (GDC), YSZ and GDC composite, 60 wt. % NiO + 40 wt. % YSZ (NiO-YSZ, 500 nm, Praxair Inc) anode disks were all fabricated by solid state reaction through mixing stoichiometric amounts of the raw powders: La_2O_3 (99.99%), $SrCO_3$, Co_3O_4 (99.9%), CeO_2 (99.9%), YSZ and Gd_2O_3 (99.9%). The sintering details can be found elsewhere [233]. YSZ and GDC composite target was sintered at 1100 ℃ for 12 h in oxygen. The phase purity of LSCO and GDC/YSZ composite targets were confirmed by X-ray diffraction (XRD).

6.3.2 Thin Film Preparation

Platinum thin layers (~100 nm) were sputtered both on single crystal $SrTiO_3$ (STO) (001) substrates as bottom electrode and on YSZ and GDC composite thin films as top contact. The YSZ and GDC composite thin films were deposited on single crystal $SrTiO_3$ (STO) (001) substrates and Pt-sputtered STO substrates in a PLD system with a KrF excimer laser (Lambda Physik Compex Pro 205, λ=248 nm). The deposition frequency varied from 1 Hz to 10 Hz to optimize the column width and interface density. The laser beam with approximately 5 $J \cdot cm^{-2}$ in energy density was focused on the targets

at a 45 ° incidence angle. An optimized substrate temperature of 700 ℃ and oxygen pressure of 200 mTorr was employed for the depositions. After the deposition, the films were cooled down at 10 ℃ min^{-1} under oxygen pressure of 200 Torr to assure proper film stoichiometry. The phase and orientation of the films were examined by XRD (θ–2θ scan with Cu Kα radiation, λ = 1.5406 Å, Bruker D8 Discover X-ray powder diffractometer).

6.3.3 Single Cells Fabrication

To prepare the anode-supported single cells, commercial NiO-YSZ cermet powder was compacted into anode disks under uniaxial pressure using a die set of 1 inch (2.54 cm) in diameter. The disks were then sintered at 1300 ℃ for 3 h. Thin film electrolytes were coated by PLD with a growth rate of ~ 0.8, ~ 0.9 and ~ 0.9Å/s for YSZ, GDC and YSZ/GDC VAN layers separately. The YSZ layer thickness was kept ~ 1.5 μm for all single cell samples. The pure GDC layer with the thickness of ~ 4.5 μm was coated as the reference sample. To study the electrolyte architecture effect on overall power density, the GDC and YSZ/GDC VAN electrolyte were coated with different sequence by keeping the total thickness of GDC and YSZ/GDC VAN electrolyte ~ 4.5 μm. A screen printed LSCO cathode layer was then screen printed onto a NiO-YSZ anode disk substrate. All of the cells were annealed at 1150 ℃ for 2 h with a ramping rate of 2 ℃ min^{-1} to ensure fair comparison.

6.3.4 Microstructure and Electrochemical Properties Characterization

The microstructure of these films was first characterized by a high resolution field emission scanning electron microscope (FE-SEM, JEM-7500F Cold Emission SEM) and by transmission electron microscopy (TEM) (JEOL JEM-2010 and FEI Tecnai G2 F20 operated at 200 kV). Cross-sectional and plan-view samples for TEM analysis were prepared by a standard manual grinding and thinning procedure followed by a final polishing step in a precision ion polishing system (PIPS 691, Gatan). STEM was conducted on the FEI Tecnai F20 with a point-to-point resolution of 0.27 nm.

Platinum grids were gently pressed onto Pt top contact and were used as current collectors. Using a potentiostat/impedance analyzer (Reference 600^{TM}, Potentionstat/ Galvanstat/ ZRA, GAMRY INSTRUMENTS), AC impedance spectroscopy measurements were conducted in the frequency range of 10^{-1} – 3×10^{5} Hz in the temperature range from 400 to 700 ℃. The AC impedance data were measured after a waiting period of an hour for temperature stabilization. The anode-supported single cells prepared with and without the interlayer were used to evaluate the VAN electrolyte effect on the single cell performance. Humidified H_2 with a constant flow rate of 80 $mL{\cdot}min^{-1}$ and air with at a constant flow rate of 120 $mL{\cdot}min^{-1}$ were supplied as the fuel and the oxidant, respectively, during single-cell performance test.

6.4. Results and Discussion

The XRD pattern of the YSZ and GDC composite target is shown in Fig. 6.2a. The diffraction peaks of GDC and YSZ reveal the typical fluorite structure of GDC and

YSZ, [234] indicating no obvious solid state reaction between GDC and YSZ. Fig. 6.2b shows the XRD θ–2θ scan of a typical YSZ and GDC nanocomposite film deposited at 10 Hz. The (002) peaks for GDC and YSZ slightly overlap as a possible result of the vertical strain coupling between the two phases. It can be clearly seen that only the (002) peaks of both the GDC and YSZ phases are observed, indicating that both phases have grown highly textured along (00l) on the STO (001) substrate. Considering the lattice parameter for STO, YSZ and GDC is 3.91 Å, 5.13 and 5.41 Å, respectively, YSZ and GDC will prefer an epitaxial cubic on cubic growth with a 45 ° in-plane rotation with STO substrate in order to minimize the lattice mismatch (as illustrated in Fig. 6.2c). The epitaxial growth of YSZ/GDC composite on STO results in the preferred (001) out-of-plane texture. Several small peaks, which are also observed in the baseline scan on STO single crystalline substrates, are marked in the XRD profile as background peaks from the substrate and the XRD holder.

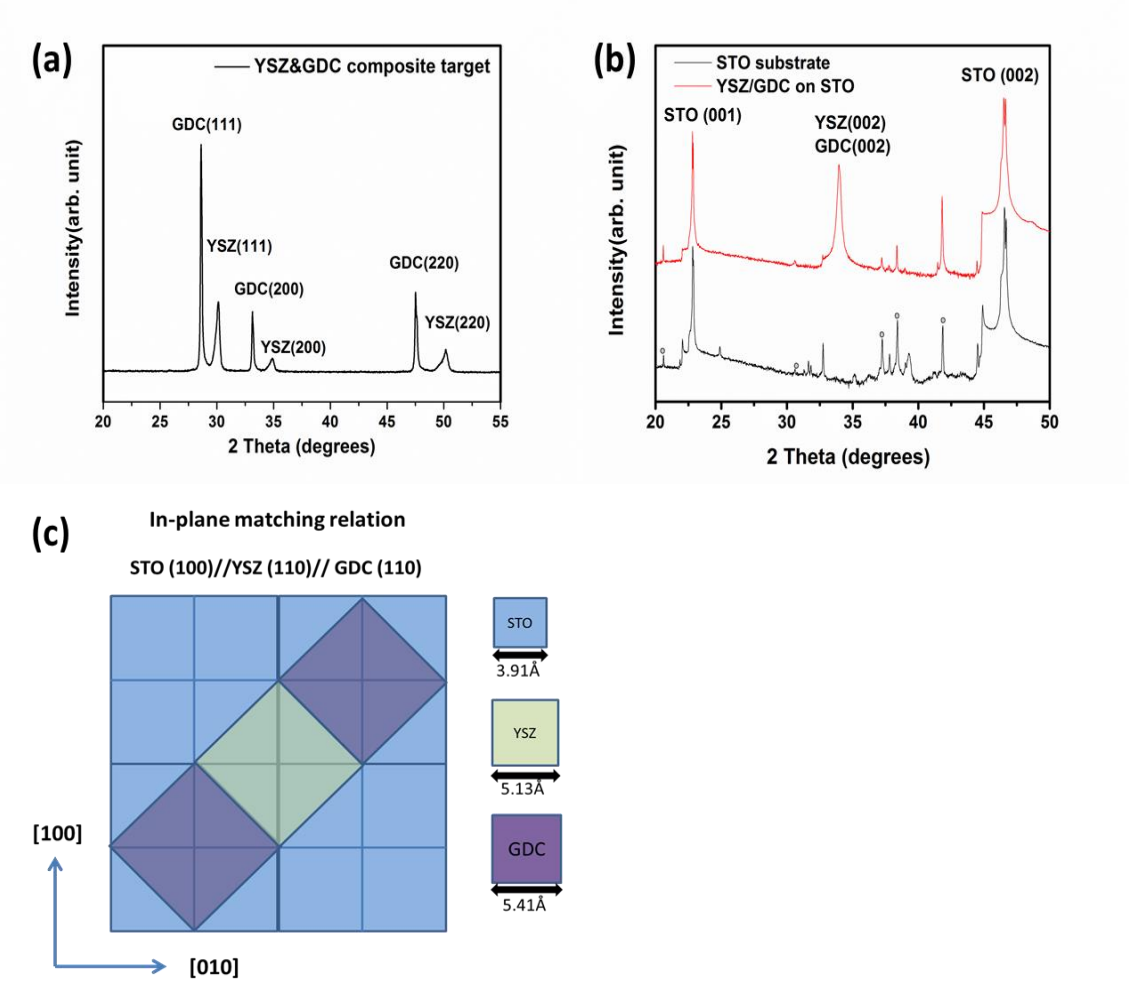

Fig. 6.2. X-ray diffraction (XRD) pattern of a) the YSZ and GDC composite target showing no inter-reaction between YSZ and GDC and b) a typical YSZ/GDC nanocomposite film deposited at 10 Hz showing an epitaxial growth of YSZ/GDC nanocomposite film.

TEM was conducted to examine the microstructure of films deposited under different deposition frequencies. Fig. **6.**3(a) and (b) show the cross-sectional TEM images for the YSZ/GDC nanocomposite films on the STO (001) deposited at 1 Hz and 10 Hz, respectively. It can be seen that the sub-20 nm epitaxial growth of YSZ and GDC columns are vertically aligned on the substrate, indicating the self-assembled VAN structures. It could be seen that the average column width decreases as the deposition frequency increases due to the reduced diffusion length of the adatoms as deposition frequency increases. Fig. 6.3c and d are the corresponding selected area electron diffraction (SAED) patterns of Fig. 6.3a and b. The orientation relations between both of the YSZ/GDC nanocomposite films and the substrates are determined to be YSZ (002) /GDC (002)/ STO (002), and YSZ [220] /GDC [220] /STO [200]. This in-plane 45^{o} rotation enables a better lattice matching of YSZ and GDC with the underlying STO (a=3.905 Å). The relative strain (ε) is estimated from the equation: $\varepsilon = \alpha\text{-}\alpha_{bulk}/\alpha_{bulk}$, where α_{bulk} is the lattice constant of unstrained bulk material (For GDC a = 5.418 Å, and for YSZ, a = 5.147Å). The out-of-plane lattice parameters of YSZ and GDC are calculated as 5.27 Å and 5.28 Å based on the XRD and SAED patterns. The YSZ/GDC VAN electrolyte results in a ~2.6 % compressive strain for GDC and a ~2.2 % tensile strain for YSZ out-of-plane.

To confirm that YSZ and GDC grow as alternating columns without intermixing, scanning transmission electron microscopy (STEM) was conducted under a high-angle annular dark field (HAADF) condition, where the contrast is roughly proportional to atomic number square (Z^2, also called Z-contrast imaging). A typical Z-contrast image over a large area of YSZ/GDC VAN structure is shown in Fig. 6.3e. Because of the higher Z numbers of Ce and Gd, GDC columns have much higher contrast (brighter columns) than YSZ columns. The GDC and YSZ grains grow into well-aligned vertical columns and alternate with each other with a column size of ~ 5-15 nm. Energy dispersive X-ray (EDX) line scan was conducted over the same area (not shown here), and no obvious intermixing was observed. The plan-view TEM seen in Fig. 6.3f shows the nanoscale checkerboard-like microstructure of YSZ/GDC nanocomposite film, indicating a spontaneous phase ordering of the two phases.

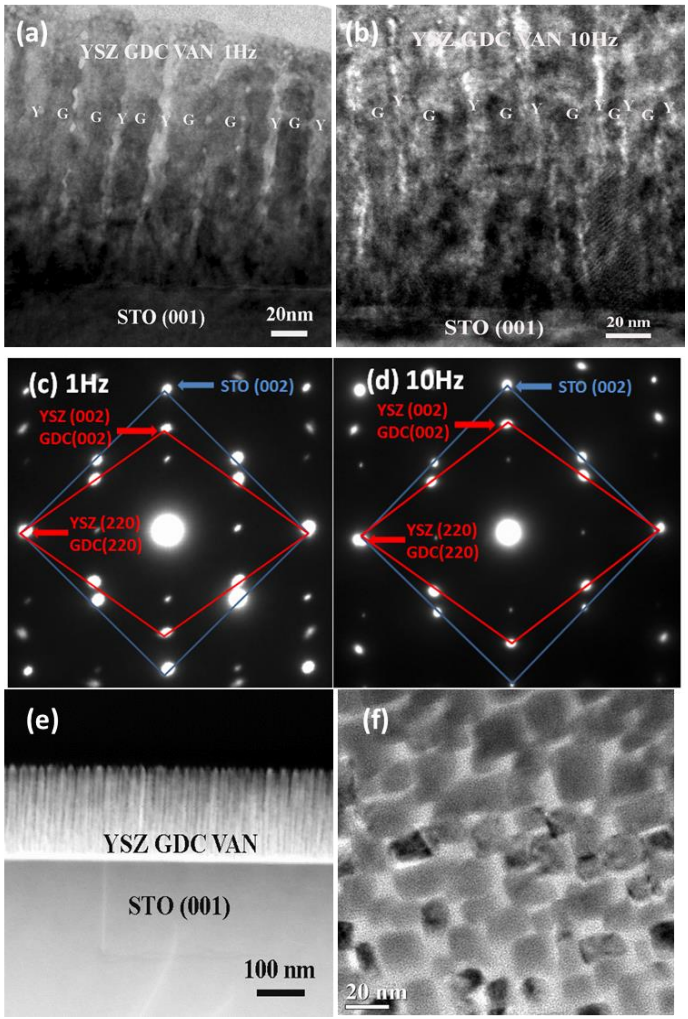

Fig. 6.3. Cross-sectional TEM images for the YSZ/GDC nanocomposite films on STO(001) deposited at a) 1 Hz and b)10 Hz, which clearly demonstrate different column size by different deposition frequencies. The selected area electron diffraction (SAED) patterns of YSZ/GDC nanocomposite films on STO(001) deposited at c) 1 Hz and d)10 Hz indicating a 45 degree rotation matching on STO substrate. The cross-sectional STEM images e) and f) plan-view TEM images of YSZ and GDC nanocomposite thin film show the phase separation and arrangement.

In order to measure the electrochemical characteristics and test the performance of the VAN electrolyte, multilayer samples of Pt/VAN/Pt on STO (001) substrates were prepared. The total VAN electrolyte thickness is about 1 μm. The inset of Fig. 6.4 shows the typical impedance spectra measured in air at 600 ℃ for pure GDC thin film and YSZ/GDC VAN thin films. A single RC element (*i.e.*, a resistor (R) in parallel with a capacitor (C)) is used as the equivalent circuit to obtain the impedance-frequency relation at various temperatures. A single impedance arc of the thin films is ascribed to the total contribution of grains and grain boundaries of the ionic resistivity. The ionic conductivity dominates in these materials including YSZ and GDC at the measured temperatures ranges.[5] The thin film ionic conductivity could be calculated as $\sigma_{ionic} = l/AR$, where σ_{ionic} is the ionic conductivity, R is the thin film resistance, l is the length of the thin film and A is the cross-sectional area. The total ionic conductivity follows the Arrhenius law :

$$\sigma T = \sigma_0 \exp(-E_a/kT) \quad (6.1)$$

where σ_o, a constant related to the density oxide vacancies, is the pre-exponential factor, E_a is the activation energy for ionic migration and k is the Boltzmann constant.

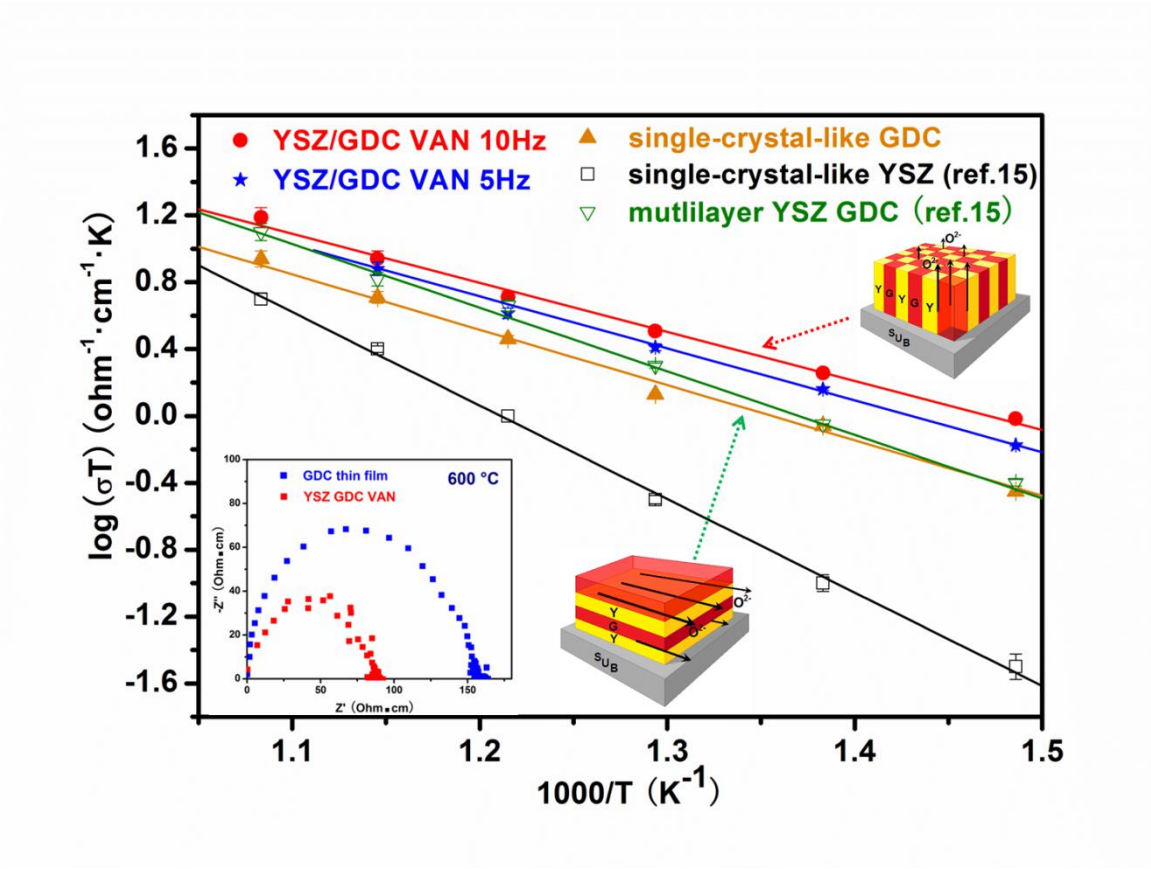

Fig. 6.4. An Arrhenius plot of ionic conductivity as a function of temperature showing enhanced ionic conductivity for YSZ/GDC VAN electrolyte compared to pure GDC and YSZ thin film. The inset is a specific impedance plot of GDC film and YSZ and GDC VAN film at 600 ℃.

The Arrhenius plots of ionic conductivity multiply temperature versus reciprocal temperature for GDC thin film and YSZ/GDC VAN thin film are plotted in Fig. 6.4. The Arrhenius plots of ionic conductivity of the single-crystal-like YSZ thin film and YSZ/GDC multilayer film are also presented for a comparison.[85] Previously, the ionic

conductivity multiply temperature of single-crystal-like YSZ thin film and YSZ/GDC multilayer film was reported to be 0.41 and 0.82 $ohm^{-1}cm^{-1}K$ at 600 ℃, respectively.[85] In comparison with the ionic conductivity of pure YSZ thin film and pure GDC thin film, the ionic conductivity of the YSZ/GDC VAN thin film is higher for the entire temperature range by applying the VAN microstructure. Both the VAN samples deposited with different frequencies show enhanced conductivity, *e.g.*, ionic conductivities multiply temperature for 5 Hz and 10 Hz samples are 0.88 and 0.96 $ohm^{-1}cm^{-1}K$ at 600 ℃, respectively. The higher the deposition frequency for the VAN electrolyte, the higher the ionic conductivity is. Since the vertically aligned interface density increases as deposition frequency increases, the result indicates that the ionic conductivity properties of VAN electrolyte dominate by interfaces rather than intragrain. It is also observed that the activation energy for the VAN electrolyte film is lower than that for the pure YSZ and GDC film, indicating lower oxygen ion migration energy for the VAN electrolyte film, thus may benefit its application in LT SOFCs.

The maximum value for the ionic conductivity appears to be at least 2 times higher than that of single-crystal-like YSZ thin film and ~50% higher than that of single-crystal-like GDC thin film reported. Since there are strong indications of carrier depletion for YSZ and GDC oxide systems with increasing interface density and the Debye screening length is inversely proportional to the square root of the carrier density which is only ~0.1 nm in this system, [226, 235] the enhanced oxide ion conductance may be resulting from the lattice strain near the layer interfaces or high oxide ion mobility along the interface. Fig. 6.5a is the high resolution TEM (HRTEM) micrograph

showing the vertical interface between YSZ and GDC. To better illustrate the dislocation features at the interface, Fourier-filtered image of HRTEM is shown in Fig. 6.5b. The interface dislocations are identified by the dashed-line circles in the filtered image. The dislocation density is similar at each YSZ/GDC interface regardless of the number of interfaces in these films. Those vertical interfaces with extended defects due to the lattice mismatch may provide fast channels for oxide ion transportation out-of-plane. Besides the interfaces, the lattices strain may also play a role. For the oxide ion conductor including YSZ, GDC and etc., there is an exponential dependence of the ionic conductivity $\sigma_{O^{2-}_{int}}$ in the ionic conductor close to the interface on the migration volume ΔV_v^M of vacancies and on the lattice misfit f_{12}:

$$\ln(\sigma_{O^{2-}_{int}}/ \sigma_{O^{2-}_{vol}}) \sim \Delta V_v^M f_{12} \quad (6.2)$$

where $\sigma_{O^{2-}_{int}}/ \sigma_{O^{2-}_{vol}}$ is the ratio of ionic conductivity of the interface regime and the bulk.[88] For oxide systems including YSZ, GDC etc., which have a vacancy-type diffusion mechanism, the migration volume is usually positive.[87] Thus, the tensile strain has a positive effect on the interfacial ionic conductivity for YSZ and GDC systems which were also demonstrated by previous work.[89, 90] In this work, there are 2.6% out-of-plane compressive strain for each GDC column and a 2.2% out-of-plane tensile strain for each YSZ column. The overall ionic conductivity enhancement may be resulted from both higher ionic transporting along vertical interfaces and the strain effects within the two vertical phases in which the fast ionic transport along the interlayer plays a dominant role. Considering the ionic resistance for YSZ is higher than that of GDC, the increase of ionic conductivity of YSZ from tensile strain may exceed

the decrease of ionic conductivity of GDC due to the compressive strain. Therefore, an overall enhanced ionic conductivity for YSZ/GDC VAN electrolyte is observed. The vertical strain could be further optimized by the composition and column width.

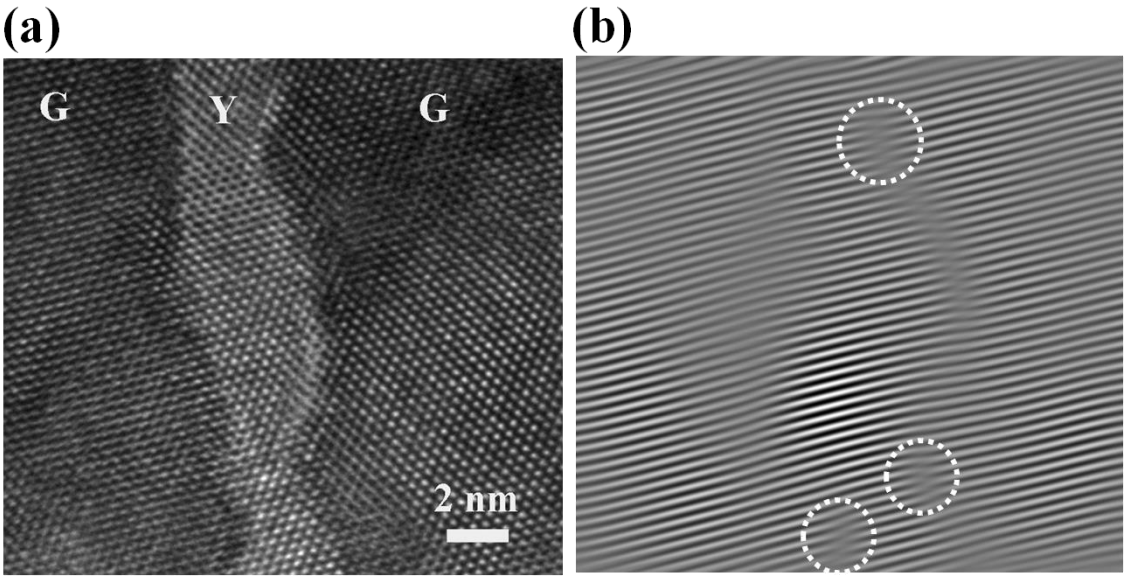

Fig. 6.5. (a) Cross-sectional HRTEM image of YSZ/GDC VAN thin film and (b) its corresponding FFT image suggest the strain coupling along the vertical YSZ/GDC interfaces.

To demonstrate the VAN electrolyte effect on the overall cell performance, anode-supported single cells with and without the VAN electrolyte were prepared. As seen from the cross-sectional backscattered SEM images of single cells with the VAN electrolyte, the dense and crack-free electrolytes were successfully prepared on porous

NiO-YSZ anodes. A single cell with the bi-layer electrolyte of YSZ (~1.5 μm) and GDC (~4.5 μm) (without VAN layer) is used as a reference sample.[41] The single cells with VAN electrolytes applied either in the middle of YSZ and GDC electrolyte (Fig. 6.6a) or on top of YSZ and GDC electrolyte (Fig. 6.6b) were prepared to optimize the electrolyte structure. The columnar feature with different contrasts is observed for the VAN electrolyte layer. A YSZ thin layer is applied to prevent the reduction of Ce^{4+} into Ce^{3+} which occurs in hydrogen atmosphere and leads to the decrease of open circuit voltage (OCV).[203]

The growth of dual-phase electrolyte mainly involves two stages, the clusters nucleation and film growth. At the very early stage of composite film growth, different adatoms will arrive at the substrate surface simultaneously. Same phase molecules will accumulate and nucleate to minimize the total system free energy. The phase column widths are determined by the adatoms' diffusivity as a competition. The following film growth will perform as homogeneous phase growth mode in vertical and heterogeneous growth in lateral, defined by the energy minima and to reduce the lattice mismatch.

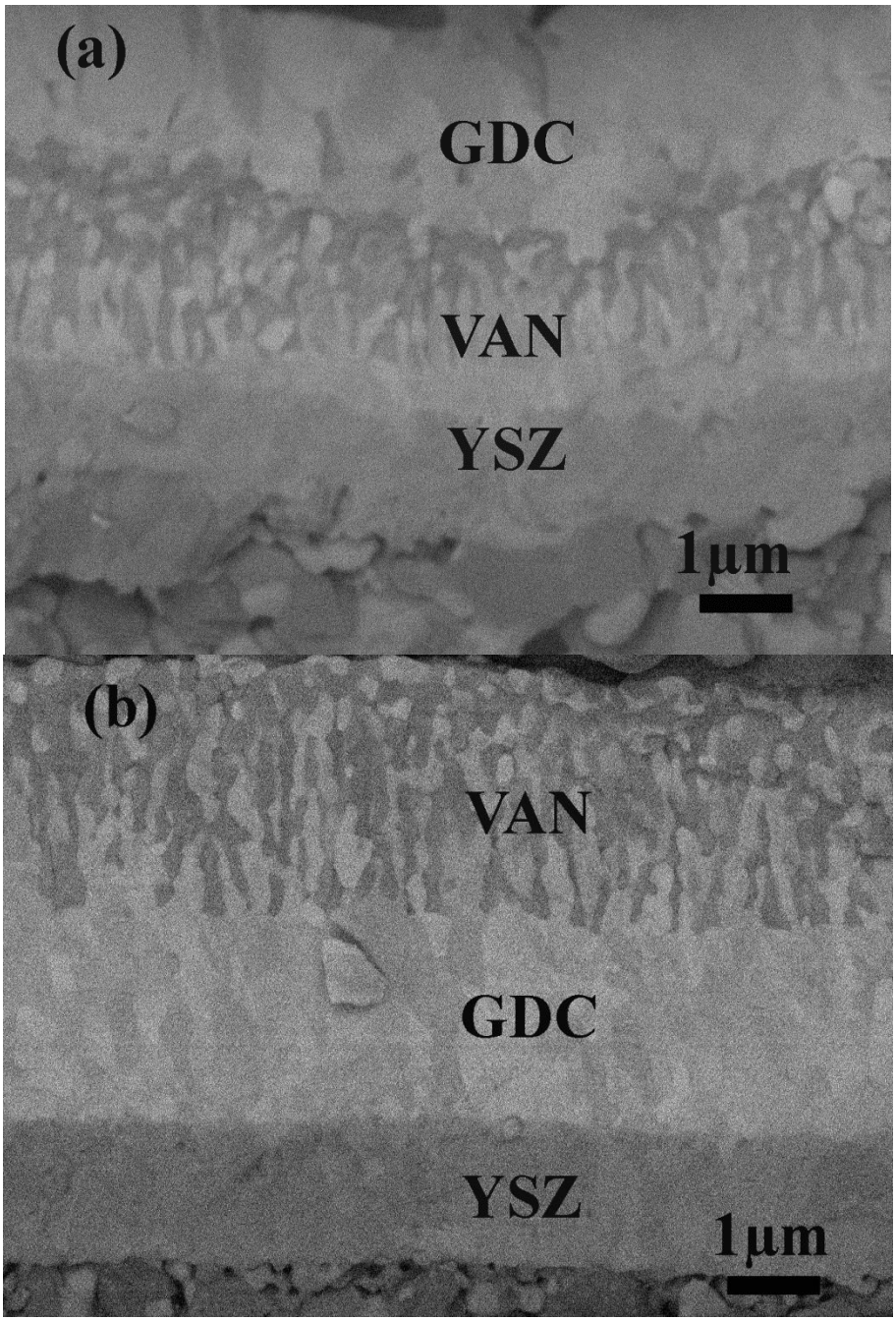

Fig. 6.6. Cross-sectional backscattered SEM images of single cells with VAN electrolyte a) in the middle of YSZ and GDC electrolyte and b) on the top of YSZ and GDC electrolyte.

Compared with the vertically-aligned dual phase structure achieve on single crystal substrate, alternating columns can be achieved on polycrystalline anode substrate either in perfectly vertically-aligned or tilted at a certain angle as seen in the illustration in Fig. 6.7a. To confirm, cross-sectional TEM has been conducted on the YSZ/GDC composite electrolyte on polycrystalline anode substrate. Fig. 6.7b is the TEM image of the top portion of YSZ/GDC composite electrolyte on NiO-YSZ polycrystalline anode substrate coated with YSZ and GDC. The alternating columns with different contrasts indicate that dual-phase solid electrolyte has an alternating columnar growth and the VAN-like microstructure could extend to over micron range. Perhaps due to the surface roughness of polycrystalline substrate, the nanocolumns are either vertically-aligned or tilted at a certain angle which demonstrates that a VAN-like microstructure has been successfully fabricated on a polycrystalline anode substrate regardless of the surface roughness. Fig. 6.7c is the high resolution TEM image of selected area in Fig 7b. The alternating sub-20nm columns are observed where the average column width of GDC is ~13 nm and average column width of YSZ is ~ 5 nm. Those results have been further confirmed by the STEM study in Fig. 6.7d where different contrasts of columns can be seen, demonstrating two-phase structure without obvious intermixing. It is found that the average column width obtained from TEM images is smaller than that obtained from backscattered SEM image possibly because of the resolution limitation of SEM, i.e., one column observed in SEM may contain several nanocolumns identified by TEM.

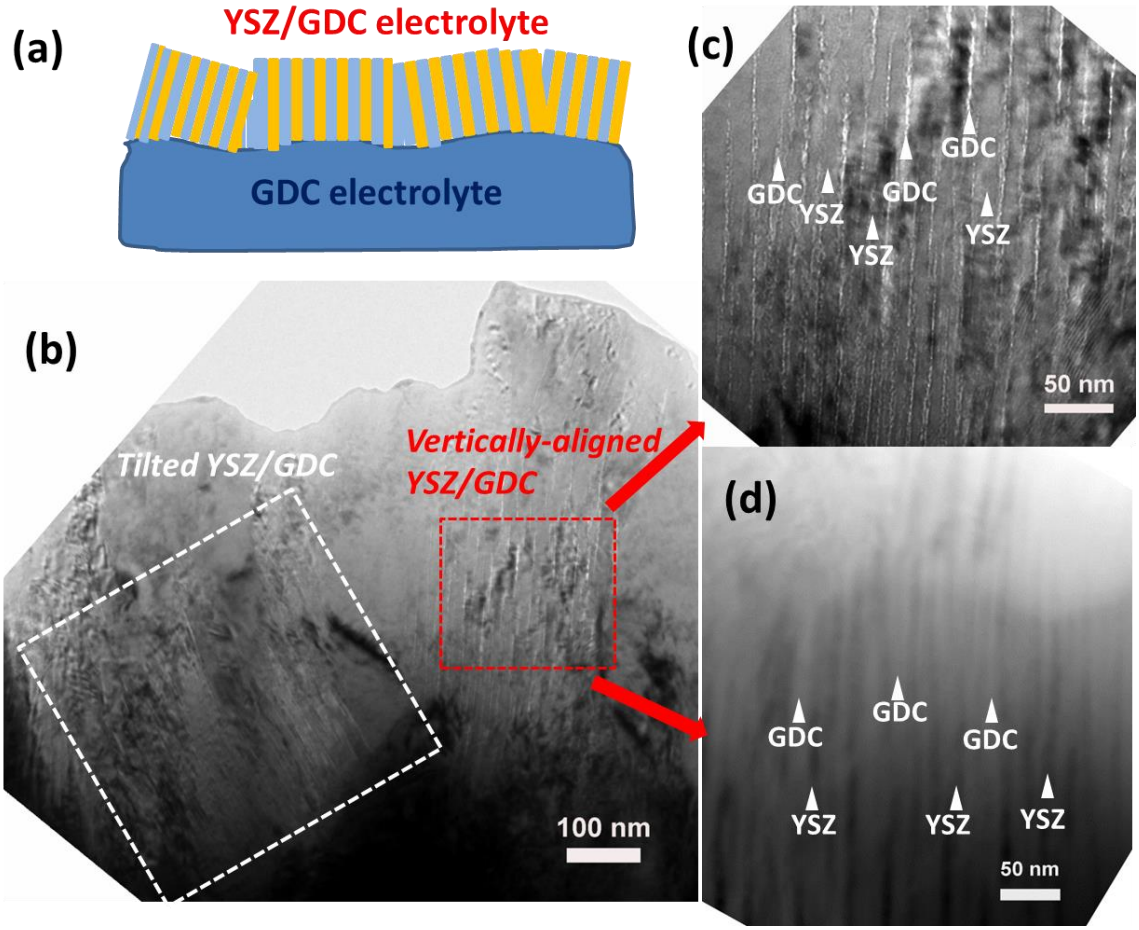

Fig. 6.7. (a) Schematic illustration of YSZ/GDC composite electrolyte coated on polycrystalline substrate, (b) cross-sectional TEM image of YSZ/GDC composite electrolyte coated on polycrystalline substrate showing alternating YSZ and GDC columns either vertical aligned or slightly tilted, (c) high resolution TEM image and (d) STEM image of YSZ/GDC composite electrolyte demonstrating dual-phase electrolyte without formation of solid solution.

A nanoporous LSCO cathode layer has been applied between the electrolyte and screen printed LSCO cathode to improve the electrochemical performance of the cathode layer as well as the overall cell performance and cell integrity. [41, 209]A heating treatment at 1150 ℃ for 2 h is adopted to ensure the adhesion for the screen printed cathode. Concerning the possible formation of CeO_2-ZrO_2 solid solution, there could be some minor Ce^{4+} diffusion into YSZ matrix based on a previous study. [234] However the two phase separation in the YSZ and CGO VAN structure is evident based on TEM, STEM and backscattered SEM images in Fig. 6.3, 6.6 and 6.7, respectively, for the VAN samples grown on STO and polycrystalline substrates. Therefore, it is believed that the diffusion is minor and it does not significantly affect the cell performance.

The current–voltage (I–V) characteristics of the anode-supported single cells with and without the VAN electrolyte were measured using a two-electrode set-up. Pt wires were used as electrical contacts held by Pt paste. The cell performance was measured at the temperatures ranging from 700 to 800 ℃. The cell voltage and power density as a function of current density for the sample without VAN electrolyte is shown in Fig. 6.8a. The open circuit voltage (OCV) is 1.03 V at 700 ℃ and the maximum power densities of the cell are 0.227, 0.376 and 0.571 $W.cm^{-2}$ (highlighted with red arrow) at 700, 750 and 800 ℃, respectively. The overall trend is that the cell potential decreases as a result of the increasing polarization losses across the cell with increasing current density, and the power density also decreases as the operating temperature decreases. The cell with the YSZ/GDC VAN electrolyte applied in the middle of YSZ and GDC electrolyte (i.e., YSZ/VAN/GDC) (Fig. 6.6a) provides an OCV of 1.04 V at

700 ℃ and the maximum power densities of 0.432, 0.623 and 0.783 W.cm^{-2} (highlighted with red arrow) at 700, 750 and 800 ℃, respectively. Compared with the cell without the VAN electrolyte, there is ~40% increase at 800 ℃ for the cells with the VAN electrolyte in middle. There is a further increase for the fuel cell performance with the VAN electrolyte applied on top of the YSZ and GDC bi-layer electrolyte (*i.e.*, YSZ/GDC/VAN) (Fig. 6.6b) which provides an OCV of 1.01 V at 700 ℃ and the maximum power densities of 0.488, 0.694, and 0.883 W cm^{-2} (highlighted with red arrow), at, 700, 750, and 800 ℃, respectively. The possible reason for the further improvement is that the YSZ/GDC VAN electrolyte enhances the oxygen dissociation and surface oxygen exchange rate at the cathode/electrolyte interface.[236] Compared with the cell without the VAN electrolyte, the cells with the VAN electrolyte at the top show ~90% increase in the overall maximum power density at temperature range from 700 to 750 ℃ and ~55% increase at 800 ℃. It is interesting to observe that applying VAN electrolyte benefits more at lower operation temperatures for SOFCs.

Considering the resistivity of YSZ is higher than that of GDC and VAN, a concern was raised on that the overall electrolyte resistance could be dominated by the YSZ layer. However the overall thickness of the electrolyte is ~6 μm while the YSZ layer thickness is ~1.5 μm and the ionic resistance of YSZ is ~4 times higher than GDC at 700 °C. [15] Therefore both GDC and VAN layers (~4.5 μm in total) in the cells still contribute to the overall electrolyte resistivity at the operation temperature range from 700 to 800 ℃. More importantly, the overall cell performance enhancement for the cells with VAN is evident and the trend has been repeated in another identical set of three

cells (with over 30% power density enhancement by applying VAN electrolyte). The performance enhancement is therefore believed to be mainly resulted by that the VAN electrolyte with vertical interfaces provides fast channels for the oxide-ion diffusion and lower migration energy. The possible reason for the enhancement is that the overall electrolyte resistance decreases by applying VAN electrolyte with superior ionic conductivity. In addition, the high ionic conductivity and low oxide-ion migration energy of VAN electrolyte will result in higher oxide-ion concentration in YSZ electrolyte compared with that in conventional YSZ electrolyte. This could also contribute to the enhanced power output for the cells applying VAN electrolyte.

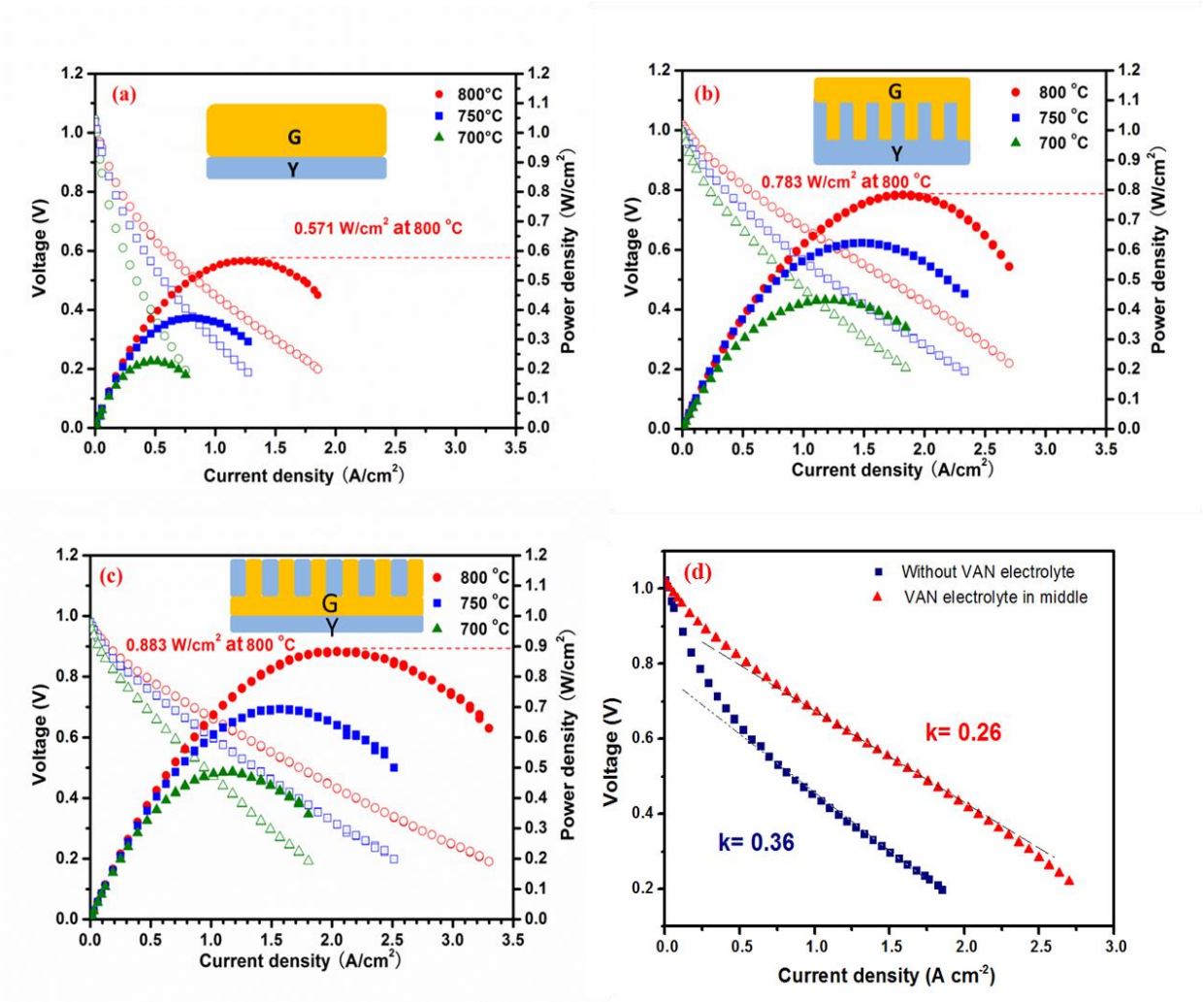

Fig. 6.8. The power densities of single cells a) without VAN, (b) with VAN in middle of the electrolyte and (c) on the top of the electrolyte, demonstrating the enhanced cell performance by applying VAN electrolyte. (d) The V-I curve of the single cells with and without VAN electrolyte at 800 ℃.

To further demonstrate that the power output comes primarily from the electrolyte, the power density data of single cells with VAN electrolyte in middle and without VAN electrolyte at 800 ℃ is plotted and fitted in Fig. 6.8d. At the Ohmic polarization dominated regimes (current density in the range of ~0.5 - ~2 A cm^{-2}), the slope could be treated as the Ohmic resistance of the electrolyte. As seen in Fig. 6.8d, the slope of the electrolyte with VAN in middle is ~30% smaller than that of the conventional single cell with YSZ/GDC bilayer electrolyte. It demonstrates that the improvement is primarily from the electrolyte. Furthermore, the power measurement shows the single cell with YSZ (~1.5 μm) and VAN electrolyte (~4.5 μm) exhibits even higher power density output (for example, 0.957 W cm^{-2} at 800 ℃) than the single cells with VAN electrolyte on top and in middle reported in this work. It is evident that the VAN electrolyte could be applied in real cells and enhances the overall power density.

To preliminarily test the durability of YSZ/GDC VAN electrolyte, the post-measurement cross-sectional backscattered SEM images of the single cells with the VAN electrolyte in the middle of the electrolyte stack as well as the top of the electrolyte stack are shown as Fig. 6.9a and b. No formation of pore or crack is observed and the VAN electrolyte remains its columnar structure after ~ 2-3 days of power measurements at high temperatures indicating the good high temperature stability properties of the YSZ/GDC VAN electrolyte.

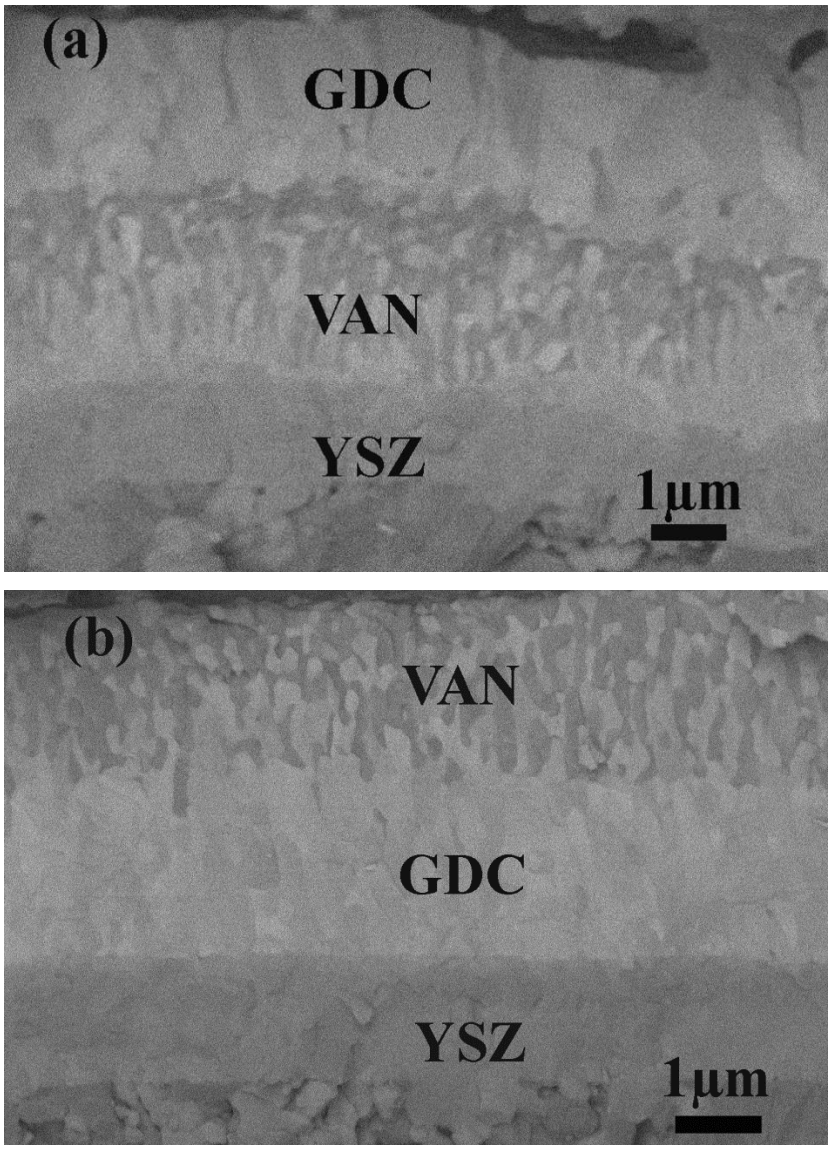

Fig. 6.9. The post measurement backscattered SEM images of single cell with YSZ/GDC VAN electrolyte (a) in the middle and (b) on the top, showing excellent cell integrity after high temperature cell measurement.

6.5. Conclusions

YSZ/GDC VAN electrolyte with vertically aligned nanocolumns have been successfully fabricated by PLD. The ionic conductivity of YSZ/GDC VAN electrolyte appears to be at least 2 times higher than that of single crystal like YSZ thin film and 50% higher than that of single crystal like GDC thin film. As the deposition frequency of the YSZ/GDC VAN electrolyte increases, the interface density increases and the ionic conductivity of YSZ/GDC VAN electrolyte improves. The enhanced oxygen ion conductivity may result from lattice strain near the layer interfaces as well as the fast transport path along the vertical interfaces. The anode-supported single cells with YSZ/GDC VAN electrolyte demonstrated enhanced power performance at all temperatures compared with the cells without the VAN electrolyte. Compared with the cell without the VAN electrolyte, the fuel cells with VAN electrolyte show more than 40% increase in the overall maximum power density. Overall, the results strongly support that the YSZ/GDC VAN electrolyte with vertical aligned interfaces improves the ionic conductivity as well as the overall fuel cell performance. Building vertically aligned interfaces provides a novel approach to achieve enhanced ionic conductivity compared to single phase materials and may improve the performance of other electrochemical devices beyond SOFCs.

7. VERTICALLY ALIGNED NANOCOMPOSITE $La_{0.8}Sr_{0.2}MnO_{3-\delta}/Zr_{0.92}Y_{0.08}O_{1.96}$ THIN FILMS AS ELECTRODE/ELECTROLYTE INTERFACIAL LAYER FOR SOLID OXIDE REVERSIBLE FUEL CELLS

7.1 Overview

A thin layer with a vertically aligned nanocomposite (VAN) structure of $La_{0.8}Sr_{0.2}MnO_{3-\delta}$ (LSM) and $Zr_{0.92}Y_{0.08}O_{1.96}$ (YSZ) between the oxygen electrode and the electrolyte has been fabricated by a pulsed laser deposition (PLD) technique for solid oxide reversible fuel cells (SORFCs). The high quality epitaxial growth of VAN structured LSM/YSZ has been achieved on single crystal $SrTiO_3$ substrate at high-deposition temperatures. The symmetric cells with the VAN interlayer are found to have a lower area specific resistance compared to that without the interlayer. The enhancement in performance has been demonstrated by increased oxygen electrode catalytic properties and porous oxygen electrode microstructure. The cell with the VAN interlayer shows an OCV of 1.00 V at 650 ℃ and maximum power densities of 0.22, 0.32, 0.43 and 0.55 $W{\cdot}cm^{-2}$ at 650, 700, 750 and 800 ℃, respectively. Compared with the cell without an interlayer, the cells with the interlayer have ~2 times of the overall maximum power density at the measured temperature range, demonstrating that the VAN interlayer significantly enhances the oxygen electrode performance.

7.2. Introduction

Because of their high energy conversion efficiency and cost-effectiveness, solid oxide fuel cells (SOFCs) and solid oxide electrolysis cells (SOECs) are considered to be one of the most promising energy conversion and storage devices [5, 9, 237, 238]. SOFCs are electrochemical energy conversion devices directly converting chemical energy in fuel into heat and electricity while SOECs utilizes the heat and electrical power to produce fuel and store energy in other fuel form [4, 238]. Although SOECs and SOFCs have opposite working mechanisms, both have similar cell structure composed of hydrogen electrode, electrolyte and oxygen electrode and the criteria of materials selection are very alike. SOECs and SOFCs therefore can be combined as solid oxide reversible fuel cells (SORFCs) which work in both ways. To lower materials and manufacturing process cost, enhance structural integrity of the cells, extend selection of materials, and increase lifetime of the cells, intermediate operating temperatures (600–800 ℃) are needed to enable their wide applications [1, 3, 13, 14]. However, the oxygen electrode polarization resistance significantly increases at low operating temperatures which becomes one of the major limiting factors in the overall performance of the intermediate temperature SOFCs and SOECs as well as SORFCs.

$La_{0.8}Sr_{0.2}MnO_{3-\delta}/Zr_{0.92}Y_{0.08}O_{1.96}$ (LSM/YSZ) is a widely-studied composite electrode material for SOFCs, SOECs and SORFCs, because of its decent oxygen catalytic property at high operating temperature (800-1000 ℃), high thermal and chemical stability, and relatively good compatibility [239]. It is also treated as a standard electrode material for fundamental research about electrode kinetics and limitation

factors for oxygen reduction reaction [9]. However, due to the insufficient catalytic property and limited length of TPBs at the intermediate temperature range [240, 241], the conventional composite LSM/YSZ cathode did not exhibit desirable performance at this temperature range. Another main issue for LSM/YSZ oxygen electrode is the interfacial electrical and mechanical degradation. Liu *et al.* reported that the interfacial degradation of LSM/YSZ electrode is due to the loss of TPBs length by a reduction in the LSM coverage and formation of secondary phases [161]. In addition, the degradation behavior was investigated by Knibbe *et al.* and they observed that delamination or hole/pore formation along the grain boundaries of YSZ electrolyte close to the LSM/YSZ oxygen electrode under high current densities [162]. The degradation mechanism proposed by Virkar and Chen indicated that insufficient interfacial ionic conductivity between the electrolyte and oxygen electrode causes high internal oxygen pressure. It leads to tensile strain close to the oxygen electrode/electrolyte interface and formation of hole/pores or delamination [163, 164]. Therefore, interface between the electrode and electrolyte where the reactions take place plays a key role on cell performance and durability.

On the other hand, interface modification by implementing new nanostructured interlayer to enhance interface area or by inserting a thin interlayer for lowering the reaction barrier and enhancing the catalytic reaction probability provides intriguing approaches for enhancing cell performance and durability [51, 156]. For example, a nanoporous LSM interlayer prepared by metal-organic deposition was applied between the electrode and electrolyte to not only increase the power density but also long-term

and thermal-cycling stability [143]. A $La_{0.5}Sr_{0.5}CoO_{3-\delta}$ /$Gd_{0.1}Ce_{0.9}O_{1.95}$ vertically aligned nanocomposite (VAN) interlayer has been applied between the cathode and the electrolyte previously [15]. It effectively increases the cathode/electrolyte interface as well as the TPBs, resulting in enhanced power density of the cells. It suggests that the microstructural variations in the electrolyte and the electrode could affect the reaction kinetics of the cell, lower the polarization resistance at the electrode/electrolyte interface, and enhance the power output in SOFCs [41, 49, 95, 157].

In this work, a new binary VAN interlayer consisting of the oxygen electrode material LSM and the electrolyte YSZ is deposited for SOFCs and SOECs. A schematic illustration of the binary LSM/YSZ VAN interlayer is shown in Fig. 7.1. The goal of this work is to enable large electrode/electrolyte interface area using this new VAN structure and to increase the cell performance as well as the mechanical and thermal integrity between the electrode and the electrolyte in single cells. The VAN interlayer will significantly increase the TPBs length and catalytic properties of oxygen electrode. Also, the interfacial ionic conductivity of LSM/YSZ composite electrode could be enhanced by building the VAN microstructure with vertical interfaces which mitigate the delamination issue in SOEC mode [242]. Over all, this new cell structure could take advantage of the increased cathode/electrolyte interfacial area and achieve a much better overall cell performance.

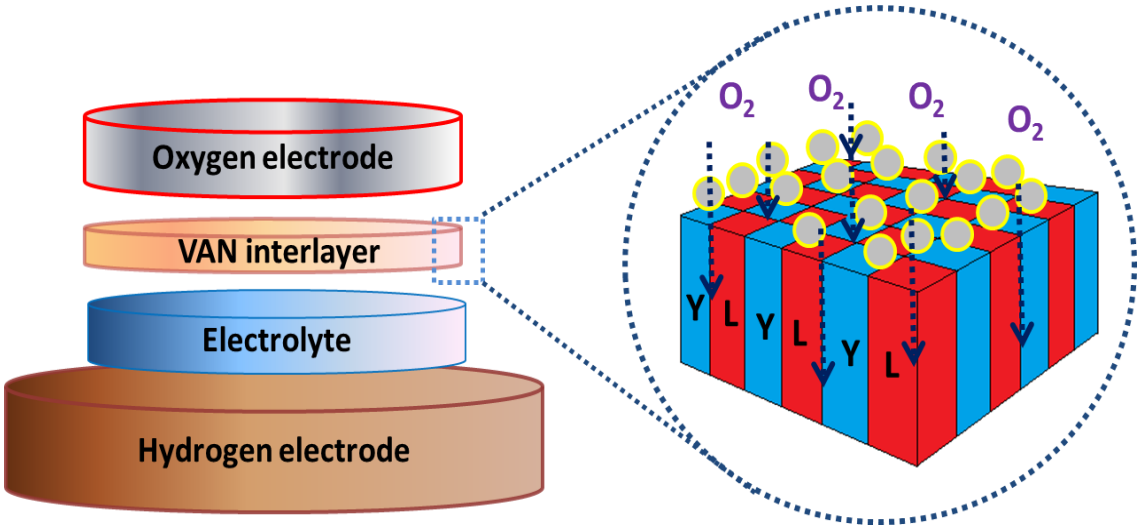

Fig. 7.1. Schematic diagram of an anode supported single cell with VAN interlayer where "L" and "Y" refer, respectively, to LSM and YSZ columns.

7.3. Experimental

7.3.1. LSM Powder and PLD Target Processing

The PLD targets including LSM + YSZ, 8 mol% Yttria stabilized zirconia (YSZ) (500 nm, Tosoh Co.), $Ce_{0.9}Gd_{0.1}O_{1.95}$ (GDC), 60 wt% NiO + 40 wt% YSZ (NiO-YSZ, 500 nm, Praxair Inc.) and YSZ electrolyte disks were all fabricated by solid state reaction through mixing stoichiometric amounts of the raw powders: La_2O_3 (99.99%), $SrCO_3$ (99.9%), Mn_3O_4 (99.9%), CeO_2 (99.9%), Gd_2O_3 (99.9%), and YSZ. The phase purity of LSM and YSZ were confirmed by X-ray diffraction (XRD). The LSM powders for the preparation of screen printing slurry were obtained from the LSM target with pseudo-cubic structure. The LSM target was crushed into powders and then the powders were mixed with YSZ powder and ball milled for 48 h to refine the powder size.

7.3.2. Symmetric Cells and Single Cells Fabrication

The LSM/YSZ VAN interlayer with different thicknesses and vertical interface densities were deposited onto pressed sintered YSZ disks in a PLD system with a KrF excimer laser (Lambda Physik Compex Pro 205, λ=248 nm). The laser beam was focused on the targets at a 45 ° incidence angle with an energy density of approximately 5 $J \cdot cm^{-2}$. The thickness and vertical interface density of the VAN interlayer were controlled by deposition time and laser frequency. In order to fabricate the symmetric cells for impedance measurement, the LSM/YSZ slurry was screen printed onto YSZ substrates coated with and without PLD VAN interlayer, followed by an annealing process at 1100 ℃ for 2 h with a ramping rate of 2 ℃ min^{-1}. The commercial NiO-YSZ cermet powder was pressed into 1 inch (2.54 cm) in diameter anode disks under uniaxial pressure for single cell preparation. The anode substrates were then sintered at 1300 ℃ for 3 h. Subsequently, a bi-layer electrolyte (~1 μm YSZ deposited prior to a ~5 μm GDC layer), a LSM/YSZ VAN interlayer and a screen printed LSM/YSZ oxygen electrode layer were deposited onto a NiO-YSZ anode disk substrate, following the procedure described elsewhere [51, 199].

7.3.3. Microstructural Characterizations

A high resolution field emission scanning electron microscope (FE-SEM, JEM-7500F Cold Emission SEM) and a transmission electron microscope (TEM) (JEOL JEM-2010 and FEI Tecnai G2 F20 operated at 200 kV) were used to characterize the microstructure of these films. Scanning transmission electron microscope (STEM, FEI

Tecnai F20) was conducted with a point-to-point resolution of 0.27 nm. The preparation of cross-sectional TEM samples followed a standard manual grinding and thinning procedure. Then a final polishing step was conducted in a precision ion polishing system (PIPS 691, Gatan).

7.3.4 ASR of Symmetric Cells and Power Density Measurements of Single Cells

Platinum grids, which were gently pressed onto porous electrodes, were used as current collectors, AC impedance spectroscopy measurements were conducted with a potentiostat/impedance analyzer (Reference 600^{TM}, Potentionstat/ Galvanstat/ ZRA, GAMRY INSTRUMENTS) in the frequency range of 10^{-1}–3×10^{5} Hz from 600 to 800 ℃. An awaiting period of an hour for temperature stabilization was adapted for the AC impedance measurements. To evaluate the VAN interlayer effect on the oxygen electrode performance, the anode-supported single cells were prepared with and without then VAN interlayer. During the single-cell performance test, humidified H_2 with a constant flow rate of 80 mL·min^{-1} and air with at a constant flow rate of 120 mL·min^{-1} were supplied as the fuel and the oxidant, respectively. Measurement details can be found elsewhere [199].

7.4. Results and Discussion

A set of LSM/YSZ nanocomposite films were prepared on STO (001) substrates in the temperature range of 500–750 ℃ and with different deposition frequencies. The microstructural characterization of LSM/YSZ thin films was first performed with X-ray

diffraction (XRD). Note that the XRD pattern of LSM/YSZ thin film exhibits excellent crystallinity with the deposition temperature beyond 500 ℃ and there is no significant difference for those thin films deposited with different frequencies. Fig. 7.2 shows the typical XRD patterns of the LSM/YSZ nanocomposite films deposited at 700 ℃ with a thickness of ~ 150 nm. The LSM phase exhibits highly textured growth along (0 0 2) orientation while the YSZ phase shows (1 0 2) out-of-plane orientation matching to minimize the strain energy. In addition, the strain state of LSM phase in LSM/YSZ nanocomposite film has a 2.3% tensile stress along the out-of-plane direction based on the calculated lattice parameter of 0.396 nm (the bulk parameter of LSM is c = 0.387 nm). This suggests that a further tensile stress is introduced by the YSZ secondary phase.

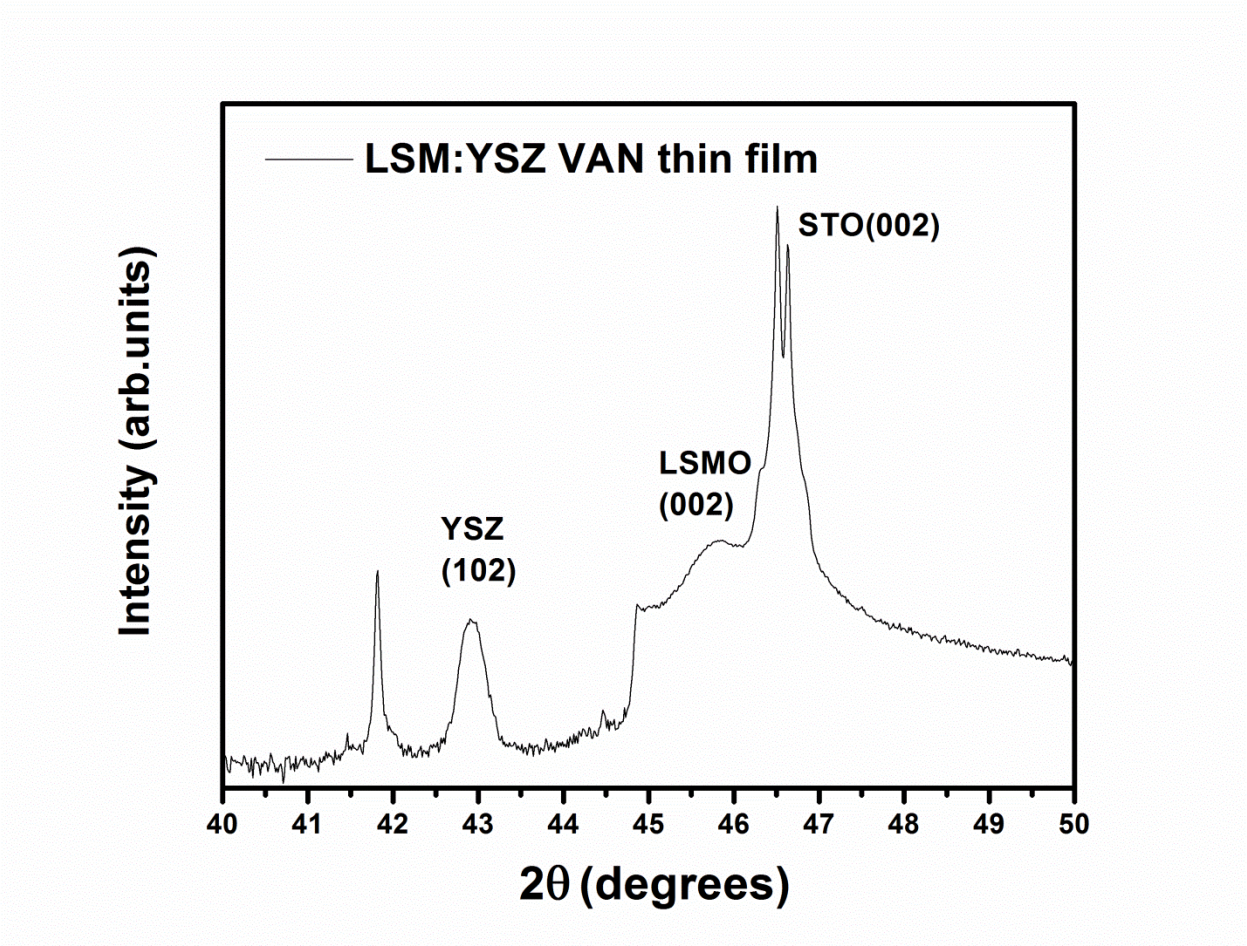

Fig. 2. XRD pattern of LSM/YSZ composite film deposited at 700 ℃.

High resolution cross-sectional TEM image of the LSM/YSZ thin films is shown in Fig. 7.3a. The film deposited at 700 ℃ shows alternating columns of LSM and YSZ indicating a typical VAN structure with excellent epitaxial quality. To confirm that LSM and YSZ grow as alternate columns without intermixing, the STEM images were taken under high angle annular dark field (HAADF) mode (also called Z contract images) where the contrast is proportional to approximately square of atomic weight ($\sim Z^2$). One

such image in Fig. 7.3b shows well-aligned vertical columns with the different contrasts from the LSM (brighter contrast) and YSZ (darker contrast) columns, which is consistent with the TEM observations. The average column width for LSM and YSZ is ~6 and ~4 nm, respectively. It demonstrates vertically aligned alternating LSM and YSZ columns without obvious intermixing.

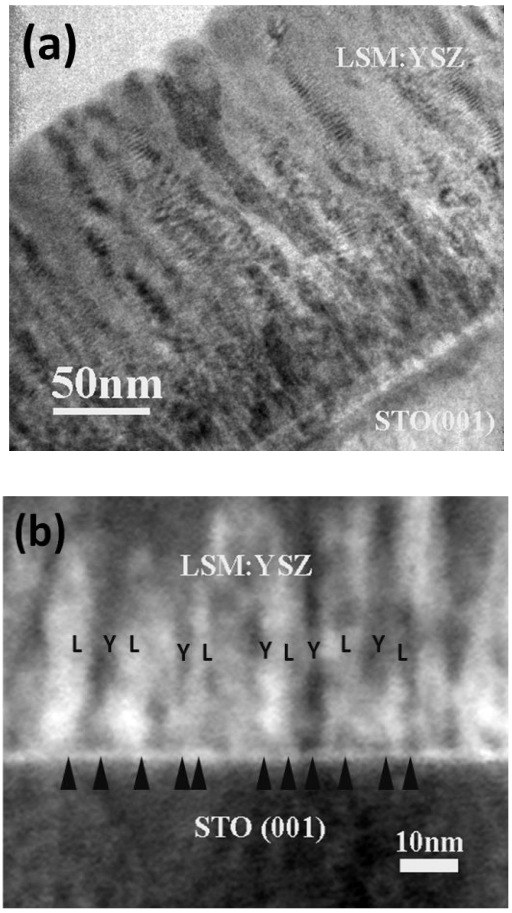

Fig. 7.3. (a) The cross-sectional TEM images for the LSM/YSZ nanocomposite films on STO (001) deposited at 10 Hz. (b) The cross-sectional STEM images of LSM and YSZ nanocomposite thin film.

The plan-view SEM of screen printed LSM/YSZ oxygen electrode films with and without VAN interlayer were characterized to examine the interlayer effect on the microstructure of the LSM/YSZ oxygen electrode films, as shown in Fig. 7.4a and b. Compared with the LSM/YSZ screen-printed only films (Fig. 7.4b), the LSM/YSZ films prepared with the VAN interlayer as seen in Fig. 7.4a shows smaller grains with more porous microstructure indicating that the interlayer could significantly enhance the nucleation sites of the screen-printed layer. This interlayer effect has also been demonstrated by our previous work [13, 41] and it results in good grain connectivity between the electrolyte and oxygen electrode films.

To measure the electrochemical performance of the LSM/YSZ screen printed oxygen electrodes with and without the VAN interlayer, corresponding symmetric cells were prepared. These results were evaluated using the equivalent circuit shown in Fig. 7.5a. In this model, the intercepts of the impedance arcs with the real axis at high frequencies correspond to the resistance of the electrolyte R_0 and L was the inductance of Pt wires. (R1, CPE1), (R2, CPE2) and (R3, CPE3) represent the resistance from high-frequency, medium-frequency, and low-frequency arc, respectively.

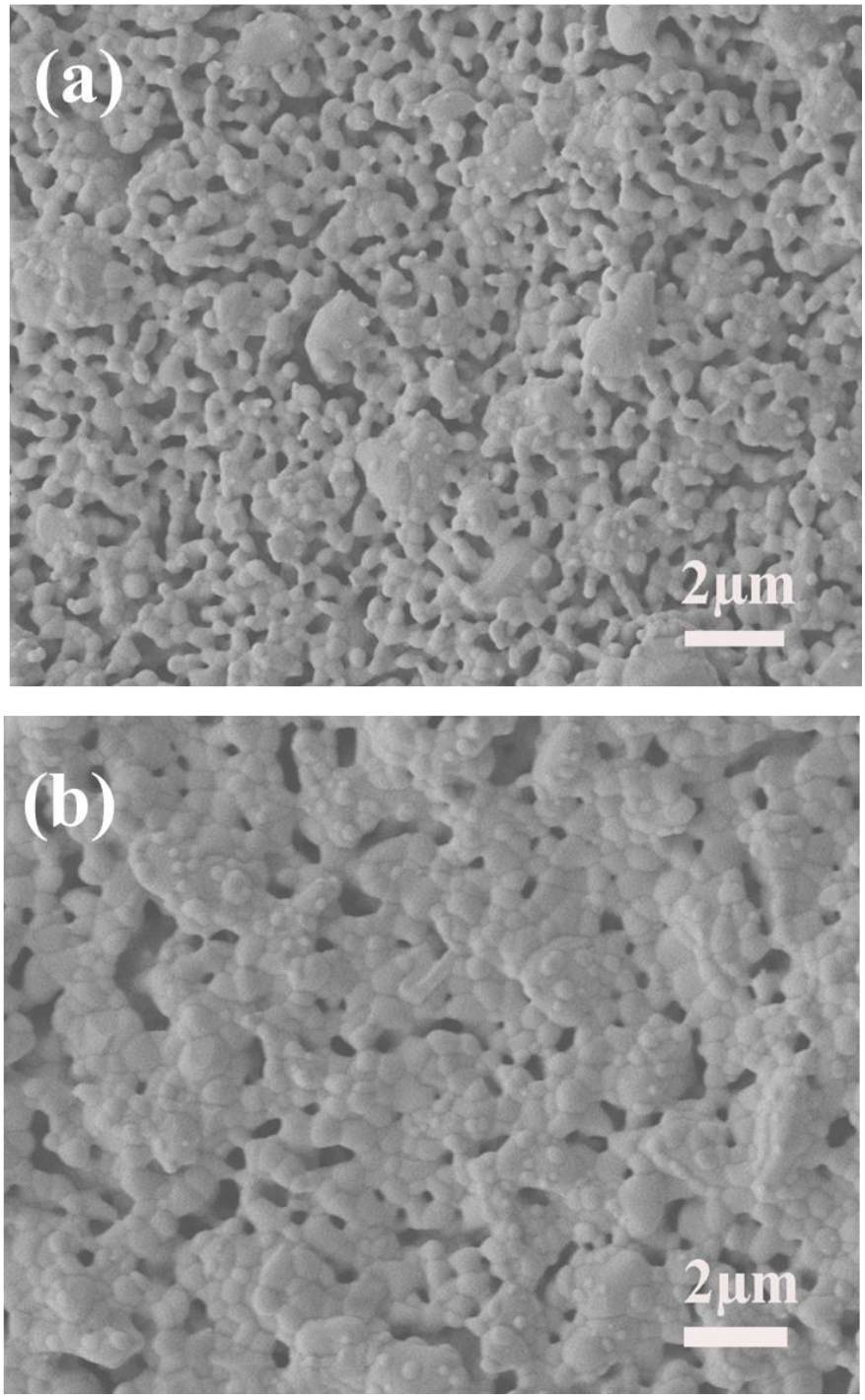

Fig. 7.4. Plan-view SEM images of the screen printing LSM/YSZ cathode (a) with and (b) without VAN interlayer.

In the fitting, a constant phase element (CPE) is used to study the inhomogeneous porous electrode/electrolyte systems for exact fitting results. As shown in Fig. 5b, investigations on the LSM/YSZ electrode with and without the VAN interlayer revealed three separable arcs with characteristic frequency, in good agreement with the low, medium and high frequency peaks, respectively. The high frequency arc, which is not dependent on pO_2, was attributed to O^{2-} transfer from the YSZ to the TPB electrolyte near the YSZ–LSM/YSZ interfaces [239]. In addition, the medium frequency arc with characteristic frequency of 10–100 Hz was ascribed to dissociative adsorption/desorption of O_2 and transfer of species across the TPB. Moreover, the low frequency arc was corresponding to O_2 gas diffusion [94, 239, 243]. The fitting results (seen as the inset table in Fig. 7.5b) show that R2 and R3 decrease with inserting the LSM/YSZ VAN interlayers while R1 is almost the same. Considering R1 was attributed to O^{2-} transfer from the YSZ to the TPB electrolyte, the similar R1 value suggests that the VAN interlayer does not significantly affect the O^{2-} transfer process. The decrease in R2 indicates that the LSM/YSZ VAN interlayer expands the TPBs length of the screen printed LSM/YSZ oxygen electrode and enhances the oxygen electrode catalytic property. In addition, the VAN interlayer enhances the nucleation sites for screen printing LSM/YSZ oxygen electrode, resulting in more porous microstructure and decreases the diffusion barrier (R3) for LSM/YSZ oxygen electrode.

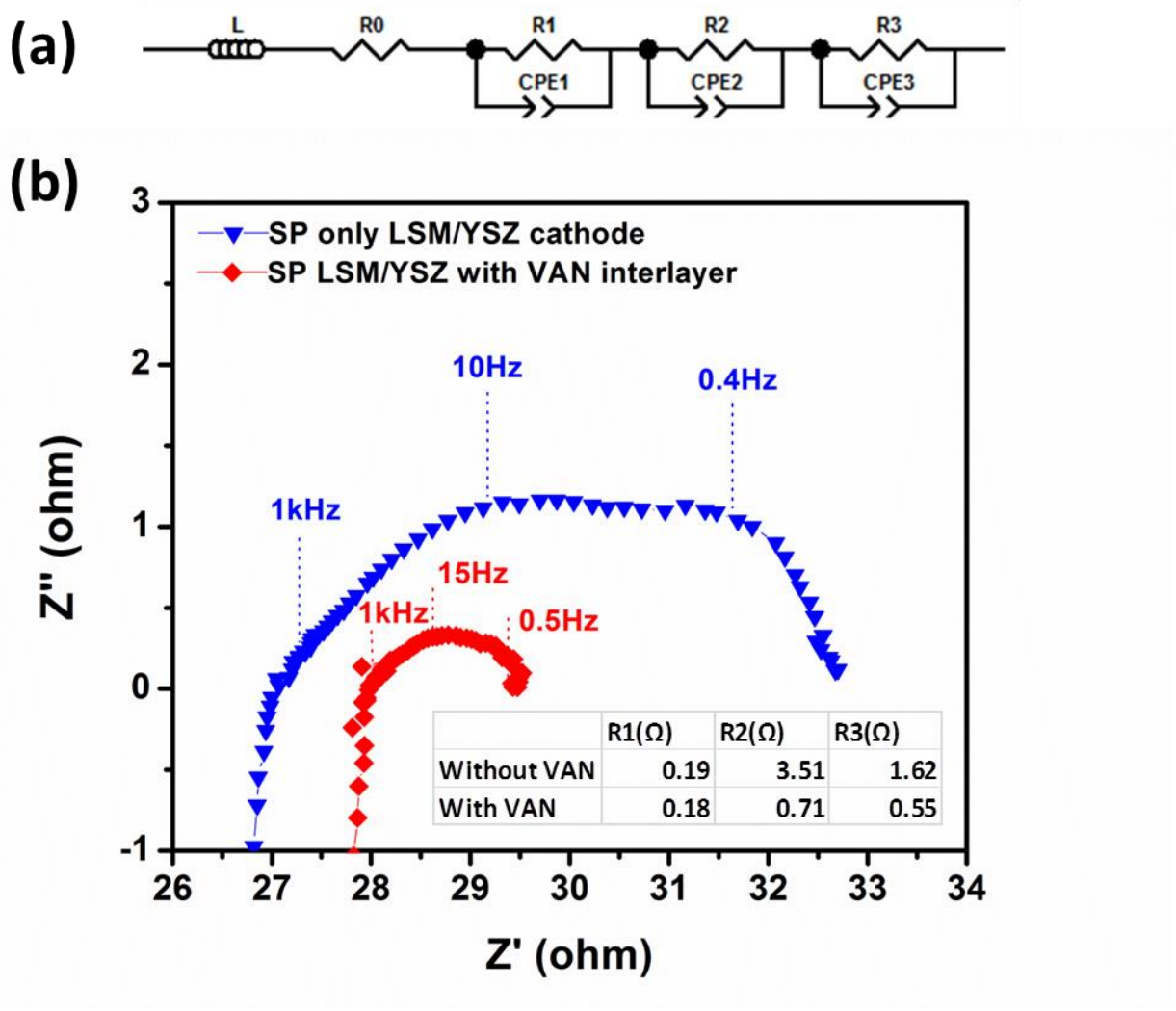

Fig. 7.5. (a) The equivalent circuit model used to fit the impedance data and (b) the typical impedance plot the LSM/YSZ cathode with and without VAN interlayer at 700 ℃ showing the enhanced electrochemical performance for cathode with VAN. The inset table lists fitting results for the LSM/YSZ cathode with and without VAN interlayer.

The polarization resistance (Rp) is defined as Rp = R1 + R2 + R3. The following equation (7.1) is used to calculate the area specific resistance (ASR):

$$ASR = R_p * A/2, \quad (7.1)$$

where Rp is the electrode polarization resistance and A is the geometric electrode area. An Arrhenius plot of ASR as a function of temperature for the oxygen electrode layers with and without the LSM/YSZ VAN interlayer is plotted in Fig. 7.6, where the calculation was based on the AC impedance data under air in the temperature range of 600–800 ℃. As shown in Fig. 7.6, the ASR of the cell with VAN interlayers shows ~ two times lower value in comparison to the results obtained for the cell without the interlayer. For example, the cell without the VAN interlayer has a higher ASR (0.98 $\Omega \cdot cm^{-2}$) than that with the interlayer (0.35 $\Omega \cdot cm^{-2}$) at 700 ℃. Therefore, the incorporation of the VAN LSM/YSZ interlayer between screen printed LSM/YSZ oxygen electrode and electrolyte can affect the total oxygen electrode polarization with increasing effective area of the TPBs. It results in improving the catalytic reaction probability at the gas–oxygen electrode–electrolyte TPBs. Accordingly, a decrease of the ASR of the oxygen electrode could lead to better performance in thin-film SOFCs. It is interesting to notice that the screen printed LSM/YSZ oxygen electrode with the VAN interlayer deposited at higher frequency (10 Hz) shows slightly lower ASR than that with the VAN interlayer deposited at lower frequency (2 Hz). Considering that the higher vertical interfacial density of the VAN interlayer will be achieved by deposited at higher frequency, the result suggests that the vertical interfaces may enhance the TPBs length or the oxide-ion incorporation kinetics.[244] For the screen printed LSM/YSZ

oxygen electrodes with the VAN interlayer thickness ranges from ~50 to 150 nm, there is no significant difference in ASR, indicating that the VAN interface property plays a dominant role for oxygen reaction kinetics and porous oxygen electrode microstructure.

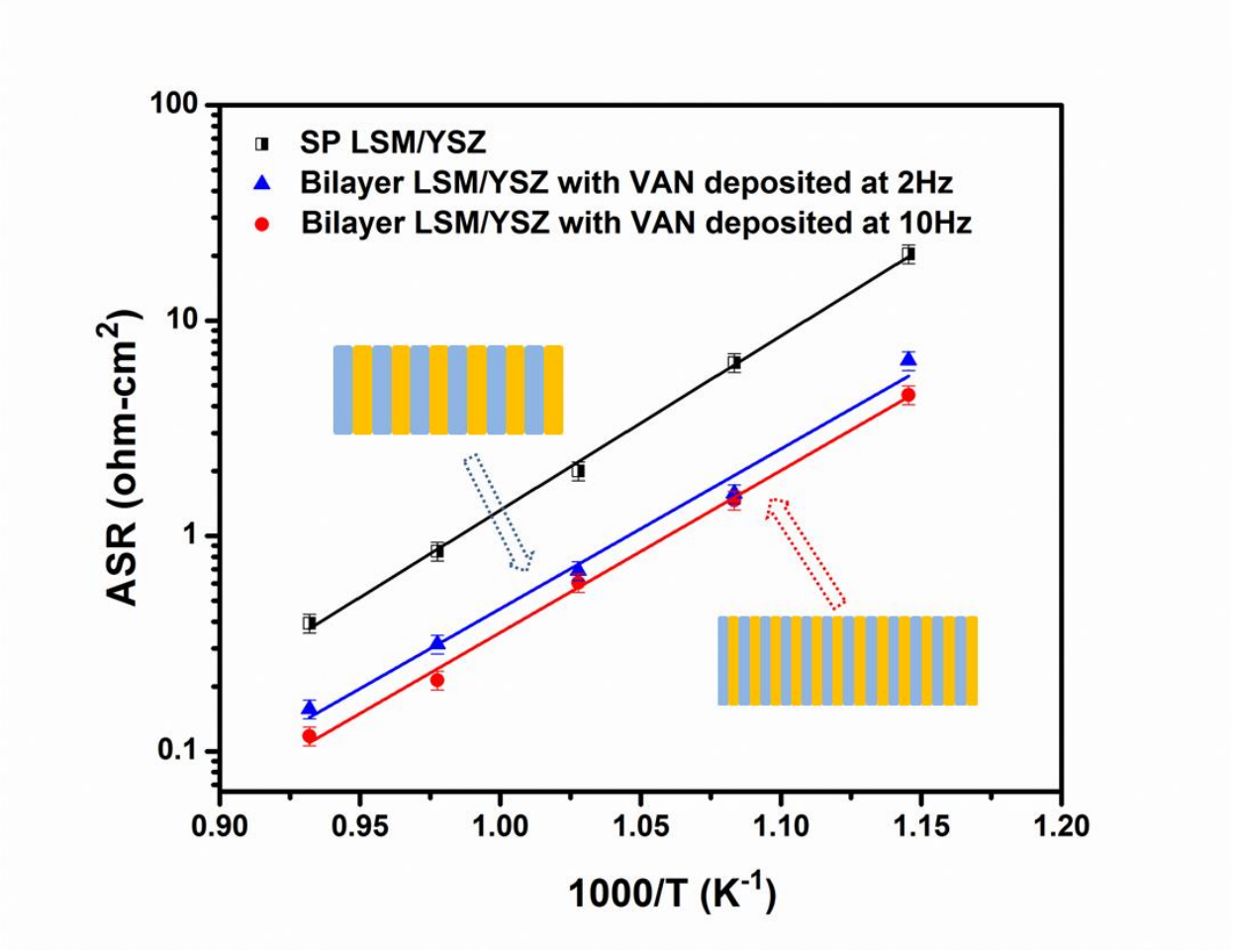

Fig. 7.6. An Arrhenius plot of ASR of LSM/YSZ cathode with and without VAN interlayers as a function of temperature.

To demonstrate the LSM/YSZ VAN interlayer effect on the overall cell performance, anode-supported single cells with and without the VAN interlayers were prepared. The single cell with interlayer thickness of ~100 nm was selected to ensure the enhancement is observable. The current–voltage (I–V) characteristics of the anode-supported single cells were measured by a two-electrode set-up where Pt wires were used as electrical contacts held by Pt paste. The performance was measured at the temperatures ranging from 650 to 800 ^{o}C. The cell voltage and power density as a function of current density for the sample without PLD interlayer is shown in Fig. 7.7a. The open circuit voltage (OCV) is 0.99 V at 650 ^{o}C, and the maximum power densities of the cell are 0.10, 0.16, 0.22 and 0.30 $W{\cdot}cm^{-2}$ (highlighted with a red arrow) at 650, 700, 750 and 800 ℃, respectively. The overall trend is that the power density decreases as the measurement temperature decreases, and the cell potential also decreases as a result of the increasing polarization losses across the cell with increasing current density. The cell with the PLD interlayer provides an OCV of 1.00 V at 650 ℃ and the maximum power densities of 0.22, 0.32, 0.43 and 0.55 $W{\cdot}cm^{-2}$ (highlighted with a red arrow) at 650, 700, 750 and 800 ℃, respectively. Compared with the cell without an interlayer, the cells with the interlayer have ~two times of the overall maximum power density at the measured temperature range, demonstrating that the VAN interlayer significantly enhances the oxygen electrode performance.

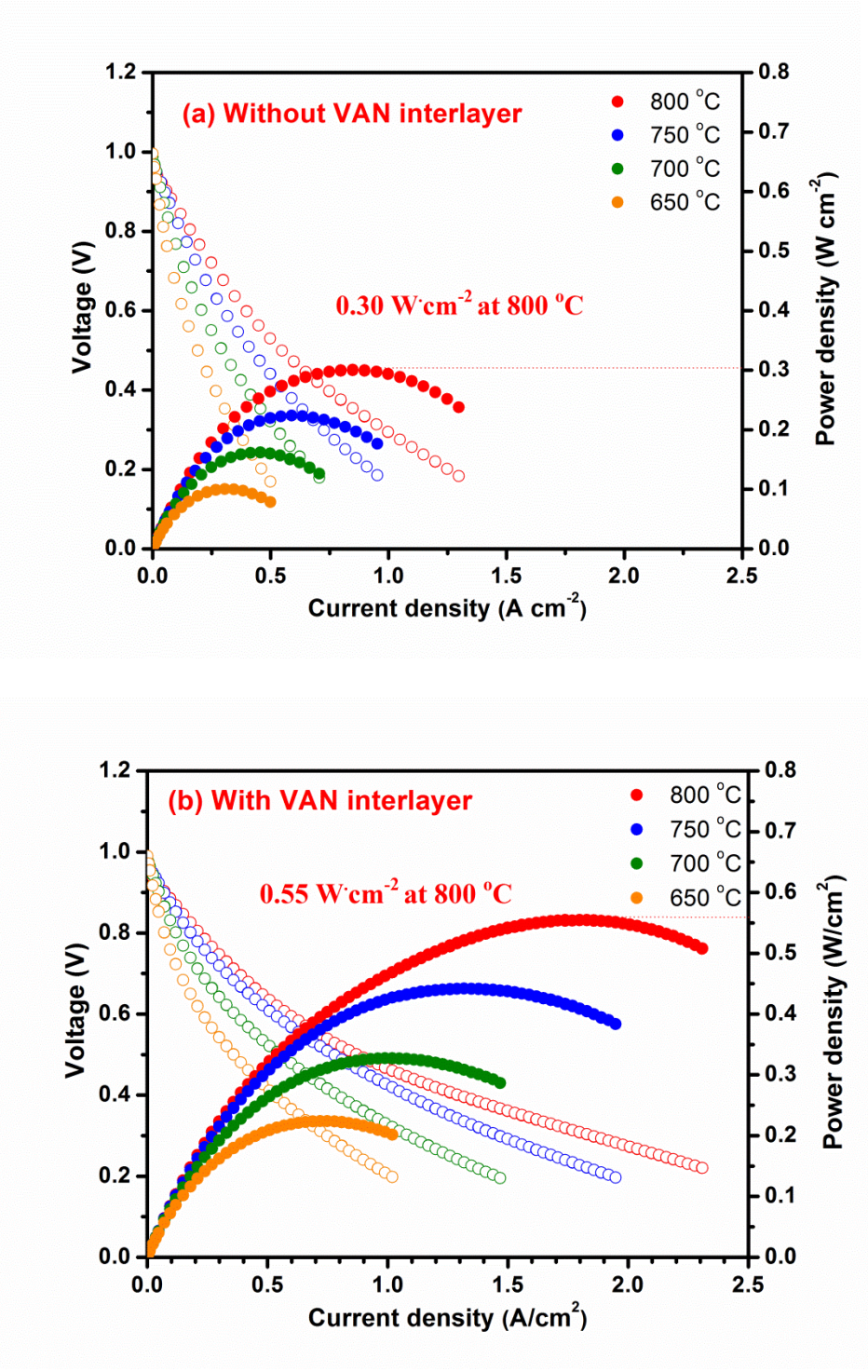

Fig. 7.7. I–V curve of the anode-supported single cells (a) without and (b) with the LSM/YSZ interlayer at different temperatures of 650 ~ 800 ℃.

Fig. 7.8 shows the post-measurement cross-sectional SEM image of the anode-supported single cell with the VAN interlayer. The YSZ/GDC bilayer electrolyte shows a fully dense structure with an obvious interface between the YSZ and GDC layers in the cell and the LSM/YSZ oxygen electrode and NiO–YSZ anode exhibits a porous structure with uniform pore distribution. It is evident that there is no crack or delamination issue observed at the interfaces in between the oxygen electrode, interlayer, and electrolyte thin film layers. This result suggests that besides the power density enhancement demonstrated in the cells with a VAN interlayer, the LSM/YSZ interlayer acts as an effective transition layer and improves the adhesion properties between the oxygen electrode and electrolyte and mitigates thermal stress. It could lead to a longer lifetime and better cycle-ability for the cells under thermal cycles [143] Also, by building the VAN interlayer between the electrode and electrolyte, it might enhance the oxide-ion transport across the electrode/electrolyte interface so as to avoid or lessen the delamination issue of the LSM/YSZ electrode in solid oxide electrolysis cell [162-164].

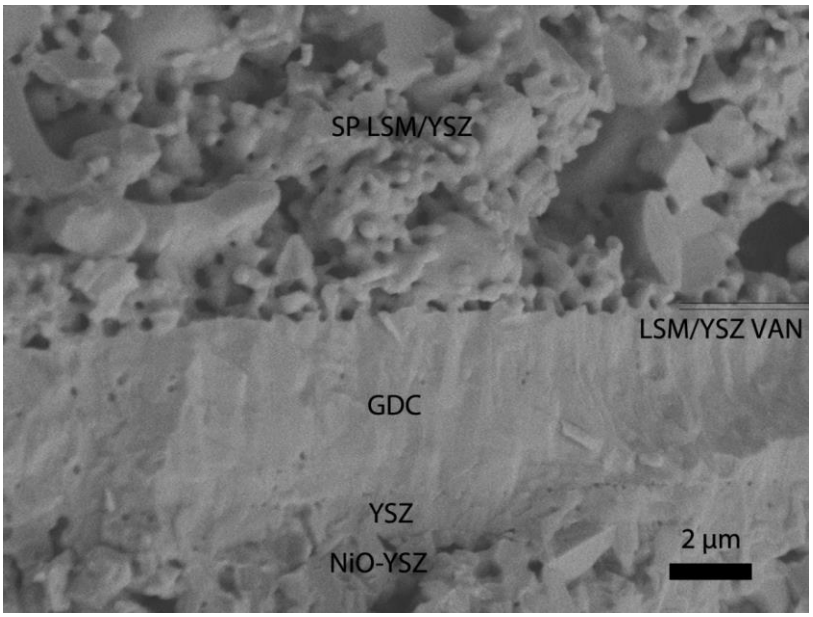

Fig. 7.8. The after-measurement cross-sectional SEM images of LSM/YSZ cathode with VAN interlayer.

7.5. Conclusions

In summary, LSM/YSZ VAN with vertically aligned nanocolumns have been successfully fabricated by PLD. The VAN layer has been inserted between conventional screen-printed LSM/YSZ oxygen electrode and electrolyte. Compared with screen printed LSM/YSZ oxygen electrode without the VAN interlayer, the oxygen electrode with the VAN interlayer shows much higher film porosity with smaller grains and more uniform pore structures. The ASR of oxygen electrode with VAN interlayer is about 2 times lower than that of the oxygen electrode without the VAN. There is no obvious interlayer thickness-dependent effect on ASR with the thickness range from ~50 to 150 nm. However, the vertical interface density of VAN did play a positive role on the oxygen reduction kinetics. The anode-supported single cells with the VAN interlayers demonstrated enhanced power performance at all temperatures compared with the cells without the interlayer. The cell with the VAN interlayer provides an OCV of 1.00 V at 650 ℃ and the maximum power densities of 0.22, 0.32, 0.43 and 0.55 $W \cdot cm^{-2}$ at 650, 700, 750 and 800 ℃, respectively. Compared with the cell without an interlayer, the cells with the interlayer have ~ two times of the overall maximum power density at the measured temperature range, which demonstrates that the VAN interlayer significantly enhances the oxygen electrode performance. Overall, the results strongly support that the thin VAN interlayer improves the electrochemical performance of the oxygen electrode layer as well as the overall cell performance and cell integrity.

8. SUMMARY AND CONCLUSIONS

Designing nanoengineered thin films of bi-layer LSCO cathode, LSM:YSZ oxygen electrode, YSZ/GDC VAN electrolyte have been demonstrated and reaction mechanism of bi-layer LSCO cathode has been investigated for solid oxide fuel cells.

First, the bi-layer cathodes have been successfully fabricated by combining the PLD and screen printing methods. Compared with the screen printing LSCO layer directly on CGO electrolyte, the LSCO layer with PLD seed layer has higher film density with uniform nanopore structures, better mechanical properties and higher thermal stability. The ASR of these bi-layer cathodes is ~5 times lower than that of the single layer cathode because of the desired microstructure of the PLD seed layer. The PLD seed layer could also enhance the catalytic reaction probability at the gas-cathode-electrolyte TPBs by increasing the effective areas. It could provide better adhesion between the electrolyte and the screen printing cathode layer. The hybrid method combines the advantages of both PLD and screen printing techniques and offers a cost-effective approach in fabricating thick and high quality cathode films.

Second, bi-layer cathodes with different PLD interlayer thicknesses have been successfully fabricated by combining PLD with the screen printing method. Compared with layers of screen printed LSCO directly onto a CGO electrolyte, the LSCO layers with a thin PLD interlayer (< 50 nm) shows moderate grain size and enhanced film porosity, while the LSCO layers with a thick PLD interlayer (thickness ≥1 00 nm) have much higher film porosity with small grains and uniform pore structures. The

mechanical and electrochemical measurement results of those cathodes agree well with the microstructure analysis. The anode-supported single cells with PLD interlayers demonstrated enhanced power performance at all temperatures compared with the cells without the interlayer. There is a 50 % enhancement in power density in the temperature range from 650 to 700 ℃ and ~ 30% increase at 800 ℃. Overall, the results strongly support that the thin PLD interlayer improves the electrochemical performance of the cathode layer as well as the overall cell performance and cell integrity.

Third, the electrochemical properties of LSCO cathode with and without nanoporous LSCO interlayer were studied with ac impedance spectroscopy under controlled temperature and pO_2 conditions. Two reaction steps, i.e., the gas phase oxygen exchange at the electrode surface and oxygen mass transfer, are co-limited the electrode kinetic performance. A corresponding equivalent circuit model is proposed to interpret the observed impedance spectra. The oxygen chemical surface exchange resistance decreases as a function of temperature and interlayer thickness. The surface exchange resistance decreases as interlayer thickness increases which is due to the increased activated reaction sites. The activated reaction sites of cathodes with the LSCO interlayer (>100 nm thickness) is ~2 times of the cathode without interlayer resulting in the enhancement of the cathode performance. Thicker LSCO interlayer results in more reaction sites in the cathode. The oxygen mass transfer resistance also decreases because of more porous microstructure of the cathode with PLD interlayer.

Fourth, YSZ/GDC VAN electrolyte with vertically aligned nanocolumns have been successfully fabricated by PLD. The ionic conductivity of YSZ/GDC VAN

electrolyte appears to be at least 2 times higher than that of single crystal like YSZ thin film and 50% higher than that of single crystal like GDC thin film. The enhanced oxygen ion conductivity may result from lattice strain near the layer interfaces as well as the fast transport path along the vertical interfaces. Compared with the cell without the VAN electrolyte, the fuel cells with VAN electrolyte show more than 40% increase in the overall maximum power density. Overall, the results strongly support that the YSZ/GDC VAN electrolyte with vertical aligned interfaces improves the ionic conductivity as well as the overall fuel cell performance. Building vertically aligned interfaces provides a novel approach to achieve enhanced ionic conductivity compared to single phase materials and may improve the performance of other electrochemical devices beyond SOFCs.

Fifth, LSM/YSZ VAN with vertically aligned nanocolumns have been successfully fabricated by PLD. The VAN layer has been inserted between conventional screen-printed LSM/YSZ oxygen electrode and electrolyte. Compared with screen printed LSM/YSZ oxygen electrode without the VAN interlayer, the oxygen electrode with the VAN interlayer shows much higher film porosity with smaller grains and more uniform pore structures. The ASR of oxygen electrode with VAN interlayer is about 2 times lower than that of the oxygen electrode without the VAN. There is no obvious interlayer thickness-dependent effect on ASR with the thickness range from ~50 to 150 nm. However, the vertical interface density of VAN did play a positive role on the oxygen reduction kinetics. The anode-supported single cells with the VAN interlayers demonstrated enhanced power performance at all temperatures compared with the cells

without the interlayer, which demonstrates that the VAN interlayer significantly enhances the oxygen electrode performance.

The future work could focus on fundamental understanding of the growth mechanism of the binary VAN structure and development of devices based on VAN structure.

REFERENCES

[1] A.B. Stambouli, E. Traversa, Renewable and Sustainable Energy Reviews, 6 (2002) 433-455.

[2] S.M. Haile, Acta Materialia, 51 (2003) 5981-6000.

[3] B.C.H. Steele, A. Heinzel, Nature, 414 (2001) 345-352.

[4] S.C. Singhal, Solid State Ionics, 135 (2000) 305-313.

[5] N.Q. Minh, Journal of the American Ceramic Society, 76 (1993) 563-588.

[6] M. Kuzmenko, N. Poryadchenko, Nato Sci Ser Ii Math, 202 (2005) 253-258.

[7] S. Ahmed, M. Krumpelt, International Journal of Hydrogen Energy, 26 (2001) 291-301.

[8] J. Padullés, G.W. Ault, J.R. McDonald, J Power Sources, 86 (2000) 495-500.

[9] S.B. Adler, Chem Rev, 104 (2004) 4791-4843.

[10] W. Nernst; Z. Elektrochem., 6 (1899), p. 41

[11] Fuel Cell Handbook (7th ed.), Tech. Rep. DOE/NETL 2004/1206, National Energy Technology Laboratory, Morgantown, WV 2004. (http://www.netl.doe.gov).

[12] G. Hoogers, Fuel Cell Technology Handbook, CRC, Boca Raton, FL 2003.

[13] Q. Su, S.M. Cho, Z.X. Bi, A.P. Chen, H.Y. Wang, Electrochim Acta, 56 (2011) 3969-3974.

[14] A. Hauch, S.H. Jensen, S. Ramousse, M. Mogensen, J Electrochem Soc, 153 (2006) A1741-A1747.

[15] A. Negishi, K. Nozaki, T. Ozawa, Solid State Ionics, 3–4 (1981) 443-446.

[16] S. de Souza, S.J. Visco, L.C. De Jonghe, Solid State Ionics, 98 (1997) 57-61.

[17] J. Will, A. Mitterdorfer, C. Kleinlogel, D. Perednis, L.J. Gauckler, Solid State Ionics, 131 (2000) 79-96.

[18] P.J. Kelly, R.D. Arnell, Vacuum, 56 (2000) 159-172.

[19] T.W. Kueper, S.J. Visco, L.C. De Jonghe, Solid State Ionics, 52 (1992) 251-259.

[20] N.M. Sammes, Y. Du, R. Bove, J Power Sources, 145 (2005) 428-434.

[21] S. Sameshima, T. Ichikawa, M. Kawaminami, Y. Hirata, Materials Chemistry and Physics, 61 (1999) 31-35.

[22] A.J. Jacobson, Chem Mater, 22 (2010) 660-674.

[23] J.B. Goodenough, Y.-H. Huang, J Power Sources, 173 (2007) 1-10.

[24] J.W. Fergus, Solid State Ionics, 177 (2006) 1529-1541.

[25] C. Sun, U. Stimming, J Power Sources, 171 (2007) 247-260.

[26] S.P. Jiang, S.H. Chan, J Mater Sci, 39 (2004) 4405-4439.

[27] C.W. Keep, R.T.K. Baker, J.A. France, Journal of Catalysis, 47 (1977) 232-238.

[28] E.P. Murray, T. Tsai, S.A. Barnett, Nature, 400 (1999) 649-651.

[29] S.D. Park, J.M. Vohs, R.J. Gorte, Nature, 404 (2000) 265-267.

[30] H. Kim, C. Lu, W.L. Worrell, J.M. Vohs, R.J. Gorte, J Electrochem Soc, 149 (2002) A247-A250.

[31] Y.H. Huang, R.I. Dass, Z.L. Xing, J.B. Goodenough, Science, 312 (2006) 254-257.

[32] R. Mukundan, E.L. Brosha, F.H. Garzon, Electrochem Solid St, 7 (2004) A5-A7.

[33] A. Lashtabeg, S.J. Skinner, J Mater Chem, 16 (2006) 3161-3170.

[34] P.N. Huang, A. Petric, J Electrochem Soc, 143 (1996) 1644-1648.

[35] B.C.H. Steele, J Mater Sci, 36 (2001) 1053-1068.

[36] K.Q. Huang, R.S. Tichy, J.B. Goodenough, Journal of the American Ceramic Society, 81 (1998) 2565-2575.

[37] K.Q. Huang, R.S. Tichy, J.B. Goodenough, Journal of the American Ceramic Society, 81 (1998) 2576-2580.

[38] T. Ishihara, H. Matsuda, Y. Takita, J Am Chem Soc, 116 (1994) 3801-3803.

[39] K. Eguchi, T. Setoguchi, T. Inoue, H. Arai, Solid State Ionics, 52 (1992) 165-172.

[40] H. Inaba, H. Tagawa, Solid State Ionics, 83 (1996) 1-16.

[41] Q. Su, D. Yoon, Y.N. Kim, W. Gong, A. Chen, S. Cho, A. Manthiram, A.J. Jacobson, H. Wang, Journal of Power Sources, 218 (2012) 261-267.

[42] E.P. Murray, T. Tsai, S.A. Barnett, Solid State Ionics, 110 (1998) 235-243.

[43] I. Yasuda, K. Ogasawara, M. Hishinuma, T. Kawada, M. Dokiya, Solid State Ionics, 86–88, Part 2 (1996) 1197-1201.

[44] Y. Huang, J.M. Vohs, R.J. Gorte, J Electrochem Soc, 152 (2005) A1347-A1353.

[45] C.W. Sun, R. Hui, J. Roller, J Solid State Electr, 14 (2010) 1125-1144.

[46] F.C. Krebs, Sol Energ Mat Sol C, 93 (2009) 394-412.

[47] W.F. Chu, Solid State Ionics, 52 (1992) 243-248.

[48] D. Burnat, P. Ried, P. Holtappels, A. Heel, T. Graule, D. Kata, Fuel Cells, 10 (2010) 156-165.

[49] E. Koep, C. Jin, M. Haluska, R. Das, R. Narayan, K. Sandhage, R. Snyder, M. Liu, J Power Sources, 161 (2006) 250-255.

[50] J. Yoon, R. Araujo, N. Grunbaum, L. Baque, A. Serquis, A. Caneiro, X.H. Zhang, H.Y. Wang, Appl Surf Sci, 254 (2007) 266-269.

[51] J. Yoon, S. Cho, J.H. Kim, J. Lee, Z.X. Bi, A. Serquis, X.H. Zhang, A. Manthiram, H.Y. Wang, Advanced Functional Materials, 19 (2009) 3868-3873.

[52] E.D. Wachsman, K.T. Lee, Science, 334 (2011) 935-939.

[53] S.Q. Hui, J. Roller, S. Yick, X. Zhang, C. Deces-Petit, Y.S. Xie, R. Maric, D. Ghosh, J Power Sources, 172 (2007) 493-502.

[54] J.B. Goodenough, Annu Rev Mater Res, 33 (2003) 91-128.

[55] J.B. Goodenough, Nature, 404 (2000) 821-823.

[56] S.P.S. Badwal, F.T. Ciacchi, D. Milosevic, Solid State Ionics, 136–137 (2000) 91-99.

[57] G. Xu, Y.-W. Zhang, C.-S. Liao, C.-H. Yan, Solid State Ionics, 166 (2004) 391-396.

[58] Y. Arachi, H. Sakai, O. Yamamoto, Y. Takeda, N. Imanishai, Solid State Ionics, 121 (1999) 133-139.

[59] T.I. Politova, J.T.S. Irvine, Solid State Ionics, 168 (2004) 153-165.

[60] T. Ishihara, J. Tabuchi, S. Ishikawa, J. Yan, M. Enoki, H. Matsumoto, Solid State Ionics, 177 (2006) 1949-1953.

[61] A. Matraszek, L. Singheiser, D. Kobertz, K. Hilpert, M. Miller, O. Schulz, M. Martin, Solid State Ionics, 166 (2004) 343-350.

[62] S. Wang, T. Kato, S. Nagata, T. Kaneko, N. Iwashita, T. Honda, M. Dokiya, Solid State Ionics, 152–153 (2002) 477-484.

[63] S.R. Wang, T. Kobayashi, M. Dokiya, T. Hashimoto, J Electrochem Soc, 147 (2000) 3606-3609.

[64] F.Y. Wang, S.Y. Chen, W. Qin, S.X. Yu, S.F. Cheng, Catal Today, 97 (2004) 189-194.

[65] X.F. Guan, H.P. Zhou, Z.H. Liu, Y.A. Wang, J. Zhang, Mater Res Bull, 43 (2008) 1046-1054.

[66] S. Lübke, H.D. Wiemhöfer, Solid State Ionics, 117 (1999) 229-243.

[67] X. Sha, Z. Lü, X. Huang, J. Miao, Z. Liu, X. Xin, Y. Zhang, W. Su, Journal of Alloys and Compounds, 433 (2007) 274-278.

[68] M. Mogensen, D. Lybye, N. Bonanos, P.V. Hendriksen, F.W. Poulsen, Solid State Ionics, 174 (2004) 279-286.

[69] T.S. Zhang, J. Ma, Y.J. Leng, S.H. Chan, P. Hing, J.A. Kilner, Solid State Ionics, 168 (2004) 187-195.

[70] E. Jud, Z. Zhang, W. Sigle, L.J. Gauckler, J Electroceram, 16 (2006) 191-197.

[71] R.N. Vannier, G. Mairesse, F. Abraham, G. Nowogrocki, Solid State Ionics, 70 (1994) 248-252.

[72] F. Abraham, J.C. Boivin, G. Mairesse, G. Nowogrocki, Solid State Ionics, 40-1 (1990) 934-937.

[73] T. Takahashi, H. Iwahara, Y. Nagai, J Appl Electrochem, 2 (1972) 97-104.

[74] T. Takahashi, H. Iwahara, T. Arao, J Appl Electrochem, 5 (1975) 187-195.

[75] K.Z. Fung, H.D. Baek, A.V. Virkar, Solid State Ionics, 52 (1992) 199-211.

[76] J.Y. Park, H. Yoon, E.D. Wachsman, Journal of the American Ceramic Society, 88 (2005) 2402-2408.

[77] J.A. Kilner, R.A. DeSouza, Riso Mat Sci, (1996) 41-54.

[78] E. Saiz, R.M. Cannon, A.P. Tomsia, Adv Mater, 12 (2000) 1952-+.

[79] X. Guo, Solid State Ionics, 99 (1997) 137-142.

[80] X. Guo, Solid State Ionics, 96 (1997) 247-254.

[81] I. Kosacki, C.M. Rouleau, P.F. Becher, J. Bentley, D.H. Lowndes, Solid State Ionics, 176 (2005) 1319-1326.

[82] T.Y. Tien, Journal of the American Ceramic Society, 47 (1964) 430-433.

[83] A. Tschöpe, R. Birringer, Journal of Electroceramics, 7 (2001) 169-177.

[84] N. Sata, K. Eberman, K. Eberl, J. Maier, Nature, 408 (2000) 946-949.

[85] S. Azad, O.A. Marina, C.M. Wang, L. Saraf, V. Shutthanandan, D.E. McCready, A. El-Azab, J.E. Jaffe, M.H. Engelhard, C.H.F. Peden, S. Thevuthasan, Applied Physics Letters, 86 (2005).

[86] C. Korte, A. Peters, J. Janek, D. Hesse, N. Zakharov, Phys. Chem. Chem. Phys., 10 (2008) 4623-4635.

[87] C. Korte, N. Schichtel, D. Hesse, J. Janek, Monatsh Chem, 140 (2009) 1069-1080.

[88] J.P. Locquet, C. Marchiori, M. Sousa, J. Fompeyrine, J.W. Seo, J Appl Phys, 100 (2006).

[89] A. Peters, C. Korte, D. Hesse, N. Zakharov, J. Janek, Solid State Ionics, 178 (2007) 67-76.

[90] K.M. Kant, V. Esposito, N. Pryds, Applied Physics Letters, 100 (2012).

[91] J. Garcia-Barriocanal, A. Rivera-Calzada, M. Varela, Z. Sefrioui, E. Iborra, C. Leon, S.J. Pennycook, J. Santamaria, Science, 321 (2008) 676-680.

[92] M.S. Dyer, G.R. Darling, J.B. Claridge, M.J. Rosseinsky, Angew Chem Int Edit, 51 (2012) 3418-3422.

[93] A. Rivera-Calzada, M.R. Diaz-Guillen, O.J. Dura, G. Sanchez-Santolino, T.J. Pennycook, R. Schmidt, F.Y. Bruno, J. Garcia-Barriocanal, Z. Sefrioui, N.M. Nemes, M. Garcia-Hernandez, M. Varela, C. Leon, S.T. Pantelides, S.J. Pennycook, J. Santamaria, Adv Mater, 23 (2011) 5268-5274.

[94] M.J. Jorgensen, M. Mogensen, J Electrochem Soc, 148 (2001) A433-A442.

[95] B. Kenney, K. Karan, Solid State Ionics, 178 (2007) 297-306.

[96] S.B. Adler, J.A. Lane, B.C.H. Steele, J Electrochem Soc, 143 (1996) 3554-3564.

[97] A. Tarancon, M. Burriel, J. Santiso, S.J. Skinner, J.A. Kilner, J Mater Chem, 20 (2010) 3799-3813.

[98] F. Mauvy, J.M. Bassat, E. Boehm, P. Dordor, J.C. Grenier, J.P. Loup, J Eur Ceram Soc, 24 (2004) 1265-1269.

[99] A. Petric, P. Huang, F. Tietz, Solid State Ionics, 135 (2000) 719-725.

[100] J.A. Lane, S.J. Benson, D. Waller, J.A. Kilner, Solid State Ionics, 121 (1999) 201-208.

[101] L. Wang, R. Merkle, J. Maier, T. Acarturk, U. Starke, Appl Phys Lett, 94 (2009).

[102] E. Boehm, J.M. Bassat, P. Dordor, F. Mauvy, J.C. Grenier, P. Stevens, Solid State Ionics, 176 (2005) 2717-2725.

[103] C.N. Munnings, S.J. Skinner, G. Amow, P.S. Whitfield, I.J. Davidson, Solid State Ionics, 176 (2005) 1895-1901.

[104] A. Tarancon, S.J. Skinner, R.J. Chater, F. Hernandez-Ramirez, J.A. Kilner, J Mater Chem, 17 (2007) 3175-3181.

[105] G. Kim, S. Wang, A.J. Jacobson, L. Reimus, P. Brodersen, C.A. Mims, J Mater Chem, 17 (2007) 2500-2505.

[106] B.A. Boukamp, Nat Mater, 2 (2003) 294-296.

[107] S. Tao, J.T.S. Irvine, J.A. Kilner, Adv Mater, 17 (2005) 1734-+.

[108] S.P. Jiang, J Mater Sci, 43 (2008) 6799-6833.

[109] P. Plonczak, M. Gazda, B. Kusz, P. Jasinski, J Power Sources, 181 (2008) 1-7.

[110] A. Mai, V.A.C. Haanappel, S. Uhlenbruck, F. Tietz, D. Stöver, Solid State Ionics, 176 (2005) 1341-1350.

[111] S.P. Simner, J.P. Shelton, M.D. Anderson, J.W. Stevenson, Solid State Ionics, 161 (2003) 11-18.

[112] G.W. Coffey, J. Hardy, L.R. Pedersen, P.C. Rieke, E.C. Thomsen, M. Walpole, Solid State Ionics, 158 (2003) 1-9.

[113] G.W. Coffey, J.S. Hardy, L.R. Pederson, P.C. Rieke, E.C. Thomsen, Electrochem Solid St, 6 (2003) A121-A124.

[114] A. Weber, E. Ivers-Tiffée, J Power Sources, 127 (2004) 273-283.

[115] J.M. Bae, B.C.H. Steele, Solid State Ionics, 106 (1998) 247-253.

[116] V. Dusastre, J.A. Kilner, Solid State Ionics, 126 (1999) 163-174.

[117] C. Xia, M. Liu, Solid State Ionics, 144 (2001) 249-255.

[118] S.Z. Wang, T. Chen, S.P. Chen, J Electrochem Soc, 151 (2004) A1461-A1467.

[119] H. Lv, Y.j. Wu, B. Huang, B.y. Zhao, K.a. Hu, Solid State Ionics, 177 (2006) 901-906.

[120] Z.P. Shao, S.M. Haile, Nature, 431 (2004) 170-173.

[121] Z.H. Chen, R. Ran, W. Zhou, Z.P. Shao, S.M. Liu, Electrochim Acta, 52 (2007) 7343-7351.

[122] W. Zhou, R. Ran, Z.P. Shao, J Power Sources, 192 (2009) 231-246.

[123] V.V. Kharton, A.A. Yaremchenko, A.L. Shaula, M.V. Patrakeev, E.N. Naumovich, D.I. Logvinovich, J.R. Frade, F.M.B. Marques, Journal of Solid State Chemistry, 177 (2004) 26-37.

[124] A.A. Yaremchenko, V.V. Kharton, M.V. Patrakeev, J.R. Frade, J Mater Chem, 13 (2003) 1136-1144.

[125] J. Wan, J.B. Goodenough, J.H. Zhu, Solid State Ionics, 178 (2007) 281-286.

[126] S.J. Skinner, J.A. Kilner, Solid State Ionics, 135 (2000) 709-712.

[127] A. Aguadero, M.J. Escudero, M. Perez, J.A. Alonso, V. Pomjakushin, L. Daza, Dalton T, (2006) 4377-4383.

[128] F. Mauvy, J.M. Bassat, E. Boehm, P. Dordor, J.P. Loup, Solid State Ionics, 158 (2003) 395-407.

[129] A. Aguadero, J.A. Alonso, M.J. Escudero, L. Daza, Solid State Ionics, 179 (2008) 393-400.

[130] A. Maignan, C. Martin, D. Pelloquin, N. Nguyen, B. Raveau, Journal of Solid State Chemistry, 142 (1999) 247-260.

[131] V. Pralong, V. Caignaert, S. Hebert, A. Maignan, B. Raveau, Solid State Ionics, 177 (2006) 1879-1881.

[132] C. Frontera, A. Caneiro, A.E. Carrillo, J. Oro-Sole, J.L. Garcia-Munoz, Chem Mater, 17 (2005) 5439-5445.

[133] A.A. Taskin, A.N. Lavrov, Y. Ando, Applied Physics Letters, 86 (2005).

[134] Z. Yuan, J. Liu, C.L. Chen, C.H. Wang, X.G. Luo, X.H. Chen, G.T. Kim, D.X. Huang, S.S. Wang, A.J. Jacobson, W. Donner, Appl Phys Lett, 90 (2007).

[135] C. Grygiel, S.R.C. McMitchell, Z. Xu, L. Yan, H.J. Niu, D. Giap, J. Bacsa, P.R. Chalker, M.J. Rosseinsky, Chem Mater, 22 (2010) 1955-1957.

[136] S.Q. Hui, A. Petric, J Electrochem Soc, 149 (2002) J1-J10.

[137] A. Chang, S.J. Skinner, J.A. Kilner, Solid State Ionics, 177 (2006) 2009-2011.

[138] A. Tarancón, J. Peña-Martínez, D. Marrero-López, A. Morata, J.C. Ruiz-Morales, P. Núñez, Solid State Ionics, 179 (2008) 2372-2378.

[139] W. Gong, M. Yadav, A.J. Jacobson, MRS Online Proceedings Library, 1126 (2008) null-null.

[140] J.H. Kim, A. Manthiram, J Electrochem Soc, 155 (2008) B385-B390.

[141] J.H. Kim, F. Prado, A. Manthiram, J Electrochem Soc, 155 (2008) B1023-B1028.

[142] J.H. Kim, A. Manthiram, Electrochim Acta, 54 (2009) 7551-7557.

[143] E. Ivers-Tiffee, A. Weber, D. Herbstritt, J Eur Ceram Soc, 21 (2001) 1805-1811.

[144] V.A.C. Haanappel, J. Mertens, D. Rutenbeck, C. Tropartz, W. Herzhof, D. Sebold, F. Tietz, J Power Sources, 141 (2005) 216-226.

[145] S.P. Jiang, W. Wang, Solid State Ionics, 176 (2005) 1185-1191.

[146] S.P. Jiang, Materials Science and Engineering: A, 418 (2006) 199-210.

[147] J.M. Vohs, R.J. Gorte, Adv Mater, 21 (2009) 943-956.

[148] J.D. Nicholas, S.A. Barnett, J Electrochem Soc, 157 (2010) B536-B541.

[149] Y. Ji, J. Liu, T. He, L. Cong, J. Wang, W. Su, Journal of Alloys and Compounds, 353 (2003) 257-262.

[150] A. Subramania, T. Saradha, S. Muzhumathi, J Power Sources, 165 (2007) 728-732.

[151] S. Zha, Y. Zhang, M. Liu, Solid State Ionics, 176 (2005) 25-31.

[152] X. Xu, C. Xia, G. Xiao, D. Peng, Solid State Ionics, 176 (2005) 1513-1520.

[153] N.T. Hart, N.P. Brandon, M.J. Day, J.E. Shemilt, J Mater Sci, 36 (2001) 1077-1085.

[154] P. Holtappels, C. Bagger, J Eur Ceram Soc, 22 (2002) 41-48.

[155] C.R. Xia, W. Rauch, W. Wellborn, M.L. Liu, Electrochem Solid St, 5 (2002) A217-A220.

[156] Z. Fan, F.B. Prinz, Nano Lett, 11 (2011) 2202-2205.

[157] M.H. Hung, M.V.M. Rao, D.S. Tsai, Materials Chemistry and Physics, 101 (2007) 297-302.

[158] M. Ni, M.K.H. Leung, D.Y.C. Leung, International Journal of Hydrogen Energy, 33 (2008) 2337-2354.

[159] J.S. Herring, J.E. O'Brien, C.M. Stoots, G.L. Hawkes, J.J. Hartvigsen, M. Shahnam, International Journal of Hydrogen Energy, 32 (2007) 440-450.

[160] S.D. Ebbesen, M. Mogensen, J Power Sources, 193 (2009) 349-358.

[161] Y.L. Liu, A. Hagen, R. Barfod, M. Chen, H.J. Wang, F.W. Poulsen, P.V. Hendriksen, Solid State Ionics, 180 (2009) 1298-1304.

[162] R. Knibbe, M.L. Traulsen, A. Hauch, S.D. Ebbesen, M. Mogensen, J Electrochem Soc, 157 (2010) B1209-B1217.

[163] A.V. Virkar, International Journal of Hydrogen Energy, 35 (2010) 9527-9543.

[164] K.F. Chen, S.P. Jiang, International Journal of Hydrogen Energy, 36 (2011) 10541-10549.

[165] H. Yang, H.Y. Wang, J. Yoon, Y.Q. Wang, M. Jain, D.M. Feldmann, P.C. Dowden, J.L. MacManus-Driscoll, Q.X. Jia, Advanced Materials, 21 (2009) 3794-3798.

[166] R. Eason, Pulsed Laser Deposition of Thin Films: Applications-Led Growth of Functional Materials, Wiley, New York, 2006.

[167] R.K. Singh, O.W. Holland, J. Narayan, J Appl Phys, 68 (1990) 233-247.

[168] R.K. Singh, J. Narayan, Phys Rev B, 41 (1990) 8843-8859.

[169] T.C. Jeffrey, History and fundamentals of pulsed laser deposition, Pulsed Laser Deposition of Thin Films, Wiley, New York, 1994.

[170] G.J.H.M. Rijnders, G. Koster, D.H.A. Blank, H. Rogalla, Appl Phys Lett, 70 (1997) 1888-1890.

[171] C. Suryanarayana, M.G. Norton, X-Ray Diffraction: A Practical Approach, Springer, New York, 1998.

[172] J. Als-Nielsen, D. McMorrow, Elements of Modern X-ray Physics, John Wiley & Sons Ltd., West Sussex UK, 2001.

[173] V. Holy, U. Pietsch, T. Baumbach, High Resolution X-ray Scattering from Thin Films and Multilayers, Springer 2003.

[174] B. Fultz, J. Howe, Transmission Electron Microscopy and Diffractometry of Materials, 3rd ed., Springer, Verlag Berlin, 2007.

[175] P.J. Goodhew, F.J. Humphreys, R. Beanland, Electron Microscopy and Analysis,, Taylor & Francis, London-New York, 2000.

[176] M.A. O'Keefe, Proceedings of the 3rd Pfeffercorn Conference on Electron Optical Systems, (1984).

[177] D.B. Williams, C.B. Carter, Transmission Electron Microscopy A Textbook for Materials Science, 2nd ed., Springer, New York, 2008.

[178] Y.L. Yang, C.L. Chen, S.Y. Chen, C.W. Chu, A.J. Jacobson, Journal of the Electrochemical Society, 147 (2000) 4001-4007.

[179] Q.-A. Huang, R. Hui, B. Wang, J. Zhang, Electrochim Acta, 52 (2007) 8144-8164.

[180] Y.M.L. Yang, A.J. Jacobson, C.L. Chen, G.P. Luo, K.D. Ross, C.W. Chu, Appl Phys Lett, 79 (2001) 776-778.

[181] H. Apfel, M. Rzepka, H. Tu, U. Stimming, Journal of Power Sources, 154 (2006) 370-378.

[182] H.U. Anderson, Solid State Ionics, 52 (1992) 33-41.

[183] E. Maguire, B. Gharbage, F.M.B. Marques, J.A. Labrincha, Solid State Ionics, 127 (2000) 329-335.

[184] X. Ge, X. Huang, Y. Zhang, Z. Lu, J. Xu, K. Chen, D. Dong, Z. Liu, J. Miao, W. Su, J Power Sources, 159 (2006) 1048-1050.

[185] M. Prestat, A. Morandi, A. Heel, L. Holzer, P. Holtappels, T.J. Graule, Electrochemistry Communications, 12 (2010) 292-295.

[186] X. Chen, N.J. Wu, D.L. Ritums, A. Ignatiev, Thin Solid Films, 342 (1999) 61-66.

[187] N. Pryds, B. Toftmann, J. Schou, P.V. Hendriksen, S. Linderoth, Appl Surf Sci, 247 (2005) 466-470.

[188] F.S. Baumann, J. Fleig, H.U. Habermeier, J. Maier, Solid State Ionics, 177 (2006) 1071-1081.

[189] S.Y. Wang, J. Yoon, G. Kim, D.X. Huang, H.Y. Wang, A.J. Jacobson, Chem Mater, 22 (2010) 776-782.

[190] S. Adler, M. Scherrer, F.D. Daschner, Journal of Hospital Infection, 40 (1998) 125-134.

[191] A.B. Bieberle-Hutter, H.L. Tuller, J Electroceram, 16 (2006) 151-157.

[192] T. Kawada, K. Masuda, J. Suzuki, A. Kaimai, K. Kawamura, Y. Nigara, J. Mizusaki, H. Yugami, H. Arashi, N. Sakai, H. Yokokawa, Solid State Ionics, 121 (1999) 271-279.

[193] F. Zhao, R. Peng, C. Xia, Mater Res Bull, 43 (2008) 370-376.

[194] B.C.H. Steele, J.M. Bae, Solid State Ionics, 106 (1998) 255-261.

[195] D. Beckel, U.P. Muecke, T. Gyger, G. Florey, A. Infortuna, L.J. Gauckler, Solid State Ionics, 178 (2007) 407-415.

[196] C. Peters, A. Weber, E. Ivers-Tiffee, J Electrochem Soc, 155 (2008) B730-B737.

[197] M. Sase, J. Suzuki, K. Yashiro, T. Otake, A. Kaimai, T. Kawada, J. Mizusaki, H. Yugami, Solid State Ionics, 177 (2006) 1961-1964.

[198] F. Tietz, H.P. Buchkremer, D. Stover, Solid State Ionics, 152 (2002) 373-381.

[199] J.H. Kim, A. Manthiram, J Electrochem Soc, 155 (2008) B385-B390.

[200] S. Biswas, T. Nithyanantham, N. Saraswathi, S. Bandopadhyay, J Mater Sci, 44 (2009) 778-785.

[201] I. Petrov, P.B. Barna, L. Hultman, J.E. Greene, J Vac Sci Technol A, 21 (2003) S117-S128.

[202] R. Messier, A.P. Giri, R.A. Roy, Journal of Vacuum Science & Technology a-Vacuum Surfaces and Films, 2 (1984) 500-503.

[203] M. Mogensen, N.M. Sammes, G.A. Tompsett, Solid State Ionics, 129 (2000) 63-94.

[204] J.M. Ralph, C. Rossignol, R. Kumar, Journal of the Electrochemical Society, 150 (2003) A1518-A1522.

[205] Q. Su, D. Yoon, A. Chen, F. Khatkhatay, A. Manthiram, H. Wang, J Power Sources.

[206] M.S.D. Read, M.S. Islam, G.W. Watson, F.E. Hancock, J Mater Chem, 11 (2001) 2597-2602.

[207] J.M. Bassat, P. Odier, A. Villesuzanne, C. Marin, M. Pouchard, Solid State Ionics, 167 (2004) 341-347.

[208] H.U. Krebs, M. Weisheit, J. Faupel, E. Suske, T. Scharf, C. Fuhse, M. Stormer, K. Sturm, M. Seibt, H. Kijewski, D. Nelke, E. Panchenko, M. Buback, Adv Solid State Phys, 43 (2003) 505-517.

[209] Q. Su, S. Cho, Z. Bi, A. Chen, H. Wang, Electrochimica Acta, 56 (2011) 3969-3974.

[210] S.B. Adler, Solid State Ionics, 111 (1998) 125-134.

[211] Y.L. Yang, C.L. Chen, S.Y. Chen, C.W. Chu, A.J. Jacobson, Journal of the Electrochemical Society, 147 (2000) 4001-4007.

[212] Z.G. Lu, J. Hardy, J. Templeton, J. Stevenson, J Power Sources, 196 (2011) 39-45.

[213] B.W. Liu, Y. Zhang, L.M. Zhang, International Journal of Hydrogen Energy, 34 (2009) 1008-1014.

[214] D.J. Chen, R. Ran, K. Zhang, J. Wang, Z.P. Shao, J Power Sources, 188 (2009) 96-105.

[215] T. Kawada, J. Suzuki, M. Sase, A. Kaimai, K. Yashiro, Y. Nigara, J. Mizusaki, K. Kawamura, H. Yugami, Journal of the Electrochemical Society, 149 (2002) E252-E259.

[216] S. Wang, J. Yoon, G. Kim, D. Huang, H. Wang, A.J. Jacobson, Chemistry of Materials, 22 (2010) 776-782.

[217] S. Kim, S. Wang, X. Chen, Y.L. Yang, N. Wu, A. Ignatiev, A.J. Jacobson, B. Abeles, J Electrochem Soc, 147 (2000) 2398-2406.

[218] S.P. Jiang, International Journal of Hydrogen Energy, 37 (2012) 449-470.

[219] J. Hayd, L. Dieterle, U. Guntow, D. Gerthsen, E. Ivers-Tiffee, J Power Sources, 196 (2011) 7263-7270.

[220] L. Dieterle, P. Bockstaller, D. Gerthsen, J. Hayd, E. Ivers-Tiffee, U. Guntow, Adv Energy Mater, 1 (2011) 249-258.

[221] Y. Matsuzaki, I. Yasuda, Solid State Ionics, 132 (2000) 271-278.

[222] C. Zuo, S. Zha, M. Liu, M. Hatano, M. Uchiyama, Advanced Materials, 18 (2006) 3318-3320.

[223] E. Ivers-Tiffée, A. Weber, D. Herbstritt, Journal of the European Ceramic Society, 21 (2001) 1805-1811.

[224] O. Yamamoto, Electrochimica Acta, 45 (2000) 2423-2435.

[225] T. Takahashi, T. Esaka, H. Iwahara, J Appl Electrochem, 7 (1977) 299-302.

[226] X.X. Guo, J. Maier, Advanced Materials, 21 (2009) 2619-2631.

[227] J.L. MaCmanus-Driscoll, P. Zerrer, H.Y. Wang, H. Yang, J. Yoon, A. Fouchet, R. Yu, M.G. Blamire, Q.X. Jia, Nat Mater, 7 (2008) 314-320.

[228] Z.X. Bi, J.H. Lee, H. Yang, Q.X. Jia, J.L. MacManus-Driscoll, H.Y. Wang, J Appl Phys, 106 (2009).

[229] A.P. Chen, Z.X. Bi, C.F. Tsai, J. Lee, Q. Su, X.H. Zhang, Q.X. Jia, J.L. MacManus-Driscoll, H.Y. Wang, Advanced Functional Materials, 21 (2011) 2423-2429.

[230] A.P. Chen, Z.X. Bi, H. Hazariwala, X.H. Zhang, Q. Su, L. Chen, Q.X. Jia, J.L. MacManus-Driscoll, H.Y. Wang, Nanotechnology, 22 (2011).

[231] S.A. Harrington, J.Y. Zhai, S. Denev, V. Gopalan, H.Y. Wang, Z.X. Bi, S.A.T. Redfern, S.H. Baek, C.W. Bark, C.B. Eom, Q.X. Jia, M.E. Vickers, J.L. MacManus-Driscoll, Nat Nanotechnol, 6 (2011) 491-495.

[232] Z.X. Bi, E. Weal, H.M. Luo, A.P. Chen, J.L. MacManus-Driscoll, Q.X. Jia, H.Y. Wang, J Appl Phys, 109 (2011).

[233] J. Yoon, S. Cho, J.H. Kim, J. Lee, Z. Bi, A. Serquis, X. Zhang, A. Manthiram, H. Wang, Advanced Functional Materials, 19 (2009) 3868-3873.

[234] X.D. Zhou, B. Scarfino, H.U. Anderson, Solid State Ionics, 175 (2004) 19-22.

[235] Y. Chen, J.R. Sellar, Solid State Ionics, 86-8 (1996) 207-211.

[236] J.H. Shim, J.S. Park, T.P. Holme, K. Crabb, W. Lee, Y.B. Kim, X. Tian, T.M. Gur, F.B. Prinz, Acta Mater, 60 (2012) 1-7.

[237] S.H. Jensen, P.H. Larsen, M. Mogensen, International Journal of Hydrogen Energy, 32 (2007) 3253-3257.

[238] A. Brisse, J. Schefold, M. Zahid, International Journal of Hydrogen Energy, 33 (2008) 5375-5382.

[239] J.D. Kim, G.D. Kim, J.W. Moon, Y.I. Park, W.H. Lee, K. Kobayashi, M. Nagai, C.E. Kim, Solid State Ionics, 143 (2001) 379-389.

[240] R.A. De Souza, J.A. Kilner, J.F. Walker, Materials Letters, 43 (2000) 43-52.

[241] S. Carter, A. Selcuk, R.J. Chater, J. Kajda, J.A. Kilner, B.C.H. Steele, Solid State Ionics, 53-56 (1992) 597-605.

[242] Q. Su, D. Yoon, A. Chen, F. Khatkhatay, A. Manthiram, H. Wang, Journal of Power Sources, 242 (2013) 455-463.

[243] J. Wang, Y. Zhang, T.X. Liang, C.S. Deng, J.M. Xu, J Power Sources, 208 (2012) 415-420.

[244] J.H. Shim, J.S. Park, T.P. Holme, K. Crabb, W. Lee, Y.B. Kim, X. Tian, T.M. Gür, F.B. Prinz, Acta Materialia, 60 (2012) 1-7.